Principles and Applications of Thermally Generated Flows at the Nanoscale

Von der Fakultät für Physik und Geowissenschaften

der Universität Leipzig

eingereichte

DISSERTATION

zur Erlangung des akademischen Grades

doctor rerum naturalium

Dr. rer. nat.

vorgelegt

von M. Sc., Martin Fränzl

geboren am 26.09.1990 in Annaberg-Buchholz

Gutachter: Prof. Dr. Frank Cichos
Prof. Dr. Ralf Seemann

Tag der Verleihung: 25.04.2022

Bibliographic Description

Fränzl, Martin
Principles and Applications of Thermally Generated Flows at the Nanoscale
Universität Leipzig, Dissertation
164 Pages, 332 References, 135 Figures, 14 Tables

Abstract

This thesis studies principles and applications of thermally generated flows in small liquid volumes with a focus on temperature-induced micro- and nanoscale phenomena such as thermal convection, thermophoresis, depletion forces, thermoelectricity as well as thermo-osmotic flows. The first part of this thesis investigates these principle mechanisms in a thin liquid film over a gold surface and utilizes thermo-osmotic flows combined with attractive van der Waals or depletion forces for the hydrodynamic manipulation of nano-objects. The second part introduces a symmetric self-thermophoretic microswimmmer actuated with a feedback-controlled heating laser and investigates its propulsion velocity and localization accuracy as function of the feedback delay. To achieve the actuation of these active particles also in heterogeneous particle ensembles, part three of this thesis introduces a neural network for the real-time detection in feedback-controlled systems. The last part presents the application of a thermophoretic trap for the investigation of protein aggregation. With this approach we enable the long-time observation of freely diffusion amyloid aggregates and introduce the rotational diffusion coefficient as a very sensitive measure for the growth and fragmentation of single amyloid fibrils.

Referat

Diese Arbeit untersucht Prinzipien und Anwendungen thermisch erzeugter Flüsse in kleinen Flüssigkeitsvolumen mit einem Fokus auf temperaturinduzierte mikro- und nanoskalige Phänomene wie thermische Konvektion, Thermophorese, Depletionskräfte, Thermoelektrizität sowie thermoosmotischen Flüsse. Der erste Teil dieser Arbeit untersucht diese prinzipiellen Mechanismen in einem dünnen Flüssigkeitsfilm über einer Goldoberfäche und nutzt thermoosmotische Flüsse in Kombination mit anziehenden Van-der-Waals- oder Depletionskräften zur hydrodynamischen Manipulation von Nanoobjekten. Der zweite Teil stellt einen symmetrischen, selbstthermophoretischen Mikroschwimmer vor, welcher mit einem rückkopplungsgesteuerten Heizlaser betrieben wird und untersucht dessen Fortbewegungsgeschwindigkeit und Lokalisierungsgenauigkeit als Funktion der Rückkopplungsverzögerung. Um die Steuerung dieser aktiven Partikel auch in heterogenen Partikelensembles zu erreichen, wird im dritten Teil dieser Arbeit ein neuronales Netzwerk für die Echtzeitdetektion in rückkopplungsgesteuerten Systemen vorgestellt. Der letzte Teil stellt die Anwendung einer thermophoretischen Falle zur Untersuchung von Proteinaggregation vor. Mit diesem Ansatz ermöglichen wir die Langzeitbeobachtung frei diffundierender Amyloidaggregate und führen den Rotationsdiffusionskoeffizienten als sehr empfindliche Messgröße für das Wachstum und die Fragmentierung einzelner Amyloidfibrillen ein.

Abbreviations

AOD	Acousto-Optic Deflector
Au	Gold
COM	Center Of Mass
CNN	Convolutional Neural Network
Cr	Chrome
DLVO	Derjaguin–Landau–Verwey–Overbeek
EMCCD	Electron Multiplying Charge-Coupled Device
e.g.	*exempli gratia* – for example
et al.	*et alia* – and others
Eq.	Equation
Fig.	Figure
i.e.	*id est* – that is
IOU	Intersection Over Union
MF	Melamine Formaldehyd
MSD	Mean-Squared Displacement
NA	Numerical Aperture
NMS	Non-Maximum Suppression
NP	Nanoparticle
PEG	Polyethylene Glycol
PDMS	Polydimethylsiloxane
PS	Polystyrene
Ref.	Reference
RMSE	Root-Mean-Square Error
SDS	Sodium Dodecyl Sulfate
Sec.	Section
SEM	Scanning Electron Microscope
SNR	Signal-to-Noise Ratio
SSE	Sum-Squared Error
Tab.	Table
ThT	Thioflavin T
vdW	van der Waals
5CB	4-Cyano-4'-Pentylbiphenyl
1D	One-Dimensional
2D	Two-Dimensional
3D	Three-Dimensional

Contents

Bibliographic Description i

Abbreviations ii

Contents iii

1 Preface 1

2 Theoretical Background 5
- 2.1 Transport in Isothermal Liquids 5
  - 2.1.1 Motion at Low Reynolds Numbers 5
  - 2.1.2 Brownian Motion 6
  - 2.1.3 Brownian Motion Close to Surfaces 9
  - 2.1.4 Sedimentation 10
- 2.2 Forces between Nano-Objects and Surfaces 11
  - 2.2.1 Electrostatic Forces 11
  - 2.2.2 Van der Waals Forces 13
  - 2.2.3 DLVO Theory 14
  - 2.2.4 Beyond DLVO Theory 15
- 2.3 Transport in Liquids of Non-Uniform Temperature 16
  - 2.3.1 Phenomenological Description 16
  - 2.3.2 Thermo-Osmotic Flows 17
  - 2.3.3 Thermophoresis in External Temperature Gradients 21
  - 2.3.4 Depletion Forces 23
  - 2.3.5 Self-Thermophoresis 24
  - 2.3.6 Thermal Convection 25
- 2.4 Interaction of Light with Nano-Objects 26
  - 2.4.1 Gaussian Beams 26
  - 2.4.2 Mie Theory 27
  - 2.4.3 Metal Films 28
  - 2.4.4 Optical Forces 28
- 2.5 Optical Heating of Metal Nanoparticles and Nanostructures 29
  - 2.5.1 Heat Equation 30
  - 2.5.2 Point-Like Heat Source 30
  - 2.5.3 Gaussian Beam Heat Source 31

3 Experimental Prerequisites 33
- 3.1 Experimental Setup 1 33
- 3.2 Experimental Setup 2 34
- 3.3 Sample Preparation 34
- 3.4 Temperature Measurements Using 5CB 35
- 3.5 Zeta Potential Measurements 37

4 Publications 39
- 4.1 Hydrodynamic Manipulation of Nano-Objects by Thermo-Osmotic Flows 41
  - 4.1.1 Abstract 41

4.1.2 Introduction . . . 42
4.1.3 Results and Discussion . . . 43
4.1.4 Conclusion . . . 50
4.1.5 Supplementary Information . . . 51
4.2 Fully Steerable Symmetric Thermoplasmonic Microswimmers . . . 63
4.2.1 Abstract . . . 63
4.2.2 Introduction . . . 64
4.2.3 Results and Discussion . . . 65
4.2.4 Conclusion . . . 73
4.2.5 Supplementary Information . . . 75
4.3 Active Particle Feedback Control with a Single-Shot Detection Neural Network . 83
4.3.1 Abstract . . . 83
4.3.2 Introduction . . . 84
4.3.3 Results and Discussion . . . 85
4.3.4 Conclusion . . . 92
4.3.5 Supplementary Information . . . 93
4.4 Thermophoretic Trap for Protein Aggregation Studies . . . 105
4.4.1 Abstract . . . 105
4.4.2 Introduction . . . 106
4.4.3 Results and Discussion . . . 107
4.4.4 Conclusion . . . 114
4.4.5 Supplementary Information . . . 115

5 Summary and Outlook 127

A Appendix 131
A1 Theoretical Background . . . 131
A2 Experimental Prerequisites . . . 141

List of Publications 143

Declaration 146

Acknowledgement 147

Bibliography 148

Preface

1

Temperature-driven effects have been used for the trapping of micro- and nanoparticles[1–6] and single molecules[7,8] as well as for the driving of self-propelled Janus particles[9–12] and already found applications in catalytic chemistry[13–15] and biotechnology[16–18]. This has sparked the interest of an increasing number of research areas, ranging from thermophotovoltaics[19,20] and waste-heat harvesting[21] to photonics[22,23] and nanomedicine[24–26]. Within the last decades the generation of heat at the nanoscale has advanced from an often undesired side effect into the fields of thermoplasmonics[27,28] and thermo-optofluidics[29,30], where optically heated plasmonic nanostructures are purposefully employed as highly efficient nanoscale sources of heat, remotely controlled by light[28,31]. As these systems are typically implemented in liquid environments, one of the key challenges for the development of future applications is the characterization and design of thermally generated flows. In small liquid volumes non-uniform temperatures induce a series of micro- and nanoscale phenomena such as thermal convection[32–34], thermophoresis[35–45], depletion forces[46,47], thermoelectricity[35,48] as well as thermo-osmotic flows[49]. In spite of extensive experimental[3–6,32,33,35–52] and theoretical efforts[53–59] many of these mechanisms are still a matter of debate and there is only a very limited understanding of their interplay. In particular, the composition of the liquid (concentration and type of salt, surfactant molecules, polymers, . . .) and the influence of interfacial properties (electric double layer, van der Waals forces, molecular surface coatings, . . .) are a subject of ongoing discussions. In thermo-optofluidic experiments the above mentioned temperature-driven effects are typically superimposed and observed at the same time. Nevertheless, in many experimental works the temperature-induced transport of particles and molecules is only discussed in terms of thermophoresis, ignoring thermo-osmotic flows induced at the boundaries of the sample[60,61], or the observations are primarily attributed to thermoelectric effects, while forces arising from thermally driven depletion are neglected[62]. The lack of experimental methods to individually quantify these effects has recently led to an increasing number of inconclusive interpretations of experimental results[3–6,52,61] in the field of thermo-optofluidics. In publication P1 of this thesis we aim to disentangle these effects in a simple sample geometry and provide evidence for the central role of thermo-osmotic flows within a quantitative framework. By characterizing the individual contributions of thermal convection, thermo-osmotic flows, thermophoresis and thermally driven depletion we establish a general scheme for nanofluidic manipulations. Based on the concept of thermo-osmotic flows, publications P2 and P3 then study a symmetric self-thermophoretic microswimmer and investigate its feedback-controlled actuation. Finally, publication P4 presents a thermophoretic trap for the investigation of protein aggregation, where our previous findings on thermophoresis established the principles for the trap design and its characterization.

Whenever a liquid–solid interface is subjected to a non-uniform temperature, interfacial flows are induced: Within a small liquid layer close to the interface the liquid interacts with the solid surface (electric double layer, van der Waals forces, . . .) and, as the strength of these interactions depends on temperature, a non-uniform temperature along the interface will cause an osmotic pressure in the liquid interaction layer that leads to a slip flow parallel to the solid surface[63]. These thermo-osmotic flows have been directly measured only recently[49] even though they have been theoretically described already in 1941[64,65]. So far, characterized only at the water–glass interface[49], one of the open questions is the strength of these flows at the interface between water and gold. In particular this raises the question which type of interaction dominates on metal–water interfaces. In publication P1 we use a thin gold film on a glass substrate, locally heated by a focused laser, and study the transport of particles suspended in a liquid over the gold film. This allows the direct measurement of the thermo-osmotic slip flow on the water–gold interface as well as the identification of contributions from varying compositions of the liquid as well as different types of particles. We substantiate our experimental results with a quantitative theoretical description providing a fundamental understanding for further applications and attempt to clarify frequent misconceptions in literature. The hydrodynamic forces caused by the thermo-osmotic flow field combined with attractive van der Waals or depletion forces enable the trapping of single and multiple nanoparticles as well as their transport and accumulation. Furthermore, a flow field multiplexing scheme has been developed to allow for the simultaneous manipulation of many individual nano-objects and the generation of complex effective flow patterns. Combined with other thermally induced effects such as thermophoresis, depletion forces, and thermoviscous flows[66,67], we outline a highly versatile nanofluidic system on a chip.

In the pursuit towards engines and machines at the smallest length scales, recently a large variety of artificial micro- and nanoswimmers has been developed[9,68–75]. With a wealth of different propulsion mechanisms these self-propelled particles allow to construct complex self-assembled micromachines[76–79] and provide valuable physical insights into the collective behaviour of active particle systems[80]. Yet, all of these systems employ microswimmers with a structural asymmetry required for a self-propelled motion at low Reynolds numbers[71,73,74,81–84]. This asymmetry binds the propulsion direction to the particles' symmetry axis, and hence, rotational Brownian motion randomizes its directed motion on long time scales. The control over the propulsion direction on the individual level can be regained when the propulsion mechanism is switchable, for example, when using self-thermophoretic Janus particles[10,11]. Their feedback-controlled actuation scheme is, nevertheless, limited to the time scale of the rotational diffusion. To overcome this limitation, publication P2 of this thesis introduces a symmetric self-thermophoretic microswimmer. Its propulsion direction is set by the location of the heating laser itself, providing a higher level of control than possible for Janus-type particles. These symmetric thermoplasmonic microswimmers are already of great interest in the field of active matter and have recently been employed to study structures emerging from information exchange[85]. So far, their actuation scheme has not been investigated in detail. Publication P2 provides a quantitative model for their self-thermophoretic propulsion as well as optimal parameters to maximize their propulsion velocity and localization accuracy. We find a dependence on the feedback delay as well as on the displacement of the laser focus which is confirmed within our model. Furthermore, we reveal a directional uncertainty caused by the delayed response, suggesting that, if microscopic objects try to reach a target, large propulsion velocities are actually not beneficial if the objects respond with a delay. Finally, we demonstrate the individual control of multiple symmetric swimmers with a multiplexed actuation scheme of interest for the development of more complex self-propelled particle systems[86,87] as well as for the study of active matter[80,88].

To achieve the actuation of active particles also in heterogeneous particle ensembles, publication P3 introduces a real-time detection neural network for feedback-controlled applications. The real-time detection of objects in optical microscopy allows their direct manipulation, which has recently become a new tool in the fields of single molecule detection[8,89,90] and synthetic active matter[10,11,85]. The recent advances in these fields require to be able to localize and classify more complex objects than single particles, which may have a very heterogeneous contrast and low signal-to-noise ratios in the images. This task is becoming increasingly difficult with conventional particle tracking approaches[91–99]. We demonstrate an approach using a single-shot neural network that is capable of localizing and classifying a large number of objects in optical microscopy images. In contrast to other approaches[100–106], that target the post-processing of images, our network is optimize for a small latency to allow for high frame rates. This real-time processing enables us to provide feedback even to complex samples with objects of different signal-to-noise ratios and at high accuracy. The detection speed is thereby independent of the number of particles and the complexity of the image and able to detect objects at very low signal-to-noise ratios. We demonstrate its experimental application to the feedback-controlled self-thermophoretic microswimmers introduced in publication P2 and evaluate the accuracy of the neural network in terms of particle localization and classification under different conditions.

The aggregation of soluble proteins into highly ordered insoluble amyloid fibrils is fundamental for life and characteristic for a large range of disorders as well as functional structures[107–113]. One of the challenges in the study of protein aggregation and amyloid formation is the disentanglement of the sample heterogeneity that is inherent to the nucleation and growth process of protein aggregates. So far, most of the information on the growth of fibrillar protein structures is inferred from studies of the ensemble growth kinetics, where all species ranging from monomers via oligomers, protofibrils and fibrils of different length are probed at the same time[114–118]. From these results, combined with modeling approaches[119], a number of processes termed secondary nucleation have been suggested which involve, for example, the branching and fragmentation of fibrils as important processes for the formation of pathogenic structures. Though, none of these secondary processes has ever been observed directly due to the lack of experimental techniques which allow observing a single fibril for longer time periods free in solution. Since the invention of optical tweezers, the trapping of nano-objects has evolved into an integral part of life science[120–122]. To scale this concept down to the single molecule level, advanced techniques[123] such as electrokinetic[90] and thermophoretic traps[8] have been developed. In particular, these methods have the unique potential to study the aggregation of proteins on the level of single molecules without surface attachment. In publication P4 we present a thermophoretic trap for single amyloid fibrils that allows the investigation of fibril growth, secondary nucleation or fibril breakup that is typically hidden in the average ensemble. The trapping scheme is based on the thermophoretic drift of macromolecules[124] allowing to probe the dynamics of a single fibril at various stages of its growth. It is shown that the rotational diffusion coefficient provides a unique measure to follow the growth of single fibrils with a precision below the optical resolution.

Structure of this Thesis

- **Chapter 1** is the present preface.

- **Chapter 2** provides the common theoretical background for the publications presented in Chapter 4. Sec. 2.1 starts with the fundamental principles of transport in isothermal liquids. This section gives an introduction to diffusion and Brownian motion and discusses fluid dynamics at low Reynold numbers. In particular, this section focuses on the diffusion close to surfaces. Sec. 2.2 provides an overview on forces between nano-objects and surfaces in liquid environments. This section introduces the electric double layer followed by the van der Waals interaction between two surfaces. The van der Waals interaction together with the interaction of two electric double layers then leads to the Derjaguin–Landau–Verwey–Overbeek (DLVO) theory. Within Sec. 2.3 the transport in liquids of non-uniform temperature is discussed. This section starts with an introduction to thermo-osmotic flows and proceeds to a description of particle thermophoresis as well as self-thermophoresis within the context of thermo-osmotic flows. Sec. 2.4 then reviews the interaction of light with nano-objects in the framework of Mie theory and discusses the optical properties of thin metal films. The last part, Sec. 2.5, presents analytical and numerical results for the optical heating of plasmonic nano-objects and their surroundings.

- **Chapter 3** introduces the experimental prerequisites for this thesis. First, Secs. 3.1 and 3.2 explain the two experimental setups used throughout this thesis. Sec. 3.3 then describes the basic sample preparation. Next, Sec. 3.4 presents the experimental methods used to estimate the temperature increment in the samples. The last part, Sec. 3.5, provides details on the zeta potential measurements used in Sec. 4.1.

- **Chapter 4** contains the main results of this thesis and is divided into four different sections, each corresponding to a peer-reviewed journal publication (P1–P4). These sections feature individual abstract, introduction, results and discussion as well as conclusion subsections. The text and figures of the original publications have been edited and adapted to integrate into the layout of this thesis. Parts from the publications' supplementary information have been moved to chapter 2 or the results and discussion sections to provide an improved reading experience. Sec. 4.1 investigates the trapping and manipulation of nano-objects by thermo-osmotic flows in close proximity to an optically heated gold surface. A detailed analysis of the flow fields, the localization accuracy of nano-objects and a comparison with numerical and theoretical predictions provide a quantitative understanding of these effects. Sec. 4.2 studies a fully steerable symmetric thermoplasmonic microswimmer. We investigate their self-thermophoretic propulsion in detail and highlight the influence of the feedback delay. In this context Sec. 4.3 introduces a single-shot detection neural network that enables the real-time localization and classification of objects in microscopic images. We analyze the network performance with synthetic test images and demonstrate its experimental application to the feedback control of self-thermophoretic microswimmers introduced in the previous section. Finally, Sec. 4.4 presents a thermophoretic trapping platform for protein aggregation studies. It demonstrates a method for the observation of single amyloid fibrils that allows the investigation of fibril growth, secondary nucleation or fibril breakup. Furthermore, it is shown that the rotational diffusion coefficient provides a unique measure to follow the growth of single fibrils with a precision below the optical resolution limit.

- **Chapter 5** presents a summary of the results and provides an overall outlook.

Theoretical Background

2

2.1 Transport in Isothermal Liquids

The aim of this section is to provide an introduction into the physics of fluid motion and diffusion on microscopic length scales. The first part presents the governing equations of fluid motion and emphasizes the consequences of the low Reynolds number regime. This is followed by a description of Brownian motion and diffusion and complemented by a discussion of Brownian motion close to surfaces. The section closes with a description of sedimentation.

2.1.1 Motion at Low Reynolds Numbers

Based on the conservation of mechanical momentum the Navier–Stokes equation (NSE) describes the velocity field $\boldsymbol{v}(\boldsymbol{r},t)$ within a fluid due to pressure gradients and external forces. If the fluid is a liquid, the velocity field can be treated as incompressible, $\nabla \cdot \boldsymbol{v} = 0$, and the NSE reads[125]

$$\varrho \left(\frac{\partial \boldsymbol{v}}{\partial t} + (\boldsymbol{v} \cdot \nabla)\boldsymbol{v} \right) = -\nabla p + \eta \nabla^2 \boldsymbol{v} + \boldsymbol{f} \ , \tag{2.1}$$

where p is the pressure in the liquid, f the external force density, ϱ is the density and η the viscosity of the liquid. Besides pressure gradients ∇p and external forces $\boldsymbol{f}$ the liquid may be driven by time-dependent boundary conditions. The ratio between the inertial forces, $\varrho\,(\boldsymbol{v} \cdot \nabla)\boldsymbol{v}$, and viscous forces, $\eta \nabla^2 \boldsymbol{v}$, is defined as Reynolds number Re. If we identify the operator ∇ with the inverse of a length scale, $\nabla \sim L^{-1}$, we find[126]:

$$\mathrm{Re} = \frac{\varrho\, v^2 L^{-1}}{\eta\, v L^{-2}} = \frac{\varrho\, v L}{\eta} \ . \tag{2.2}$$

For a microscopic length and velocity scale of $L \sim 1$ µm and $v \sim 1$ µm s^{-1} and a density and viscosity of $\varrho = 10^3\,\mathrm{kg\,m^{-3}}$ and $\eta = 10^{-3}\,\mathrm{Pa\,s}$ for water the Reynolds number yields $\mathrm{Re} \sim 10^{-6} \ll 1$. Hence, the inertial forces $\varrho\,(\boldsymbol{v} \cdot \nabla)\boldsymbol{v}$ in Eq. (2.1) can be neglected leading to an entirely laminar flow in microscopic systems. In the stationary case, $\partial \boldsymbol{v}/\partial t = 0$, Eq. (2.1) further reduces to the Stokes equation:

$$\eta \nabla^2 \boldsymbol{v} = \nabla p - \boldsymbol{f} \ . \tag{2.3}$$

If we identify the time derivative with an inverse time scale $\partial/\partial t \sim v/L$, we find that also the term $\varrho\, \partial \boldsymbol{v}/\partial t$ in Eq. (2.1) scales with the Reynolds number. Hence, at low Reynolds numbers any change of the pressure gradient or external force density will result in a quasi-instantaneous change of the velocity field.

Using Eq. (2.3) it can be shown that the friction coefficient γ, defined as

$$\boldsymbol{F} = \gamma \boldsymbol{u} \ , \tag{2.4}$$

to drag a sphere with velocity $\boldsymbol{u}$ through a liquid by an external force $\boldsymbol{F}$ is given by[125]

$$\gamma = 6\pi\eta R \ , \tag{2.5}$$

where R is the radius of the sphere. The velocity field around the particle is long-ranged and decays with $v \propto r^{-1}$, where r is the distance from the particle (Fig. 2.1).

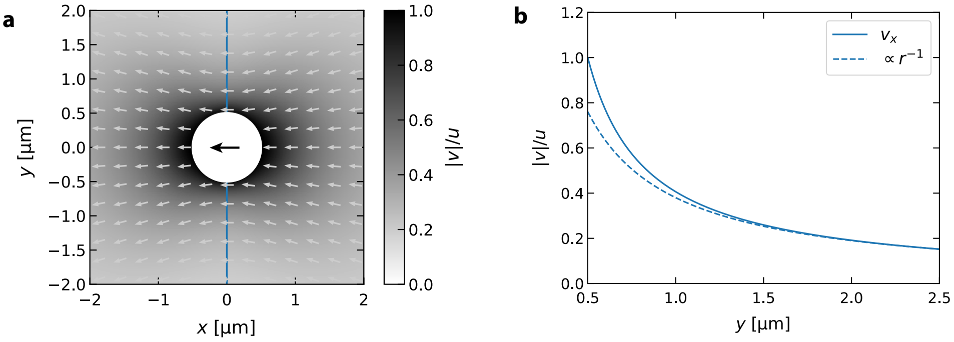

Fig. 2.1: **a**, The velocity field $|v|/u$ past a sphere that is dragged through a liquid with velocity u by an external force in the laboratory frame (see Appendix A1.1 for details). The arrows depict the normalized direction vectors. The sphere has a radius of $R = 0.5$ µm. **b**, The x-component of the velocity along the blue line in (**a**).

Consider a sphere of radius $R = 1$ µm that is dragged through water with a velocity $u_0 = 10\ \mu\mathrm{m\,s^{-1}}$ by an external force (Fig. 2.1) . Its deceleration, once the force is removed, is determined by $m\,\mathrm{d}u/\mathrm{d}t = -\gamma u$ where m is the mass of the sphere and γ the friction coefficient given in Eq. (2.5). We find:

$$u(t) = u_0 \exp\left(-\frac{\gamma}{m}t\right) \tag{2.6}$$

with a decay time of $\tau = m/\gamma \sim 0.1$ µs and a displacement of less than $\Delta d = u_0\tau \sim 0.01$ nm. We have used $m = \varrho V$ with a density in the order of $\varrho \sim 10^3\ \mathrm{kg\,m^{-3}}$ and $V = 4/3\pi R^3$ for the volume of the sphere. This example illustrates that at low Reynolds numbers any interia is immediately suppressed by viscous forces, rendering the motion in microscopic systems overdamped. This imposes fundamental constraints on the self-propulsion of microswimmers[81] that will be further emphasized in Sec. 4.2.

2.1.2 Brownian Motion

Brownian motion denotes the stochastic motion of micro- and nano-objects suspended in liquids caused by random collisions with the molecules of the liquid. A mathematical description of Brownian motion can be either given by focusing on the stochastic trajectory $x(t)$ of a single particle or in terms of the probability density distribution $p(x,t)$ of an ensemble of Brownian particles. Both approaches are closely related, each providing a different view on the problem. The probability density distribution is obtained from averaging over many individual realizations of a trajectory while the statistical properties of stochastic trajectories are connected to the probability density distribution. This section will give an overview of these theories.

Langevin Equation A microscopic description of Brownian motion can be given in terms of the Langevin equation by adding a stochastic force to Newton's equation of motion[127–129]:

$$m\frac{\mathrm{d}^2x}{\mathrm{d}t^2} = -\gamma\frac{\mathrm{d}x}{\mathrm{d}t} - \frac{\mathrm{d}}{\mathrm{d}x}U(x) + \sqrt{2D}\gamma\,\xi(t) \ . \tag{2.7}$$

Here, the term $F = -\gamma\,\mathrm{d}x/\mathrm{d}t$ resembles the drag force introduced in Eq. (2.4) and the term $F = -\mathrm{d}U(x)/\mathrm{d}x$ describes the force exerted by an external potential $U(x)$. The function $\xi(t)$

in the stochastic force term, $\sqrt{2D}\gamma\,\xi(t)$, is a stochastic variable with zero mean and a delta-correlated Gaussian distribution:

$$\langle \xi(t) \rangle = 0 \ , \quad \langle \xi(t)\xi(t') \rangle = \delta(t-t') \ . \tag{2.8}$$

The factor $\sqrt{2D}$ used for the weighting of $\xi(t)$ will be motivated below. In the low Reynolds number regime the inertial force on the left side of Eq. (2.7) can be dropped and one obtains the overdamped Langevin equation[129]:

$$\frac{\mathrm{d}x}{\mathrm{d}t} = -\frac{1}{\gamma}\frac{\mathrm{d}}{\mathrm{d}x}U(x) + \sqrt{2D}\,\xi(t) \ . \tag{2.9}$$

First, we consider the case of no external potential, $U(x) = 0$, where Eq. (2.9) simplifies to:

$$\frac{\mathrm{d}x}{\mathrm{d}t} = \sqrt{2D}\,\xi(t) \ . \tag{2.10}$$

As $\xi(t)$ is a stochastic variable, the particle position $x(t) = x(0) + \sqrt{2D}\int_0^t \xi(t')\,\mathrm{d}t'$ is a stochastic variable as well and no prediction can be made for the realization of an individual trajectory (Fig. 2.2a). The mean particle displacement averaged over many individual realizations vanishes, $\langle \Delta x(t) \rangle = \langle x(t) - x(0) \rangle = 0$, whereas the mean squared displacement (MSD) takes a finite value:

$$\langle \Delta x^2(t) \rangle = \langle (x(t) - x(0))^2 \rangle = 2Dt \ . \tag{2.11}$$

For a derivation of Eq. (2.11) see Appendix A1.2. Considering an ensemble of Brownian particles, their probability density distribution is defined by

$$p(x,t) = \langle \delta(x - x(t)) \rangle \ , \tag{2.12}$$

where the average, again refers to the mean of many individual realizations of the stochastic variable $x(t)$. The function $p(x,t)$ describes the probability $p(x,t)\,\mathrm{d}x$ to find a Brownian particle within the interval $x + \mathrm{d}x$ at time t and is normalized such that $\int_{-\infty}^{\infty} p(x,t)\,\mathrm{d}x = 1$. Combining Eqs. (2.12) and (2.10) leads to the free diffusion equation (Appendix A1.3):

$$\frac{\partial p(x,t)}{\partial t} = D\,\frac{\partial^2 p(x,t)}{\partial x^2} \ , \tag{2.13}$$

where we identify D as the diffusion coefficient, motivating the initial weighting of $\xi(t)$ with $\sqrt{2D}$. From a macroscopic point of view the probability density distribution $p(x,t)$ is fully equivalent to a concentration $c(x,t)$. Eq. (2.13) is then called Fick's second law, $\partial_t c = D\,\partial_x^2 c$.

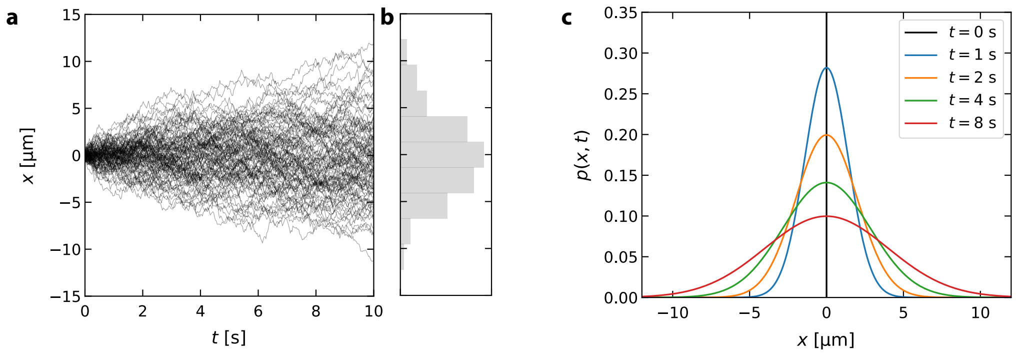

Fig. 2.2: **a**, Simulated trajectories $x(t)$ of Brownian particles ($N = 100$) released at $t = 0$ s from $x(0) = 0$ µm with $D = 1$ µm^2 s^{-1}. We used $x(t + \Delta t) = x(t) + \sqrt{2D}\sqrt{\Delta t}\,\xi_t$ for the discretisation of Eq. (2.10)[130] and Gaussian distributed random numbers ξ_t with zero mean and variance one. **b**, Histogram of the particle positions in (**a**) at $t = 10$ s. **c**, The time evolution of the corresponding probability density distribution $p(x,t)$ according to Eq. (2.16).

As the particle number needs to be constant, we can introduce the continuity equation:

$$\frac{\partial p(x,t)}{\partial t} = -\frac{\partial j(x,t)}{\partial x} \; , \tag{2.14}$$

where $j(x,t)$ is the particle flux. From a comparison of Eqs. (2.14) and (2.13) we find

$$j_\mathrm{D}(x,t) = -D\frac{\partial p(x,t)}{\partial x} \tag{2.15}$$

for the particle flux due to diffusion. For a delta-distributed initial distribution, $p(x,0) = \delta(x - x_0)$, the solution of Eq. (2.13) reads (Fig. 2.2c):

$$p(x,t) = \frac{1}{\sqrt{4\pi D t}} \exp\left(-\frac{(x-x_0)^2}{4Dt}\right) . \tag{2.16}$$

We find a Gaussian distribution with a mean of $\langle x \rangle = x_0$ and a variance $\langle x^2 \rangle$ of:

$$\langle x^2 \rangle = \int_{-\infty}^{\infty} x^2 \, p(x,t) \, \mathrm{d}x = 2Dt \; , \tag{2.17}$$

equivalent to the MSD defined in Eq. (2.11). In two dimensions the probability density distribution is given by the product of two independent one-dimensional distributions $p(r,t) = p(x,t)\,p(y,t)$ and the two-dimensional MSD is $\langle r^2 \rangle = 4Dt$ with $r^2 = x^2 + y^2$. Hence, in two dimensions Eq. (2.11) reads:

$$\langle \Delta \boldsymbol{r}^2(t) \rangle = \langle (\boldsymbol{r}(t) - \boldsymbol{r}(0))^2 \rangle = 4Dt \; . \tag{2.18}$$

Fokker–Planck Equation A generalization of the free diffusion equation, Eq. (2.13), is obtained in case an external potential $U(x)$ is exerting a force $F(x) = -\partial_x U(x)$ on the particle. In view of Eq. (2.3) the force $F(x)$ induces a particle velocity of $u(x) = F(x)/\gamma$ and the total particle flux is then given by:

$$j(x,t) = j_\mathrm{U}(x,t) + j_\mathrm{D}(x,t) = u(x)\,p(x,t) - D\frac{\partial p(x,t)}{\partial x} \; , \tag{2.19}$$

where $j_\mathrm{U}(x,t) = u(x)\,p(x,t)$ is the particle flux due to the presence of an external potential and $j_\mathrm{D}(x,t)$ the diffusive particle flux given in Eq. (2.15). Using Eq. (2.14) we obtain the Fokker–Planck equation[131,132]:

$$\frac{\partial p(x,t)}{\partial t} = \frac{\partial}{\partial x}\left(\frac{1}{\gamma}\frac{\partial U(x)}{\partial x} p(x,t) + D\frac{\partial p(x,t)}{\partial x}\right) . \tag{2.20}$$

Boltzmann Distribution In the presence of an external potential the equilibrium probability density distribution is given by the Boltzmann distribution

$$p(x) = p_0 \exp\left(-\frac{U(x)}{k_\mathrm{B}T}\right) , \tag{2.21}$$

where $p_0 = (\int_{-\infty}^{\infty} p(x)\,\mathrm{d}x)^{-1}$ is the normalization factor. In equilibrium the probability density distribution does not depend on time, $\partial_t p(x,t) = 0$, and Eq. (2.20) needs to satisfy:

$$-\frac{1}{\gamma}\frac{\partial U(x)}{\partial x} p(x) = D\frac{\partial p(x)}{\partial x} \; . \tag{2.22}$$

Inserting the spatial derivative of Eq. (2.21) then leads to:

$$-\frac{1}{\gamma}\frac{\partial U(x)}{\partial x} p(x) = -\frac{D}{k_\mathrm{B}T}\frac{\partial U(x)}{\partial x} p(x) \; , \tag{2.23}$$

and we obtain the Einstein–Smoluchowski relation[133,134]:

$$D = \frac{k_\mathrm{B}T}{\gamma} \ . \tag{2.24}$$

Eq. (2.24) relates the thermal fluctuations (D) to the dissipation of kinetic energy (γ) and is a simple representative of the fluctuation-dissipation theorem[135]. For a spherical particle with 1 µm diameter in water ($\eta = 10^{-3}$ Pa s) we find $D = k_\mathrm{B}T/(6\pi\eta R) = 0.43\ \mu\mathrm{m}^2\,\mathrm{s}^{-1}$ at 20 °C ($T = 293.15$ K), where we have used Eq. (2.5) for the friction coefficient of a sphere.
With Eq. (2.24) the Fokker-Planck equation, Eq. (2.20), can be generalized to:

$$\frac{\partial p(x,t)}{\partial t} = \frac{\partial}{\partial x}\left(\frac{1}{k_\mathrm{B}T} D(x) \frac{\partial U(x)}{\partial x} p(x,t) + D(x)\frac{\partial p(x,t)}{\partial x}\right) \tag{2.25}$$

with a position-dependent diffusion coefficient $D(x) = k_\mathrm{B}T/\gamma(x)$. Eq. (2.25) emphasizes that the time evolution of the probability density can also be influenced by a spatial dependence of the diffusion coefficient. The stationary probability distribution, nevertheless, does not depend on the diffusion coefficient and is solely defined by the potential $U(x)$ in terms of the Boltzman distribution, Eq. (2.21). This will be of particular importance in Sec. 4.1.

2.1.3 Brownian Motion Close to Surfaces

The friction of a confined particle increases due to hydrodynamic interactions with the confining surfaces resulting in lower diffusion coefficients. In particular, the friction is different for a motion parallel and perpendicular to a surface. For spherical particles the correction factor $\lambda_\parallel$ for the friction coefficient parallel to a surface, $\gamma_\parallel = \gamma\lambda_\parallel$, can be approximated by[136]

$$\lambda_\parallel^{-1}(z) = \frac{D_\parallel}{D} \approx 1 - \frac{9}{16}\frac{R}{z} + \frac{1}{8}\left(\frac{R}{z}\right)^3 - \frac{45}{256}\left(\frac{R}{z}\right)^4 - \frac{1}{16}\left(\frac{R}{z}\right)^5 \pm \dots \ , \tag{2.26}$$

where z is the distance from the particle center to the surface and R the radius of the particle (Fig. 2.3a). The correction factor $\lambda_\perp$ for the friction coefficient perpendicular to a surface, $\gamma_\perp = \gamma\lambda_\perp$, is given by the exact solution[137]

$$\lambda_\perp^{-1}(z) = \frac{D_\perp}{D} = \left(\frac{4}{3}\sinh(\alpha)\sum_{n=1}^{\infty} N_n \left(\frac{2\sinh((2n+1)\alpha) + (2n+1)\sinh(2\alpha)}{4\sinh^2((n+1/2)\alpha) - (2n+1)^2\sinh^2(\alpha)} - 1\right)\right)^{-1} \tag{2.27}$$

with $\alpha = \operatorname{arcosh}(z/R)$ and $N_n = n(n+1)/((2n-1)(2n+3))$. Fig. 2.3b depicts the predicted values for $D_\parallel/D$ and $D_\perp/D$ as function of the relative particle-surface distance z/R.

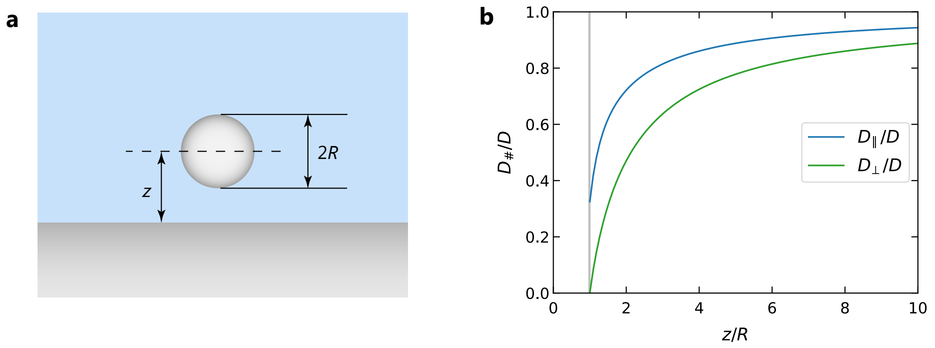

Fig. 2.3: **a**, Sketch of a spherical particle with radius R located at distance z from a surface. **b**, $D_\parallel/D$ and $D_\perp/D$ as function of the relative particle-surface distance z/R calculated from Eq. (2.26) and Eq. (2.27).

The friction parallel to the surface is smaller than in perpendicular direction and takes a finite value at $z/R = 1$. Remarkably, the perpendicular friction coefficient goes to infinity for $z/R \to 1$.

The hydrodynamic interactions are long-range; even at a distance of four times the particle diameter the diffusion coefficients are about 10% smaller than their bulk value. If the particle is located between two surfaces with distance H (Fig. 2.4a) the correction factors for the friction coefficient can be approximated by a linear superposition:

$$\lambda^{\mathrm{II}}(z) = \lambda^{\mathrm{I}}(z) + \lambda^{\mathrm{I}}(H - z) - 1 \ , \tag{2.28}$$

where $\lambda^{\mathrm{I}}(z)$ represents either $\lambda_{\|}(z)$ or $\lambda_{\perp}(z)$. An even better approximation can be given by[138]:

$$\lambda^{\mathrm{II}}(z) = 1 + \sum_{n=0}^{\infty}\left(\lambda^{\mathrm{I}}(z+nH) - 1\right) + \sum_{n=1}^{\infty}\left(\lambda^{\mathrm{I}}(nH - z) - 1\right) - 2\sum_{n=1}^{\infty}\left(\lambda^{\mathrm{I}}(nH) - 1\right) \ . \tag{2.29}$$

Fig. 2.4b compares $D_{\|}/D$ to $D_{\|}^{\mathrm{II}}/D$ for $R = 125$ nm and $H = 3$ μm. For $H/R \gg 2$ the correction factors are well approximated by the single surface correction.

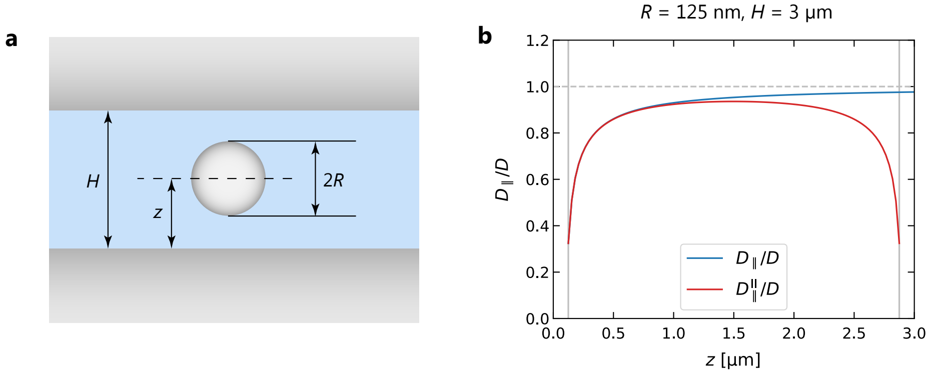

Fig. 2.4: **a**, Sketch of a spherical particle with radius R located at distance z from a surface and confined by a second surface at distance H. **b** depicts $D_{\|}/D$ and $D_{\|}^{\mathrm{II}}/D$ for $R = 125$ nm and $H = 3$ μm calculated from Eq. (2.26) and Eq. (2.29).

2.1.4 Sedimentation

In addition to Brownian motion, particles in typical experimental settings experience a gravitational force $F_{\mathrm{G}} = mg$. Here, g is the gravitational constant and $m = \varrho_1 V$ is the mass of the particle given in terms of the particle density ϱ_1 and the particle volume V. Further, considering the buoyancy force, $F_{\mathrm{B}} = \varrho_2 V g$, the sedimentation force for a spherical particle reads

$$F_{\mathrm{S}} = \frac{4}{3}\pi R^3 (\varrho_1 - \varrho_2)\, g \ , \tag{2.30}$$

where ϱ_2 denotes the density of the liquid and we have used $V = 4/3\pi R^3$ for the volume of the particle. The sedimentation potential then reads $U_{\mathrm{S}}(z) = 4/3\pi R^3(\varrho_1 - \varrho_2)\, gz$. In equilibrium with the drag force, $F = 6\pi\eta R u$, we find the sedimentation velocity $u_{\mathrm{S}} = 2/(9\eta)R^2\,(\varrho_2 - \varrho_1)\, g$. For a gold particle with $R = 125$ nm suspended in water we find $u_{\mathrm{S}} = 0.62\ \mu\mathrm{m\,s^{-1}}$, where we have used $\varrho_1 = 19.3\ \mathrm{g\,cm^{-3}}$, $\varrho_2 = 1.0\ \mathrm{g\,cm^{-3}}$, and $\eta = 0.001$ Pa s. In comparison, for a polystyrene particle ($\varrho_1 = 1.05\ \mathrm{g\,cm^{-3}}$) of the same size we find $u_{\mathrm{S}} = 0.002\ \mu\mathrm{m\,s^{-1}}$. These examples demonstrate that sedimentation can be relevant for gold nanoparticles but may be neglected for nanoparticles with low mass densities such as polystyrene. For the micrometer-sized melamine particles used in Secs. 4.2 and 4.3 ($R = 1.1$ μm, $\varrho_2 = 1.5\ \mathrm{g\,cm^{-3}}$) we find $u_{\mathrm{S}} = 1.32\ \mu\mathrm{m\,s^{-1}}$.
With a gravitational force in z-direction the Fokker–Planck equation for sedimentation reads

$$\frac{\partial p(z,t)}{\partial t} = u_{\mathrm{S}}\frac{\partial p(z,t)}{\partial z} + D\frac{\partial^2 p(z,t)}{\partial z^2} \ . \tag{2.31}$$

Eq. (2.31) is often referred to as Mason-Waever equation[139,140].

2.2 Forces between Nano-Objects and Surfaces

This section discusses liquid–solid interfaces in thermal equilibrium and the forces between nano-objects in liquid environments. The section starts with a description of the electric double layer and the forces arising from two overlapping electric double layers. This is followed by a description of van der Waals forces that leads to the DLVO potential describing the overall interaction potential between charged surfaces in liquid media closing this section.

2.2.1 Electrostatic Forces

Electric Double Layer Typically, surfaces in contact with water are charged. The charging of the surface can be caused by different processes. Oxides are often negatively charged due to the dissociation of hydroxide groups ($-\mathrm{OH} \rightarrow -\mathrm{O}^- + \mathrm{H}^+$), whereas metals attain a negative surface charge due to the adsorption of negative ions[141]. These surface charges cause an electric field that attracts counter ions from the liquid. The diffusive layer of counter ions together with the layer of fixed surfaces charges is called electric double layer (Fig. 2.5).

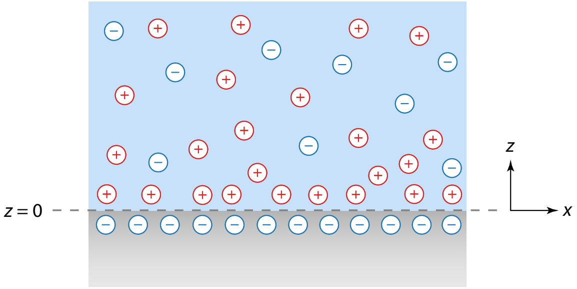

Fig. 2.5: Illustration of the electric double layer close to a negatively charged surface.

For a theoretical description the ions in the liquid are treated as a continuous charge distribution within a mean field approximation. In terms of the Boltzmann distribution the excess densities of monovalent positive and negative ions are then given by[141,142]

$$n_\pm = n_0\left(\mathrm{e}^{\mp e\psi/k_\mathrm{B}T} - 1\right) , \tag{2.32}$$

where n_0 is the bulk salinity and ψ the electric potential. The number densities n are related to concentrations c in $\mathrm{mol\,m^{-3}}$ via the Avogadro constant, $n = N_\mathrm{A}c$. For the charge density ϱ and the excess ion density n we find:

$$\varrho = e\,(n_+ - n_-) = -2en_0 \sinh(e\psi/(k_\mathrm{B}T)) , \tag{2.33}$$

$$n = n_+ + n_- = 2n_0(\cosh(e\psi/(k_\mathrm{B}T)) - 1) . \tag{2.34}$$

Note that we already used the symbol "ϱ" in Sec. 2.1 for the mass density, whereas it is used here for the charge density.

Debye–Hückel Approximation In case of weakly charged surfaces, $e|\psi| \ll k_\mathrm{B}T$, where the potential energy of the ions is smaller than their thermal energy, we can approximate:

$$\varrho \approx -\frac{\varepsilon}{\lambda_\mathrm{D}^2}\psi , \tag{2.35}$$

$$nk_\mathrm{B}T \approx \frac{\varepsilon}{2\lambda_\mathrm{D}^2}\psi^2 . \tag{2.36}$$

We introduced the static permittivity ε of the liquid and the Debye length:

$$\lambda_\mathrm{D} = \left(\frac{\varepsilon k_\mathrm{B}T}{2n_0e^2}\right)^{1/2} . \tag{2.37}$$

The spatial dependence of the potential is then defined by the Poisson equation $\partial_z^2\psi = -\varrho/\varepsilon = \lambda_\mathrm{D}^{-2}\psi$. The solution reads

$$\psi(z) = \zeta\,\mathrm{e}^{-z/\lambda_\mathrm{D}}\ , \tag{2.38}$$

where the zeta potential $\zeta = \psi(z = 0)$ is defined as the potential on the surface. The potential decreases exponentially with the Debye length. For example, the Debye length of a 10 mM aqueous solution at 20 °C is 3 nm. In water λ_D cannot be longer than 680 nm due to the self-ionization of water ($2\,\mathrm{H_2O} \rightarrow \mathrm{H_3O^+} + \mathrm{OH^-}$) as the ion concentration cannot decrease below 10^{-7} M. In practice, the Debye length even in deionized water is only a few 100 nm due to ionic impurities[141]. Fig. 2.6a illustrates the decrease of the Debye length with increasing salt concentration. For a negatively charged surface the concentration of positive ions as well as the total ion concentration are substantially increased close to the surface (Fig. 2.6b).

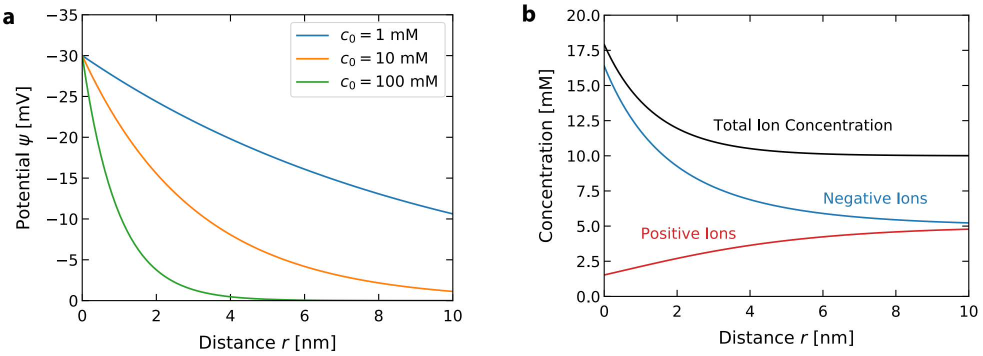

Fig. 2.6: **a**, The potential ψ as function of the distance z for a zeta potential of $\zeta = -30$ mV and different salt concentrations c_0 in water. **b**, The concentration of ions as function of the distance from a surface for a salt concentration of $c_0 = 0.1$ mM and a zeta potential of $\zeta = -30$ mV.

The overall surface charge density σ of the double layer is defined as:

$$\sigma = -\int_0^\infty \varrho\,\mathrm{d}z = \frac{\varepsilon}{\lambda_\mathrm{D}^2}\zeta\int_0^\infty \mathrm{e}^{-z/\lambda_\mathrm{D}}\,\mathrm{d}z = \frac{\varepsilon}{\lambda_\mathrm{D}}\zeta\ . \tag{2.39}$$

We find

$$\zeta = \frac{\sigma\lambda_\mathrm{D}}{\varepsilon}\ , \tag{2.40}$$

relating the zeta potential to the surface charge density. Note that the surface charge density can be a complicated function of the concentration, $\sigma(c_0)$, due to the concentration and pH dependent dissociation of surface groups[143,144]. Nevertheless, at higher salt concentrations the zeta potential will eventually approach zero as $\lambda_\mathrm{D} \propto c_0^{-1/2}$.

Highly Charged Surfaces In case the of high potentials, $e|\psi| \gg k_\mathrm{B}T$, the full one-dimensional Poisson equation $\partial_z^2\psi = 2en_0\sinh(e\psi/(k_\mathrm{B}T))/\varepsilon$ can be solved analytically. The solution reads

$$\psi(z) = \frac{4k_\mathrm{B}T}{e}\tanh^{-1}\left(\tanh\left(\frac{e\zeta}{4k_\mathrm{B}T}\right)\mathrm{e}^{-z/\lambda_\mathrm{D}}\right) \tag{2.41}$$

with the zeta potential given by

$$\zeta = \frac{2k_\mathrm{B}T}{e}\operatorname{arsinh}\left(\frac{2\pi\sigma\lambda_\mathrm{B}\lambda_\mathrm{D}}{e}\right) \tag{2.42}$$

and the Bjerrum length $\lambda_\mathrm{B} = e^2/(4\pi\varepsilon k_\mathrm{B}T)$. A derivation can be found in Appendix A1.5.

Strictly, the approximation of weakly charged surfaces ($e|\psi| \ll k_\mathrm{B}T$) is only valid for $|\psi| < 25$ mV at 20 °C ($T = 293.15$ K). Nevertheless, the Debye–Hückel approximation is still a sufficiently good approximation for potentials of up to 50 mV (Fig. 2.7). Hence, the electric double layer in this work will be mostly treated in the limit of weakly charged surfaces as the surface considered in this work have zeta potentials in the range $|\zeta| = 30 - 40$ mV.

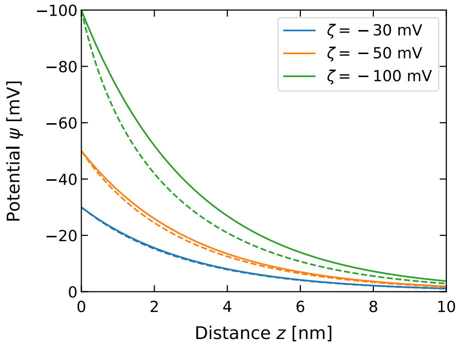

Fig. 2.7: The potential ψ as function of the distance z for a salt concentration of $c_0 = 10$ mM and different zeta potentials ζ in water. The solid curves represent the Debye–Hückel approximation, Eq. (2.38), whereas the dashed curves depict the full solution, Eq. (2.41).

Forces between Electric Double Layers If two like-charged surfaces approach each other, their electric double layers overlap and a repulsive electrostatic force arises. For a sphere close to a planar surface the electrostatic potential is described by[142,145]

$$U_\mathrm{E}(d, c_0) \approx 64\pi\varepsilon R \left(\frac{k_\mathrm{B}T}{e}\right)^2 \tanh^2\left(\frac{e\zeta}{4k_\mathrm{B}T}\right) \mathrm{e}^{-d/\lambda_\mathrm{D}} \,, \tag{2.43}$$

where R is the radius of the sphere, ε the static permittivity of the liquid and d is the surface distance (Fig. 2.8). Here, we assumed that the sphere and the planar surface have the same zeta potential ζ. In case of asymmetric zeta potentials one may approximate the term $\tanh^2(e\zeta/(4k_\mathrm{B}T))$ with $\tanh(e\zeta_1/(4k_\mathrm{B}T))\tanh(e\zeta_2/(4k_\mathrm{B}T))$, where ζ_1 and ζ_2 are the zeta potentials of the sphere and the planar surface, respectively[50]. Note that the dependence on the concentration c_0 enters Eq. (2.43) only with the Debye length λ_D. Expressions for the electrostatic potential between other geometries can be found in Ref. 142.

2.2.2 Van der Waals Forces

In addition to electrostatic forces, surfaces interact through van der Waals forces. Van der Waals forces are attractive and arise from the interaction of fluctuating dipole moments in the electron distribution of the surface atoms. For a sphere (medium 1) interacting with a planar surface (medium 2) across medium 3 the van der Waals potential is[146]

$$U_\mathrm{vdW}(d) = -\frac{A_\mathrm{H}}{6}\left(\frac{R}{d} + \frac{R}{2R+d} + \ln\left(\frac{d}{2R+d}\right)\right), \tag{2.44}$$

where A_H is the Hamaker constant. Again, R is the radius of the sphere and d the surface distance (Fig. 2.8). Based on the Lifshitz theory of the van der Waals force[142,147] a macroscopic approximation of the Hamaker constant can be given by

$$A_\mathrm{H} \approx \frac{3}{4}k_\mathrm{B}T\left(\frac{\varepsilon_1-\varepsilon_3}{\varepsilon_1+\varepsilon_3}\right)\left(\frac{\varepsilon_2-\varepsilon_3}{\varepsilon_2+\varepsilon_3}\right) + \frac{3h}{4\pi}\int_{\nu_1}^{\infty}\left(\frac{\varepsilon_1(\mathrm{i}\nu)-\varepsilon_3(\mathrm{i}\nu)}{\varepsilon_1(\mathrm{i}\nu)+\varepsilon_3(\mathrm{i}\nu)}\right)\left(\frac{\varepsilon_2(\mathrm{i}\nu)-\varepsilon_3(\mathrm{i}\nu)}{\varepsilon_2(\mathrm{i}\nu)+\varepsilon_3(\mathrm{i}\nu)}\right)\mathrm{d}\nu \,, \tag{2.45}$$

where $\varepsilon_1(\mathrm{i}\nu)$, $\varepsilon_2(\mathrm{i}\nu)$ and $\varepsilon_3(\mathrm{i}\nu)$ are the permittivities of the three media at imaginary frequencies $\mathrm{i}\nu$, ε_1, ε_2, and ε_3 are the static permittivity, $\nu_1 = 2\pi k_\mathrm{B}T/h$, and h is the Planck constant.

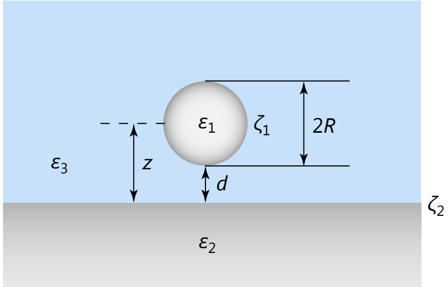

Fig. 2.8: Sketch of a sphere with radius R (medium 1) with a surface-to-surface distance $d = z - R$ from a planar surface (medium 2) surrounded by medium 3.

An approximation of Eq. (2.45) for dielectric materials is given in Appendix A1.6. As can be inferred from Tab. 2.1, the Hamaker constant of gold is about one order of magnitude larger than for dielectric media such as glass and polystyrene. Expressions for the van der Waals potential between other geometries can be found in Refs. 142.

Tab. 2.1: Hamaker constants A_H for the material systems relevant in this study. For the dielectric material systems we have used the equations and the dielectric data in Appendix A1.6. The value for the Gold/Water/Gold material system has been taken from Ref. 148. For a discussion of experimental values see Ref. 149. The value for Gold/Water/Glass has been estimated using Eq. (2.46).

Medium 1	Medium 3	Medium 2	A_H [10^{-20} J]
Glass	Water	Glass	0.6
Polystyrene	Water	Polystyrene	1.4
Polystyrene	Water	Glass	0.9
Gold	Water	Gold	10
Gold	Water	Glass	2.5

A useful combining relation to approximate unknown Hamaker constants can be derived from Eq. (2.45). If we define A_{132} as the Hamaker constant of medium 1 interacting across medium 3 with medium 2, we find[142]:

$$A_{132} \approx \sqrt{A_{131} A_{232}} \ , \tag{2.46}$$

where A_{131} is the Hamaker constant of medium 1 interacting across medium 3 with itself and A_{232} is the Hamaker constant of medium 2 interacting across medium 3 with itself.

2.2.3 DLVO Theory

The DLVO theory, named after Derjaguin, Landau, Verwey, and Overbeek, describes the total interaction potential between charged surfaces in liquid media[150,151]. As discussed previously the total potential comprises a repulsive electrostatic contribution, Eq. (2.43), and an attractive van der Waals contribution, Eq. (2.44):

$$U_\mathrm{DLVO}(d, c_0) = U_\mathrm{E}(d, c_0) + U_\mathrm{vdW}(d) \ . \tag{2.47}$$

The DLVO potential for gold particle with radius $R = 125$ nm as function of the distance d to a glass surface is shown in Fig. 2.9a for a concentration of $c_0 = 10$ mM. We have used a zeta potential of $\zeta = -30$ mV and a Hamaker constant of $A_\mathrm{H} = 2.5 \cdot 10^{-20}$ J (Tab. 2.1).

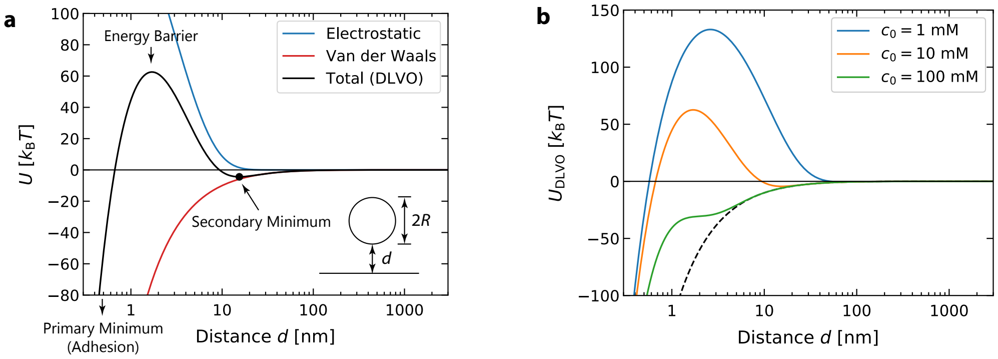

Fig. 2.9: **a**, Plot of the electrostatic and the van der Waals contribution to the DLVO potential for a gold particle with radius $R = 125$ nm as function of the distance d to a glass surface at a concentration of $c_0 = 10$ mM. We have used $\zeta = -30$ mV for the zeta potential and $A_\mathrm{H} = 2.5 \cdot 10^{-20}$ J for the Hamaker constant (Tab. 2.1). **b**, The total potential defined in (**a**) for different concentrations c_0.

The DLVO potential is described by a weak attraction at large distances, a repulsion at intermediate distance (energy barrier) and a strong attraction at short distances (primary minimum). At intermediate distances we find a potential well (secondary minimum). At different salt concentrations the different features are more or less pronounced and completely vanish at higher salt concentrations (Fig. 2.9b). At low salt concentrations the electrostatic repulsion dominates and the energy barrier is high. The thermal energy of the particle is too small to overcome the barrier during a reasonable period of time. At high salt concentrations this potential barrier decreases and the van der Waals attraction starts to dominate. This leads to adhesion and contact of the particle with the surface in the primary minimum. At very high salt concentrations the energy barrier vanishes and so the secondary minimum.

2.2.4 Beyond DLVO Theory

So far, we discussed forces between surfaces with a well-defined liquid-solid boundary. This is not the case for polymer-covered surfaces where the attached polymers form a thermally diffusive interface. When two polymer-covered surfaces approach each other they experience a repulsive force once the polymer chains start to overlap. This repulsion is caused by the entropy change of the compressed polymers and is referred to as steric repulsion[142]. For a spherical particle close to planar surface the potential of the steric repulsion can be estimated using the Alexander–de Gennes equation[152–154]:

$$U_\mathrm{P}(d) = \frac{16\pi k_\mathrm{B} T R L^2 \sigma^{\frac{3}{2}}}{35}\left(28\left(\left(\frac{2L}{d}\right)^{\frac{1}{4}} - 1\right) + \frac{20}{11}\left(1 - \left(\frac{d}{2L}\right)^{\frac{11}{4}}\right) + 12\left(\frac{d}{2L} - 1\right)\right) . \tag{2.48}$$

Here, R is the particle radius, L the length of the polymer, σ the polymer surface density (number of polymer chains per m^3) and d the surface-to-surface distance. The steric repulsion of Pluronic F-127 covered surfaces[155,156] has been used for stabilizing the particle suspensions in Secs. 4.2 and 4.3 as well as to prevent the adsorption of biomolecules[157] to the coverslips in Sec. 4.4.

2.3 Transport in Liquids of Non-Uniform Temperature

In addition to their stochastic motion, micro and nano-objects in liquids show a deterministic motion when a temperature gradient is applied. This effect is called thermophoresis or Ludwig–Soret effect[158,159]. First, this section will give a phenomenological description of thermophoresis. We then focus on the underlying microscopy mechanism of thermo-osmotic flows leading to a hydrodynamic description of thermophoresis. This is followed by a discussion of depletion forces. The section closes by drawing the line to thermally induced convection.

2.3.1 Phenomenological Description

Phenomenologically, the drift velocity in a non-uniform temperature distribution is given by

$$\boldsymbol{u} = -D_\mathrm{T} \nabla T \ , \tag{2.49}$$

where D_T is defined as the thermophoretic mobility and ∇T is the temperature gradient. The particle flux due to thermophoresis then is $j_\mathrm{T} = u(x)\, p(x,t) = -D_\mathrm{T}\, p(x,t) \partial_x T(x)$, where $p(x,t)$ is the probability density distribution of the particle. For a positive D_T, particles will migrate towards colder regions, competing with the diffusive particle flux, $j_\mathrm{D} = -D \partial_x p(x,t)$. In view of Eq. (2.19) the total particle flux reads:

$$j(x,t) = j_\mathrm{T} + j_\mathrm{D} = -D_\mathrm{T}\, p(x,t) \frac{\partial T(x)}{\partial x} - D \frac{\partial p(x,t)}{\partial x} = -D \left(S_\mathrm{T} \frac{\partial T(x)}{\partial x} p(x,t) + \frac{\partial p(x,t)}{\partial x} \right) \tag{2.50}$$

with Soret coefficient $S_\mathrm{T} = D_\mathrm{T}/D$ introduced as the ratio between the thermophoretic mobility and the diffusion coefficient. In the stationary state, $j(x,t) = 0$, the solution for the probability density distribution is

$$p(x) = p_0\, \mathrm{e}^{-S_\mathrm{T} \Delta T(x)} \ , \tag{2.51}$$

where $\Delta T(x) = T(x) - T_0$ is the temperature increment in reference to the ambient temperature T_0 and p_0 the normalization factor (Fig. 2.10) . The Soret coefficient, hence, is a measure for the thermally driven separation in the steady state.

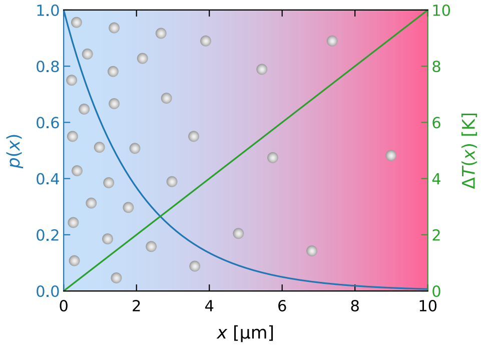

Fig. 2.10: Steady state probability distribution (blue curve) for a Soret coefficient of $S_\mathrm{T} = 0.5\ \mathrm{K}^{-1}$ and a temperature gradient of $1\ \mathrm{K\,\mu m^{-1}}$ ($\Delta T(x) = \alpha x$ with $\alpha = 1\ \mathrm{K\,\mu m^{-1}}$, green line).

Using the continuity equation, $\partial_t p(x,t) = -\partial_x j(x,t)$, one obtains the Fokker–Planck equation:

$$\frac{\partial p(x,t)}{\partial t} = \frac{\partial}{\partial x} \left(D S_\mathrm{T} \frac{\partial T(x)}{\partial x} p(x,t) + D \frac{\partial p(x,t)}{\partial x} \right) \tag{2.52}$$

for the time evolution of the probability density in presence of a temperature gradient. The comparison of Eqs. (2.52) and (2.25) shows that the temperature distribution can be interpreted as an effective potential $U(x)/(k_\mathrm{B} T) = S_\mathrm{T} \Delta T(x)$, even though no external force is applied.

2.3.2 Thermo-Osmotic Flows

In the phenomenological description the microscopic mechanisms leading to thermophoresis were hidden in the thermophoretic mobility D_{T}. Two different approaches have been used to theoretically describe thermally induced transport on the microscopic scale, i) a thermodynamic approach[38] and ii) a hydrodynamic description of the liquid boundary layer[56]. Recently, it has been shown that only a hydrodynamic approach can correctly account for all aspects of colloidal thermophoresis[58]. This section introduces the hydrodynamics of thermo-osmotic boundary flows[160] as the underlying microscopic principle of interfacial thermophoresis.

Hydrodynamics of the Boundary Layer Typically, osmosis describes the diffusion of solvent molecules through a selective membrane into a region of higher solute concentration. The same principle applies for thermo-osmosis, where we consider a liquid of non-uniform temperature instead of a non-uniform solute concentration. If there would be a membrane that lets the solvent pass but not the heat, liquid would flow from cold to hot to equilibrate temperature. Since there are no heat selective membranes, thermo-osmosis can only be observed on liquid–solid interfaces[49]. Within a small liquid layer close to the interface the liquid interacts with the solid surface. Since the strength of these interactions depends on temperature, a non-uniform temperature along the interface will cause an osmotic pressure in the liquid interaction layer that eventually leads to a slip flow parallel to the solid surface[63].

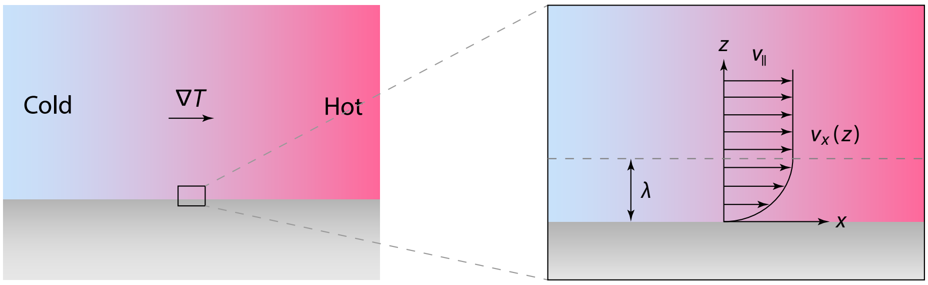

Fig. 2.11: Sketch of the boundary layer approximation. Within a small liquid boundary layer ($\lambda \approx 10$ nm) close to the interface the liquid interacts with the solid surface. Since the strength of these interactions depends on temperature, a non-uniform temperature along the interface will cause an osmotic pressure in the liquid interaction layer that leads to a slip flow parallel to the solid surface, v_x. The velocity parallel to the solid surface increases in z-direction and gets constant at distances beyond the interaction range λ, $v_x(z > \lambda) = v_\parallel$.

The velocity in the boundary layer can be described by the Stokes equation, Eq. (2.3). We consider a liquid–solid interface and coordinates as shown in Fig. 2.11. Close to the interface the vertical component of the velocity vanishes, $v_z = 0$. Since the hydrodynamic quantities vary much more rapidly in the vertical direction than parallel to the surface, we approximate $v_x(x, z) \approx v_x(z)$ and the Stokes equation can be reduced to:

$$0 = \frac{\mathrm{d}p}{\mathrm{d}z} - f_z \ , \tag{2.53}$$

$$\eta \frac{\mathrm{d}^2 v_x}{\mathrm{d}z^2} = \frac{\mathrm{d}p}{\mathrm{d}x} - f_x \ . \tag{2.54}$$

The velocity is zero at the solid surface, $v_x|_{z=0} = 0$, and takes a constant value at infinity, $v_x(\infty) := v_\parallel$. The integration yields[56,63] (Appendix A1.7):

$$v_\parallel = \frac{1}{\eta} \int_0^\infty z \left(f_x - \frac{\mathrm{d}p}{\mathrm{d}x} \right) \mathrm{d}z \ . \tag{2.55}$$

Electric Double Layer Contribution We consider an electric double layer close to a charged surface in presence of a temperature gradient (Fig. 2.12). The force density in the boundary layer of a charged surface can be written as $\boldsymbol{f} = \nabla \cdot \boldsymbol{T} + \varrho \boldsymbol{E}_0$. Here, $\boldsymbol{T}$ is the Maxwell stress tensor and the first term, $\nabla \cdot \boldsymbol{T} = \varrho \boldsymbol{E} - \frac{1}{2} E^2 \nabla \varepsilon$, comprises the electric force exerted by the charged surface on the liquid. The second term accounts for the interaction of the liquid with an external electric field $\boldsymbol{E}_0$. With the electric field given by $\boldsymbol{E} = -\nabla \psi$ the force density reads[54]:

$$\boldsymbol{f} = -\varrho \nabla \psi - \frac{1}{2} E^2 \nabla \varepsilon + \varrho \boldsymbol{E}_0 \ . \tag{2.56}$$

For the osmotic pressure, $p = n k_{\mathrm{B}} T$, we find (Appendix A1.8):

$$\nabla p = -\varrho \nabla \psi + (\varrho \psi + n k_{\mathrm{B}} T) \frac{\nabla T}{T} + n k_{\mathrm{B}} T \frac{\nabla n_0}{n_0} \ , \tag{2.57}$$

where we have used the charge density ϱ and the excess ion density n given in Eqs. (2.33) and (2.34). Together, for the right-hand side of Eq. (2.3) we get:

$$\boldsymbol{f} - \nabla p = -(\varrho \psi + n k_{\mathrm{B}} T) \frac{\nabla T}{T} - \frac{1}{2} E^2 \nabla \varepsilon - n k_{\mathrm{B}} T \frac{\nabla n_0}{n_0} + \varrho \boldsymbol{E}_0 \ . \tag{2.58}$$

Note that the terms $\varrho \nabla \psi$ have canceled out.

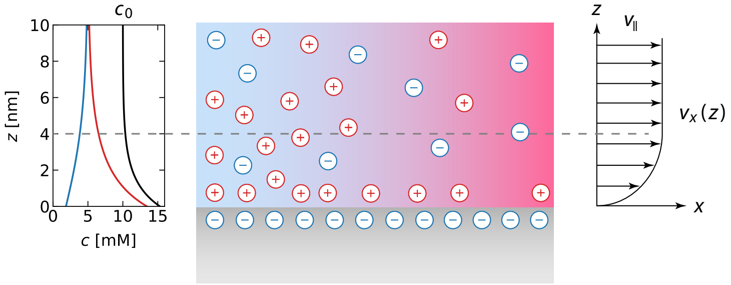

Fig. 2.12: The electric double layer close to a negatively charged surface (Sec. 2.2.1) in presence of a temperature gradient. The osmotic pressure in the boundary layer is slightly higher at the cold side and drives the charged liquid to the warm. The resulting velocity profile reaches its maximum value, $v_\parallel$ beyond the Debye length, indicated by the dashed line.

In the Debye–Hückel approximation (Sec. 2.2.1) we have $\varrho \approx -\varepsilon \psi / \lambda_{\mathrm{D}}^2$, $n k_{\mathrm{B}} T \approx \varepsilon \psi^2 / (2 \lambda_{\mathrm{D}}^2)$, $E \approx \psi / \lambda_{\mathrm{D}}$ and find[54]:

$$\boldsymbol{f} - \nabla p \approx \left(\frac{\varepsilon}{\lambda_{\mathrm{D}}^2} \psi^2 - \frac{\varepsilon}{2 \lambda_{\mathrm{D}}^2} \psi^2 \right) \frac{\nabla T}{T} - \frac{1}{2 \lambda_{\mathrm{D}}^2} \psi^2 \nabla \varepsilon - \frac{\varepsilon}{2 \lambda_{\mathrm{D}}^2} \psi^2 \frac{\nabla n_0}{n_0} - \frac{\varepsilon}{\lambda_{\mathrm{D}}^2} \psi \boldsymbol{E}_0 \tag{2.59}$$

with $\psi = \zeta \mathrm{e}^{-z/\lambda_{\mathrm{D}}}$. Solving Eq. (2.55) with Eq. (2.59) we obtain the slip velocity in the Debye–Hückel approximation:

$$v_\parallel = \frac{1}{\eta} \int_0^\infty z \left(f_x - \frac{\mathrm{d}p}{\mathrm{d}x} \right) \mathrm{d}z = \frac{\varepsilon \zeta^2}{8 \eta} \left(\frac{1}{T} \frac{\mathrm{d}T}{\mathrm{d}x} - \frac{1}{\varepsilon} \frac{\mathrm{d}\varepsilon}{\mathrm{d}x} - \frac{1}{n_0} \frac{\mathrm{d}n_0}{\mathrm{d}x} \right) - \frac{\varepsilon \zeta}{\eta} E_{0x} \ . \tag{2.60}$$

The first term originates from the osmotic pressure gradient in the electric double layer and drives the liquid in the boundary layer to the hot. The permittivity and salinity gradient can be also present without a non-uniform temperature, for example, a permittivity gradient can be caused by the alignment of water molecules at the interface[161] or a salinity gradient can be created by an external non-uniform salt concentration. In the following, we assume that these gradients are solely caused by a non-uniform temperature.

The permittivity gradient is then defined by[54]

$$\frac{\nabla \varepsilon}{\varepsilon} = -\tau \frac{\nabla T}{T} \ , \tag{2.61}$$

where τ is a dimensionless coefficient. The bulk value for water is $\tau = 1.4$[160]. However, the value of τ in the electric double layer is a matter of debate as the solvent permittivity in the electric double layer can be quite different from its bulk value[161]. In the Stern layer polarized solvent molecules are adsorbed with a specific orientation[141]. As the permittivity highly depends on the orientation of the solvent molecules, the permittivity in the electric double layer is different from its bulk value suggesting also a different value for τ. It has been speculated that τ, in the electric double layer, is even negative[4].

The salinity gradient caused by a non-uniform temperature is[55]

$$\frac{\nabla n_0}{n_0} = -\alpha \frac{\nabla T}{T} , \tag{2.62}$$

and accounts for the Soret effect of the ions (Appendix A1.9). Here, $\alpha = \alpha_+ + \alpha_-$ denotes the sum of the ionic Soret coefficients $\alpha_\pm$ (see Tab. 2.2 for bulk values in water). In the electric double layer also the ionic Soret coefficients might be different as the solvation shell of the ions is modulated close to a charged surface. Hence, the values in Tab. 2.2 are expected to be different in the electric double layer.

Tab. 2.2: The reduced ionic Soret coefficients calculated from the single-ion heat of transport in Ref. 162 using $\alpha_i = Q_i^*/(2k_\mathrm{B}T)$ and the resulting thermoelectric potential ψ_0 for several electrolytes.

Ion	H^+	Li^+	K^+	Na^+	OH^-	Cl^-
$\alpha_\pm$	2.7	0.1	0.5	0.7	3.4	0.1

Salt	NaCl	NaOH	LiCl	HCl
$\delta\alpha$	0.6	−2.7	0	2.6
ψ_0 [mV]	−16	70	0	−68

The last term in Eq. (2.60) describes the slip velocity induced by an electric field. This can be an external electric field but also a thermoelectric field caused by the difference $\delta\alpha = \alpha_+ - \alpha_-$ of the ionic Soret coefficients (Appendix A1.9). The thermoelectric field is given by[163]

$$\boldsymbol{E}_0 = -\psi_0 \frac{\nabla T}{T} , \tag{2.63}$$

where $\psi_0 = -\delta\alpha\, k_\mathrm{B}T/e$ is defined as the thermoelectric potential. Inserting Eqs. (2.61), (2.62), and (2.63) in Eq. (2.60), yields the expression

$$v_\parallel = \frac{\varepsilon\zeta^2}{8\eta}(1+\tau+\alpha)\frac{1}{T}\frac{\mathrm{d}T}{\mathrm{d}x} + \frac{\varepsilon\zeta}{\eta}\frac{\psi_0}{T}\frac{\mathrm{d}T}{\mathrm{d}x} . \tag{2.64}$$

If we assume $\tau > 0$ the term proportional to ζ^2 is always positive, driving the liquid to the hot. The term proportional to ζ may take either sign depending on the sign of ζ and the sign of ψ_0 (Tab. 2.2). The last term might even inverse the sign of the slip velocity[48,55]. If we summarize the information on the interfacial interactions in a thermo-osmotic coefficient χ, we can write

$$\boldsymbol{v}_\parallel = \chi \frac{\nabla_\parallel T}{T} . \tag{2.65}$$

If $\chi > 0$, the liquid is driven to the hot, whereas for $\chi < 0$, the liquid is driven to the cold. Considering only the osmotic pressure contribution the thermo-osmotic coefficient of the electric double layer reads[49]:

$$\chi_\mathrm{E} = \frac{\varepsilon\zeta^2}{8\eta} . \tag{2.66}$$

With $\zeta \sim -30$ mV we find $\chi_\mathrm{E} \sim 10^{-10}\ \mathrm{m^2\,s^{-1}}$ in water. For a temperature gradient in the order of 10 K µm^{-1} slip velocities in the order of µm s^{-1} are expected.

Van der Waals Contribution An additional contribution to the slip velocity arises from the temperature dependence of the van der Waals interactions in the boundary layer. The van der Waals potential of a solvent molecule at distance z from a solid surface is[56,145]

$$\varphi(z) = -\frac{A_\mathrm{H}}{3\pi z^3} V_0 \ , \tag{2.67}$$

where V_0 is the volume of a solvent molecule and A_H the Hamaker constant of the solvent interacting with the solid surface across vacuum. The number density of the solvent molecules is given by $n = 1/V_0$ and the force density on the solvent molecules is

$$\boldsymbol{f} = -n\nabla_\perp \varphi \ . \tag{2.68}$$

Note that here "n" is used for the solvent molecule density, whereas it was previously used for the excess ion density. Since the gradient in Eq. (2.68) is normal to the surface, there is no force parallel to the surface, $f_x = 0$. For the normal direction, $f_z = -n\,\partial_z\varphi$, the integration of the normal component of the Stokes equation, $\partial_z p = f_z$, yields

$$p = p_0 - n\varphi \ , \tag{2.69}$$

where we assumed that the density is constant in normal direction, $\partial_z n = 0$. We retain the concentration gradient parallel to the surface, $\partial_x p = -\varphi\,\partial_x n$, and find[164]

$$v_\parallel = \frac{1}{\eta}\int_{d_0}^{\infty} z\,\varphi \frac{\mathrm{d}n}{\mathrm{d}x}\,\mathrm{d}z = -\frac{1}{\eta}\int_{d_0}^{\infty} \frac{A_\mathrm{H}}{3\pi z^2}\frac{1}{n}\frac{\mathrm{d}n}{\mathrm{d}x}\,\mathrm{d}z = \frac{A_\mathrm{H}}{3\pi\eta d_0}\beta\frac{\mathrm{d}T}{\mathrm{d}x} \ , \tag{2.70}$$

where we have used the relations

$$\frac{\mathrm{d}n}{\mathrm{d}x} = \frac{\mathrm{d}n}{\mathrm{d}T}\frac{\mathrm{d}T}{\mathrm{d}x} \quad \text{and} \quad \beta = -\frac{1}{n}\frac{\mathrm{d}n}{\mathrm{d}T} \tag{2.71}$$

with the thermal expansion coefficient β of the solvent ($\beta = 0.2{\cdot}10^{-3}$ K^{-1} for water, see Appendix A1.14). Note that the van der Waals potential diverges at $z = 0$, where the solvent molecules are in contact with the surface. To address this singularity, we introduced a cut-off parameter d_0 corresponding to the size of a solvent molecule ($d_0 = 0.2$ nm for water). In view of Eq. (2.65) the thermo-osmotic coefficient of the van der Waals contribution is given by

$$\chi_\mathrm{vdW} = \frac{A_\mathrm{H}}{3\pi\eta d_0}\beta T \ . \tag{2.72}$$

For $A_\mathrm{H} \sim 1 \cdot 10^{-20}$ J we find $\chi_\mathrm{vdW} \sim 10^{-10}$ m^2 s^{-1} in water. For a temperature gradient in the order of 10 K µm^{-1} this yields a slip velocity in the order of µm s^{-1}, similar to the slip velocity expected from the electric double layer contribution. Note that the absolute value of χ_vdW is very sensitive to the choice of the cut-off parameter d_0, and the thermal expansion coefficient β itself is temperature dependent (Appendix A1.14). Nevertheless, for a gold surface with a Hamaker constant in the order of $A_\mathrm{H} \sim 10 \cdot 10^{-20}$ J the van der Waals contribution to the slip velocity is expected to be about one order of magnitude larger as compared to a dielectric surface.

Excess Enthalpy A generalization of Eq. (2.55) can be given by[160]

$$\boldsymbol{v}_\parallel = -\frac{1}{\eta}\int_0^{\infty} z\,h(z)\,\mathrm{d}z\,\frac{\nabla_\parallel T}{T} \ , \tag{2.73}$$

where we introduced the excess enthalpy $h(z)$ that accounts for the specific interactions between the liquid and the solid. For the electric double layer and the van der Waals contribution the excess enthalpy reads $h_\mathrm{E}(z) = \varepsilon\zeta^2/(2\lambda_\mathrm{D}^2)\,\mathrm{e}^{-2z/\lambda_\mathrm{D}^2}$ and $h_\mathrm{vdW}(z) = A_\mathrm{H}\beta T/(3\pi\eta z^3)$, respectively.

2.3.3 Thermophoresis in External Temperature Gradients

The particle velocity can be obtained from the negative surface average of the slip velocity. Using Eq. (2.65) we find[165]

$$\boldsymbol{u} = -\frac{1}{S}\int_S \boldsymbol{v}_\parallel \, \mathrm{d}S = -\frac{\chi}{T}\frac{1}{S}\int_S \nabla_\parallel T \, \mathrm{d}S \ , \tag{2.74}$$

where S is the surface area of the particle and the surface temperature gradient in its general form is given by $\nabla_\parallel T = \nabla T - \boldsymbol{n}\,(\boldsymbol{n}\cdot\nabla T)$, where $\boldsymbol{n}$ is the unit vector normal to the surface. The negative sign accounts for the force balance, since the flow on its surface will cause a particle motion in the opposite direction. For a spherical particle with radius R, using spherical coordinates with $\boldsymbol{n} = \boldsymbol{e}_r$, the surface temperature gradient simplifies to

$$\nabla_\parallel T = \frac{1}{R}\frac{\partial T}{\partial\theta}\boldsymbol{e}_\theta + \frac{1}{R\sin\theta}\frac{\partial T}{\partial\varphi}\boldsymbol{e}_\varphi \ . \tag{2.75}$$

With $\boldsymbol{e}_\theta = (\cos\theta\cos\varphi, \cos\theta\sin\varphi, -\sin\theta)^{\mathrm{T}}$ and $\boldsymbol{e}_\varphi = (-\sin\varphi, \cos\varphi, 0)^{\mathrm{T}}$ the x-component of the particle velocity then reads:

$$u_x = -\frac{\chi}{T}\frac{1}{S}\int_0^\pi\int_0^{2\pi}\left(\frac{1}{R}\frac{\partial T}{\partial\theta}\cos\theta\cos\varphi - \frac{1}{R\sin\theta}\frac{\partial T}{\partial\varphi}\sin\varphi\right)R^2\sin\theta\,\mathrm{d}\theta\,\mathrm{d}\varphi \ . \tag{2.76}$$

For a linear temperature distribution, $T(x) = \alpha x$, the temperature on the particle surface is given by $T(\theta,\varphi) = \alpha R\sin\theta\cos\varphi$. The integration of Eq. (2.76) with $\partial T/\partial\theta = \alpha R\cos\theta\cos\varphi$ and $\partial T/\partial\varphi = -\alpha R\sin\theta\sin\varphi$ yields the thermophoretic velocity:

$$u_x = -\frac{2}{3}\frac{\chi}{T}\frac{\mathrm{d}T}{\mathrm{d}x} = -\frac{2}{3}\hat{v}_\parallel \ , \tag{2.77}$$

where we have used $S = 4\pi R^2$ and $\mathrm{d}T/\mathrm{d}x = \alpha$, and $\hat{v}_\parallel$ denotes the maximum slip velocity at $\theta = 0$. The components u_y and u_z vanish. Hence, the thermophoretic velocity of a particle in a temperature gradient ∇T is defined by

$$\boldsymbol{u} = -\frac{2}{3}\chi\frac{\nabla T}{T} \ . \tag{2.78}$$

Note that for $\chi > 0$, the particle is driven to the cold, whereas for $\chi < 0$, the particle is driven to the hot.

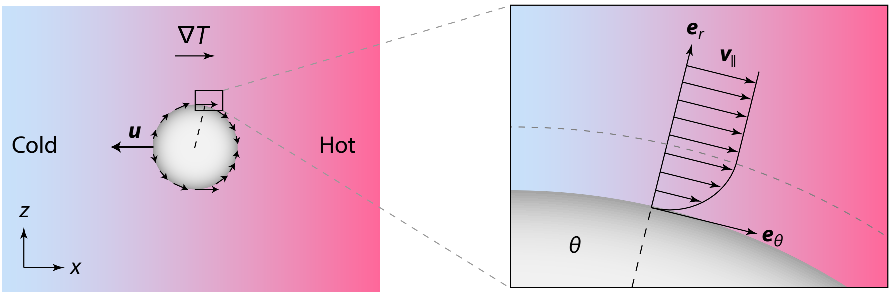

Fig. 2.13: Sketch of a spherical particle in a temperature gradient for a thermo-osmotic coefficient $\chi > 0$.

In view of Eq. (2.49) the thermophoretic mobility D_{T} is then given by

$$D_{\mathrm{T}} = \frac{2}{3}\frac{\chi}{T} \ . \tag{2.79}$$

For a dielectric particle with $\zeta \sim -30$ mV in water we have $\chi \sim 10^{-10}$ $\mathrm{m^2\,s^{-1}}$ and find $D_{\mathrm{T}} \sim 1$ $\mathrm{\mu m^2\,K^{-1}\,s^{-1}}$ at 20 °C ($T = 293.15$ K). For a temperature gradient in the order of

10 $\mathrm{K\,\mu m^{-1}}$ thermophoretic velocities in the order of $u \sim 1\ \mathrm{\mu m\,s^{-1}}$ are expected. Note that the thermophoretic mobility D_T does not depend on the particle size and is solely defined by the surface properties of the particle[53]. Since the translational diffusion coefficient is proportional to the inverse of the particle size, $D \propto R^{-1}$, the Soret coefficient, $S_\mathrm{T} = D_\mathrm{T}/D$, is expected to be proportional to the size of the particle[40]:

$$S_\mathrm{T} \propto R\,. \tag{2.80}$$

The velocity field at distances beyond the boundary layer can be obtained from the solution of the Stokes equation for a spherical particle with a boundary velocity of $v_\parallel = -\frac{3}{2}u\cos\theta$. The resulting velocity field is short-ranged and decays with $v \sim r^{-3}$ in contrast to the long-range velocity field, $v \sim r^{-1}$ of a sphere that is dragged through the liquid by an external force[166].

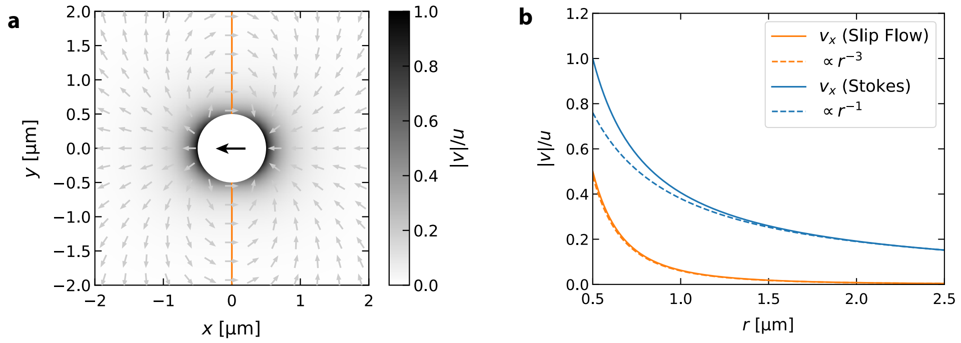

Fig. 2.14: **a**, The velocity field $|v|/u$ around a sphere that is driven by surface flows with a thermophoretic velocity u in the laboratory frame (see Appendix A1.10 for details). The arrows depict the normalized direction vectors. The sphere has a radius of $R = 0.5$ µm. **b**, The x-component of the velocity along the orange line (**a**) compared to the x-component of the velocity for a sphere dragged by an external force (Fig. 2.1b).

Metal Particles Strictly, Eq. (2.78) is only valid if the thermal conductivities of the surrounding liquid and the particle are identical. In case they are different the thermophoretic velocity reads

$$\boldsymbol{u} = -\frac{2}{3}\chi\frac{3\kappa_1}{2\kappa_1+\kappa_2}\frac{\nabla T}{T}\ , \tag{2.81}$$

where the factor $\gamma = 3\kappa_1/(2\kappa_1+\kappa_2)$ accounts for the deformation of the surface temperature gradient caused by the different thermal conductivities of the particle, κ_2, and the surrounding liquid, κ_1[56]. For dielectric particles ($\kappa_2 \approx 1\ \mathrm{W\,m^{-1}\,K^{-1}}$) suspended in water ($\kappa_1 = 0.6\ \mathrm{W\,m^{-1}\,K^{-1}}$) we find $\gamma \approx 1$ and Eq. (2.81) simplifies to Eq. (2.78). For a gold particle ($\kappa_2 = 318\ \mathrm{W\,m^{-1}\,K^{-1}}$) we find $\gamma = 0.006$ which is about two orders of magnitude smaller than for dielectric particles.

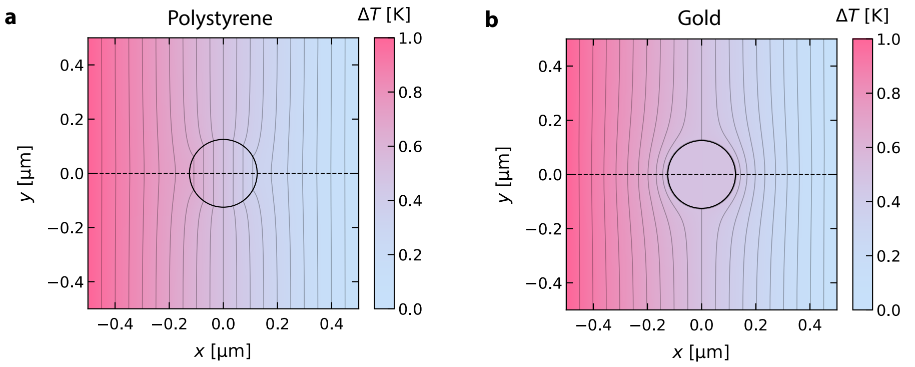

Fig. 2.15: The temperature distortion in the vicinity of a spherical particle in an external temperature gradient of 1 $\mathrm{K\,\mu m^{-1}}$ for a polystyrene particle (**a**) compared to a gold particle (**b**).

Due to their high thermal conductivity, gold particles reduce the local temperature gradient, leading to substantially smaller thermophoretic velocities. Fig. 2.15 compares the numerical simulation of the local temperature around a polystyrene and a gold particle subjected to an external temperature gradient of 1 $\mathrm{K\,\mu m^{-1}}$.

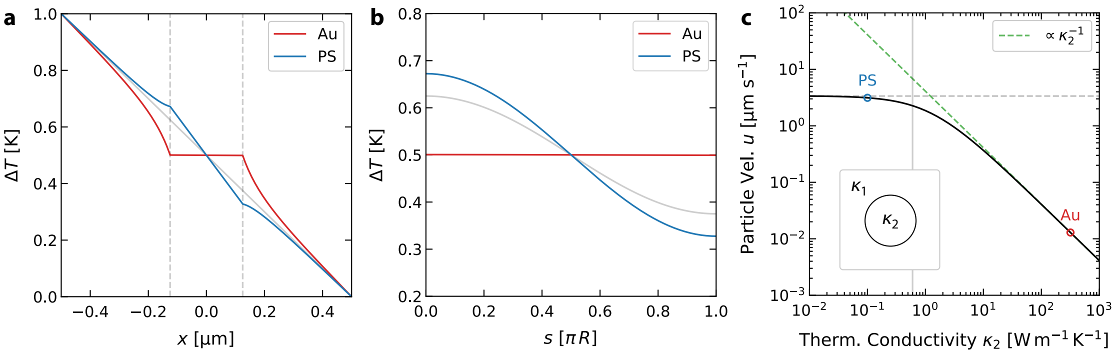

Fig. 2.16: **a**, Temperature along the dashed lines in Fig. 2.15. **b**, Temperature on the surface of the particles in Fig. 2.15. The gray lines in (**a**) and (**b**) depict the temperature profiles without a particle present ($\kappa_2 = \kappa_1$). **c**, The particle velocity u as function of the particle thermal conductivity κ_2 for $\chi = 1 \cdot 10^{-10}\ \mathrm{m^2\,s^{-1}}$ in water ($\kappa_1 = 0.6\ \mathrm{W\,m^{-1}\,K^{-1}}$). The vertical gray line indicates $\kappa_1 = \kappa_2$.

As analyzed in Fig. 2.16 the gold particle alters the local temperature (Fig. 2.16a) and quenches the temperature gradient on the particle surface (Fig. 2.16b). Fig. 2.16c depicts the thermophoretic velocity as function of the particles thermal conductivity κ_2 for $\chi = 1 \cdot 10^{-10}\ \mathrm{m^2\,s^{-1}}$ in water ($\kappa_1 = 0.6\ \mathrm{W\,m^{-1}\,K^{-1}}$). For $\kappa_2 \gg \kappa_1$ the thermophoretic velocity u scales with $u \propto \kappa_2^{-1}$. For gold particles we find a thermophoretic velocity in the order of 0.01 $\mathrm{\mu m\,s^{-1}}$ more than two orders of magnitude smaller than for dielectric particles. Hence, the thermophoretic motion of gold particles and metal particles in general can be neglected.

2.3.4 Depletion Forces

So far, we considered solutions with atomic ionic species. In solutions containing larger molecules such as surfactants or polymers, in addition, depletion forces have to be considered. The thermophoretic motion of these molecules yields a non-uniform density distribution which in turn leads to diffusiophoresis of colloidal particles. The excess pressure in the boundary layer of a particle is given by[46]

$$p = n k_\mathrm{B} T \left(\mathrm{e}^{-\varphi(z)/(k_\mathrm{B}T)} - 1\right) , \tag{2.82}$$

where n is the density of the molecules and $\varphi(z)$ is the interaction potential between a molecule and a particle. Since the lateral component of the force is zero, $f_x = 0$, Eq. (2.55) reads:

$$v_\parallel = -\frac{1}{\eta}\int_0^\infty z \frac{\mathrm{d}p}{\mathrm{d}x}\,\mathrm{d}z = -\frac{1}{\eta}\frac{\mathrm{d}}{\mathrm{d}x} n k_\mathrm{B} T \int_0^\infty z\left(\mathrm{e}^{-\varphi(z)/(k_\mathrm{B}T)} - 1\right)\mathrm{d}z \,. \tag{2.83}$$

For an infinite repulsive potential with $\varphi = \infty$ for $z < R_\mathrm{m}$ and $\varphi = 0$ for $z > R_\mathrm{m}$ the integral takes the value $\frac{1}{2}R_\mathrm{m}^2$ and we find

$$v_\parallel = -\frac{k_\mathrm{B}}{2\eta} R_\mathrm{m}^2 \frac{\mathrm{d}}{\mathrm{d}x}(nT) \,, \tag{2.84}$$

where R_m denotes the molecules' interaction range (Fig. 2.17). In view of Eq. (2.78) this yields a transport velocity of

$$\boldsymbol{u} = -\frac{k_\mathrm{B}}{3\eta} R_\mathrm{m}^2\, \nabla(nT) = -\frac{k_\mathrm{B}}{3\eta} R_\mathrm{m}^2 \left(T\nabla n + n\nabla T\right) , \tag{2.85}$$

due to depletion. With a molecular Soret coefficient $S_{\mathrm{T}}^{\mathrm{m}}$ the density gradient is defined by $\nabla n = -n S_{\mathrm{T}}^{\mathrm{m}} \nabla T$. The total transport velocity, including Eq. (2.78), then reads[56]:

$$\boldsymbol{u} = -\left(D_{\mathrm{T}} - \frac{k_{\mathrm{B}}}{3\eta} R_{\mathrm{m}}^2 \, n \left(T S_{\mathrm{T}}^{\mathrm{m}} - 1 \right) \right) \nabla T \; . \tag{2.86}$$

In case of a polyethylene glycol (PEG) with a molecular weight of $M_{\mathrm{w}} = 10000\ \mathrm{g\,mol^{-1}}$ we have $S_{\mathrm{T}}^{\mathrm{m}} \approx 0.06\ \mathrm{K^{-1}}$ [167] and the interaction range can be identified with the radius of gyration of a PEG molecule, $R_{\mathrm{m}} \approx 4\ \mathrm{nm}$[168]. For a PEG concentration of $c = 10\ \mathrm{mM}$ ($n = N_{\mathrm{A}} c$) the depletion term in Eq. (2.86) is then in the order of $10\ \mathrm{\mu m^2\,K^{-1}\,s^{-1}}$. Hence, the depletion term may easily exceed the thermophoretic mobility $D_{\mathrm{T}} \sim 1\ \mathrm{\mu m^2\,K^{-1}\,s^{-1}}$ of the colloidal particle (Sec. 2.3.3) rendering its overall mobility negative and the particle is effectively driven to the hot.

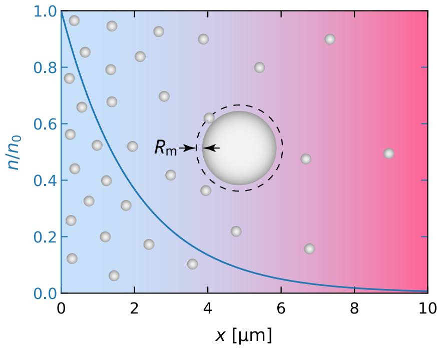

Fig. 2.17: The relative density distribution $n/n_0 = \exp(-S_{\mathrm{T}}^{\mathrm{m}} \Delta T(x))$ for a molecular Soret coefficient of $S_{\mathrm{T}}^{\mathrm{m}} = 0.06\ \mathrm{K^{-1}}$ (blue curve) and a temperature gradient of $1\ \mathrm{K\,\mu m^{-1}}$ ($\Delta T(x) = \alpha x$ with $\alpha = 1\ \mathrm{K\,\mu m^{-1}}$).

2.3.5 Self-Thermophoresis

If the non-uniform temperature is generated by the particle itself, its motion is called self-thermophoretic. In many cases, they are realized as metal-capped Janus particles, where one half of a micrometer-sized dielectric particle is covered with a thin metal film[9–11] (Fig. 2.18a). The thickness of the metal film is typically in the order of a few tens of nanometers and utilized as plasmonic heat source. A numerical simulation of the temperature distribution of a Janus particle is depicted in Fig. 2.18b[169].

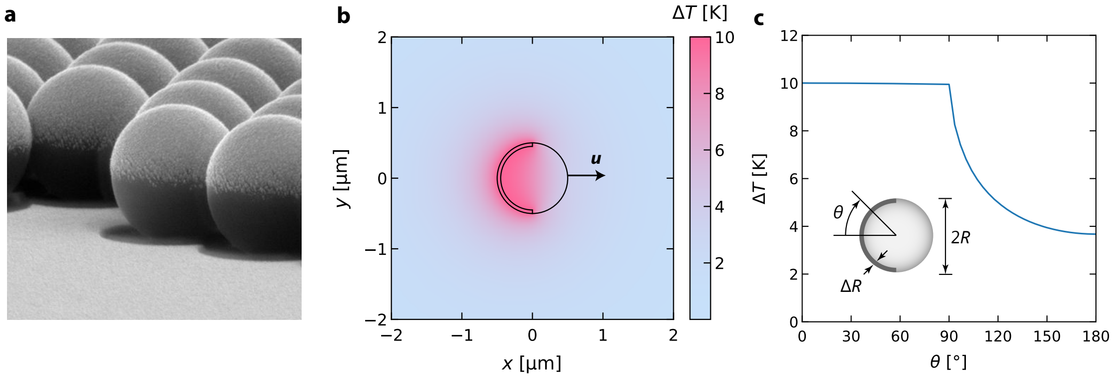

Fig. 2.18: **a**, SEM image of Janus particles fabricated by thermal evaporation of a thin gold film on polystyrene colloids taken from the Supplemenatry Information of Ref. 11. **b**, Simulated temperature distribution of a Janus particle ($R = 500$ nm, $\Delta R = 50$ nm) with the metal cap defined as a heat source with a constant heat power density. **c**, The surface temperature as function of the angle θ.

In view of Eq. (2.74) the propulsion velocity of a Janus particle is then defined by:

$$\boldsymbol{u} = -\frac{1}{S}\left(\frac{\chi_1}{T}\int_{S_1}\nabla_{\parallel}T\,\mathrm{d}S_1 + \frac{\chi_1}{T}\int_{S_2}\nabla_{\parallel}T\,\mathrm{d}S_2\right) \tag{2.87}$$

with $S = S_1 + S_2$. To account for the different surface properties, the surface integration has been split into an integral over the dielectric surface, S_1, and the metal surface, S_2. Due to its high thermal conductivity, the metal cap is basically isothermal (Fig. 2.18c) and the second integral is typically neglected. Hence, the propulsion velocity is mainly defined by the temperature gradient on the dielectric surface and its thermo-osmotic coefficient χ_1. The propulsion direction is set by the symmetry axis of the temperature distribution. For $\chi_1 > 0$ the metal cap is pointing to the opposite direction of propulsion.

Due to rotational Brownian motion, the orientation of Janus particles constantly changes and randomizes their propulsion direction. To achieve a directed motion of Janus particle techniques such as photon nudging have been developed, combing a real-time orientation detection with a switchable propulsion[10,11]. Nevertheless, these feedback-controlled actuation schemes are eventually limited to the timescale of the rotational diffusion. Sec. 4.2 introduces a self-thermometric particle where the propulsion direction can be set by the location of the heating laser itself, providing a higher level of control than possible for Janus-type particles.

2.3.6 Thermal Convection

Thermal convection describes the motion of fluids caused by temperature-induced density changes. Typically, the density of a fluid decreases as it is heated. Buoyancy causes that parts of the fluid with less density will rise leading to a bulk fluid motion called thermal convection. Hence, thermal convection is only observed in presence of a gravitational field. A theoretical description of thermal convection at low Reynolds numbers can be given by combining the Stokes equation

$$\eta\nabla^2\boldsymbol{v} = \nabla p - \varrho(T)\,\boldsymbol{g} \tag{2.88}$$

with a temperature dependent density $\varrho(T) = \varrho_0 - \varrho_0\beta(T - T_0)$ and the stationary heat equation

$$\boldsymbol{v}\cdot\nabla T - \alpha\nabla^2 T = 0\ , \tag{2.89}$$

where the first term accounts for the convective heat transfer and the second terms for the heat transferred by thermal conduction. Here, ϱ_0 is the density of the liquid at ambient temperature T_0, β is the thermal expansion coefficient and α the thermal diffusivity. The relative importance between buoyancy forces and effects of viscous forces and thermal conduction can be estimated with the Rayleigh number[170]

$$\mathrm{Ra} = \frac{\varrho_0\beta\Delta T L^3 g}{\eta\alpha}, \tag{2.90}$$

where $\Delta T = T - T_0$ is the temperature difference and L a characteristic length scale. When the Rayleigh number is small, there is no flow and the heat transfer is determined by thermal conduction. When Rayleigh number exceeds a critical value, heat is transferred by thermal convection. For a typical sample height in the order of $L \sim 1$ µm and a temperature difference of $\Delta T = 10$ K we find a Rayleigh number of $\mathrm{Ra} \sim 10^{-4}$ for water ($\varrho_0 = 10^3\ \mathrm{kg\,m^{-3}}$, $\eta = 10^{-3}\ \mathrm{Pa\,s}$, $\alpha = 0.143\ \mathrm{m^2\,s^{-1}}$, $\beta = 0.2\cdot10^{-3}\ \mathrm{K^{-1}}$). Hence, in the sample geometries employed in this thesis thermal convection can be neglected. As analysed by numerical simulations in Sec. 4.1.5.7, the flow velocities caused by thermal convection are in the order of $\mathrm{nm\,s^{-1}}$ for a typical sample geometry.

2.4 Interaction of Light with Nano-Objects

When light interacts with nano-objects, the incident electromagnetic wave is scattered and absorbed depending on the objects dielectric properties and geometry. In this thesis, the scattering of micro- and nanoparticles is typically employed for their observation, whereas the absorption of light by metal nanoparticles and thin metal films is used as a source of heat. As the light used for heating is emitted from lasers, the first part of this section introduces the basic properties of Gaussian beams. This is followed by an introduction of Mie theory describing the interaction of nanoparticles with light. Then, the optical properties of thin metal films are discussed. The section closes with a description of optical forces.

2.4.1 Gaussian Beams

The electric field distribution of light emitted from a laser can be described by the paraxial Helmholtz equation $\nabla_\perp^2 E - 2ik\partial_z E = 0$, where $\nabla_\perp^2 = \partial_x^2 + \partial_y^2$, E is the electric field, and $k = 2\pi/\lambda$ the wave number with the wavelength λ. The TEM$_{00}$ mode is one of the solutions of this equation and referred to as Gaussian beam. For a Gaussian beam propagating in z-direction the electric field is[171]

$$E(r,z) = E_0 \frac{w_0}{w(z)} \exp\left(-\frac{r^2}{w(z)^2}\right) \exp\left(-\mathrm{i}kz - \mathrm{i}k\frac{r^2}{2R(z)} + \mathrm{i}\zeta(z)\right) . \tag{2.91}$$

Here, $w(z) = w_0\sqrt{1+(z/z_\mathrm{R})^2}$ is the radius of the beam, w_0 the beam waist, $z_\mathrm{R} = \pi w_0^2/\lambda$ the Rayleigh range, $R(z) = z\,(1+(z_\mathrm{R}/z)^2)$ the curvature of the wavefronts, and $\zeta(z) = \arctan(z/z_\mathrm{R})$ the Gouy phase shift. The intensity distribution is defined by

$$I(r,z) = \frac{1}{2}c_0\varepsilon_0\,|E(r,z)|^2 = I_0\left(\frac{w_0}{w(z)}\right)^2 \exp\left(-\frac{2r^2}{w(z)^2}\right) \tag{2.92}$$

with the incident intensity $I_0 = c_0\varepsilon_0|E_0|^2/2$ and depicted in Fig. 2.19a for a wavelength of $\lambda = 532$ nm and a beam waist $w_0 = \lambda$. The radial intensity variation in the focus ($z = 0$) is Gaussian, $I(r,0) = I_0\exp(-2r^2/w_0^2)$, whereas the variation of the intensity in z-direction is $I(0,z) = I_0/(1+(z/z_\mathrm{R})^2)$ (Fig. 2.19b). Given the total power P_0 the incident intensity I_0 can be calculated as follows:

$$I_0 = \frac{2P_0}{\pi w_0^2} . \tag{2.93}$$

A derivation of Eq. (2.93) can be found in Appendix A1.11.

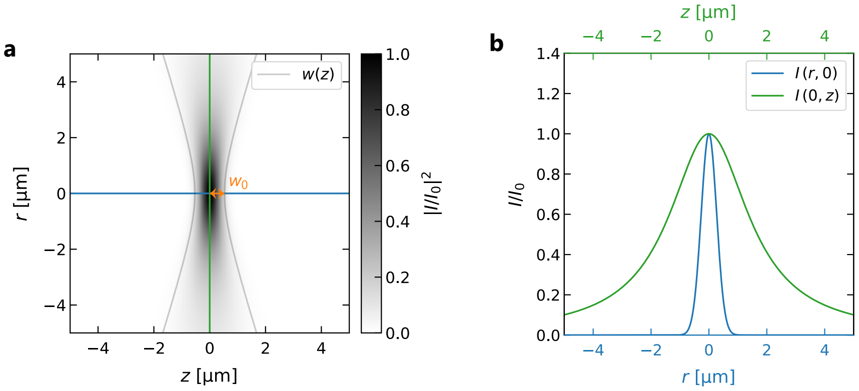

Fig. 2.19: **a**, The intensity distribution of a Gaussian beam according to Eq. (2.92) for a wavelength of $\lambda = 532$ nm and a beam waist $w_0 = \lambda$. The gray dashed lines depict the beam radius, $w(z) = w_0\sqrt{1+(z/z_\mathrm{R})^2}$. **b**, The intensity along the blue and green lines in (**a**).

2.4.2 Mie Theory

In case of nanoparticles the interaction with light is typically quantified in terms of the scattering cross-section σ_{sca} and the absorption cross-section σ_{abs} defined as ratio between the scattered or absorbed power and the incident intensity. The sum of both contributions is referred to as extinction cross-section, $\sigma_{\mathrm{ext}} = \sigma_{\mathrm{sca}} + \sigma_{\mathrm{abs}}$. Based on Mie theory, the scattering and extinction cross-sections for spherical particles illuminated by a plane wave are given by the expressions[172]:

$$\sigma_{\mathrm{sca}} = \frac{2\pi R^2}{x^2} \sum_{n=1}^{\infty} (2n+1)(|a_n|^2 + |b_n|^2) \;, \tag{2.94}$$

$$\sigma_{\mathrm{ext}} = \frac{2\pi R^2}{x^2} \sum_{n=1}^{\infty} (2n+1)\,\mathrm{Re}\,(a_n + b_n) \;\; . \tag{2.95}$$

Here, a_n and b_n are Mie coefficients defined in Appendix A1.12 and $x = 2\pi R n_1/\lambda$ is the size parameter given in terms of the particle radius R, the refractive index n_1 of the medium in which the particle is embedded, and the wavelength λ of the incident light. Note that the refractive index of the particle, n_2, enters via the Mie coefficients and the absorption cross-section can be calculated using $\sigma_{\mathrm{abs}} = \sigma_{\mathrm{ext}} - \sigma_{\mathrm{sca}}$. Typically, dielectric particles such as glass or polystyrene colloids only scatter the incident light as the imaginary part of their refractive index $n_2 = n_2' + \mathrm{i}n_2''$ is small. In contrast, metal particles scatter as well as absorb a portion of the incident light due to their complex-valued refractive index. Fig. 2.20a, b compare the optical cross-sections of two differently sized gold nanoparticles as function of the wavelength. For smaller particles the absorption dominates the scattering and we find a plasmon resonance at 530 nm, whereas for larger particles the scattering dominates and is present over a larger wavelength range.

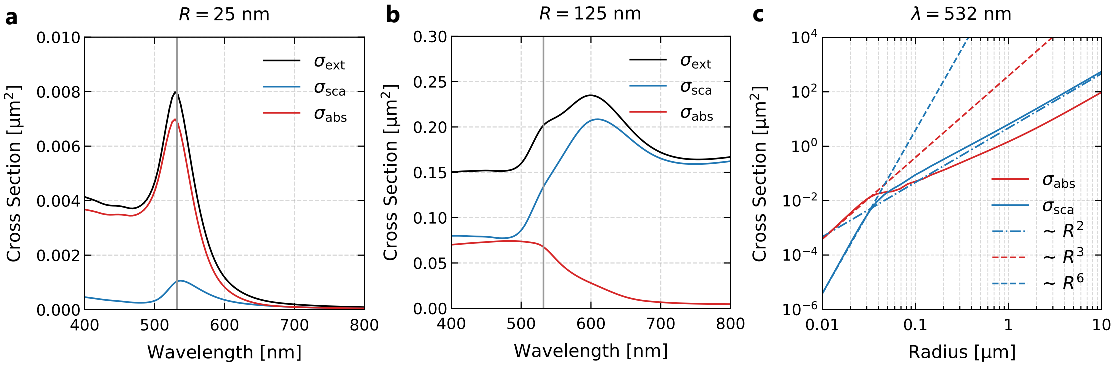

Fig. 2.20: **a**, The absorption cross-section σ_{abs} and scattering cross-section σ_{sca} of a gold nanoparticle with $R = 25$ nm radius embedded in water ($n_1 = 1.33$) as function of the wavelength λ. The wavelength-dependent refractive index of gold, $n_2(\lambda)$, has been taken from Ref. 173 (Appendix A1.15). The vertical gray line indicates the wavelength $\lambda = 532$ nm. **b**, The same as in (**a**) for a particle radius $R = 125$ nm. **c**, The size dependence of the absorption and scattering cross-section at $\lambda = 532$ nm wavelength.

From the size-dependent calculation in Fig. 2.20c we find that, for smaller particles the scattering cross-section scales with $\sigma_{\mathrm{sca}} \propto R^6$, whereas the absorption cross-section scales with $\sigma_{\mathrm{abs}} \propto R^3$. For larger particles both, the scattering and adsorption cross-section, scale approximately with $\propto R^2$. In the small particle limit, $R \ll \lambda$, the cross-sections can be expressed in terms of the Rayleigh approximation[172,174]

$$\sigma_{\mathrm{sca}} \approx \frac{k^4}{6\pi} |\alpha|^2 = \frac{8\pi}{3} k^4 R^6 \left| \frac{n_2^2 - n_1^2}{n_2^2 + 2n_1^2} \right|^2 \;, \tag{2.96}$$

$$\sigma_{\mathrm{abs}} \approx k\,\mathrm{Im}\,(\alpha) = 4\pi k R^3\,\mathrm{Im}\left(\frac{n_2^2 - n_1^2}{n_2^2 + 2n_1^2} \right) , \tag{2.97}$$

where we inserted the static polarizability $\alpha = 4\pi R^3 (n_2^2 - n_1^2)/(n_2^2 + 2n_1^2)$ with the refractive indices of the medium n_1 and the particle n_2 and recover the size dependencies found in Fig. 2.20c for $R < 50$ nm. For a spherical particle illuminated by a Gaussian beam an analytical description may be given within the framework of the generalized Lorenz–Mie theory by introducing the beam shape coefficients $g^m_{n,\mathrm{TM}}$ and $g^m_{n,\mathrm{TE}}$ (see Appendix A1.12 for details).

Beyond Generalized Lorenz-Mie Theory For arbitrary shaped objects the scattering and absorption cross-sections can be obtained from finite-element simulations using[175]

$$\sigma_{\mathrm{sca}} = \frac{1}{I_0}\int_S \langle \boldsymbol{S}_{\mathrm{sca}}\rangle \cdot \boldsymbol{n}\,\mathrm{d}S\ , \tag{2.98}$$

$$\sigma_{\mathrm{abs}} = \frac{1}{I_0}\int_V Q(\boldsymbol{r})\,\mathrm{d}V\ , \tag{2.99}$$

where I_0 is the intensity of the incident light, $\langle \boldsymbol{S}_{\mathrm{sca}}\rangle$ is the time-averaged Poynting vector of the scattered light, S is the surface of the object and $\boldsymbol{n}$ the unit vector normal to its surface, V is the volume of object and $Q(\boldsymbol{r})$ the heat power density (see Sec. 2.5 for details).

2.4.3 Metal Films

In case of metal films scattering and absorption cross-sections are not applicable for a description of their optical properties. Instead the reflectance R, transmittance T, and absorbance A are used, defined as the ratio between the reflected, transmitted and absorbed intensity and the incident intensity. For layered systems these may be calculated using the transfer-matrix method, where each layer is represented by a transfer matrix[176,177]. The reflectance and transmittance of the system is then obtained by multiplying these matrices and the absorbance is calculated from $A = 1 - (R + T)$. Fig. 2.21a depicts the reflectance, transmittance, and absorbance of a 50 nm gold film on a glass substrate embedded in water as function of the wavelength. Fig. 2.21b shows the same calculation for a 30 nm chrome film.

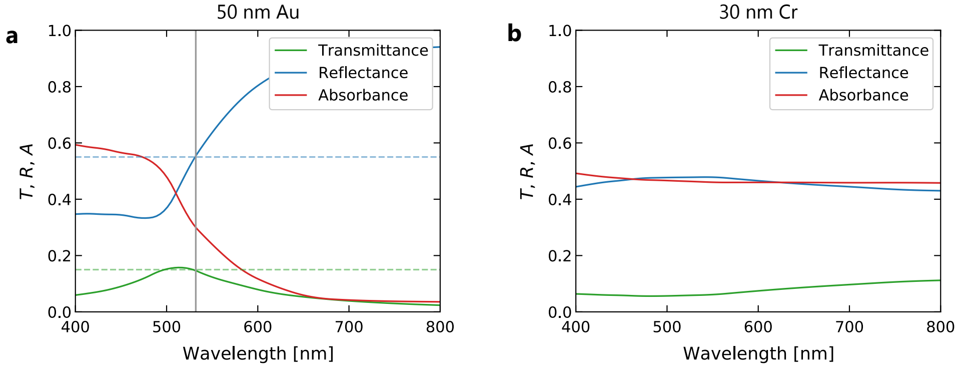

Fig. 2.21: **a**, Wavelength dependence of the reflectance R, transmittance T and absorbance A of a 50 nm gold film on a glass (BK7) substrate ($n_{\mathrm{BK7}} = 1.52$) embedded in water ($n_{\mathrm{H_2O}} = 1.33$). **b**, The same as in (**a**) for a 30 nm chrome film. The wavelength-dependent refractive indices of gold $n_{\mathrm{Au}}(\lambda)$ and chrome $n_{\mathrm{Cr}}(\lambda)$ were taken from Ref. 173 (Appendix A1.15).

While the absorbance of thin gold films decreases at larger wavelengths, thin chrome films also absorb in the near infrared range[178].

2.4.4 Optical Forces

Particles illuminated by light will experience an optical force. In the small-particle limit the time-averaged optical force can be calculated from the incident electric field as follows[129,179]:

$$\langle \boldsymbol{F}\rangle = \frac{n_1^2\varepsilon_0}{4}\mathrm{Re}(\alpha_\mathrm{r})\nabla|\boldsymbol{E}|^2 + n_1 k\,\mathrm{Im}(\alpha_\mathrm{r})\left(\frac{\mathrm{Re}(\boldsymbol{E}\times\boldsymbol{H}^*)}{2c_0} + \frac{\varepsilon_0}{4k_0\mathrm{i}}\nabla\times(\boldsymbol{E}\times\boldsymbol{E}^*)\right) \tag{2.100}$$

with the radiation-corrected polarizability $\alpha_\mathrm{r} = \alpha/(1 - \mathrm{i}k^3\alpha/(6\pi))$, $k = n_1 k_0$ and the static polarizability $\alpha = 4\pi R^3(n_2^2 - n_1^2)/(n_2^2 + 2n_1^2)$ already introduced in Sec. (2.4.2). The * denotes the complex-conjugate. The first term in Eq. (2.100) is called gradient force as it is proportional to the gradient of the electric field intensity, $I = \frac{1}{2} n_1 c_0 \varepsilon_0 |\boldsymbol{E}|^2$. If we approximate the radiation-corrected polarizability with $\alpha_\mathrm{r} \approx \alpha + \mathrm{i}k^3|\alpha|^2/(6\pi)$, we find $k\mathrm{Im}(\alpha_\mathrm{r}) \approx k\mathrm{Im}(\alpha) + k^4|\alpha|^2/(6\pi) = \sigma_\mathrm{abs} + \sigma_\mathrm{sca}$ according to Eqs. (2.96) and (2.97). Hence, the second term includes contributions from both, scattering and absorption. The term $\langle \boldsymbol{S} \rangle = \frac{1}{2}\mathrm{Re}(\boldsymbol{E} \times \boldsymbol{H}^*)$ corresponds to the time-averaged Poynting vector, whereas the term $\nabla \times (\boldsymbol{E} \times \boldsymbol{E}^*)$ relates to a polarisation gradient and vanishes for linear polarized light.

If we insert Eq. (2.91) in Eq. (2.100), an analytic expression for the optical forces of a Gaussian beam in the small-particle limit can be obtained (Eq. (A1.57) in Appendix A1.13). For particles larger than the wavelength analytic expressions for the optical force components can be obtained in the framework of the generalized Lorenz–Mie theory[180]. Fig. 2.22 depicts the optical forces exerted by a Gaussian beam ($\lambda = 532$ nm wavelength, $w_0 = \lambda/(\pi\mathrm{NA})$ beam waist with a numerical aperture of $\mathrm{NA} = 0.8$) on a $R = 25$ nm radius particle embedded in water in case the particle is composed of gold (Fig. 2.22a) and polystyrene (Fig. 2.22b). In case of gold scattering and absorption forces dominate. The particle is pushed out of the laser focus in positive z-direction. For a laser power of $P_0 = 1$ mW the forces are in the order of pN. In case of polystyrene the particle can be trapped in the focus by the gradient force as the scattering and absorption forces are sufficiently weak.

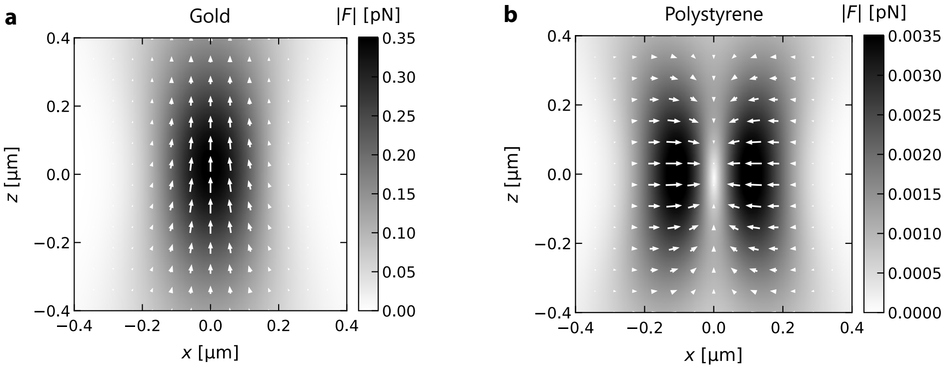

Fig. 2.22: **a**, The optical force exerted by a Gaussian beam ($\lambda = 532$ nm wavelength) on a gold particle with radius $R = 25$ nm embedded in water ($n_1 = 1.33$) calculated using Eq. (A1.57). We used $w_0 = \lambda/(\pi\mathrm{NA})$ for the beam waist, a numerical aperture of $\mathrm{NA} = 0.8$, and a laser power of $P_0 = 1$ mW. The wavelength-dependent refractive index of gold, $n_2(\lambda)$, has been taken from Ref. 173 (Appendix A1.15). **b**, The same as in (**a**) for a polystyrene particle ($n_2 = 1.59$).

For arbitrary shaped objects the optical forces acting on the object can be obtained from finite-element simulations with[129,181]

$$\langle \boldsymbol{F} \rangle = \int_S \langle \boldsymbol{T} \rangle \cdot \boldsymbol{n} \, \mathrm{d}S \ , \tag{2.101}$$

where $\boldsymbol{T}$ is the Maxwell stress tensor, $T_{ij} = \epsilon_0 \left(E_i E_j - \frac{1}{2}\delta_{ij}E^2\right) + \frac{1}{\mu_0}\left(B_i B_j - \frac{1}{2}\delta_{ij}B^2\right)$, S is the surface of the object and $\boldsymbol{n}$ the unit vector normal to its surface.

2.5 Optical Heating of Metal Nanoparticles and Nanostructures

When a metal is illuminated by light, the free electrons of the metal oscillate at the frequency of the incident light. This oscillation is nothing but an electric current in the metal that generates heat via the Joule effect. The heat power density $Q(\boldsymbol{r})$ is given by[31]

$$Q(\boldsymbol{r}) = \frac{1}{2}\mathrm{Re}(\boldsymbol{J}^* \cdot \boldsymbol{E}) \ . \tag{2.102}$$

With the electric current density $\boldsymbol{J}$ defined by the dielectric polarization density $\boldsymbol{J} = \partial_t \boldsymbol{P} = -\mathrm{i}\omega \boldsymbol{P}$ and $\boldsymbol{P} = \varepsilon_0(\varepsilon - 1)\boldsymbol{E}$ we obtain

$$Q(\boldsymbol{r}) = \frac{\omega}{2}\varepsilon_0 \mathrm{Im}(\varepsilon)|\boldsymbol{E}(\boldsymbol{r})|^2 \ , \tag{2.103}$$

where we have used $\mathrm{Re}(\mathrm{i}z) = -\mathrm{Im}(z)$ and $|\boldsymbol{E}|^2 = \boldsymbol{E}\boldsymbol{E}^*$. The total heat power released by an arbitrary metal structure is the integral of $Q(\boldsymbol{r})$ over volume of the structure, $Q_0 = \int_V Q(\boldsymbol{r}) \, \mathrm{d}V$. Hence, the heat generated in a metal structure is determined by the electric field distribution within the structure and related to the imaginary part of its permittivity $\varepsilon(\omega)$. With the electric field intensity $I = \frac{1}{2}c_0\varepsilon_0|E|^2$ we can rewrite Eq. (2.103) as follows:

$$Q(\boldsymbol{r}) = \alpha I(\boldsymbol{r}) \ , \tag{2.104}$$

where $\alpha = 4\pi n''/\lambda$ is the absorption coefficient and n'' the imaginary part of the refractive index. We used $c_0 = cn'$, $\mathrm{Im}(\varepsilon) = 2n'n''$ and $\omega/c = 2\pi/\lambda$.

2.5.1 Heat Equation

Based on the conservation of energy the time-dependent temperature distribution of a system is described by the heat equation[31]

$$\frac{\partial T}{\partial t} - \alpha\nabla^2 T = \frac{Q}{\varrho \, c_p} \ , \tag{2.105}$$

where $\alpha = \kappa/(\varrho c_p)$ is the thermal diffusivity, κ the thermal conductivity, ϱ the mass density, c_p the specific heat capacity and Q the heat power density of the heat source. We dropped the convection term $\boldsymbol{v} \cdot \nabla T$ on the left hand side of Eq. (2.105) as it can be neglected in small-scale systems (Sec. 2.3.6). Note that the symbol "α" was used in previous sections for the polarisability, whereas in terms of the heat equation it is used for thermal diffusivity. In the stationary case, $\partial T/\partial t = 0$, Eq. (2.105) simplifies to:

$$-\kappa\nabla^2 T = Q \ . \tag{2.106}$$

Note that the stationary temperature distribution is solely defined by the thermal conductivity.

2.5.2 Point-Like Heat Source

We consider a point-like heat source that starts to release heat at time $t = 0$:

$$Q(\boldsymbol{r}, t) = \begin{cases} Q_0 \, \delta(\boldsymbol{r}) & \text{for} \quad t \geq 0 \ , \\ 0 & \text{for} \quad t < 0 \ , \end{cases} \tag{2.107}$$

where Q_0 is the heating power and δ the delta function. The solution of Eq. (2.105) then reads[31]

$$\Delta T(r, t) = \frac{Q_0}{4\pi\kappa r}\left(1 - \mathrm{erf}\left(\frac{r}{2\sqrt{\alpha t}}\right)\right) , \tag{2.108}$$

where $\Delta T(r, t) = T(r, t) - T_0$. In the limit $t \to \infty$ we find $\mathrm{erf}(r/(2\sqrt{\alpha t}) \to 0$ and

$$\Delta T(r) = \frac{Q_0}{4\pi\kappa r} \tag{2.109}$$

for the solution of the stationary heat equation, Eq. (2.106). Fig. 2.23a depicts the time evolution of the temperature at $r = 10$ nm distance from a point-like heat source in water ($\alpha = 0.14 \cdot 10^{-6}$ $\mathrm{m}^2\,\mathrm{s}^{-1}$). We find a time scale of the temperature evolution in the order of 10 ns highlighting the very fast dynamics of nanoscale heat sources.

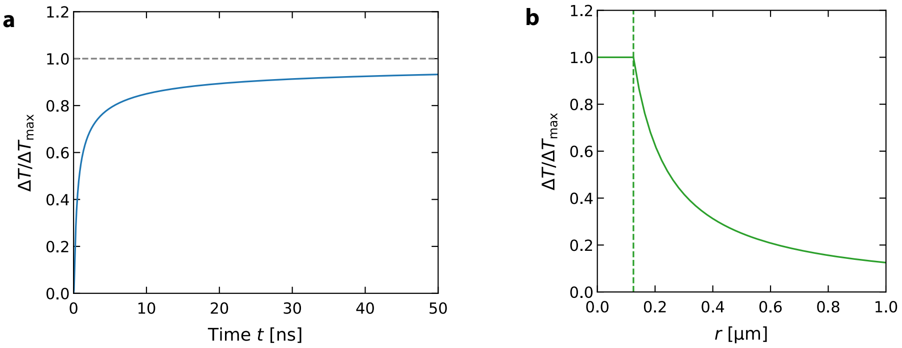

Fig. 2.23: **a**, The time evolution of the temperature at $r = 10$ nm distance from a point-like heat source in water with $\alpha = 0.14 \cdot 10^{-6}$ $\mathrm{m^2\,s^{-1}}$ and $\Delta T_{\max} = Q_0/(4\pi\kappa r)$. **b**, The radial temperature profile of a heat source with radius $R = 0.125$ nm.

If we identify $\Delta T(R) = T_{\max}$ with the surface temperature of a metal particle with radius R, we find:

$$\Delta T_{\max} = \frac{Q_0}{4\pi\kappa R} \,, \tag{2.110}$$

for the surface temperature increment, $\Delta T_{\max} = T_{\max} - T_0$, and can write:

$$\Delta T(r) = \begin{cases} \dfrac{\Delta T_{\max} R}{r} & \text{for} \quad r > R \,, \\ \Delta T_{\max} & \text{for} \quad r \leq R \,, \end{cases} \tag{2.111}$$

for the temperature distribution of a metal particle (Fig. 2.23b). Here, we assumed a uniform temperature within the particle considering its high thermal conductivity. The exact expression for the temperature within the particle be found in Ref. 31. For an optically heated particle Q_0 corresponds to the absorbed power $Q_0 = I_0\sigma_{\mathrm{abs}}$ given in terms of the incident intensity I_0 and the absorption cross-section σ_{abs} of the particle (see Eq. (2.99) for ref.). This yields:

$$\Delta T_{\max} = \frac{I_0\sigma_{\mathrm{abs}}}{4\pi\kappa R} \,. \tag{2.112}$$

For a gold particle with $R = 125$ nm radius embedded in water ($\kappa = 0.6$ $\mathrm{W\,m^{-1}K^{-1}}$) we find a temperature increment of $\Delta T_{\max} = 7.2$ K when illuminated with an intensity of $I_0 = 0.1$ $\mathrm{mW\,\mu m^{-2}}$ at a wavelength of $\lambda = 532$ nm ($\sigma_{\mathrm{abs}} = 0.068$ $\mathrm{\mu m^2}$, Fig. 2.20b). In the focus of a Gaussian beam with $I_0 = 2P_0/(\pi w_0^2)$ and $w_0 = \lambda$ the same temperature increment can be achieved with a laser power of $P_0 = 0.045$ mW.

2.5.3 Gaussian Beam Heat Source

For a Gaussian beam incident on a thin layer of absorbing material Eq. (2.104) yields:

$$Q(r, z) = P_0\,(1 - R)\,\frac{2\alpha}{\pi\omega_0^2}\,\mathrm{e}^{-2r^2/w_0^2}\,\mathrm{e}^{-\alpha z} \,, \tag{2.113}$$

for the heat power density within the layer. We have used Eq. (2.92) with $I(0, r)$ for the radial intensity distribution of the Gaussian beam and the reflectance R considering that only $P_0(1-R)$ of the incident power is entering the layer. The factor $\mathrm{e}^{-\alpha z}$ accounts for the attenuation of intensity within the material in terms of the Lambert–Beer law.

Experimental Prerequisites

3

3.1 Experimental Setup 1

Fig. 3.1 depicts a 3D illustration of the experimental setup used in Secs. 4.1, 4.2 and 4.3 (Setup 1). A more detailed sketch can be found in Appendix A2.1. Setup 1 consists of an inverted microscope (Olympus, IX71) with a mounted piezo translation stage (Physik Instrumente, P-733.3). The heating laser is a focused continuous wave (CW) laser at a wavelength of 532 nm (CNI, MGL-III-532). The beam diameter is increased by a beam expander and sent to an acousto-optic deflector (AA Opto-Electronic, DTSXY-400-532) and a lens system[182] to steer the laser focus in the sample plane. The deflected beam is focused by an oil-immersion objective (Olympus, UPlanApo ×100/1.35, Oil, Iris, NA $0.5 - 1.35$) to the sample plane ($w_0 \approx 0.8$ µm beam waist in the sample plane). The sample is illuminated with an oil-immersion darkfield condenser (Olympus, U-DCW, NA 1.2–1.4) and a white-light LED (Thorlabs, SOLIS-3C). The scattered light is imaged by the objective and a tube lens (250 mm) to an EMCCD (electron-multiplying charge-coupled device) camera (Andor, iXon DV885-LC-VP). The variable numerical aperture of the objective was set to a value below the minimum aperture of the darkfield condenser. The dichroic beam splitter was selected to reflect the laser wavelength (Omega Optical, 560DRLP) and a notch filter is used to block any remaining back reflections from the laser (Thorlabs, NF533-17). The acousto-optic deflector (AOD) as well as the piezo stage are driven by an AD/DA (analog-digital/digital-analog) converter (Jäger Messtechnik, ADwin-Gold II). A LabVIEW program running on a desktop PC (Intel Core i7-2600 4× 3.40 GHz CPU) is used to record and process the images as well as to control the AOD feedback via the AD/DA converter.

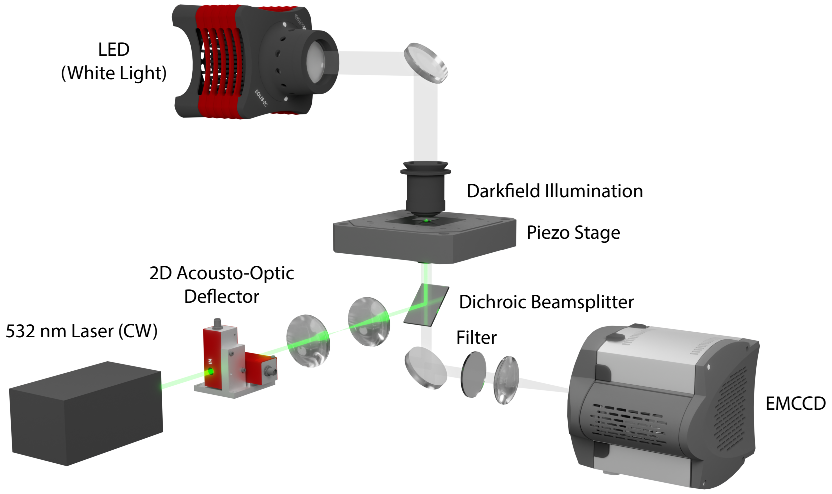

Fig. 3.1: 3D illustration of the experimental setup used in Secs. 4.1, 4.2 and 4.3.

3.2 Experimental Setup 2

Fig. 3.2 depicts a 3D illustration of the experimental setup used in Sec. 4.4 (Setup 2). A more detailed sketch can be found in Appendix A2.2. Setup 2 consists of an inverted microscope (Olympus, IX73) with a mounted piezo translation stage (Physik Instrumente, P-733.3). The chrome structures are heated by a continuous wave (CW) laser at a wavelength of 808 nm (Pegasus Lasersysteme, PL.MI.808.300). The beam diameter is increased by a beam expander and sent to an acousto-optic deflector (Brimrose, 2DS-75-40-808) and a lens system[182] to steer the laser focus in the sample plane. The deflected beam is focused by an objective lens (Olympus, ×100, 1.3 oil) to the sample plane ($w_0 = 500$ nm beam waist in the sample plane). The fluorescence of the ThT dye molecules is excited by a 445 nm laser (CNI, MDL-III-445-200), which is expanded and merged with the heating laser beam path by a pellicle beam splitter. The fluorescence excitation laser is focused to the back-focal plane to achieve homogeneous illumination in the trap center. Fluorescence is imaged by the same objective lens and a bandpass filter (Chroma, ET490/40) and a tube lens (500 mm) to an EMCCD (electron-multiplying charge-coupled device) camera (Andor, iXon3 DU-897E-CS0-#BV). A 750 nm short-pass filter (Thorlabs, FESH0750) is used to block back reflections from the heating laser. The dichroic beam splitter was selected according to the excitation, emission, and heating laser wavelength (Omega Optical, XF2034). The acousto-optic deflector as well as the piezo stage are driven by an AD/DA (analog-digital/digital-analog) converter (Jäger Messtechnik, ADwin-Gold II). A LabVIEW program running on a desktop PC (Intel Core i7-4790K 4× 4.00 GHz CPU) is used to record fluorescence images in real-time and to control the AD/DA converter.

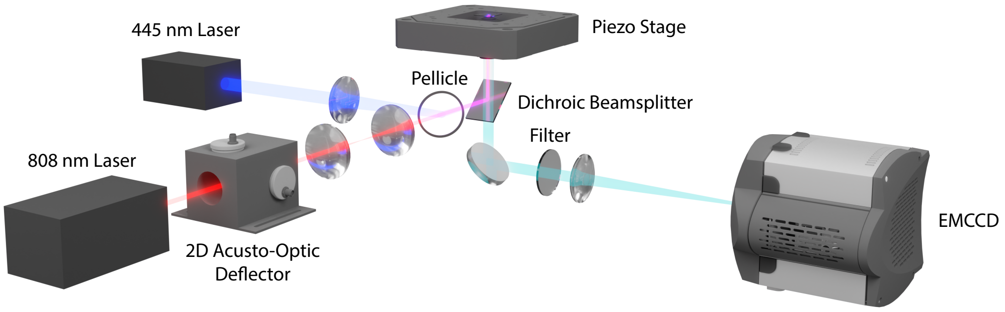

Fig. 3.2: 3D illustration of the experimental setup used in Sec. 4.4.

3.3 Sample Preparation

Typically, the samples within this thesis consist of two glass coverslips confining a thin liquid film of a few µm height. In all experiments the coverslips were thoroughly cleaned in an ultrasonic bath with Hellmanex III (1%), acetone, isopropyl and Milli-Q water followed by 3 min plasma cleaning (Harrick Plasma, PDC-32G) before usage. Between the subsequent steps the coverslips have been dried with a nitrogen gun. Then, if required by the specific experiment, one of the two coverslips was coated with a gold film or chrome structures. For the actual sample preparation the edges of one of the coverslips are covered with a thin layer of PDMS using a syringe needle.

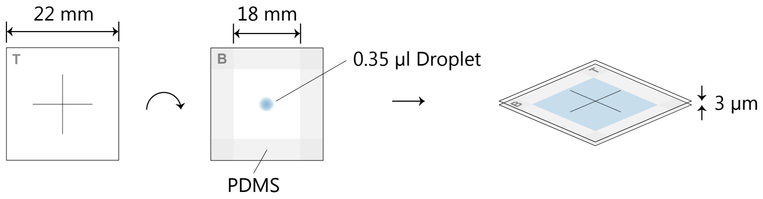

Fig. 3.3: Illustration of the sample preparation.

Then, about 0.3 µl of the solution to be investigated is pipetted in the middle of the coverslip and the sample is sealed by placing the second coverslip on top (Fig. 3.3). The area covered by the liquid determines the height of the liquid film. For a covered area of 10 mm × 10 mm and a liquid volume of 0.3 µl the liquid film height is about 3 µm. The specific sample preparation steps are provided with the Supplementary Information of each section.
To prevent the adsorption of the microparticles and biomolecules the coverslips in Secs. 4.2 – 4.4 were passivated with Pluronic F-127[157]. Pluronic is a commercially available block copolymer consisting of two poly(ethylen oxide)-blocks (PEO) with a poly(propylen oxide)-block (PPO) in the center (PEO-PPO-PEO). The central PPO-block is hydrophobic while the PEO-blocks are hydrophilic[155]. To attain the adsorption of Pluronic F-127 in a brush-like configuration, the cleaned, hydrophilic coverslips were rendered hydrophobic with a thin layer of polystyrene.

3.4 Temperature Measurements Using 5CB

The precise measurement of temperatures on nanometer length scales is essential for the analysis of all experimental results within this thesis. Existing methods to estimate temperatures locally are typically based on the optical measurement of temperature-dependent quantities such as the fluorescence emission of dye molecules[183–185], quantum dots[186], nanodiamonds[187,188] or the Raman signal of molecules[189]. These approaches usually have the disadvantage of a non-linear change of the signal with temperature and provide only the relative change of the temperature, requiring reference measurements for the estimation of absolute values. Other techniques focus on the analysis of the temperature-dependent variation of the refractive index[190]. Yet, this requires detailed information on the temperature dependence of the refractive index. Recently, it has been demonstrated that anti-Stokes thermometry can directly measure the inner temperature of gold nanoparticles[191,192]. However, so far this technique has only been applied for gold nanoparticles and the underlying mechanisms are not yet fully understood[193].
Here, we use method based on a phase transition[194] utilizing the phase transition of the liquid crystal 5CB (4-cyano-4'-pentylbiphenyl). Below the phase transition temperature of about $T_{\mathrm{pt}} = 35\,^\circ\mathrm{C}$ the liquid crystal is in its nematic phase with the molecules stacked and oriented in a preferred direction. Above the phase transition temperature the order vanishes and the liquid crystal is in its isotropic phase. An isotropic bubble around a heated nano-object occurs whenever the local temperature exceeds the phase transition temperature $T_{\mathrm{pt}} = 35\,^\circ\mathrm{C}$ as depicted in Fig. 3.4a and plotted in Fig. 3.4b. The edge of the isotropic phase becomes visible with brightfield as well as darkfield illumination due to the large refractive index difference between the isotropic phase and surrounding nematic phase[195,196] (Appendix. A2.3).

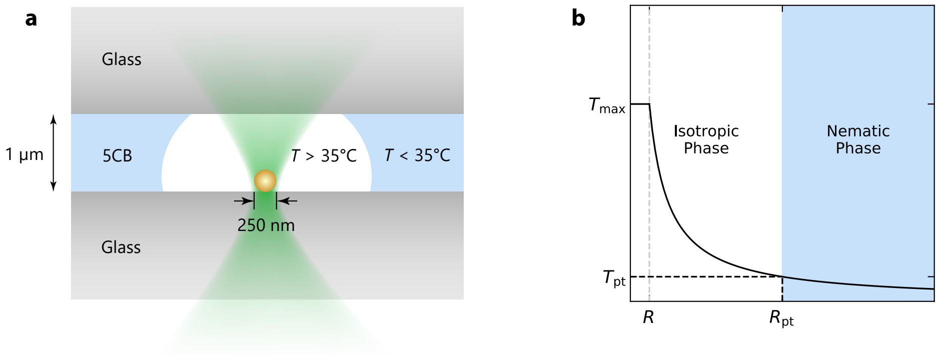

Fig. 3.4: **a**, Sketch of the measurement principle and the sample geometry. **b**, The temperature profile of a heated gold nanoparticle with radius R.

Within this section we demonstrate the method by measuring the temperature increment of a gold nanoparticle heated by a focused laser beam. In Sec. 4.1 and Sec. 4.2 the same approach is used to measure the temperature increment of a heated gold film and a symmetric swimmer particle, respectively. Here, for the sample preparation gold nanoparticles are spin-coated on a glass coverslip and embedded in a 5CB film of about 1 µm height, covered by a second glass coverslip on top. If we assume a radially symmetric temperature, the temperature increments at the distance r from the particle center is given by $\Delta T(r) = \Delta T_{\max} R/r$ (Sec. 2.5.2). The radius of the phase transition R_{pt} is then obtained by:

$$R_{\mathrm{pt}} = \frac{R}{35\,^{\circ}\mathrm{C} - T_0} \Delta T_{\max} \,. \tag{3.1}$$

Here, T_0 is the surrounding temperature. The radius of the isotropic bubble is expected to increase linearly with increasing surface temperature $\Delta T_{\max}$. Fig. 3.5a, b depict the experimental data for an $R = 125$ nm gold nanoparticle heated by a focused laser ($\lambda = 532$ nm wavelength, $w_0 = 580$ nm beam waist). The sample temperature was set to $T_0 = 25\,^{\circ}\mathrm{C}$. The blue data points in Fig. 3.5a depict the phase transition radii extracted from the optical microscopy images shown in Fig. 3.5b. The surface temperature increment $\Delta T_{\max}$ in 5CB was then calculated by rewriting Eq. (3.1) into $\Delta T_{\max} = (35\,^{\circ}\mathrm{C} - T_0)\, R_{\mathrm{pt}}/R$ (Fig. 3.5a, green data points).

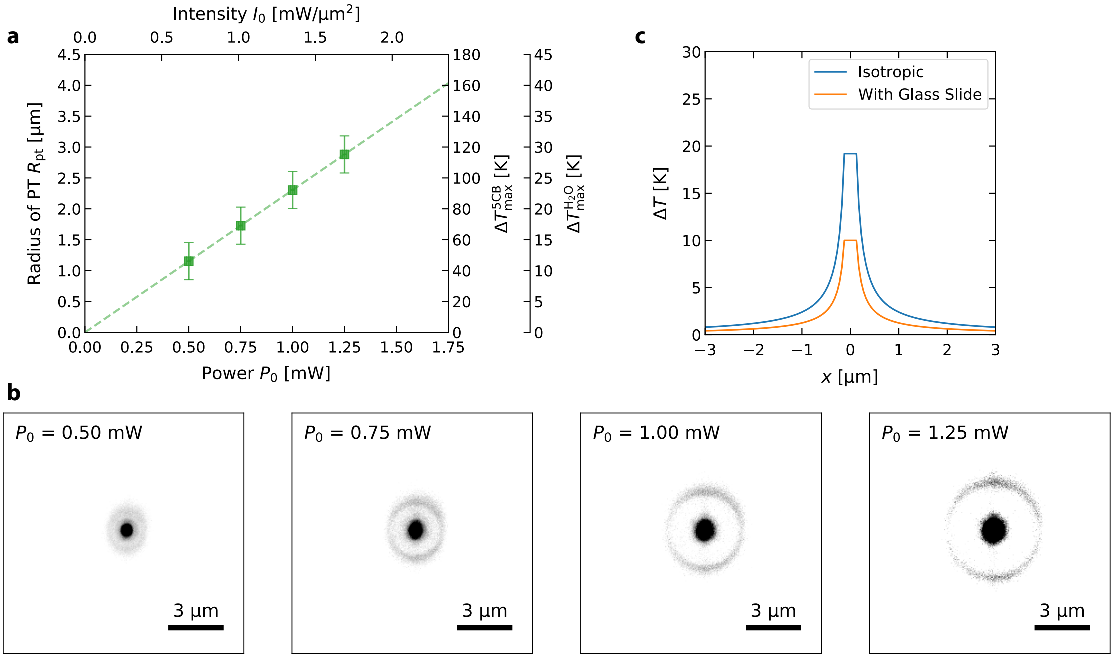

Fig. 3.5: **a**, The measured phase transition radius and the temperature increment in 5CB ($\Delta T_{\max}^{5\mathrm{CB}}$) calculated using Eq. (3.1) as functions of the incident laser power P_0. The temperature increment in water ($\Delta T_{\max}^{\mathrm{H_2O}}$) is by a factor of 4 smaller than in 5CB due to the different thermal conductivity. **b**, The darkfield optical microscopy images corresponding to the data points in (**a**). **c**, Comparison of the temperature profile of a gold nanoparticle embedded in an isotropic medium (blue curve) and located on a glass coverslip (orange curve).

The peak intensity of the focused laser beam was calculated with $I_0 = 2P_0/(\pi\omega_0^2)$. The corresponding temperature increment of the gold nanoparticle in water can be estimated by comparing the thermal conductivities of water $\kappa_{\mathrm{H_2O}}$ and the liquid crystal within its isotropic phase $\kappa_{5\mathrm{CB}}$ (Appendix A2.3). Above the phase transition temperature the value is mostly constant with $\kappa_{5\mathrm{CB}} = 0.15\ \mathrm{W\,m^{-1}K^{-1}}$. For simplicity the nematic phase is ignored since major part of the temperature profile is within the isotropic phase. The thermal conductivity of water is $\kappa_{\mathrm{H_2O}} = 0.6\ \mathrm{W\,m^{-1}K^{-1}}$. Hence, the temperature increment of the gold particle is a factor of 4 smaller when embedded in water as displayed on the right axis of Fig. 3.5a. The green dashed line represents a linear fit to the data that provides the temperature increment per heating power in water, $\Delta T_{\max}/I_0 \approx 30\ \mathrm{K\,\mu m^2\,mW^{-1}}$). The theoretical value is $\Delta\hat{T}_{\max}/I_0 = \sigma_{\mathrm{abs}}/(4\pi\kappa R)$, where $\hat{T}_{\max}$ denotes the temperature increment of the particle embedded in a medium of isotropic thermal conductivity. Here, the particle is located on a glass coverslip with significantly higher thermal conductivity ($\kappa_{\text{Glass}} \approx 1.14\ \mathrm{Wm^{-1}\,K^{-1}}$) than the surrounding liquid crystal ($\kappa_{\text{5CB}} \approx 0.15\ \mathrm{W\,m^{-1}K^{-1}}$). Thus, the temperature increment of the gold nanoparticle is smaller when located at the glass surface. This difference was quantified numerically (Fig. 3.5c). The ratio between the measured temperature increment $\Delta T_{\max}$ and the temperature increment when located in an isotropic medium $\Delta\hat{T}_{\max}$ is approximated to $\Delta\hat{T}_{\max}/\Delta T_{\max} = 1.93$. Finally, with absorption cross-section of the nanoparticle in water with $\sigma_{\text{abs}} = 0.068\ \mathrm{\mu m^2}$, estimated using Mie theory, we find $\Delta T_{\max}/I_0 \approx 32\ \mathrm{K\,\mu m^2\,mW^{-1}}$ in well agreement with the experimental estimate.

3.5 Zeta Potential Measurements

The zeta potential of the particles used in Sec. 4.1 has been measured with electrophoretic light scattering (Malvern Instruments, Zetasizer Nano ZS). The technique is based on the analysis of light scattered from a particle suspension with an applied electric field and typically measures the electrophoretic mobility μ of the particle. The electrophoretic mobility μ and the zeta potential ζ are related via[197]:

$$\mu = \frac{2}{3}\frac{\varepsilon\zeta}{\eta}f(x)\ . \tag{3.2}$$

Here, ε is the static permittivity of the solvent, η the solvent viscosity, and $f(x)$ the Henry function (Fig. 3.6) with $x = R/\lambda_{\text{D}}$, where λ_{D} is the Debye length and R the particle radius. Hence, to obtain the zeta potential from a thermophoretic mobility measurement one has to solve Eq. (3.2) for ζ, requiring the estimation of the Debye length, Eq. (2.37), and knowledge of particle radius.

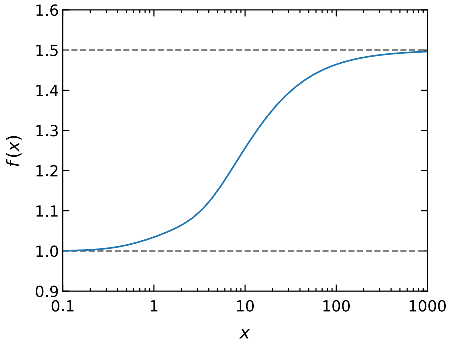

Fig. 3.6: Plot of the Henry function $f(x)$ using Eq. (3.3).

For a particle with radius $R = 125$ nm suspended in an aqueous 10 mM NaCl solution we find $\lambda_{\text{D}} = 3$ nm and $x \approx 41$ with $f(41) \approx 1.42$. For the Henry function we have used the approximation[198]

$$f(x) = 1 + \frac{1}{2}\left(1 + \frac{5}{2x(1+2\mathrm{e}^{-x})}\right)^{-3}\ . \tag{3.3}$$

In the limit $x \ll 1$ we find $f(x) \to 1$ and recover the electrophoretic mobility in the Hückel limit, whereas for $x \gg 1$, $f(x) \to 3/2$ the Smoluchoski limit is recovered.

4
Publications

This chapter contains the main results of this thesis and is divided into four different sections (Sec. 4.1–4.4), each corresponding to a peer-reviewed journal publication:

[P1] **M. Fränzl** and F. Cichos, Hydrodynamic Manipulation of Nano-Objects by Optically Induced Thermo-Osmotic Flows, *Nat. Commun.* **13**, 656 (2022).

[P2] **M. Fränzl**, S. Muiños-Landin, V. Holubec, and F. Cichos, Fully Steerable Symmetric Thermoplasmonic Microswimmers, *ACS Nano* **15**, 3434 (2021).

[P3] **M. Fränzl** and F. Cichos, Active Particle Feedback Control with a Single-Shot Detection Convolutional Neural Network, *Sci. Rep.* **10**, 12571 (2020).

[P4] **M. Fränzl**, T. Thalheim, J. Adler, D. Huster, J. Posseckardt, M. Mertig, and F. Cichos, Thermophoretic Trap for Single Amyloid Fibril and Protein Aggregation Studies, *Nat. Methods* **16**, 611 (2019).

The articles have been adapted and reworked to integrate into the layout and the framework of this thesis. Details on the author contributions are provided in the "List of Publications" section. The Supplementary Videos are available at https://www.doi.org/10.5281/zenodo.5831821.

4.1 Hydrodynamic Manipulation of Nano-Objects by Thermo-Osmotic Flows

4.1.1 Abstract

The manipulation of nano-objects at the microscale is of great technological significance to construct new functional materials, to manipulate tiny amounts of liquids, to reconfigure sensorial systems or to detect minute concentrations of analytes in medical screening. It is commonly approached by the generation of potential energy landscapes, for example, with optical fields or by using pressure driven microfluidics. Here, we show that strong hydrodynamic boundary flows enable the trapping and manipulation of nano-objects near surfaces. These thermo-osmotic flows are induced by modulating the van der Waals interaction at a liquid–solid interface with optically generated temperature fields. We use a thin gold film on a glass substrate to provide localized but reconfigurable point-like optical heating. Convergent boundary flows with velocities of tens of micrometres per second are observed and substantiated by a quantitative physical model. The hydrodynamic forces acting on suspended nanoparticles and attractive van der Waals or depletion induced forces enable precise positioning and guiding of the nanoparticles. Fast multiplexing of flow fields further provides the means for parallel manipulation of many nano-objects and the generation of complex flow fields. Our findings have direct consequences for the field of plasmonic nano-tweezers as well as other thermo-plasmonic trapping schemes and pave the way for a general scheme of nanoscopic manipulation with boundary flows.

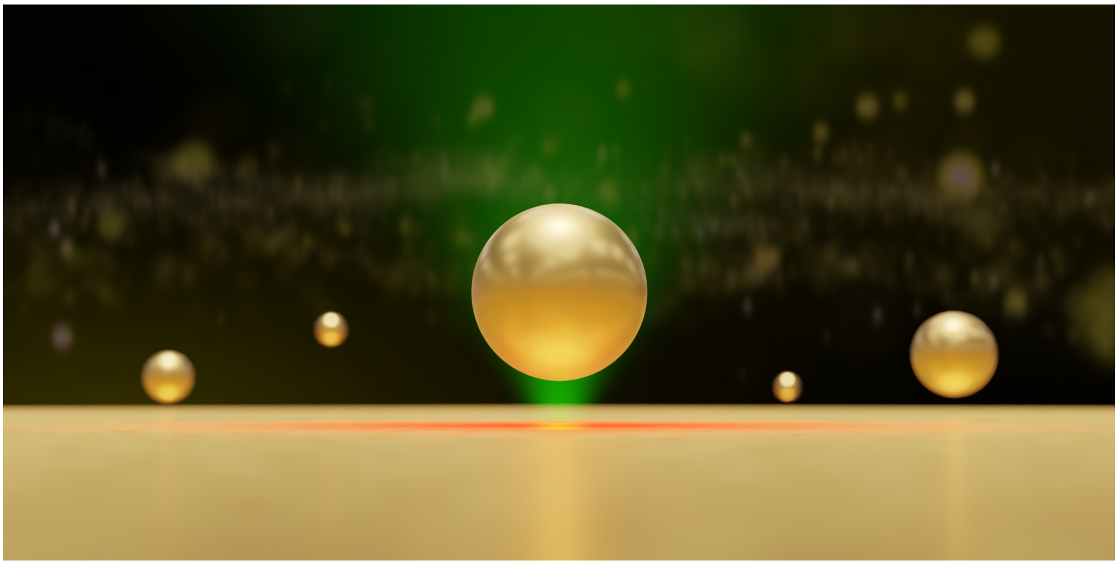

Illustration of a thermo-hydrodynamically trapped gold nanoparticle near a gold surface. Rendered using Blender 2.83 and the Cycles Renderer.

The section is based on the following article:

[P1] **M. Fränzl** and F. Cichos, Hydrodynamic Manipulation of Nano-Objects by Optically Induced Thermo-Osmotic Flows, *Nat. Commun.* **13**, 656 (2022).

The article has been adapted and revised. Details on the author contributions are provided in the "List of Publications" section.

4.1.2 Introduction

The control and manipulation of nano-objects is a key element for future nanophotonics[181,199,200], material science[3,201,202], biotechnology[199,203,204] or even quantum sensing[205]. Analytes dissolved in liquids, for example, need to be delivered, concentrated, separated or locally confined for further studies to become eventually processed and removed. Photonic elements including plasmonic nanostructures require precise positioning or controlled rearrangements to serve as adaptive functional structures[201,206]. Key elements of the control at the micro- and nanoscale are often either pressure driven fluidics transporting liquid volume and solutes or the generation of potential energy landscapes or force fields. The latter is achieved with optical[200] and plasmonic tweezers[207,208], magnetic fields[209], or using electrokinetic[90] or opto-electronic[210] effects. Especially in the field of plasmonic tweezers and nanoantennas, where light is used to excite collective electron motion in noble-metals, the Joule losses lead to the unavoidable generation of heat at boundaries as an unwanted side effect[52,211]. Yet, such optically generated temperature fields seem also suitable for the manipulation of nano-objects in liquids, for example, for the trapping of nanoparticles[1] and single molecules[8] or protein aggregates[P4] as well as for manufacturing active particles[11,46,P2,85]. Those techniques rely on a drift of molecules and particles in optically generated temperature gradients termed thermophoresis or suggest thermo-electric effects[6] relying on a thermally induced charge separation. In addition, thermo-electrohydrodynamic effects using time-varying electric fields have been proposed for rapid particle transport[212,213] and convective effects that arise from temperature-induced density changes in the large liquid cells have been reported[29,32,33,214].

Here, we report on a fundamental physical process that is able to provide a versatile trapping and manipulation of nano-objects and fluids near surfaces in the simplest geometries. Contrary to most other techniques, our scheme is based on hydrodynamic flows generated by optically induced thermo-osmosis. Thermo-osmosis relies on a perturbation of the interfacial interactions at a liquid–solid boundary and is present in all experiments involving temperature gradients in plasmonic structures including plasmonic tweezers. We show that local temperature gradients on a thin gold film induce strong interfacial flows of several 10 to 100 $\mu m\,s^{-1}$ in its direct vicinity (~ 10 nm), that results in a flow pattern reminiscent of convection. Based on a fully quantitative analysis of our experimental results we reveal that these thermo-osmotic flows on gold-water interfaces are induced by a temperature-induced perturbation of the van der Waals (vdW) interactions. Nano-objects suspended in the liquid are therefore dragged by the hydrodynamic forces originating from these flows. Utilizing attractive vdW interactions of the nano-object with the gold surface or temperature-induced depletion, we trap and manipulate different types of nano-objects near the surface. The fast heating at small scales allows us to multiplex flow fields and to manipulate multiple objects with great precision. Our detailed analysis of the flow fields, the localization accuracy of nano-objects, and a comparison with numerical and theoretical predictions provide a quantitative understanding of these effects and paves the way for controlling boundary layer dynamics to manipulate objects at the smallest length scales in solutions.

4.1.3 Results and Discussion

Experimental Configuration and Working Principle Our experiments rely on a simple sample geometry with a gold film (50 nm) that is deposited on a glass coverslip (Fig. 4.1). The sample chamber contains a suspension of gold nanoparticles (AuNPs) or other nano-objects (polystyrene NPs and ellipsoids) with a controlled amount of salt (NaCl), surfactant (SDS, sodium dodecyl sulfate) or polymers (PEG, polyethylene glycol). The gold film is heated locally in an inverted microscopy setup by a highly focused laser ($\lambda = 532$ nm wavelength) using beam steering optics (2D acousto-optic deflector). The nano-objects are observed using darkfield illumination with an oil-immersion darkfield condenser (NA 1.2) and a 100× oil-immersion objective set to NA 0.6 (see Sec. 3.1 and Sec. 4.1.5.1 for details).

The trapping of nano-objects as detailed in the following is comprising two effects. i) The vertical confinement of the suspended objects is achieved by an attractive interaction of the suspended nano-objects with the gold surface, which is found to be the vdW interaction for gold nanoparticles and can be replaced by depletion forces for other materials. ii) The generation of thermo-osmotic boundary flows that are induced by the local heating and the corresponding perturbation of the liquid–solid interactions. This boundary flow is directed radially inwards to the heated spot and provides a confining hydrodynamic force on suspended objects at the heating spot. In the following paragraphs, we detail the bare interaction of gold nanoparticles with the gold surface, which is responsible for the vertical confinement and independent of the heating. The non-equilibrium contribution to trapping is given by the thermo-osmotic flow for which we further give a quantitative analysis.

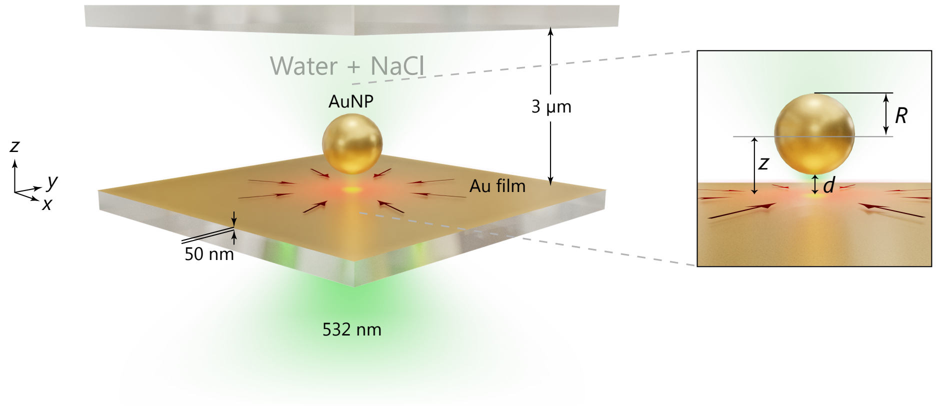

Fig. 4.1: Thermo-Hydrodynamic Manipulation of Au NPs in NaCl Solution. The sample consists of two glass coverslips that confine a 3 µm thin liquid film of gold nanoparticles (AuNPs) with radius R dispersed in aqueous NaCl solution. The lower glass coverslip carries a 50 nm Au film that is locally heated by optical absorption of a focused laser of $\lambda = 532$ nm wavelength.

Dynamics of AuNPs Close to a Au Film Consider a single AuNP with a radius of $R = 125$ nm that is suspended in an aqueous solution of NaCl at a concentration of $c_0 = 10$ mM and diffusing in a thin liquid film of about 3 µm thickness over a 50 nm Au film (Fig. 4.1). Exploring the diffusion of the particle we observe a restriction of the z-positions to a thin layer close to the gold film (see Sec. 4.1.5.2 for details). The gold particle never defocuses under these conditions while it does in deionized (DI) water (Supplementary Video 1.1). This restricted out-of-plane motion is the result of interactions comprising an attractive vdW contribution, a repulsion of the electrostatic double layers of the particle and surface[142] as described by the DLVO theory and the sedimentation potential (see Sec. 2.1.4 and Sec. 2.2.3 for details):

$$U(d, c_0) = U_\mathrm{E}(d, c_0) + U_\mathrm{vdW}(d) + U_\mathrm{S}(d) \ . \tag{4.1}$$

The total potential, Eq. (4.1), for the experimental situation is depicted in Fig. 4.2a for different salt concentrations (see Sec. 4.1.5.3 for details) as a function of the surface-to-surface distance

$d = z - R$, where z denotes the distance of the particle center from the surface (Fig. 4.1). The stronger screening of the surface charges at the gold film and the AuNP at higher salt concentration increase the importance of attractive vdW interactions to create this secondary minimum in the DLVO part of the potential. This potential influences the observed dynamics and leads also to a stronger hydrodynamic coupling of the particle to the nearby gold surface (Sec. 2.1.3). Over the course of a diffusion trajectory, the particle samples different regions according to the probability density (Boltzman distribution, Sec. 2.1.2):

$$p(d, c_0) \propto \mathrm{e}^{-U(d,c_0)/(k_\mathrm{B}T)} , \tag{4.2}$$

to be at a distance d from the surface (Fig. 4.2a, filled curves). Calculating its mean distance $\langle d \rangle$ from the surface (Fig. 4.2b, Sec. 4.1.5.3) reveals that only in the case of $c_0 = 10$ mM the particle is well confined in the DLVO potential, while at lower salt concentrations only a slightly enhanced probability of finding the particle near the surface is observed.

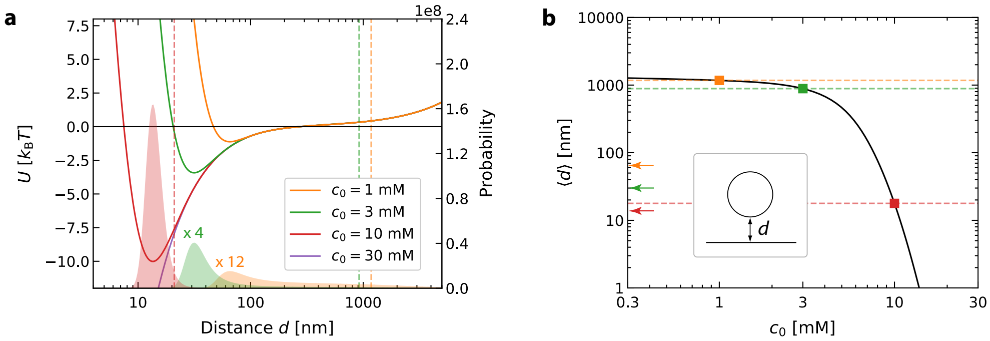

Fig. 4.2: DLVO Potential. **a**, Plot of the DLVO potential, Eq. (4.1), between a 250 nm Au NP and a 50 nm Au film on a glass surface as function of surface-to-surface distance d for different NaCl concentrations c_0. The shaded curves display the calculated probability density for finding the particle at this distance at the different salt concentrations (see Sec. 4.1.5.3 for details). The vertical dashed lines correspond to the mean distance of the particle as calculated from the probability density for a 3 µm liquid film height. **b**, Relation between the mean distance $\langle d \rangle$ and the NaCl concentration c_0. The symbols and the horizontal lines denote the calculated distances for measured concentrations. The arrows indicate the secondary minimum of the corresponding DLVO potentials in (**a**).

Fig. 4.3a depicts the mean squared displacement (MSD) measured for different NaCl concentrations (see Sec. 2.1.2 for details). The in-plane diffusion coefficients $\langle D_\parallel \rangle$ are extracted from linear fits to $\left\langle \Delta r^2(\tau) \right\rangle = 4\langle D_\parallel \rangle \tau$ (dashed lines in Fig. 4.3a) and plotted as function of the NaCl concentration in Fig. 4.3b. We find a decreasing $\langle D_\parallel \rangle$ with increasing salt concentration.

As the in-plane diffusion coefficient $D_\parallel$ is modulated with the distance z of the particle from the wall (see Sec. 2.1.3 for details) the measured in-plane diffusion coefficient $\langle D_\parallel \rangle$ is thus a weighted average of the diffusion coefficient over the different vertical positions d. Using $p(d, c_0)$ we can calculate the corresponding salt concentration dependence of the in-plane diffusion coefficient and compare that to the experimental results (see Sec. 4.1.5.3 for details). Fig. 4.3b shows that the experimentally observed $\langle D_\parallel \rangle$ is in fair agreement with the theoretical predictions for three different Hamaker constants (Fig. 4.3b, gray curves).

If one additionally calculates the mean distance $\langle d \rangle$ of the particle from the surface using $p(d)$, it can be seen that the minimum of the DLVO potential significantly affects the mean distance only for $c_0 > 3$ mM. For $c_0 = 10$ mM, the potential minimum corresponds approximately to the mean distance $\langle d \rangle$, indicating that the particle is completely trapped near the DLVO potential minimum and is not delocalized over the entire film thickness as at lower concentrations. Using the calculated mean distance as a function of concentration c_0, it is also possible to estimate the mean distance $\langle d \rangle$ of the particles from the surface in the experiments, which is about 1.5 µm and 0.9 µm at the lowest NaCl concentrations (Fig. 4.2b). At a concentration of $c_0 = 10$ mM the particle is hovering at a distance of $\langle d \rangle = 20$ nm to the surface. Note that this corresponds to values of $z/(2R) \approx 0.58$, which is far below the commonly explored region of the hydrodynamic coupling of colloids to walls[138] allowing to experimentally explore new terrains also in the field of hydrodynamic wall coupling of colloids.

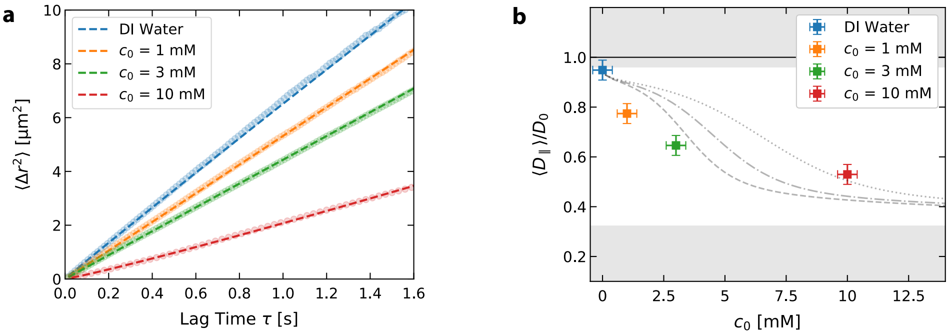

Fig. 4.3: In-Plane Diffusion Analysis. **a**, The mean squared displacement (MSD) of 250 nm AuNPs over a 50 nm gold film for different NaCl concentrations c_0. The dashed lines represent linear fits to $\langle \Delta r^2(\tau) \rangle = 4\langle D_\parallel \rangle \tau$. **b**, The measured diffusion coefficient $\langle D_\parallel \rangle / D_0$ parallel to the Au film with respect to the bulk diffusion coefficient D_0 as function of the NaCl concentration c_0. Symbols correspond to the experimental values measured without additional laser heating of the gold film. The lines reflect the theoretical prediction including a distance dependent diffusion coefficient for three different Hamaker constants, $A_\mathrm{H} = 4 \cdot 10^{-20}$ J (dotted), $A_\mathrm{H} = 5 \cdot 10^{-20}$ J (dash-dotted) and $A_\mathrm{H} = 6 \cdot 10^{-20}$ J (dashed) of gold according to a weighting with the probability density $p(d, c_0)$.

Hydrodynamic Particle Confinement When tightly focusing light of 532 nm wavelength to the gold film, about 30 % of the incident energy is absorbed (Sec. 2.4.3) and converted into heat that perturbs the liquid–solid interactions. The temperature rise at the gold surface can be determined using a thin nematic liquid crystal (5CB) film and substantiated by finite element simulations with the complete three-dimensional temperature profile in the solution (see Fig. 4.4, Secs. 4.1.5.4 and 4.1.5.5 for details).

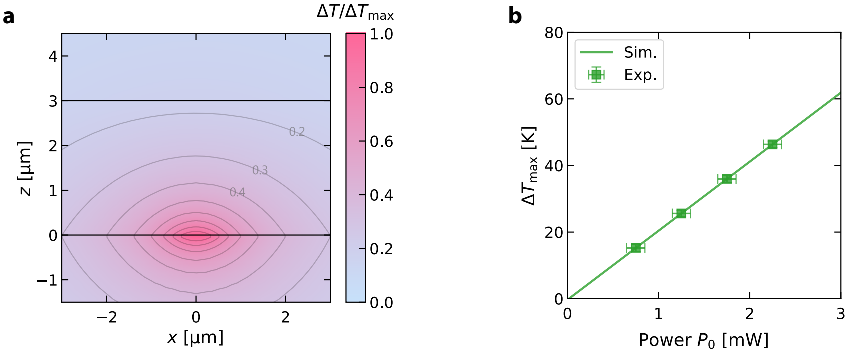

Fig. 4.4: Temperature Distribution. **a**, Simulation of the relative temperature increment in the xz-plane of the sample. **b**, Experimentally obtained temperature increment ΔT_max as a function of the incident laser power P_0 (green data points) compared to the simulated values (green curve).

These local temperature perturbations of the liquid–solid interactions at the interface induce a thermo-osmotic flow[49,56] (see Sec. 2.3.2 for details). Taking a liquid volume element close to the solid from the cold side and exchanging that with one at the hot side would not only transport heat since the liquid volumes have different temperatures, but also additional free energy as the liquid has a different interaction with the solid in these regions. The flow is induced in an ultrathin boundary layer corresponding in thickness to the length scale of liquid–solid interactions. Since the characteristic interaction length of liquid–solid interactions is only a few nanometers, the boundary flow on the substrate can be collapsed into a hydrodynamic slip boundary condition:

$$v_\parallel = \chi \frac{\nabla_\parallel T}{T} \, , \tag{4.3}$$

where η is the viscosity of the fluid, χ the thermo-osmotic coefficient, T the temperature and $\nabla_{\|}T$ is the temperature gradient parallel to the surface. The thermo-osmotic coefficient χ contains all information about the interfacial interaction between the liquid and the solid (see Sec. 2.3.2 for details). If $\chi < 0$ the liquid is driven to the cold, whereas for $\chi > 0$, the liquid is driven to the hot. These boundary flows are present at all liquid–solid interfaces with tangential temperature gradients, though, they are commonly overlooked. They become particularly important for plasmonic and thermo-plasmonic trapping[211], as those techniques rely on the dynamics of molecules and particles in the direct vicinity of plasmonic nanostructures.

The boundary flow drives the flow field inside the fluid film. The resulting volumetric flow field can be tracked experimentally by single AuNPs in DI water, where the particles are not confined to a surface layer as reported above. We analyze the in-plane (xy) position of the particle and its z-position, where the latter is estimated from the radius r_0 of the defocussed particle images (see Supplementary Video 1.2 and Sec. 4.1.5.2 for details). The measured velocity distributions in the xy-plane near the gold layer and in the xz-plane are shown in Fig. 4.5a, b and compare well to simulation results in Fig. 4.5d, e (Sec. 4.1.5.6).

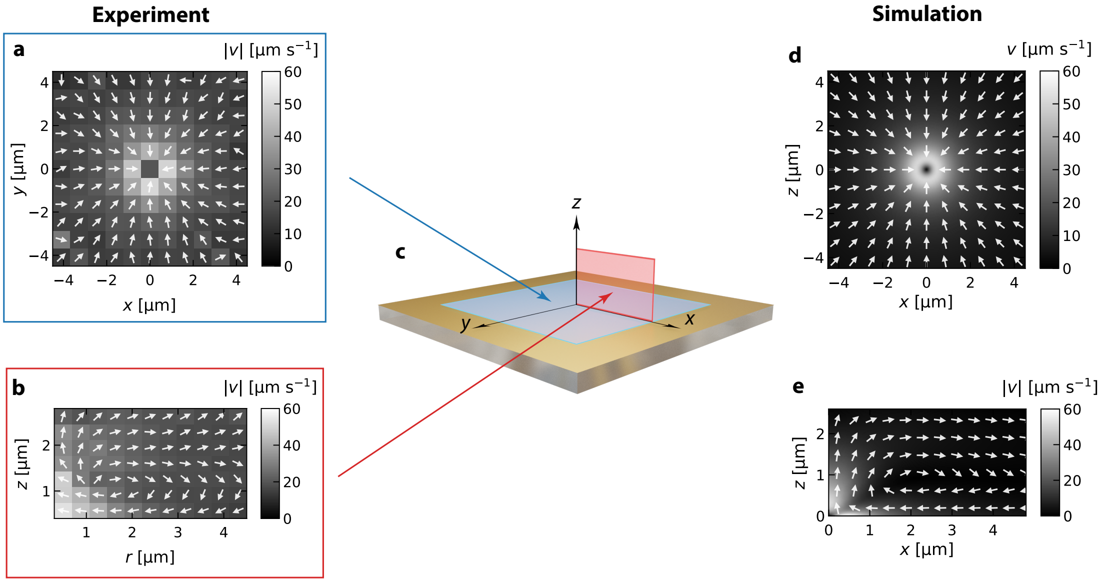

Fig. 4.5: Thermo-Osmotic Flow Field. **a**, Measured thermo-osmotic flow field in the xy-plane in close proximity to the gold film ($z < 500$ nm). **b**, Measured thermo-osmotic flow field in the xz-plane. **c**, Illustration of the flow field planes in (**a**) and (**b**). **d**, **e**, The corresponding simulation results.

From these measurements, we extract a thermo-osmotic coefficient on the order of $\chi \sim 10 \cdot 10^{-10}\ \mathrm{m^2\,s^{-1}}$. We can break down the contributions to this value into an electric double layer contribution and a vdW contribution using the experimental parameters. We find

$$\chi_{\mathrm{E}} = \frac{\varepsilon\zeta^2}{8\eta} \approx 0.8 \cdot 10^{-10}\ \mathrm{m^2/s^{-1}}\ . \tag{4.4}$$

for the double layer contribution, where we used a zeta potential of $\zeta = -30$ mV[149] and a static permittivity of $\varepsilon = 80\,\varepsilon_0$. An estimate of the vdW contribution can be given by

$$\chi_{\mathrm{vdW}} = \frac{A_{\mathrm{H}}\beta T}{3\pi\eta d_0} \approx 9.3 \cdot 10^{-10}\ \mathrm{m^2\,s^{-1}}\ , \tag{4.5}$$

in terms of the Hamaker constant A_{H} between water and the Au film with $\beta = 0.2 \cdot 10^{-3}\ \mathrm{K^{-1}}$ being the thermal expansion coefficient of water (Appendix A1.14) and $d_0 = 0.2$ nm the cut-off parameter[56] (see Sec. 2.3.2 for details). The sum of both contributions $\chi = \chi_{\mathrm{E}} + \chi_{\mathrm{vdW}} = 10.1 \cdot 10^{-10}\ \mathrm{m^2\,s^{-1}}$ matches well with the experimental result and suggests that thermo-osmosis at water–gold interfaces is governed by vdW interactions. The obtained quasi slip velocities are ranging up to 80 $\mu\mathrm{m\,s^{-1}}$s and provide, due to their omnipresence, a unique tool for nanofluidics. These thermo-osmotic flows are induced without any external pressure difference. They can be controlled by the light intensity of the heating laser and are quickly switched due to the extremely fast heat conduction at these length scales (Sec. 2.5). Moreover, the finding of the vdW dominated thermo-osmotic flows suggests that such contributions must be present in any plasmonic trapping experiment with extended gold structures[52,208,211,213].

Using $F_x^{\mathrm{TF}} = 6\pi\eta R\lambda_{\parallel}v_x$ and $F_z^{\mathrm{TF}} = 6\pi\eta R\lambda_{\perp}v_z$, where $\lambda_{\parallel}$ and $\lambda_{\perp}$ are the correction factors for the friction coefficient of a sphere close to a surface (Sec. 2.1.3), we are able to extract the hydrodynamic forces that are exerted on the AuNP tracers. The lateral forces allow to confine objects at the heating spot, yet the hydrodynamic force normal to the surface (z-direction) is repulsive without any additional interaction. Finally, such boundary flows with substantial vertical velocity gradients also exhibit a vorticity, $\boldsymbol{\omega} = \nabla \times \boldsymbol{v}$, that generates a torque on suspended objects causing them to rotate[215] (see Sec. 4.1.5.6 for details).

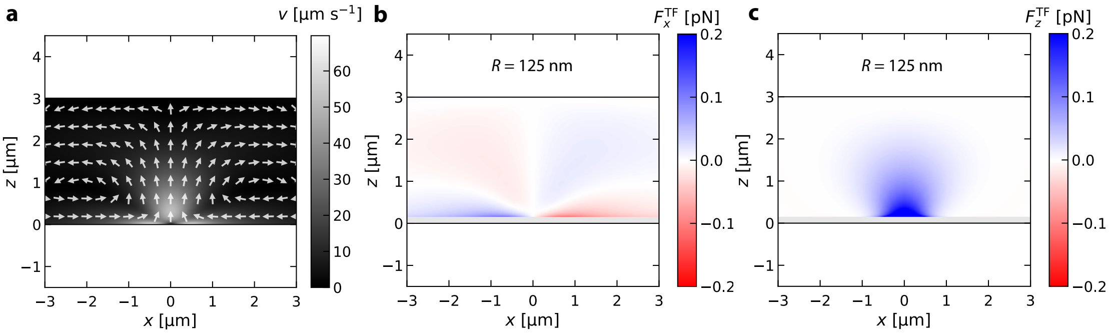

Fig. 4.6: Simulated Thermo-Osmotic Flow and Force Field. **a**, Simulated thermo-osmotic flow field in the xy-plane obtained for the temperature distribution in Fig. 4.4a by imposing a slip velocity $v_{\parallel} \propto \mathrm{d}T/\mathrm{d}x$ on the water–gold interface at $z = 0$ (see Sec. 4.1.5.6 for details). **b**, **c**, The x- and z-component of the hydrodynamic force exerted on the AuNP by the thermo-osmotic flow as function of the NP position. The gray areas are not accessible by the particle, since $z > R$.

Single Particle Trapping and Flow Field Multiplexing The vertical hydrodynamic drag force F_z^{TF} is superimposed with and attractive force due to the DLVO potential when increasing the NaCl concentration. The surface-to-surface distance between AuNP and gold film and the depth of the appearing secondary DLVO potential minimum can be controlled by the NaCl concentration. At a NaCl concentration of about $c_0 = 10$ mM, the attractive potential has a depth of about $10\,k_{\mathrm{B}}T$ (Fig. 4.2a) and is strong enough to compete with the vertical drag force and additional optical forces on the AuNP to trap the particle above the heating spot.

Supplementary Video 1.3 demonstrates this trapping of an AuNP above the hot spot on the Au surface. This is purely the result of the hydrodynamic drag forces generated by the thermo-osmotic flow and the attractive vdW interaction between the AuNP and the Au film. This observation is substantiated by a quantitative evaluation of the lateral trap stiffness and vertical forces, as depicted in Fig. 4.7a, b. The fluctuations of the particle in the hydrodynamic flow arise from a balance of the restoring hydrodynamic currents and the diffusive currents. Analysis of the lateral position histograms (Fig. 4.7c, inset) yields an effective stiffness of the trap (Fig. 4.7a) that well matches the predictions based on the thermo-osmotic flow (Fig. 4.6b, c), when converting the lateral flow speeds into forces using the previously mentioned Stokes friction force for F_z^{TF}. The hydrodynamic trapping stiffness increases linearly up to a heating power of about 1.8 mW. At this power, the vertical forces become strong enough to let the particle escape the secondary DLVO minimum. The AuNPs are then observed to move vertically out of the DLVO potential to follow the flow inside the sample and to eventually return to the boundary flow via sedimentation (Fig. 4.7d, Supplementary Video 1.4). The forces which eject the particle from the potential comprise the hydrodynamic and the optical forces due to the radiation pressure from the heating laser leaked through the film. We have evaluated the individual contributions in simulations. They are shown together with the hydrodynamic force and the total vertical force as compared to the attractive force of the DLVO potential (Fig. 4.7b) and provide quantitative agreement (threshold heating power of 2.25 mW) with our experimental results. Note that while the stationary distribution of particles in the vertical direction is not influenced by the diffusive dynamics, the escape rate from the potential well is heavily altered by the fact that the vertical diffusion coefficient $D_\perp$ of the particle is decreasing to zero when approaching the gold film. This is enhancing the trapping times considerably (see Sec. 4.1.5.3 for details) but also increases the time required for the particle to enter the DLVO minimum by diffusion.

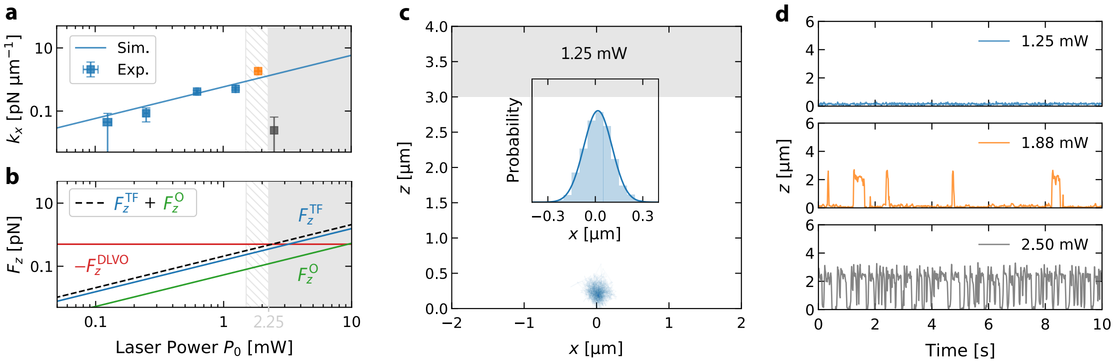

Fig. 4.7: Forces on Trapped NPs in 10 mM NaCl. **a**, The lateral trap stiffness k_x obtained from the variance σ_x^2 of the experimental lateral position histograms as function of the laser power P_0 (blue data points, $k_x = k_\mathrm{B}T/\sigma_x^2$, see the inset in (**c**) for the lateral position histogram at $P_0 = 1.25$ mW). The blue solid line represents the simulation result obtained from the lateral velocity field in Fig. 4.6b. Within the dashed area the particle intermittently escapes the trapping potential in vertical direction and transitions into a regime of instant vertical repulsion for higher laser powers (shaded area). **b**, The z-component of the thermo-osmotic drag force F_z^{TF} (blue line), the optical force F_z^{OF} (green line) and the total force $F_z^{\mathrm{OF}} + F_z^{\mathrm{TF}}$ (black dashed line) as function of the incident laser power P_0 for a NP located at $x = 0$, $d = 30$ ($z = d + R$). The attractive DLVO force F_z^{DLVO} is independent of the incident laser power and depicted as horizontal, red line. **c**, Trajectory of a AuNP for a heating laser power of 1.25 mW (see Supplementary Video 1.2 for details). The inset shows the corresponding lateral distribution histogram. **d**, Time traces of the z-position for three different laser powers.

The observed trapping is, hence, a vdW assisted thermo-hydrodynamic process. Vertical confinement is achieved by vdW attraction and double layer repulsion, while lateral confinement is the result of thermo-osmotic flows induced in an ultra-thin sheet of liquid at the interface. No additional contributions, for example, due to convective flows with similar flow patterns (see Sec. 4.1.5.7 for details) or thermoelectric effects are required for a quantitative description[3,6,62,214]. Precise tuning of the DLVO potential enables the trapping of even smaller Au NPs (Fig. 4.8a, Supplementary Video 1.5).

The speed of heat diffusion, which is about 4 orders of magnitude faster than the particle diffusion[28] allows us to introduce a flow field multiplexing. We switch the heating location between different positions inducing thermo-osmotic flow fields for time periods of about 100 µs. With the help of this multiplexing, we are able to hold multiple $R = 125$ nm AuNPs (Fig. 4.8b, c) at distances of less than 1 µm, which would not be possible with continuous heating of close-by locations (Supplementary Videos 1.6 and 1.7). A trapped AuNP can also be guided along the predefined path over the Au film as fast as 10 µm s^{-1} (Fig. 4.8d, Supplementary Video 1.8). At larger manipulation speeds ($f > 100$ Hz) and higher heating power ($P_0 > 10$ mW) the thermo-osmotic attraction to the heating spot is combined with thermo-viscous flows[67,216]. These flows originate from the temperature dependent viscosity $\eta(T)$ of the liquid and are directed opposite to the scanning direction of the laser[216]. The result of this combination of thermo-osmosis and thermo-viscous flows is a rotating ring-like particle structure (Fig. 4.9a and Supplementary Video 1.9). These different effects, that can be exploited in a simple planar geometry, give rise to numerous applications including for example a freely configurable nanoparticle on mirror geometry for plasmonic sensing[206,217]. The multiplexing of local flow field may be helpful to construct more complex effective flow fields for an efficient transport of analytes without external pressure.

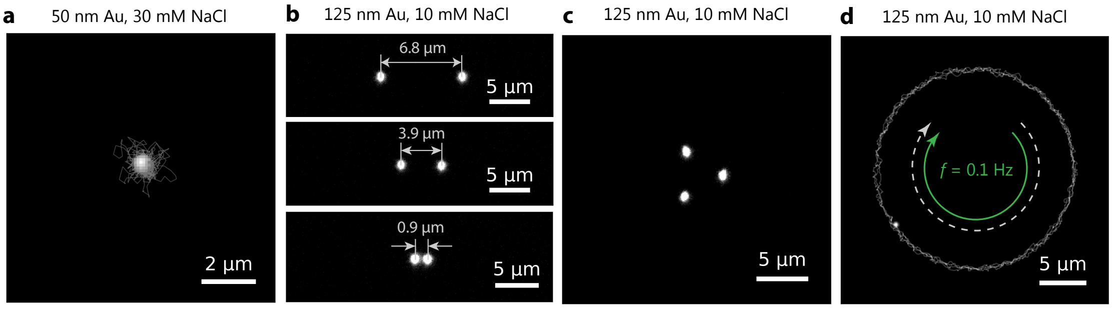

Fig. 4.8: Manipulation of NPs over a Au Film in NaCl and SDS Solution. **a**, A AuNP with 50 nm radius trapped at a NaCl of 30 mM (Supplementary Video 1.5). **b**, Manipulation of two AuNPs by a multiplexed laser beam (Supplementary Video 1.6). **c**, Control of three AuNPs (Supplementary Video 1.7). **d**, Actuation of a single AuNP on a circular trajectory by a steerable laser beam (Supplementary Video 1.8). The green and white, dashed arrows denote the moving direction of the laser focus and particle, respectively.

Beyond Thermo-Osmotic van der Waals Trapping So far, the presented manipulation is based on thermo-osmotic flows that drive the lateral motion of suspended colloids and a vertical confinement due to the secondary minimum of the DLVO potential between AuNP and Au film. While the thermo-osmotic flows are characteristic for all systems containing a heated gold-water interface including all previous studies on thermo-plasmonic trapping, the DLVO potential minimum is much weaker for other materials like polymer colloids or macromolecules due to their smaller vdW attraction. Often, those systems even show a repulsion from the heat source due to thermophoresis, which is not present for AuNP (Sec. 2.3.3). A more generalized strategy therefore needs additional attractive contributions, which confine suspended colloids or molecules to regions close to the gold surface to take advantage of the thermo-osmotic flow.

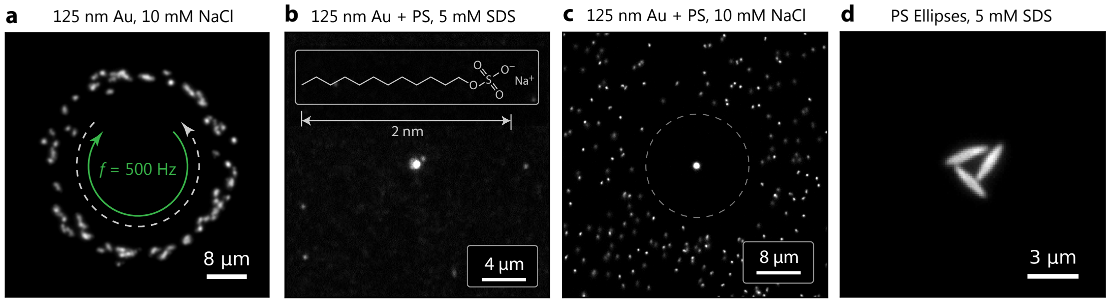

Fig. 4.9: Manipulation of NPs in NaCl and SDS Solution. **a**, Generation of thermo-viscous flows by rotating the laser focus on a circle with a rotation frequency of $f = 500$ Hz at high laser powers (Supplementary Video 1.9). Note that laser movement (green arrow) and the thermo-viscous flow (white, dashed arrow) have opposite directions. **b**, Attraction of a AuNP and PS NPs in 5 mM SDS due to depletion (Supplementary Video 1.10). **c**, A AuNP (125 nm radius) trapped in an ensemble of polystyrene (PS) NPs of the same size at 10 mM NaCl (Supplementary Video 1.11), where the PS-particles are repelled due to thermophoresis. **d**, Attraction of PS ellipsoids (2.39 µm major-axis length, 0.34 µm minor-axis length) in 5 mM SDS (Supplementary Video 1.12) due to depletion.

Such attractive contributions can arise from depletion interactions[46,218] (Sec. 2.3.4). Thereby a temperature gradient repels dissolved molecules from the heated regions generating a concentration gradient that drives suspended nano-objects to the heating spot. To demonstrate this effect we use the surfactant sodium dodecyl sulfate (SDS) at a concentration of 5 mM well below the critical micelle concentration (8.2 mM[219]) to avoid complications of micelle formation. We suspend polystyrene (PS) particles and AuNPs of the same size ($R = 125$ nm) in the solution and compare their dynamics to a solution with AuNPs and PS particles without SDS but 10 mM NaCl. Remarkably, the heated spot is attractive for both AuNPs and for PS NPs (Fig. 4.9b, Supplementary Video 1.10) in the SDS solution showing even PS colloidal crystal growth, while only the AuNP is trapped in the NaCl solution and the PS particles are repelled by thermophoresis (Fig. 4.9c, Supplementary Video 1.11).

The observations in NaCl are readily explained by the fact that the AuNP is confined in the DLVO minimum as demonstrated above but the PS particle is not due to a 10 times lower Hamaker constant (see Sec. 4.1.5.3 for details). The PS particle samples the whole liquid film thickness equally and not preferentially the region close to the Au film and experiences an additional thermophoretic drift velocity given by

$$\boldsymbol{u} = -\frac{2}{3}\chi\frac{\nabla T}{T} = -D_{\mathrm{T}}\nabla T \ , \tag{4.6}$$

where D_{T} is the thermophoretic mobility[56] and ∇T the temperature gradient (Fig. 4.9c, Supplementary Video 1.11). For $\chi > 0$ the particle is driven to the cold. From Eq. (4.4) we find $\chi \approx \chi_{\mathrm{E}} = 1.28 \cdot 10^{-10}\ \mathrm{m^2\,s^{-1}}$ and $D_{\mathrm{T}} \approx 0.3\ \mathrm{\mu m^2\,K^{-1}\,s^{-1}}$, where we have used a measured zeta potential of $\zeta \approx -38$ mV. The vdW contribution χ_{vdW} to either the thermophoretic drift or the attraction to the gold surface can be neglected due to the smaller Hamaker constant of PS. From the stationary probability distribution of the PS NP we find a Soret coefficient of $S_{\mathrm{T}} \approx 0.24\ \mathrm{K^{-1}}$ in agreement with our theoretical prediction $S_{\mathrm{T}} = D_{\mathrm{T}}/D_{\|} \approx 0.21\ \mathrm{K^{-1}}$.

In the SDS solution, the additional surfactant molecules now undergo thermophoresis to yield a concentration gradient in which suspended colloidal particles drift. The lower concentration in the heated regions promotes an effective attractive interaction of suspended colloids with the gold surface due to depletion forces (see Sec. 2.3.4 and Sec. 4.1.5.9 and for details). The total drift velocity inducing depletion is then described by[46,56,218]:

$$\boldsymbol{u} = -\left(D_{\mathrm{T}} - \frac{k_{\mathrm{B}}}{3\eta}R_{\mathrm{m}}^2 c_0 N_{\mathrm{A}}\left(TS_{\mathrm{T}}^{\mathrm{m}} - 1\right)\right)\nabla T \ . \tag{4.7}$$

Here R_{m} is the size of the SDS molecule, c_0 the concentration in units of mol/l, N_{A} the Avogadro constant and $S_{\mathrm{T}}^{\mathrm{m}}$ the Soret coefficient of SDS. For $R_{\mathrm{m}} = 2$ nm[45], $c_0 = 5$ mM and $S_{\mathrm{T}}^{\mathrm{m}} = 0.03\ \mathrm{K^{-1}}$[148] we find $-0.43\ \mathrm{\mu m^2\,K^{-1}\,s^{-1}}$ for the additional depletion contribution, which exceeds the thermophoretic mobility, $D_{\mathrm{T}} \approx 0.3\ \mathrm{\mu m^2\,K^{-1}\,s^{-1}}$, rendering the overall mobility negative. The PS NPs and the AuNPs are thus driven to the heated Au film surface (Fig. 4.9c, Supplementary Video 1.10) which allows for further transport in the thermo-osmotic boundary flow. Additional contributions, as for example thermoelectric fields may even enhance the attractive components. Overall, this concept is readily transferred to other objects as shown in Fig. 4.9d and Supplementary Video 1.12, where we have trapped ellipsoidal PS particles in a 5 mM solution of SDS. Note that as compared to other schemes, our approach always includes thermo-osmotic flows.

4.1.4 Conclusion

In conclusion, we have demonstrated that thermo-hydrodynamic boundary flows can manipulate nano-objects with unprecedented flexibility in a very simple sample geometry. These flows are the key for future thermo-optofluidic implementations with an extensive range of applications in the fields of i) nanoparticle sorting and separation[202]; ii) assembly of nanophotonic circuits[220] and plasmonic quantum sensors[201,206]; iii) biotechnology on-chip laboratories[221] and iv) manufacturing of nanomaterials[3,201] and functional nanosurfaces[222,223]. We have substantiated our experimental findings of thermo-osmotic flow assisted trapping with a quantitative theoretical description. A flow field multiplexing scheme has been further developed to allow for the simultaneous manipulation of many individual nano-objects and the generation of complex effective flow patterns. Our concept can be combined with other thermally induced effects such as thermophoresis, depletion forces and thermoviscous flows to form a fully-featured nanofluidic system-on-a-chip. Besides direct consequences for the field of plasmonic nano-tweezers and other thermoplasmonic trapping schemes, the use of thermo-hydrodynamic flows as a tool for nanofluidic applications will extend the limits at the forefront of nanotechnology and help to develop artificial intelligence and feedback controlled schemes for material synthesis.

4.1.5 Supplementary Information

4.1.5.1 Sample Preparation

The sample consists of two glass coverslips (22 mm × 22 mm) confining a thin liquid film. First, the coverslips were thoroughly cleaned in an ultrasonic bath with Hellmanex III (1%), acetone, isopropyl and Milli-Q water followed by 3 min plasma cleaning (Harrick Plasma, PDC-32G). Then, one of the coverslips was coated with a 50 nm gold film using a thermal evaporator (Leybold, UNIVEX 300) and a 5 nm chrome adhesion layer. Subsequently, the edges of the uncoated coverslip were covered with a thin layer of PDMS for sealing. The particle solution used for the experiments was prepared by dispersing gold nanoparticles (Cytodiagnostics), PS particles (microParticles) in different solutions of NaCl, SDS and PEG. Finally, 0.6 µl of the mixed particle suspension is pipetted in the middle of one of the coverslips and the other is placed on top. Depending on the area covered by the liquid, typically about 14 mm × 14 mm, the resulting liquid film height is about 3 µm. Chemicals, if not otherwise specified, have been obtained from Sigma-Aldrich.

4.1.5.2 Particle Tracking

The main steps to detect the particle positions from a recorded image (Fig. 4.10a) are as follows: First, we reduce the noise in the image using a two pixel median filter and then compute a binary image using a global threshold. Subsequently, a connected-component labeling algorithm is used to identify and filter connected regions according to their pixel area (Fig. 4.10b). The particles center position is then calculated from the center of mass of the unweighted pixel area and stored along with additional parameters such as the maximum intensity detected within that area. Finally, the particle positions are connected into trajectories using a linking algorithm[91,224]. The z-position of the particle is estimated from the defocusing of the particle[225]. To find a relation between the detected particle radius r_0 and its z-position we performed a reference measurement where we detect r_0 of a particle fixed to the gold film ($z = 0$) and measure the change in z-position using the piezo stage (Fig. 4.10c). Note that in all experiments the focal plane of the objective has been set to the gold film ($z = 0$).

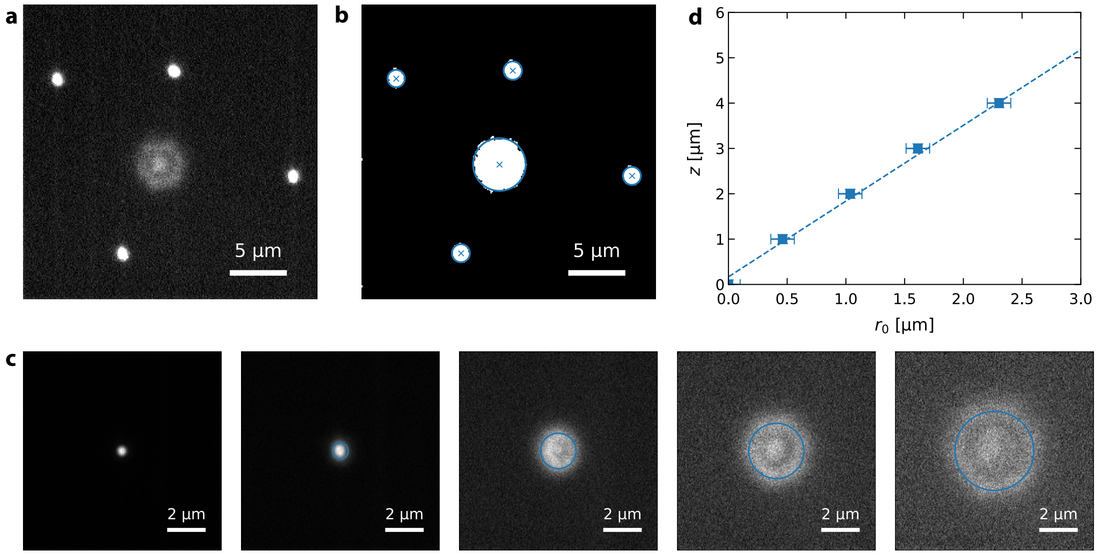

Fig. 4.10: a, The recorded image. **b**, The binary representation of the image processed with a two pixel median filter and a global threshold value. The detected particle centers and radii from the connected-component labeling are depicted in blue. **c**, The defocusing of a particle fixed to the gold film. The smallest particle radius is defined as $z = 0$ and the change in z-position is measured using the piezo stage. **d**, The relation between the particle's z-position and its detected particle radius r_0.

4.1.5.3 DLVO Potential

Concentration Dependence Fig. 4.11a, b show the DLVO potential of a AuNP ($R = 125$ nm) as function of the surface-to-surface distance d to an Au surface for different concentrations c_0. The depth of the secondary minimum U_{min} increases linearly with increasing concentration (Fig. 4.11c) and the minimum location, d_{min}, is shifted to smaller distances and scales with $d_{\mathrm{min}} \propto c_0^{-3/4}$ (Fig. 4.11d). Furthermore, the potential barrier towards the primary minimum decreases with increasing concentration c_0. If c_0 is too high (> 48 mM) the secondary minimum vanishes (Fig. 4.11a, dashed black line) and the AuNPs will adhere to the Au surface (primary minimum of the DLVO potential). Experimentally, we were able to realize concentrations down to 10 mM. For concentrations above 10 mM, even though possible in theory, all AuNPs are immobilized at the Au surface as a consequence of the lowered potential barrier towards the primary minimum. When the coverslips are assembled the AuNPs attain enough potential energy to overcome the lower potential barrier and adhere to the Au surface.

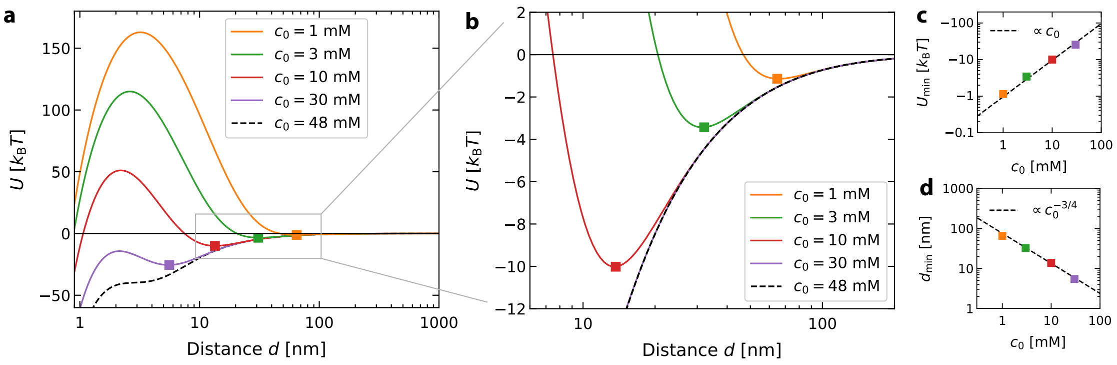

Fig. 4.11: a, Plot of the DLVO potential between a AuNP ($R = 125$ nm) and a Au surface as function of the distance d for different concentrations c_0 ($\zeta = -35$ mV, $A_{\mathrm{H}} = 5 \cdot 10^{-20}$ J). **b** shows a zoomed-in view of (**a**). **c** and **d** depict the depth U_{min} and the location d_{min} of the secondary minimum corresponding to the squares in (**a**) as function of the concentration c_0, respectively.

Size Dependence The influence of the AuNP radius R on the DLVO potential is depicted in Fig. 4.12a for a concentration of 10 mM. The depth of the secondary minimum U_{min} increases with increasing NP radius R and scales with $U_{\mathrm{min}} \propto R^{4/3}$ (Fig. 4.12b), whereas the location of the minimum is nearly unchanged (Fig. 4.12a, dashed gray line).

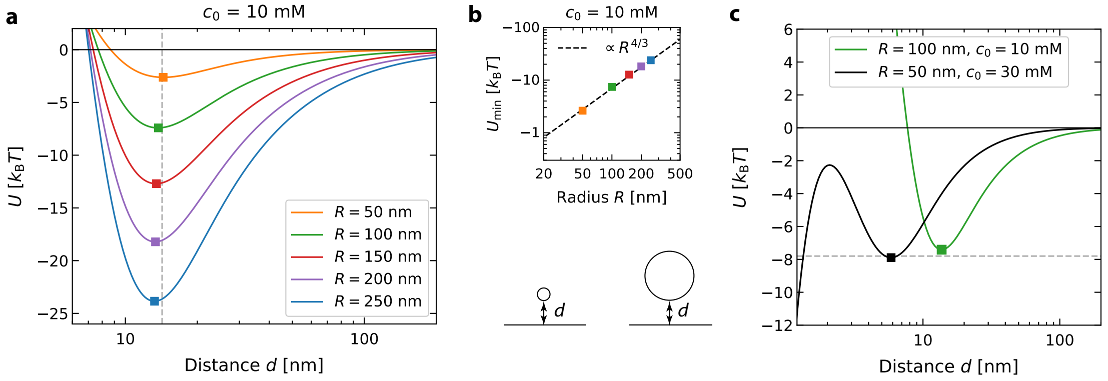

Fig. 4.12: a, Plot of the DLVO potential between a AuNP and a Au surface as function of the distance d for different NP radii R at a concentration of c_0 ($\zeta = -35$ mV, $A_{\mathrm{H}} = 5 \cdot 10^{-20}$ J). **b** depicts the depth U_{min} of the secondary minimum corresponding to the squares in (**a**) as function of the NP radius R.

Given a AuNP with $R = 100$ nm at $c_0 = 10$ mM the same depth of the secondary minimum can be achieved for a smaller NP size ($R = 50$ nm) by increasing the concentration to $c_0 =$

30 mM (Fig. 4.12c). In view of Fig. 4.11 the secondary minimum is then observed at a smaller distance d_{min}. The confinement of a NP with $R = 50$ nm at a concentration of 30 mM NaCl is demonstrated in Supplementary Video 1.5.

Material Dependence The material dependence of the DLVO potential is defined by the Hamaker constant A_{H} of the material system and the zeta potential ζ of the surfaces. The macroscopic Hamaker constant defines the interaction of medium 1 with medium 2 across medium 3 and a theoretical description is given within the Lifschitz theory of the Hamaker constant (see Sec. 2.2.2 for details). Typically, the Hamaker constant of metals is larger than for dielectric media. The theoretical value for the Au/water/Au system is $10 \cdot 10^{-20}$ J. However, for a thin Au film on a glass surface slightly lower values of the Hamaker constant are expected[149]. We have used $A_{\mathrm{H}} = 5 \cdot 10^{-20}$ J. In case of polystyrene (PS) NPs we have employed $A_{\mathrm{H}} = 1 \cdot 10^{-20}$ J for the PS/water/Au system. The corresponding DLVO potential is plotted in Fig. 4.13 for a PS NP ($R = 125$ nm) with a zeta potential of $\zeta = -35$ mV to allow for a direct comparison with Fig. 4.11. For a given concentration, for example, 10 mM, the secondary minimum is smaller in comparison to the AuNP system. Remarkably, with increasing concentration large values of $-U_{\mathrm{min}}$ can be achieved before the secondary minimum vanishes at about 1 M.

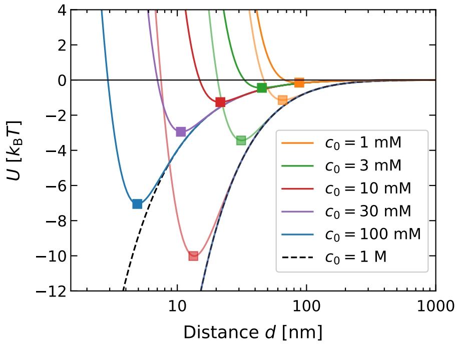

Fig. 4.13: Plot of the DLVO potential between a PS NP ($R = 125$ nm) and a Au surface as function of the distance d for different concentrations $c_0 = 10$ mM ($\zeta = -35$ mV, $A_{\mathrm{H}} = 1 \cdot 10^{-20}$ J). The faint curves in the background depict the corresponding potentials for a AuNP of the same size (Fig. 4.11b).

Force Calculation The force exerted on the NP is readily obtained from:

$$F = -\frac{\partial U}{\partial d} \ . \tag{4.8}$$

Fig. 4.14a depicts the DLVO potential for a AuNP with $R = 125$ nm radius at $c_0 = 10$ mM. The corresponding force calculation is shown in Fig. 4.14b.

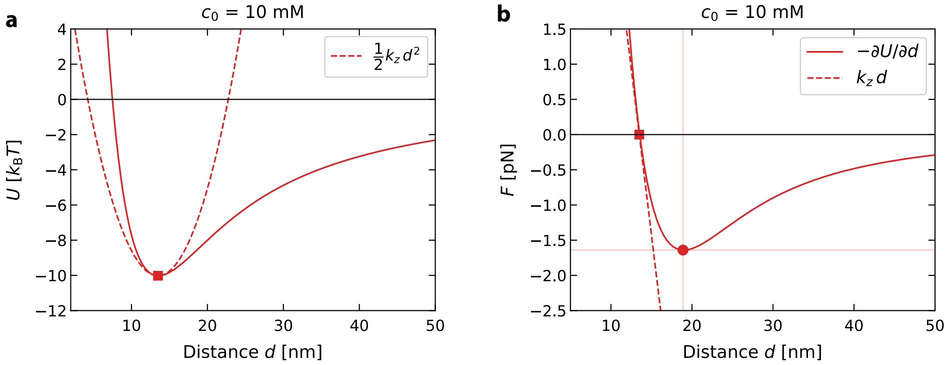

Fig. 4.14: **a**, The DLVO potential for a AuNP with $R = 125$ nm radius at $c_0 = 10$ mM. **b**, The force corresponding to (**a**) calculated using $F = -\partial U/\partial d$.

At a distance of 20 nm we obtained a maximum force of −1.6 pN. The DLVO potential in the vicinity of the secondary minimum is non-harmonic. A rough approximation with a harmonic potential is shown in Fig. 4.14a and yields to a vertical trap stiffness k_z in the order of 500 $\mathrm{pN\,\mu m^{-1}}$.

Probability Distribution The probability to find a particle at a given z-position in the sample is given by the Boltzmann distribution (Sec. 2.1.2):

$$p(d, c_0) = p_0\, \mathrm{e}^{-U(d,c_0)/(k_\mathrm{B}T)} \ , \tag{4.9}$$

where $d = z - R$ is the surface-to-surface distance and $U(d, c_0)$ is the DLVO potential given in Eq. (4.1). The normalizing constant p_0 is defined as:

$$p_0 \int_0^{H-R} \mathrm{e}^{-U(d,c_0)/(k_\mathrm{B}T)}\, \mathrm{d}d = 1 \ , \tag{4.10}$$

where the upper limit of the integration is given by the sample height H minus the particle radius R. The mean surface-to-surface distance $\langle d \rangle$ is then defined by:

$$\langle d \rangle = p_0 \int_0^{H-R} d\, \mathrm{e}^{-U(d,c_0)/(k_\mathrm{B}T)}\, \mathrm{d}d \ . \tag{4.11}$$

Fig. 4.15a depicts $\langle d \rangle$ as function of the concentration c_0 for a sample height of $H = 3$ µm.

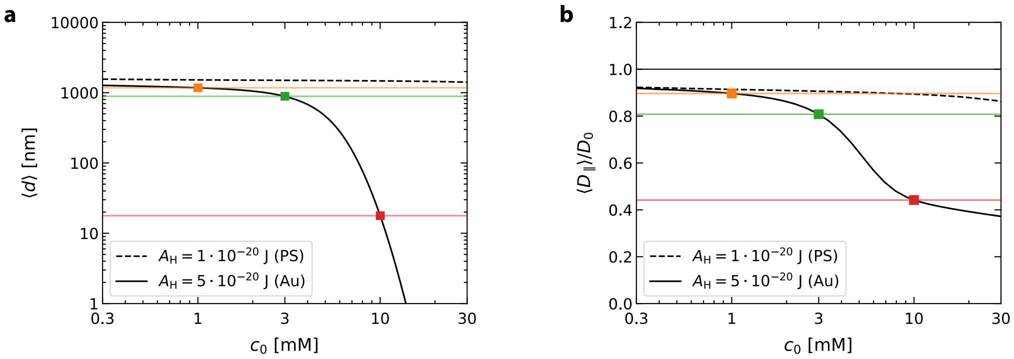

Fig. 4.15: **a**, The mean distance $\langle d \rangle$ as function of the concentration c_0 according to Eq. (4.11) for a sample height of $H = 3$ µm and a particle radius of $R = 125$ nm. The black solid line corresponds to the DLVO potential defined as in Fig. 4.11 ($A_\mathrm{H} = 5 \cdot 10^{-20}$ J), whereas the black dashed line corresponds to a Hamaker constant of $A_\mathrm{H} = 1 \cdot 10^{-20}$ J. **b**, The mean in-plane diffusion coefficient $\langle D_\| \rangle$ as function of the concentration c_0 according to Eq. (4.12) for the sample parameters as used in (**a**).

Similar, the mean in-plane diffusion coefficient is defined by:

$$\langle D_\| \rangle = p_0 \int_0^{H-R} D_\|(d)\, \mathrm{e}^{-U(d,c_0)/(k_\mathrm{B}T)}\, \mathrm{d}d \ . \tag{4.12}$$

where $D_\|(d)$ denotes the distance-dependent in-plane diffusion coefficient (Sec. 2.1.3). Fig. 4.15b depicts $\langle D_\| \rangle$ as function of the concentration c_0 for a sample height of $H = 3$ µm.

Escape from DLVO Potential With a distance-dependent diffusion coefficient $D_\perp(d)$ and a potential $U(d)$ the mean first passage time is given by (Appendix A1.4)

$$\langle \tau \rangle = \int_{d_\mathrm{min}}^{d_\mathrm{max}} \left(\frac{\mathrm{e}^{U(x')/(k_\mathrm{B}T)}}{D_\perp(x')} \int_{-\infty}^{x'} \mathrm{e}^{-U(x'')/(k_\mathrm{B}T)}\, \mathrm{d}x'' \right) \mathrm{d}x' \ , \tag{4.13}$$

where d_{min} is the location of the secondary minimum, d_{max} the escape distance and $D_{\perp}(d)$ the out-off-plane diffusion coefficient (Sec. 2.1.3). Here, d_{max} defines as the distance where we assume the particle has escaped the potential. Fig. 4.16 depicts the mean first passage time as function of the concentration c_0 for an escape distance of $d_{\mathrm{max}} = 500$ nm calculated from a numerical integration of Eq. (4.13).

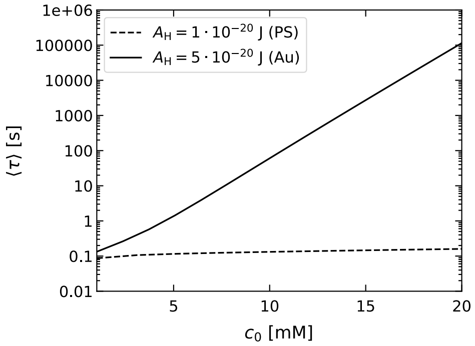

Fig. 4.16: The mean first passage time $\langle\tau\rangle$ as function of the concentration c_0 for an escape distance of $d_{\mathrm{max}} = 500$ nm. The black solid line corresponds to the DLVO potential defined as in Fig. 4.11 ($A_{\mathrm{H}} = 5 \cdot 10^{-20}$ J), whereas the black dashed line corresponds to a Hamaker constant of $A_{\mathrm{H}} = 1 \cdot 10^{-20}$ J.

4.1.5.4 Temperature Simulation

The stationary temperature distribution in the sample was deduced from finite-element simulations using the heat transfer module of COMSOL Multipyhsics 5.1. The sample geometry was represented by a 2D axisymmetric model as depicted in the Fig. 4.17.

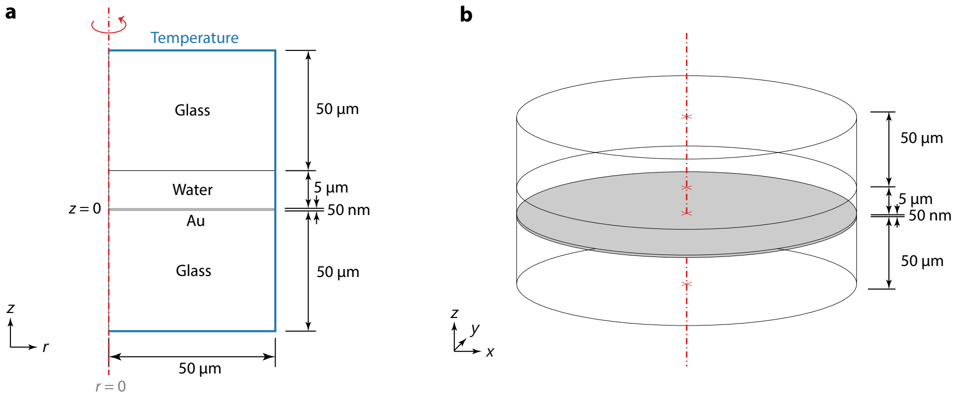

Fig. 4.17: **a**, Sketch of the 2D axisymmetric model employed to simulate the temperature distribution in the sampled using COMSOL Multipyhsics 5.1 (dimensions are not to scale). The heat source domain, that is, the gold film, is colored in gray. **b**, The revolved simulation geometry in 3D.

In the simulation we set the outer boundary layers to room temperature $T_0 = 293.15$ K and neglected thermal convection in the liquid film due to its small height (see Sec. 4.1.5.7 for details). The heat source within the gold film domain (gray domain) is defined with Eq. (2.113)

$$Q(r,z) = P_0\,(1-R)\,\frac{2\alpha}{\pi w_0^2}\,\mathrm{e}^{-2r^2/w_0^2}\,\mathrm{e}^{-\alpha z}\ , \tag{4.14}$$

where P_0 is the incident laser power, w_0 the beam waist of the focused laser, R the reflectance and α absorption coefficient of the gold film at the laser wavelength $\lambda = 532$ nm. For $\lambda = 532$ nm we find $R = 0.6$ (Fig. 2.21a) and an absorption coefficient of $\alpha = 4\pi n''\lambda = 5.3{\cdot}10^7\ \mathrm{m}^{-1}$, where n'' denotes the imaginary part of the refractive index at the given wavelength (Appendix A1.15). For the thermal conductivity of the gold film we have used $\kappa \approx 150\ \mathrm{W\,m^{-1}\,K^{-1}}$ according to Ref. 226, whereas for the other material properties we have taken the bulk values (Appendix A1.16). Fig. 4.18 depicts the simulated temperature distribution for an incident laser power $P_0 = 1$ mW. We obtain a maximum temperature increment at the heat spot of about $\Delta T_{\max} = 25$ K. The related temperature gradient is plotted in Fig. 4.19.

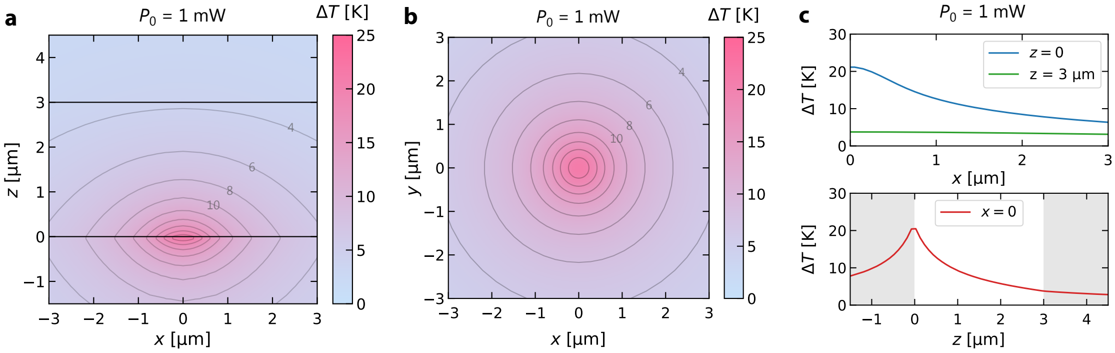

Fig. 4.18: Simulated temperature distribution for an incident laser power of $P_0 = 1$ mW. **a**, Cross-section of temperature distribution in the xz-plane at $y = 0$. **b**, Top view of the temperature distribution in the xy-plane at $z = 0$. **c**, Radial temperature profile in x-direction for $y = 0$ at different heights ($z = 0, 5$ µm) in the liquid film. **d**, Vertical temperature profile in z-direction at $x, y = 0$.

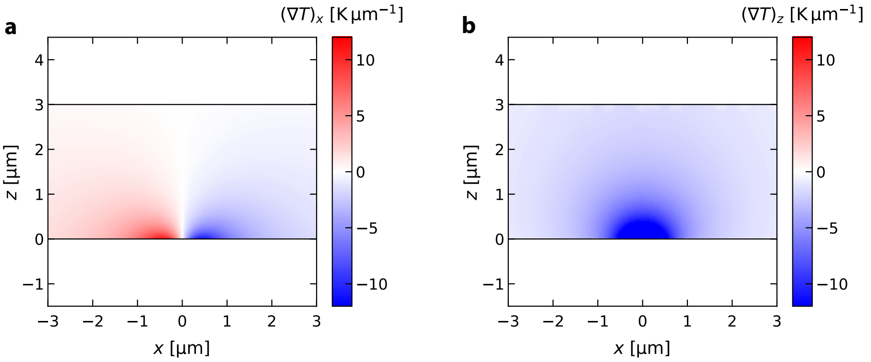

Fig. 4.19: The temperature gradient calculated from Fig. 4.18a. **a**, x-component of the temperature gradient. **b**, z-component of the temperature gradient.

The maximum temperature increment $\Delta T_{\max}$ as function of the incident laser power is plotted in Fig. 4.20 and reveals a linear dependence, $\Delta T_{\max} \propto P_0$.

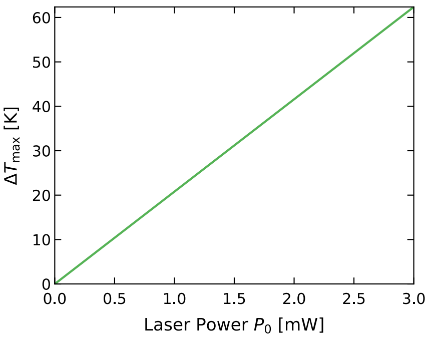

Fig. 4.20: Simulated maximum temperature increment $\Delta T_{\max}$ as function of the incident laser power P_0.

4.1.5.5 Temperature Measurement

To estimate the temperature increment on the gold film the method introduced in Sec. 3.4 is used. Therefore, the gold film was embedded in a 5CB sample and heated with a focused laser as illustrated in Fig. 4.21a. The radius of the phase transition is expected to increase linearly with the incident laser power since $\Delta T \propto P_0$. The blue squares in Fig. 4.21b depict the obtained phase transition radius R_{pt} as function of the incident laser power P_0 for a gold film thickness of 50 nm. The corresponding darkfield microscopy images are shown in Fig. 4.21c. The temperature increment in 5CB is then given by

$$\Delta T_{\max}^{5\mathrm{CB}} = \frac{(35\,^{\circ}\mathrm{C} - T_0)}{P_0^{\mathrm{pt}}} P_0 \,, \tag{4.15}$$

where $T_0 = 25\,^{\circ}\mathrm{C}$ is the ambient temperature and P_0^{pt} the power where the phase transition temperature $T_{\mathrm{pt}} = 35\,^{\circ}\mathrm{C}$ is first reached. We find $P_0^{\mathrm{pt}} = 0.48$ mW from a linear fit (blue dashed line) in Fig. 4.21b.

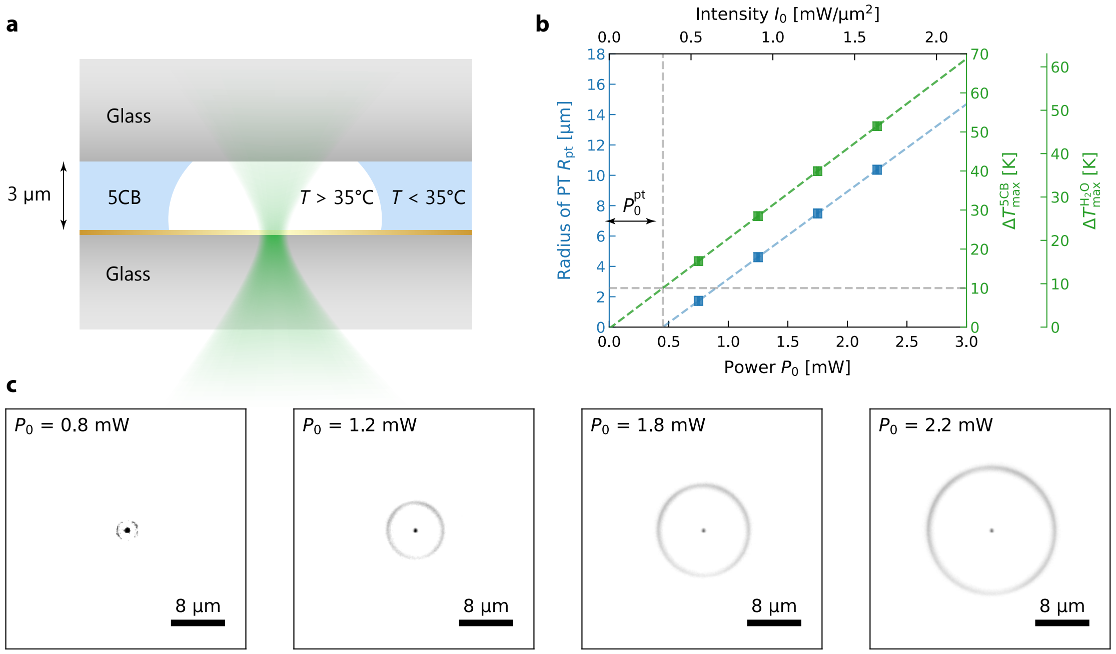

Fig. 4.21: **a**, Sketch of the measurement principle and the sample geometry. **b**, The measured phase transition radius (R_{pt}, blue squares) and the temperature increment in 5CB ($\Delta T_{\max}^{5\mathrm{CB}}$, green squares) calculated using Eq. (4.15) as functions of the incident laser power P_0. The temperature increment in water ($\Delta T_{\max}^{H_2O}$) is by a factor of 0.9 smaller than in 5CB according to the numerical simulation in Sec. 4.1.5.4. **c**, The darkfield optical microscopy images corresponding to the data points in (**b**).

The temperature increment in water is calculated as $\Delta T_{\max}^{H_2O} = 0.9\,\Delta T_{\max}^{5\mathrm{CB}}$, where the factor 0.9 accounts for the higher thermal conductivity of water and is obtained from a numerical simulation. The thermal conductivity of 5CB in its isotropic phase is about $\kappa_{5\mathrm{CB}} = 0.15\ \mathrm{W\,m^{-1}\,K^{-1}}$ [227] (Appendix A2.3), whereas the thermal conductivity of water is $\kappa_{H_2O} = 0.6\ \mathrm{W\,m^{-1}\,K^{-1}}$ (Appendix A1.16). Hence, the temperature increment of the gold film is expected to be smaller when embedded in water. The finally obtained temperature increment ($\Delta T_{\max}^{H_2O}$, Fig. 4.21b) agrees well with the simulation result in Fig. 4.20.

4.1.5.6 Thermo-Osmotic Flow

To simulate the thermo-osmotic flow field we combined the temperature simulation with the laminar flow simulation. The sample geometry is the same as in Sec. 4.1.5.4, where the laminar flow simulation is defined only in the fluid domain (Fig. 4.22, gray area).

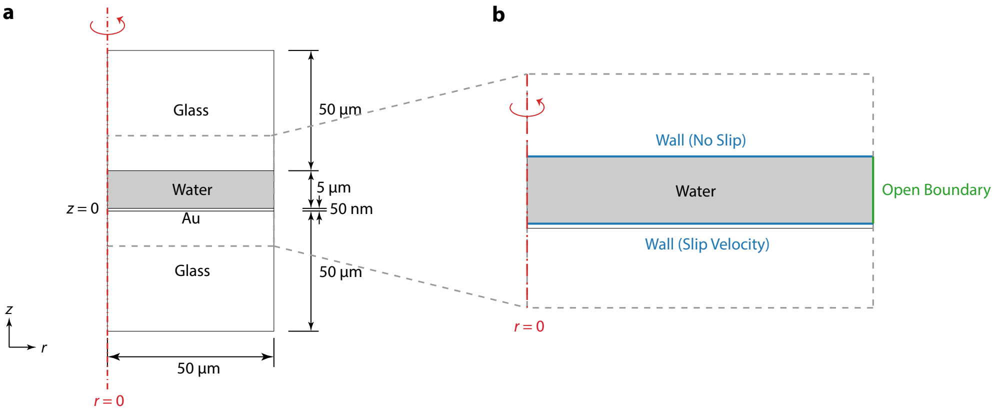

Fig. 4.22: a, Sketch of the 2D axisymmetric model employed to simulate the thermo-osmotic flow field in the sample using COMSOL Multipyhsics 5.1 (dimensions are not to scale). The laminar flow domain, that is, the liquid film, is colored in gray. **b**, The revolved simulation geometry in 3D.

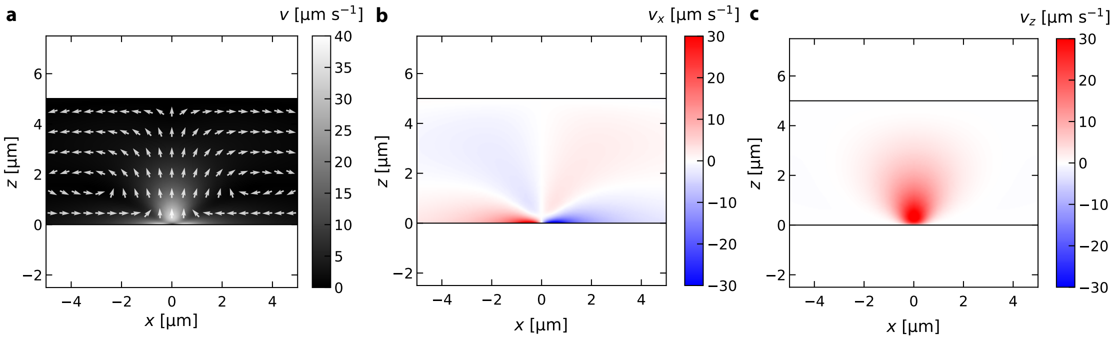

Fig. 4.23: Simulated thermo-osmotic flow field for an incident laser power of 1 mW. **a**, The magnitude of the flow velocity and its direction (arrows) in the xz-plane at $y = 0$. **b**, x-component of the flow velocity shown in (**a**). **c**, z-component of the flow velocity in (**a**).

To account for the thermo-osmotic slip flow the lower boundary was defined as a wall with a slip velocity

$$v_{\parallel} = \frac{\sigma_{\mathrm{T}}\,\eta}{\varrho}\frac{\nabla_{\parallel} T}{T} \,, \tag{4.16}$$

where σ_{T} is a dimensionless thermal slip coefficient, η the viscosity and ϱ the density of the fluid. In case of water ($\eta = 0.001$ Pa s, $\varrho = 1000\ \mathrm{kg\,m^{-3}}$) the thermal slip coefficient σ_{T} is related to the thermo-osmotic coefficient χ with:

$$\sigma_{\mathrm{T}} = \chi \cdot 10^{6}\ \mathrm{m^{-2}\,s} \,. \tag{4.17}$$

In our simulation we have used $\chi = 10 \cdot 10^{-10}\ \mathrm{m^2\,s^{-1}}$, hence, $\sigma_{\mathrm{T}} = 0.001$. The upper boundary was defined as wall with no slip and the boundary on the right-hand side as open boundary.

Fig. 4.24 depicts the vorticity $\boldsymbol{\omega} = \nabla \times \boldsymbol{v}$ calculated from the flow field in Fig. 4.23. In leading order a sphere will rotate with a frequency Ω of half the vorticity[215], $\Omega = \omega/2$.

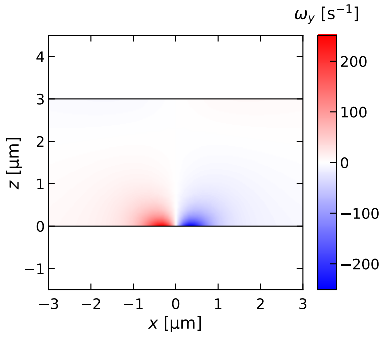

Fig. 4.24: The vorticity $\boldsymbol{\omega} = \nabla \times \boldsymbol{v}$ of the flow field in Fig. 4.23.

4.1.5.7 Thermal Convection

To estimate the contribution of thermal convection we again combined the heat transfer simulation with the laminar flow simulation but in addition considered the temperature-dependent density $\varrho(T)$ of the liquid. The simulation approach is similar to Fig. 4.22 where thermal convection was introduced by defining a gravitational force density $f_z = -\varrho(T)g$ within the liquid sample domain. In contrast to Fig. 4.22 the lower and upper boundary have been defined as walls with no slip. Fig. 4.25 depicts the resulting temperature distribution and the relative density change within the sample. Note that the temperature distribution is essentially the same as in Fig. 4.18 and the effect of thermal convection on the temperature distribution can be neglected due to the small sample height (Sec. 2.3.6).

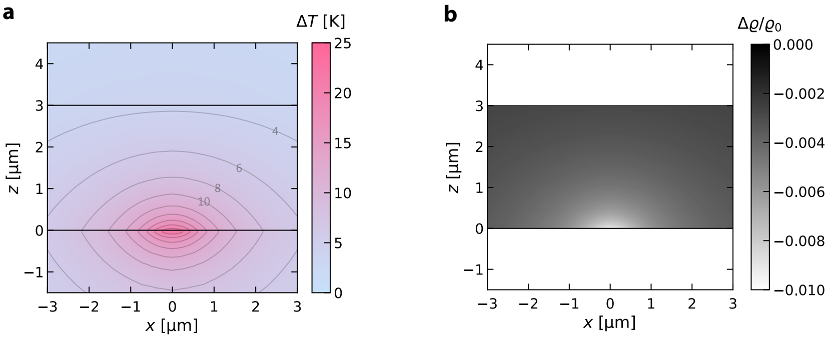

Fig. 4.25: Simulated temperature distribution and density change considering thermal convection. **a**, Temperature distribution in the *xz*-plane ($y = 0$). **b**, The relative density change in the *xz*-plane ($y = 0$).

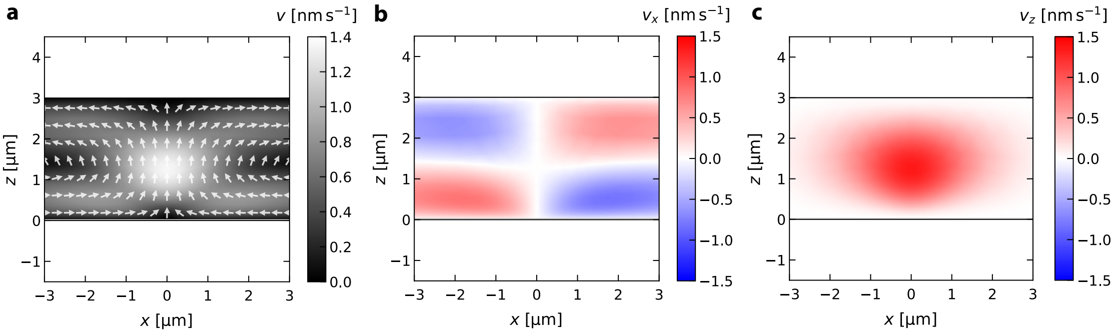

Fig. 4.26: Simulated flow field due to thermal convection for a laser power of 1 mW. **a**, Magnitude of the flow velocity and its direction (arrows) in the *xz*-plane ($y = 0$). **b**, *x*-component of the flow velocity shown in (**a**). **c** *z*-component of the flow velocity in (**a**).

The resulting convective flow field is depicted in Fig. 4.26. The expected flow velocities due to thermal convection are in the order of several $\mathrm{nm\,s^{-1}}$. This is four orders of magnitude smaller than the observed thermo-osmotic flow velocities (Fig. 4.23). Hence, the contribution of thermal convection is negligible for the given sample height (5 µm). The maximum velocity $v_{\max}$ in the sample increases with the sample height (Fig. 4.27). Nevertheless, even for a sample height of $H = 80$ µm flow velocities well below 1 $\mathrm{\mu m\,s^{-1}}$ are expected. Notably, the maximum velocity close to the gold film ($z = 125$ nm) saturates with increasing sample height[32].

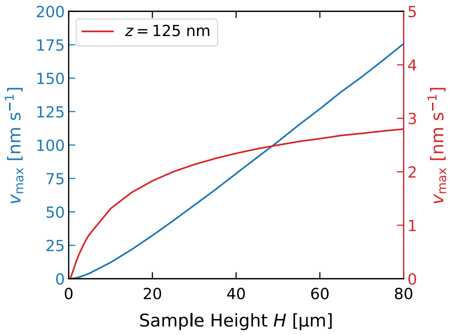

Fig. 4.27: The maximum velocity $v_{\max}$ due to thermal convection as function of the sample height H in the sample volume (blue curve) and close to the gold film ($z = 125$ nm, red curve).

4.1.5.8 Optical Forces

The optical forces on the NP have been estimated with Eq. (A1.57). Instead of the static polarizability, $\alpha = 4\pi R^3(\varepsilon_2 - \varepsilon_1)/(\varepsilon_2 + 2\varepsilon_1)$, we used the expression[228]

$$\alpha = \frac{1 - (1/10)(\varepsilon_2 + \varepsilon_1)\,\xi^2}{(1/3 + \varepsilon_1/(\varepsilon_2 - \varepsilon_1)) - (1/30)(\varepsilon_2 + 10\varepsilon_1)\,\xi^2 - \mathrm{i}4\pi^2\varepsilon_1^{3/2}V/(3\lambda^3)}\,, \tag{4.18}$$

that is valid also for larger particles with $R \approx \lambda$. Here, $\xi = 2\pi R/\lambda$ is a size parameter and $V = 4/3\pi R^3$ the volume of the particle. Fig. 4.28a depicts the calculated z-component of the total force on a $R = 125$ nm AuNP in water as function of the NP position for a laser power of $P_0 = 1$ mW. We have used $\lambda = 532$ nm for the a wavelength and a beam waist of $w_0 = 0.56$ µm.

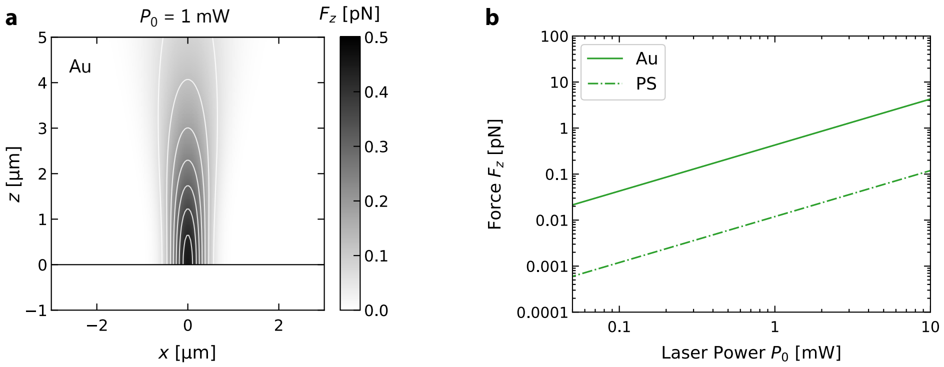

Fig. 4.28: **a**, The z-component of the total force on a $R = 125$ nm AuNP in water as function of the NP position for laser power of $P_0 = 1$ mW. We have used $\lambda = 532$ nm for the wavelength and a beam waist of $w_0 = 0.56$ µm. **b**, The z-component of the total optical force at $z = 20$ nm as function of the incident laser power for a AuNP (solid line) and a PS NP (dash-dotted line) of the same size.

For the given set of parameters the total force is mainly defined by the force in z-direction and the y-component can be neglected. The force as function of the incident laser power is depicted in Fig. 4.28b and compared between a Au and a PS NP of the same size. Due to their larger scattering and absorption cross-section the force on a AuNP is more than one order of magnitude larger than for a PS NP. Since only 10 % of the incident laser power is transmitted by the gold film (Fig. 2.21a) the optical force in Fig. 4.7b was divided by a factor of 10.

4.1.5.9 Depletion Forces in SDS

If we assume a molecular Soret coefficient S_T^m the surfactant concentration is given by $n(\boldsymbol{r}) = n_0 \exp(-S_\mathrm{T}^\mathrm{m} \Delta T(\boldsymbol{r}))$. The relative density distribution n/n_0 for the temperature distribution in Fig. 4.18 is plotted in Fig. 4.29, where we have used $S_\mathrm{T}^\mathrm{m} = 0.03\ \mathrm{K}^{-1}$ for SDS.

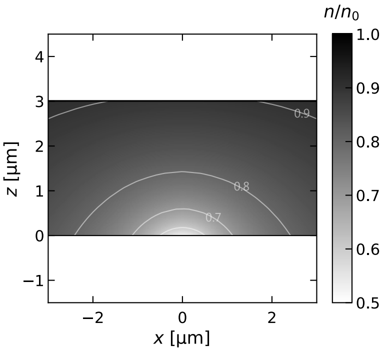

Fig. 4.29: The relative density distribution $n/n_0 = \exp(-S_\mathrm{T}^\mathrm{m} \Delta T(\boldsymbol{r}))$ for the temperature distribution given in Fig. 4.18. Here, we have used $S_\mathrm{T}^\mathrm{m} = 0.03\ \mathrm{K}^{-1}$.

4.1.5.10 Video Files

The Supplementary Videos are available at https://www.doi.org/10.5281/zenodo.5831821.

Video 1.1: Free diffusion of AuNPs over a Au film in DI water (left) and in 10 mM NaCl (right) without heating. The AuNPs have a radius of 125 nm.

Video 1.2: AuNP over a locally heated Au film in DI water for a laser power of 2 mW (left) and the detected particle size and location (right). The AuNP has a radius of 125 nm.

Video 1.3: AuNP over a locally heated Au film in DI water (left) and 10 mM NaCl (right) for a laser power of 1.25 mW. The AuNP has a radius of 125 nm.

Video 1.4: Trapped AuNP over a locally heated Au film in 10 mM NaCl for three different laser powers. The AuNP has a radius of 125 nm.

Video 1.5: Trapped AuNP with 50 nm radius over a heated Au film in 30 mM NaCl for a laser power of 1.0 mW.

Video 1.6: Two AuNPs trapped at three different distances using a multiplex, focused laser beam with a laser power of 2 mW. The AuNPs have a radius of 125 nm.

Video 1.7: Three AuNPs trapped in a triangular pattern using a multiplex, focused laser beam with a laser power of 3 mW. The AuNPs have a radius of 125 nm.

Video 1.8: Trapped AuNP dynamically manipulated to follow a circular path. The AuNP has a radius of 125 nm.

Video 1.9: AuNPs driven by thermo-viscous and thermo-osmotic flows. The laser beam scans a circular path at high frequency ($f = 0.5$ kHz) in clock-wise direction with a laser power of 10 mW.

Video 1.10: Single AuNP in an ensemble of PS NPs over a locally heated Au film in 5 mM SDS for a laser power of 1.5 mW. The AuNP as well as the PS NPs have a radius of 125 nm.

Video 1.11: Single AuNP in an ensemble of PS NPs ($R = 250$ nm) over a locally heated Au film in 10 mM NaCl for a laser power of 1 mW. The AuNP as well as the PS NPs have a radius of 125 nm.

Video 1.12: Three PS ellipsoids (2.39 µm major-axis length, 0.34 µm minor-axis length) over a locally heated Au film in 5 mM SDS for a laser power of 1.5 mW.

4.2 Fully Steerable Symmetric Thermoplasmonic Microswimmers

4.2.1 Abstract

A cornerstone of the directed motion of microscopic self-propelling particles is an asymmetric particle structure defining a polarity axis along which these tiny machines move. This structural asymmetry ties the orientational Brownian motion to the microswimmers directional motion limiting their persistence and making the long time motion effectively diffusive. Here, we demonstrate a completely symmetric thermoplasmonic microswimmer, which is propelled by laser-induced self-thermophoresis. The propulsion direction is imprinted externally to the particle by the heating laser position. The orientational Brownian motion, thus, becomes irrelevant for the propulsion allowing enhanced control over the particles dynamics with almost arbitrary steering capability. We characterize the particle motion in experiments and simulations, and also theoretically. The analysis reveals additional noise appearing in these systems, which is conjectured to be relevant for biological systems. Our experimental results show that even very small particles can be precisely controlled, enabling more advanced applications of these micromachines.

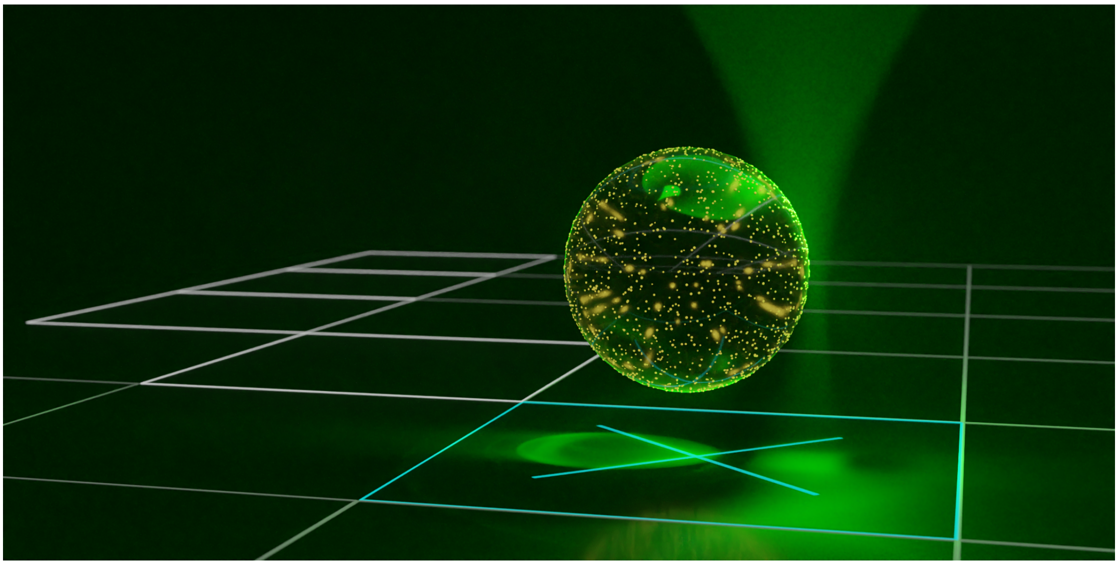

A physical based render of a symmetric swimmer particle illuminated with a focused ray of light. Rendered using Blender 2.83 and the LuxCore Renderer.

The section is based on the following article:

[P2] **M. Fränzl**, S. Muiños-Landin, V. Holubec, and F. Cichos, Fully Steerable Symmetric Thermoplasmonic Microswimmers, *ACS Nano* **15**, 3434 (2021)

The article has been adapted and revised. Details on the author contributions are provided in the “List of Publications” section.

4.2.2 Introduction

Artificial self-propelled micro- and nano-particles are synthetic active matter objects that are capable of using energy to move persistently in liquid environments. They are often recognized as simple building blocks that allow to explore emergent collective states of non-equilibrium biological systems and the corresponding non-equilibrium structures[88]. With a variety of different propulsion mechanisms[9,68–71,73,74] a wealth of different self-propelled particles is available that allows to construct complex self-assembled autonomous micromachines giving valuable physical insights[77] and also offering environmental[229,230] and medical[231] applications. All of these systems share a structural asymmetry allowing them to break the temporal symmetry of hydrodynamics at low Reynolds numbers.[71,73,74,81–84] This asymmetry binds the propulsion direction to the particles symmetry axis and hence, its random reorientation due to the rotational Brownian motion randomizes the microswimmers motion to an effectively diffusive one on long timescales. To regain control over the active motion, steering of the propulsion direction has been achieved by applying external electric or magnetic fields[73,232–234]. Yet, precise and independent control of multiple microswimmers remains a challenging task for these external forcings[235]. Control of active particles on the individual level can be obtained when the propulsion mechanism is switchable, for example, when using thermophoresis[9,11,236,237] or other light-controlled mechanisms such as temperature-induced diffusiophoresis[238] or photocatalytic reactions[239]. For example, a self-thermophoretic microswimmer contains a heat source that generates an asymmetric temperature distribution on the microswimmer surface. In many cases they are realized as metal-capped Janus-particles, where one-half of a polymer sphere is covered with a thin metal film[9]. The metal cap is then heated, for example, by optical absorption[28], and generates a temperature gradient along the polymer surface which in turn propels the particle by thermo-osmotic boundary flows[49,169,240]. With such switchable propulsion, the technique of photon nudging uses a feedback loop[165,241] to control self-thermophoretic Janus particles by harnessing the rotational diffusion as an efficient reorientation process for micron-sized particles[10,11]. Other approaches use large particles with slow rotational diffusion and active orientation steering to circumvent the orientational randomization[80].

Here, we introduce a symmetric self-thermophoretic microswimmer for which an asymmetric temperature distribution is induced by the heating laser itself. The actuation scheme does not depend on the time scale of the rotational diffusion providing a substantially better control than techniques used for Janus-type particles. The symmetric thermoplasmonic microswimmers are already of great interest in the field of active matter. They have been recently employed to study structures emerging from information exchange[85] and machine learning techniques at the microscopic scale[242,243] with the ultimate goal to reach autonomous exploratory behavior. Here, we investigate their self-thermophoretic propulsion and confirm a delay-induced directional uncertainty which may actively contribute to the steering behavior of biological species.

4.2.3 Results and Discussion

The symmetric swimmer particle is a melamine formaldehyd (MF) microparticle with $R = 1.1$ µm radius uniformly coated with AuNPs (Fig. 4.30a). They have been obtained from microParticles GmbH and prepared by binding $\mathrm{AuCl_4^-}$ precursor ions to the surface of chemically modified microparticles, followed by their reduction to individual AuNPs. Fig. 4.30b depicts a SEM image of the particle surface showing the individual AuNPs. Using a difference of Gaussian algorithm we computed a binary representation of Fig. 4.30b as depicted in Fig. 4.30c and find $R_{\mathrm{NP}} = 4$ nm for the average radius of the AuNPs. The ratio between white and black pixels yields a surface coverage of about 10 %. Hence, the approximate number of AuNPs on the surface of the microparticle is $N = 0.1 \cdot 4\pi R^2/(\pi R_{\mathrm{NP}}^2) \approx 30{,}000$. The AuNPs are thermally isolated from each other and act as point-like heat sources when heated with a laser beam with a wavelength close to their plasmon resonance. When illuminated asymmetrically with a highly focused laser beam, the AuNPs generate an inhomogeneous surface temperature distribution resulting in a self-thermophoretic propulsion away from the laser focus (Fig. 4.30a) based on the same principle than previously reported for Janus particles[11].

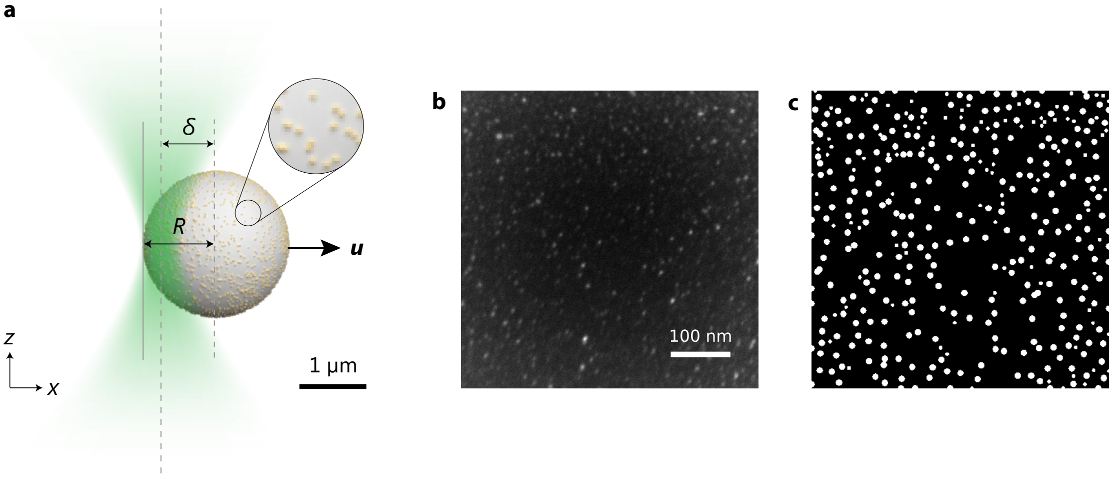

Fig. 4.30: **a**, Sketch of a symmetric microswimmer asymmetrically heated with a focused laser. The microswimmer is composed of a melamine formaldehyd (MF) microparticle with $R = 1.1$ µm radius. 10 % of its surface is uniformly covered with gold nanoparticles of about 4 nm radius. When asymmetrically heated with a focused laser, an inhomogeneous surface temperature is generated resulting in a self-thermophoretic motion away from the laser focus. **b**, SEM image of the swimmer surface. **c**, A binary representation of (**b**) obtained using a difference of Gaussian algorithm for feature detection.

Experiments have been carried out using experimental setup 1 (Sec. 3.1). A sample consists of two glass coverslips confining a 3 µm thin liquid film of the diluted particle suspension. The particles are observed using darkfield illumination with an oil-immersion darkfield condenser (NA 1.2) and a 100× oil-immersion objective set to NA 0.6. Details of the sample preparation are available in Sec. 4.2.5.1.

Fig. 4.31a depicts the actuation principle of the symmetric microswimmer. To direct the particle to a target position $\boldsymbol{r}_{\mathrm{t}}$, the directional vector $\boldsymbol{r}_{\mathrm{pt}} = \boldsymbol{r}_{\mathrm{t}} - \boldsymbol{r}_{\mathrm{p}}$ between the particle center $\boldsymbol{r}_{\mathrm{p}}$ and the target position $\boldsymbol{r}_{\mathrm{t}}$ is calculated and the focus of the heating laser is placed at $\boldsymbol{r}_{\mathrm{h}} = \boldsymbol{r}_{\mathrm{p}} + \delta\, \boldsymbol{r}_{\mathrm{pt}}/\left|\boldsymbol{r}_{\mathrm{pt}}\right|$, where δ is the radial displacement from the particle center and typically a negative number. Due to the self-propulsion of the particle as well as its diffusive motion, the position of the heating laser needs to be constantly adapted in a feedback loop with the detection of the particle center (Sec. 4.2.5.2) to control its motion direction or position.

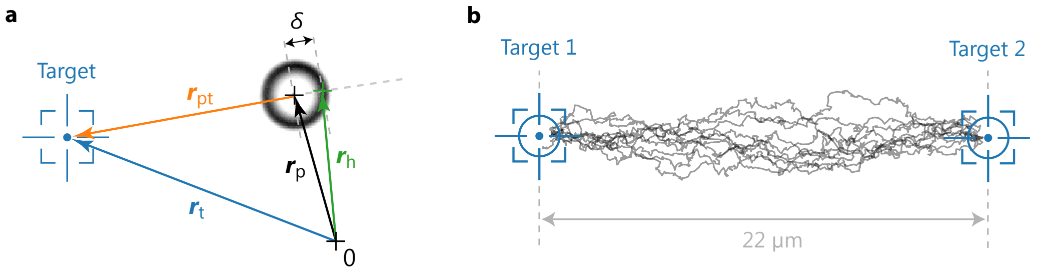

Fig. 4.31: a, A darkfield microscopy image of a symmetric swimmer detected in our experimental setup. To control the propulsion direction of the swimmer, the laser focus is placed with an offset δ from the particle center at $\boldsymbol{r}_{\text{h}}$, opposite to the desired target location $\boldsymbol{r}_{\text{t}}$. **b**, Trajectories for driving a $R = 1.1$ µm symmetric swimmer between two target positions for $P = 0.04$ mW and $\delta = -0.5$ µm (Supplementary Video 2.1). The acceptance radius of the targets is depicted in blue and was set to 0.5 µm

The dependence of the swimmer velocity on the laser displacement δ and the laser power P_0 can be obtained from measurements driving the particle between two target positions (Fig. 4.31b, Supplementary Video 2.1). The velocity is extracted from the time required to travel the distance between the two targets. For each set of parameters, five trajectories (from target 1 to target 2 and back) have been recorded and averaged. The resulting velocity as a function of the laser displacement, plotted in Fig. 4.32, shows a clear maximum. For the power of $P_0 = 0.1$ mW the maximum velocity of $u_{\text{max}} = 9\ \mu\text{m}\,\text{s}^{-1}$ is observed for a displacement $\delta_{\text{max}} = -0.5$ µm (dashed blue line in Fig. 4.32).

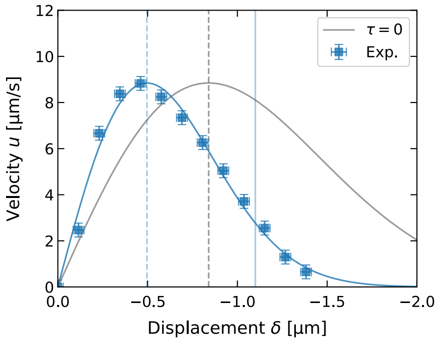

Fig. 4.32: The propulsion velocity as function of the laser displacement δ for a laser power of 0.1 mW and an inverse frame rate $\tau = 30$ ms (blue squares). The blue curve represents a fit to the numerical result where the dashed blue line depicts the optimal displacement $\delta_{\text{max}} = -0.5$ µm. The gray curve represents the numerical result for $\tau = 0$ with an optimal displacement of $\delta_{\text{max}} = -0.84$ µm depicted as dashed gray line. The radius of the particle ($R = 1.1$ µm) is depicted as solid blue line.

The solid blue curve in Fig. 4.32 depicts a fit to the numerical approximation function:

$$u(\delta) = u_{\text{max}} \frac{\delta}{\delta_{\text{max}}} \, \mathrm{e}^{(-\delta^2 + \delta_{\text{max}}^2)/(2\delta_{\text{max}}^2)} \, , \tag{4.19}$$

where $u(\delta_{\text{max}}) = u_{\text{max}}$ (see Sec. 4.2.5.3 for details).

Propulsion Velocity The self-thermophoretic propulsion velocity $\boldsymbol{u}$ of the swimmer is determined by the temperature distribution along the swimmers surface[165] (Sec. 2.3.3):

$$\boldsymbol{u} = -\frac{\chi}{T} \frac{1}{S} \int_S \nabla_{\|} T \, \mathrm{d}S \, . \tag{4.20}$$

Here, χ is the thermo-osmotic coefficient, T the temperature, $S = 4\pi R^2$ the surface area of the particle and $\nabla_{\|} = (1 - \boldsymbol{e}_r \boldsymbol{e}_r) \cdot \nabla$ the surface gradient operator for a spherical surface.

To estimate the temperature distribution on the particle surface, we assume that the AuNPs on the surface of the microswimmer are heated with a Gaussian beam (Sec. 2.4.1) with the intensity distribution

$$I(x, y, z) = I_0 \left(\frac{w_0}{w(z)}\right)^2 \exp\left(-\frac{2((x-\delta)^2 + y^2)}{w(z)^2}\right) , \tag{4.21}$$

where the center of the Gaussian beam is displaced by δ with respect to the particle center (Fig. 4.30a). If we introduce spherical coordinates r, θ, φ and assume that the temperature increment $\Delta T(\theta,\varphi) = T(\theta,\varphi) - T_0$ on the particle surface is proportional to the incident intensity, $\Delta T(\theta,\varphi) \propto I(\theta,\varphi)$, we obtain:

$$T(\theta,\varphi) \propto \frac{1}{1 + (R\cos\theta/z_\mathrm{R})^2} \exp\left(-\frac{2((R\sin\theta\cos\varphi - \delta)^2 + (R\sin\theta\sin\varphi)^2)}{w_0^2(1 + (R\cos\theta/z_\mathrm{R})^2)}\right) + T_0 . \tag{4.22}$$

The relative temperature increment $\Delta T/T_\mathrm{max}$ on the swimmer surface for four different beam displacements δ is illustrated in Fig. 4.33.

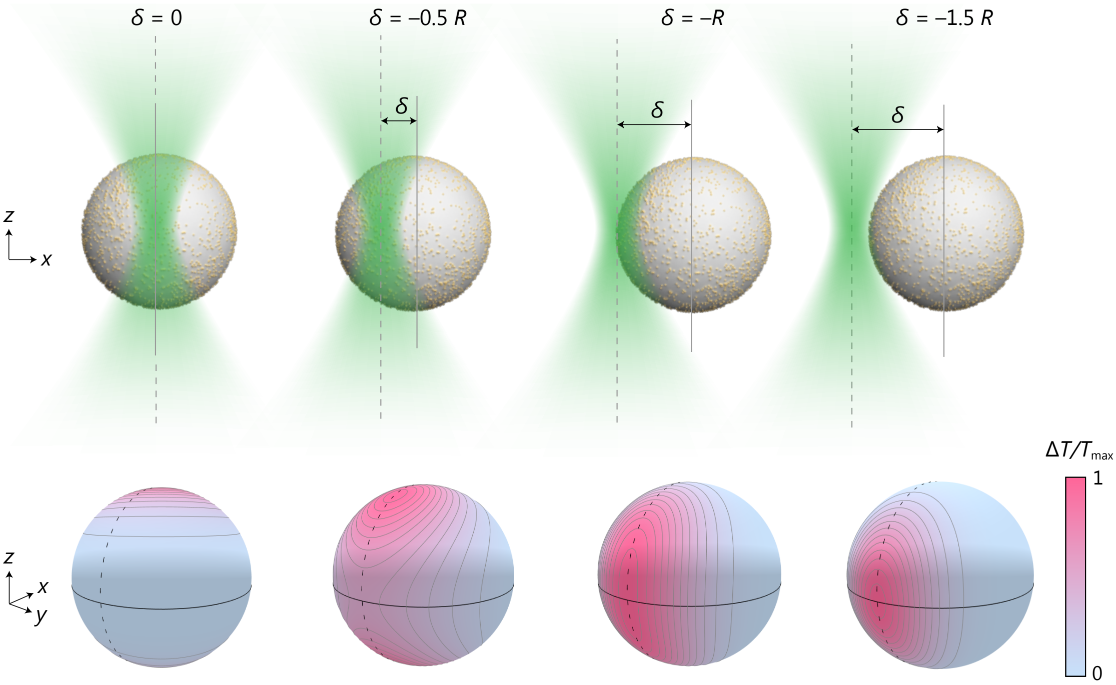

Fig. 4.33: The relative temperature increment $\Delta T/T_\mathrm{max}$ on the swimmer surface according to Eq. (4.22) for different beam displacements δ.

The self-thermophoretic propulsion velocity can then be obtained using Eq. (2.76):

$$u = -\frac{\chi}{T_0}\frac{1}{S}\int_0^{\pi}\int_0^{2\pi}\left(\frac{1}{R}\frac{\partial T(\theta,\varphi)}{\partial\theta}\cos\theta\cos\varphi - \frac{1}{R\sin\theta}\frac{\partial T(\theta,\varphi)}{\partial\varphi}\sin\varphi\right)R^2\sin\theta\,\mathrm{d}\theta\,\mathrm{d}\varphi , \tag{4.23}$$

where $T(\theta,\varphi)$ is the surface temperature given by Eq. (4.22) and the surface gradient operator has been expressed in spherical coordinates (see Sec. 2.3.3 for details). The propulsion velocity as function of the displacement δ obtained from the integration of Eq. (4.23) is depicted as solid gray curve Fig. 4.32. A detailed parameter discussion can be found in Secs. 4.2.5.4 and 4.2.5.5.

The projection of the laser intensity yields only the relative surface temperature increment $\Delta T/T_\mathrm{max}$. To find a numerical estimate for the absolute temperature increment ΔT_max, we use a superposition of the temperature field of N point-like heat sources, which are randomly distributed over the surface of a sphere with radius R:

$$\Delta T(\boldsymbol{r}) = \sum_{N} \frac{I(\boldsymbol{r})\sigma_{\mathrm{abs}}}{4\pi\kappa\, r} \; . \tag{4.24}$$

Here, $I(\boldsymbol{r})$ is the intensity of the Gaussian beam, Eq. (4.21), σ_{abs} the absorption cross-section of the AuNPs and $\kappa = (\kappa_{\mathrm{H_2O}} + \kappa_{\mathrm{MF}})/2$ the averaged thermal conductivity around the AuNPs (Fig. 4.35a, b). The absorption cross-section σ_{abs} of a AuNPs in water as function of the wavelength is plotted in Fig. 4.34 for three NPs radii R_{NP}. For the wavelength of $\lambda = 532$ nm used in our experiments and a AuNP radius of $R_{\mathrm{NP}} = 4$ nm, we obtain an absorption cross-section of about $\sigma_{\mathrm{abs}} = 2.5 \cdot 10^{-5}$ µm^2 (Fig. 4.34).

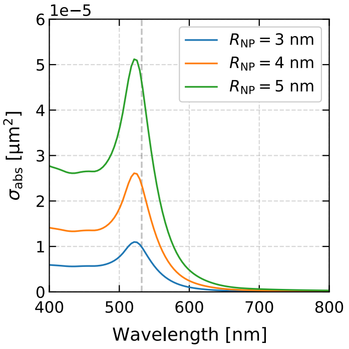

Fig. 4.34: The absorption cross-section σ_{abs} of a AuNP in water with radius R_{NP} as function of the wavelength calculated using Mie theory (Sec. 2.4.2). The dielectric function of gold was adapted from Ref. 173 and for the refractive index of water we used $n = 1.33$. The vertical gray line depicts the laser wavelength used in our experiments ($\lambda = 532$ nm).

The numerical evaluation of Eq. (4.24) yields a linear increase of ΔT_{max} with P_0 and predicts a maximum temperature increment of $\Delta T_{\mathrm{max}} = 12$ K for the maximum laser power used in our experiments ($P_{\mathrm{max}} = 0.4$ mW).

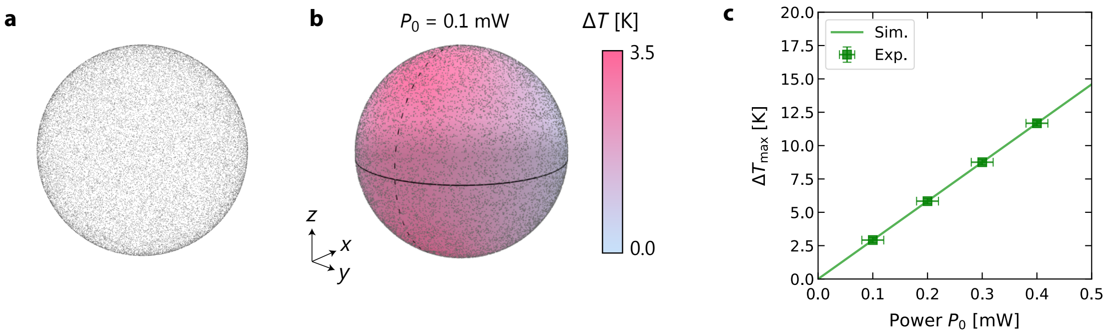

Fig. 4.35: **a**, $N = 30{,}000$ point-like heat sources randomly distributed over the surface of a sphere with radius $R = 1.1$ µm. **b**, Simulated surface temperature increment corresponding to (**a**), calculated using Eq. (4.24) for a heating power of $P_0 = 0.1$ mW and a laser displacement of $\delta = -0.5\,R$. **c**, Maximum temperature increment as function of the heating power P_0.

Experimental insight into the surface temperature rise of the swimmer can be obtained with the help of the nematic/isotropic phase transition of the liquid crystal 5CB (Sec. 3.4). For the heating power $P_{\mathrm{max}} = 0.4$ mW we find $\Delta T_{\mathrm{max}} = 12$ K in perfect agreement with the numerical simulation (see Fig. 4.35c and Sec. 4.2.5.6 for details). Fig. 4.35b is still only an approximation of the real temperature distribution since the deflection of the Gaussian beam by the MF particle is neglected in Eq. (4.24).

For a laser power of $P_0 = 0.1$ mW and the corresponding temperature increment $\Delta T_{\mathrm{max}} = 3$ K (Fig. 4.35b), the numerical evaluation of Eq. 4.20 yields a maximum velocity $u_{\mathrm{max}} = 8$ µm s^{-1} in agreement with the experimental result (Fig. 4.32). We have used a thermometric mobility coefficient $\chi = 10 \cdot 10^{-10}$ m^2 s^{-1} previously reported in Ref. 49 for surfaces covered with the block-copolymer Pluronic F-127. In contrast to the experimental result, the evaluation of Eq. (4.20) yields an optimal displacement of $\delta_{\mathrm{max}} = -0.84$ µm (Fig. 4.32, gray curve). The deviation of

$\delta_{\max}$ is a consequence of the experimental feedback delay. The position of the laser focus can only be adapted with a certain delay due to the finite frame rate τ^{-1} of the image acquisition. During the time τ the position of the laser is fixed, whereas the particle is self-propelled away from the laser focus. Since the propulsion velocity depends on the distance to the laser focus (Fig. 4.32) the detected velocity will always be smaller than the instantaneous velocity. The detected, averaged velocity reads:

$$\langle u \rangle = \frac{1}{\tau} \int_0^{\tau} u(\delta(t))\ \mathrm{d}t\ . \tag{4.25}$$

This equation can be integrated numerically for different initial displacements (see Sec. 4.2.5.7 details) leading to velocity profiles depicted in Supplementary Fig. (4.49). With increasing τ, the optimal initial displacement $\delta_{\max}$ is indeed decreasing. When the laser focus is placed closer to the particle center, the particle will pass through the velocity maximum during the time τ instead of moving away from it, leading to a higher averaged velocity. For $\tau = 30$ ms, the numerical evaluation of Eq. (4.25) yields an optimal displacement of $\delta_{\max} = -0.69$ µm. We attribute the even smaller experimental value ($\delta_{\max} = -0.5$ µm, Fig. 4.32) to additional delays due to the time required for the image processing and laser adjustment not considered in Eq. (4.25).

To find the dependence of the particle velocity on the incident laser power, the experiment depicted in Fig. 4.31b is repeated for laser powers varying from 0.04 to 0.4 mW with a fixed displacement of $\delta_{\max} = -0.5$ µm. We find a non-linear scaling of the velocity with the laser power (Fig. 4.36a). For an inverse frame rate $\tau = 30$ ms, a maximum velocity $u_{\max} = 14$ µm s^{-1} is found. The non-linear power dependence of the velocity is, again, the result of the finite exposure time. Within the time τ, the particle moves and the instantaneous velocity changes while the laser is spatially fixed. If we assume that $u_{\max} \propto P_0$, the detected velocity as function of the power can be obtained from the evaluation of Eq. (4.25) for different $u_{\max}$ (see Sec. 4.2.5.8 for details). The result is in agreement with our experimental findings (Fig. 4.36a, solid lines) and predicts that the velocity at high laser powers is proportional to τ^{-1}. This dependence is also confirmed by our experimental results depicted in Fig. 4.36b.

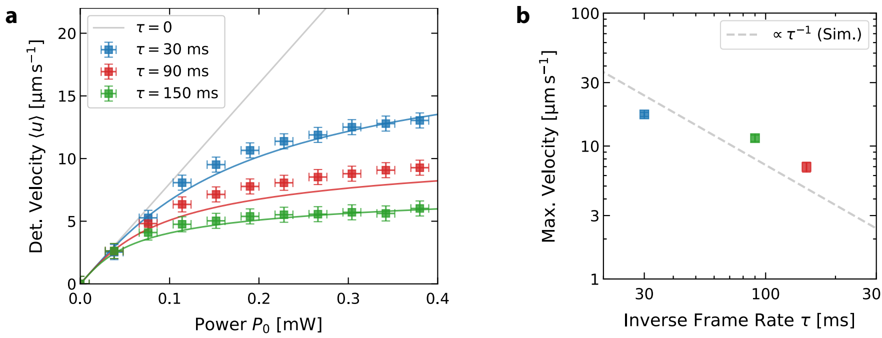

Fig. 4.36: a, The detected propulsion velocity $\langle u \rangle$ as function of the incident laser power P_0 and the inverse frame rate τ (symbols) for $\delta = -0.5$ µm. The solid curves represent the numerical results according to Eq. 4.25. The dashed lines depict the velocity $\langle u \rangle_{\max}$ at maximum power $P_0 = P_{\max}$. **b**, Dependence of the maximum velocity $\langle u \rangle_{\max}$ as function of the inverse frame rate τ.

Positioning Accuracy Based on this understanding of the propulsion mechanism and its dependency on the power, delay and displacement, we are now able to explore in detail the accuracy to control the particle. The control precision is best deduced from an experiment localizing the particle at a fixed (target) position in the sample by continuous actuation (Fig. 4.37, Supplementary Video 2.2). The localization is then characterized by the positioning error $\rho = \sqrt{\langle (\boldsymbol{r} - \boldsymbol{r}_{\mathrm{t}})^2 \rangle}$, where $\boldsymbol{r}$ and $\boldsymbol{r}_{\mathrm{t}}$ are the coordinates of the particle and the target, respectively. The positioning error has two regimes. If the particle displacement due to the self-propulsion during the inverse frame rate τ is smaller than the displacement due to the diffusion, the positioning error follows from a simple sedimentation model. The particle is radially driven towards the target with a velocity u against its diffusive motion with the diffusion coefficient D. In the steady state, the characteristic length scale is $\rho_1 = \sqrt{6}D/u$ as indicated by the dashed-dotted curve in Fig. 4.37a.

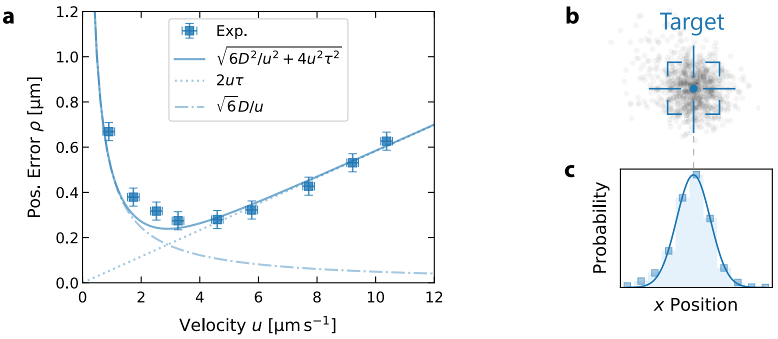

Fig. 4.37: **a**, The symbols show the positioning error as a function of the laser power derived from an experiment confining a single particle for a certain time at a target position (Supplementary Video 2.2). The dashed-dotted and dotted curves are the contributions from the 2D sedimentation (dashed-dotted) and the particle overshooting (dotted). The sum of both contributions is represented by the solid curve. **b**, Example of a position distribution around a target for a laser power of $P_0 = 0.01$ mW ($u = 0.01$ µm s^{-1}). **c**, Probability distribution of the x-position corresponding to (**b**).

For a large particle velocity, the positioning error gets mainly defined by an overshooting of the particle over the target position. This is again due to the finite sampling of the particle position with the inverse frame rate τ. The overshooting distance is twice the distance traveled within the inverse frame rate $\rho_2 = 2u\tau$ and increases with increasing power as shown by the dotted curve in Fig. 4.37a. The sum of both contributions, $\rho = \sqrt{\rho_1^2 + \rho_2^2}$, yields

$$\rho = \sqrt{6D^2/u^2 + 4u^2\tau^2}\ , \tag{4.26}$$

and is depicted as solid curve in Fig. 4.37a with no free parameters. We have used $D = 0.20\ \mu\mathrm{m}^2\,\mathrm{s}^{-1}$ and $\tau = 30$ ms. The diffusion coefficient was calculated from $D = k_\mathrm{B}T_0/(6\pi\eta R)$ with $T_0 = 25\,°\mathrm{C}$, $\eta = 0.001$ Pa s and $R = 1.1$ µm. The minimum $\rho_\mathrm{min} = 240$ nm in the positioning error is found for $u_\mathrm{min} = 3.0\ \mu\mathrm{m\,s}^{-1}$. The positioning error decreases with the inverse frame rate τ. The minimal positioning error is, nevertheless, limited by the Brownian motion and thus the diffusion coefficient D of the microswimmer. As compared to optical tweezers that trap similar sized dielectric particles with powers of several 10 mW or more, our particle control is achieved with a few 100 µW only. A major difference is thereby also the fact that the self-propulsion works without an external force, due to a force balance in the sample, while optical tweezers exert external forces on the particle. Therefore the hydrodynamics involved in the active particle motion is short ranged and different from the long ranged flow fields generated by external body forces (see Fig. 2.14b for ref.).

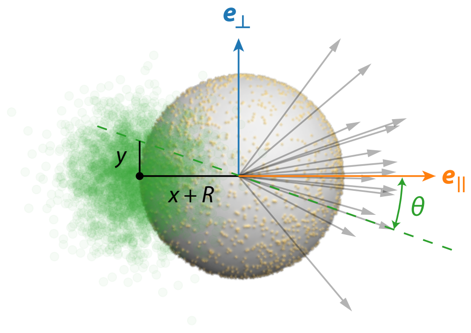

Fig. 4.38: Illustration of the directional noise. The angle θ between the intended and the actual propulsion direction is a result of the diffusion of the microswimmer from the position $(0, 0)$ to the position (x, y) during the time interval τ between the measurement and switching on the laser.

Noise Influence Besides influencing the localization accuracy, Brownian motion also impacts the directed motion of the swimmer. Analyzing the trajectory in Fig. 4.31b for $\tau = 30$ ms, we extract the displacements $\Delta\boldsymbol{r}$ between subsequent frames and project them on the desired direction to the target ($\boldsymbol{e}_\parallel$) and a direction perpendicular to it ($\boldsymbol{e}_\perp$) as depicted in Fig. 4.38.

Fig. 4.39a shows the experimental result for a laser power of $P_0 = 0.3$ mW shifting the starting point of all displacements to the origin. The endpoints of the displacements of the motion in the horizontal direction are distributed along the horizontal and vertical direction with an opening angle $\theta_{\mathrm{FWHM}} = 2\sqrt{2\ln 2}\,\sigma_\theta\, 360°/(2\pi)$ of about 53° (Fig. 4.39a, b). Measuring the occurrences of horizontal and vertical displacements yields the histograms in Fig. 4.39c. Horizontal displacements have a non-zero mean value, which measures the propulsion velocity $u_\parallel$ along the horizontal direction. The displacements along the vertical direction have a zero mean, indicating no effective propulsion along this direction. Yet, the observed variance of the horizontal and vertical distribution differ considerably for the specific delay of $\tau = 30$ ms.

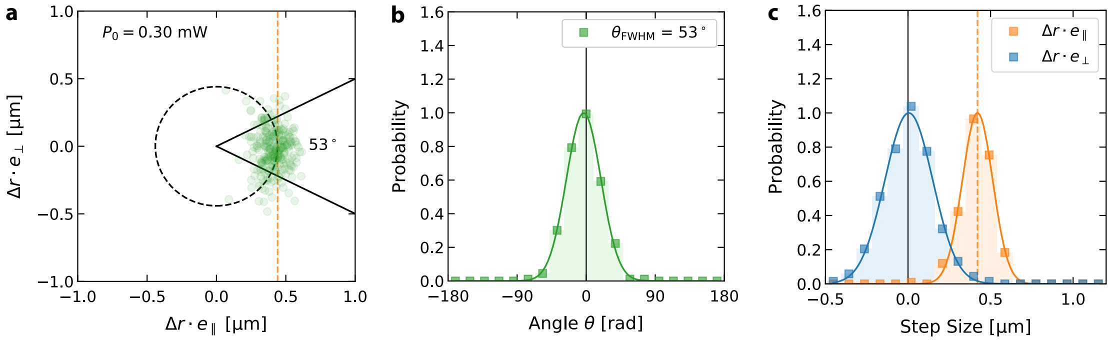

Fig. 4.39: Noise Influence. **a**, The displacement vectors projected tangential and perpendicular to the target direction for a laser power of $P_0 = 0.3$ mW and an inverse frame rate of $\tau = 30$ ms. The solid black lines depict the opening angle $\theta_{\mathrm{FWHM}} = 53°$. **b**, The angular distributions measured from the displacement vectors in (**a**). **c**, The probability distribution of the projected displacement vectors in (**a**). The mean of the tangential step size distribution (blue dashed line) corresponds to the velocity $u_\parallel = \langle \Delta \boldsymbol{r} \cdot \boldsymbol{e}_\parallel \rangle / \tau$.

To understand the observed effects, we model the particle motion with the help of a Langevin equation (Sec. 2.1.2). In the model, the directional uncertainty is again a result of the delayed response of the feedback loop. During the delay time τ, the particle diffuses away from the detected spot in the camera image giving rise to a deviating particle position and, thus, a propulsion direction different than the intended one. This results in an angular distribution of the propulsion velocities around the target direction $p(\theta)$ that can be approximated by

$$p(\theta) \approx (2\pi\sigma_\theta^2)^{-1/2} \mathrm{e}^{-\theta^2/(2\sigma_\theta^2)} \;, \tag{4.27}$$

with $\sigma_\theta^2 = 2D\tau/R^2$ (see Sec. 4.2.5.9 for details). The important consequence is that the particle motion not only possesses an active component along the target direction but also perpendicular to it. The spread of positions perpendicular to the motion towards the target grows with an active component and is not purely diffusive. Using the Langevin model, detailed in Sec. 4.2.5.9, we find for the variances in tangential ($\sigma_\parallel$) and perpendicular direction ($\sigma_\perp$):

$$\sigma_\parallel^2 = (1 - \sigma_{y\theta}^2) u_\theta^2 \tau^2 - \mathrm{e}^{-\sigma_\theta^2} u_\theta^2 \tau^2 + 2D\tau \;, \tag{4.28}$$

$$\sigma_\perp^2 = \sigma_{y\theta}^2 u_\theta^2 \tau^2 + 2D\tau \;, \tag{4.29}$$

with $\sigma_{y\theta}^2 = (1 - \mathrm{e}^{-2\sigma_\theta^2})/2$ and $u_\theta = \mathrm{e}^{\sigma_\theta^2/2} u_\parallel$. As can be seen from Eq. (4.29), the perpendicular component of the displacement $\sigma_\perp$ has now a term proportional to the velocity (first term) and the expected diffusive term. Thus, one expects that for small delays and small velocities the uncertainty $\sigma_\perp$ is governed by the diffusive motion (second term), while with larger velocities and delays the first term dominates.

The angular distribution, Eq. (4.27), predicts an opening angle that is independent of the propulsion velocity $u_\parallel$. This is confirmed in our experiments where we find a constant opening angle of about $\theta_{\mathrm{FWHM}} \approx 50°$ (Fig. 4.40a). Furthermore, Fig. 4.40b shows that the experimental results for $\sigma_\parallel^2$ (blue circles) and $\sigma_\perp^2$ (red squares) as functions of the velocity $u_\parallel$ are in good agreement with Eqs. (4.28) and (4.29) for the experimental opening angle 53°.

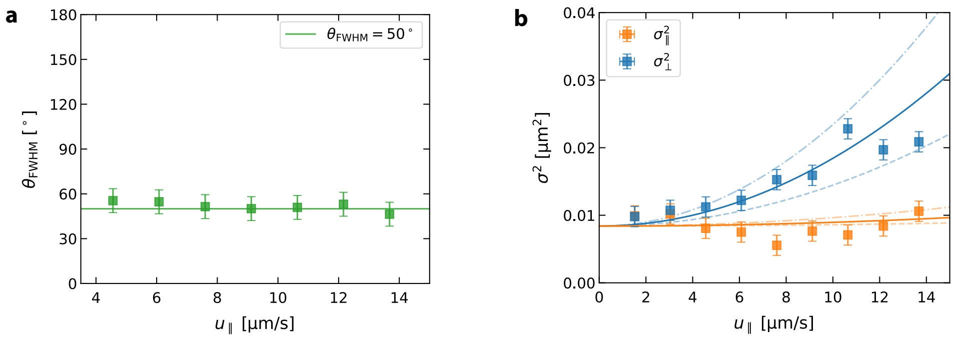

Fig. 4.40: **a**, The measured opening angle θ_{FWHM} as function of the propulsion velocity $u_\parallel$ (green symbols). **b**, The experimental variances of the tangential (orange symbols) and perpendicular (blue symbols) step size distributions as functions of the velocity $u_\parallel$ compared to the theoretical model for $\theta_{\mathrm{FWHM}} = 40^\circ$ (dashed lines), $\theta_{\mathrm{FWHM}} = 50^\circ$ (solid lines) and $\theta_{\mathrm{FWHM}} = 60^\circ$ (dash-dotted lines).

This active directional uncertainty due to the delayed response might have important consequences also for the motion of microscopic living systems such as bacteria. It suggests that a large propulsion speed is actually not beneficial if the object responds with a delay to a specific environmental signal[244]. The delay, active propulsion, and Brownian noise will induce a directional uncertainty that grows with increasing speed and lets the propelled object fail to reach the target, while on average it has the right propulsion direction.

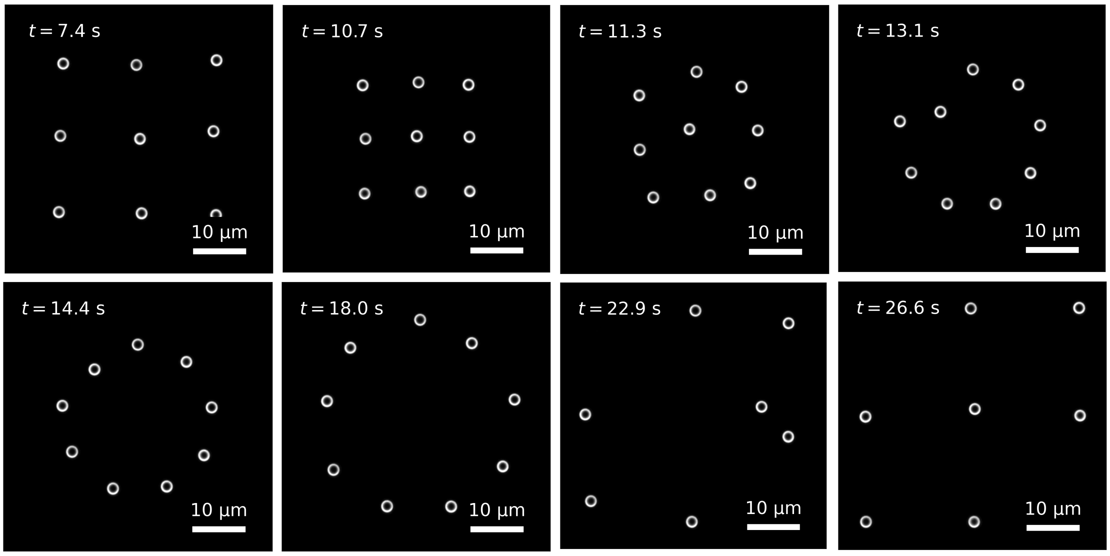

Fig. 4.41: Experimental feedback control of nine individual symmetric swimmers that are arranged on a grid and reconfigured to a circle (Supplementary Video 3.3).

Control of Multiple Swimmers The actuation scheme, so far discussed only for a single microswimmer, can be extended to control a larger number of swimmers by quickly multiplexing the laser focus between different particle positions within the time of the inverse frame rate τ. Fig. 4.41 and Supplementary Video 3.3 demonstrate the control of nine individual symmetric swimmers that are arranged on a grid pattern and reconfigured to a circle. Initially, the particles are randomly distributed in the field of view. When the feedback control is enabled, each particle is driven towards its nearest target and eventually confined there. As the resulting arrangement is constantly actuated, the structure is dynamic as can be seen from Supplementary Video 3.3. A fully simultaneous feedback control of multiple particles might be achieved using a spatial light modular or a digital micro-mirror device.

4.2.4 Conclusion

We have presented a fully steerable thermoplasmonic symmetric microswimmer that is self-propelled by laser-induced self-thermophoresis. The asymmetry, inherently required for a self-propulsion at low Reynolds numbers, is induced by the heating laser itself. In this way, the active particle motion becomes independent of the rotational diffusion providing a substantially higher level of control than previously possible for microswimmers with an asymmetric geometry, for example, Janus-type particles. We find a dependence of the active particle velocity on the feedback cycle time as well as on the displacement of the control laser, which can be completely understood with our theoretical model. This model also suggests that microscopic objects subjected to positional noise with a delayed response develop an active propulsion uncertainty. This uncertainty could set, for example, a speed limit to bacteria targeting the propulsion towards a specific goal. The design of the symmetric microswimmer enables an actuation with high precision at the micrometer scale. The precise control of active particles will thereby allow to create, for example, active particle systems in well controlled initial conditions, to explore their mutual interactions and collective behaviors. Our approach can prepare dense ensembles with a well defined number of members to lead self-assembly of non-equilibrium structures due to phoretic and hydrodynamic interactions[245–248]. The feedback control allows the incorporation of non-reciprocal and delayed interactions with other active and passive real world objects, where collective phenomena can emerge in an ensemble. We anticipate that the presented results will be of relevance for the development of more complex self-propelled particle systems and nanomachines as well as to study synthetic active particles systems.

4.2.5 Supplementary Information

4.2.5.1 Sample Preparation

The sample consists of two glass coverslips (22 mm × 22 mm) confining a thin liquid film. First, the coverslips were cleaned by rinsing successively with acetone, isopropyl and Milli-Q water and dried with a nitrogen gun. To prevent sticking of the microparticles, the glass surfaces were passivated with Pluronic F-127. To attain the adsorption of Pluronic F-127 in a brush-like configuration the cleaned, hydrophilic coverslips were rendered hydrophobic with a thin layer of polystyrene. Therefore, 30 µl of 1 % polystyrene (PSS-Polymer, $M_\mathrm{w} = 88$ kDa, PDI = 1.66) dissolved in toluene was spin-coated at 8,000 rpm onto the coverslips, resulting in a polystyrene layer thickness of about 100 nm. Subsequently, the coverslips are immersed in 1 % Pluronic F-127 solution for 10 min. Thereafter, the coverslips were briefly dipped in Milli-Q water and dried with a nitrogen gun. Subsequently, the edges of one coverslip were covered with a thin layer of PDMS for sealing. The particle solution used for the experiments was prepared by dispersing 2.2 µm diameter gold-coated melamine formaldehyde (MF) particles (microParticles) in 0.1 % Pluronic F-127 solution. To passivate the surface of the particles, they have been washed in a 1 % Pluronic F-127 solution before mixing. Finally, 0.6 µl of the mixed particle suspension is pipetted in the middle of one of the coverslips and the other is placed on top. Depending on the area covered by the liquid, typically about 14 mm × 14 mm, the resulting liquid film height is about 3 µm. Chemicals, if not otherwise specified, have been obtained from Sigma-Aldrich.

4.2.5.2 Particle Tracking

The particle centers are detected as follows. First, we reduce the noise in the recorded image using a two pixel median filter (Fig. 4.42a). Then we compute an inverted binary image using a global threshold (Fig. 4.42b, c). Subsequently, a connected-component labeling algorithm is used to identify and filter connected white pixel regions according to their pixel area (Fig. 4.42c). The particles center position is then calculated from the center of mass of the detected inner particle area.

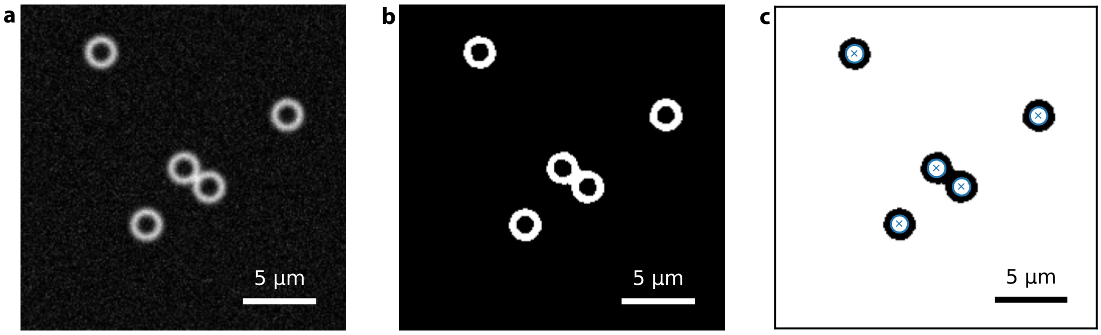

Fig. 4.42: **a**, The recorded image. **b**, The binary representation of the image processed with a two pixel median filter and a global threshold value. **c**, The inverted binary image with the detected particle centers from the connected-component labeling depicted in blue.

4.2.5.3 Propulsion Velocity

The solid blue curve Fig. 4.43 depicts the self-propulsion velocity as function of the displacement δ for a particle radius of $R = 1.1$ µm and a beam waist of $w_0 = 0.81$ µm obtained from the numerical integration of Eq. (4.23). The result can be well approximated by the function

$$u(\delta) = u_{\max} \frac{\delta}{\delta_{\max}} \, \mathrm{e}^{(-\delta^2+\delta_{\max}^2)/(2\delta_{\max}^2)} \tag{4.30}$$

with $u(\delta_{\max}) = u_{\max}$ (Fig. 4.43, dashed blue curve).

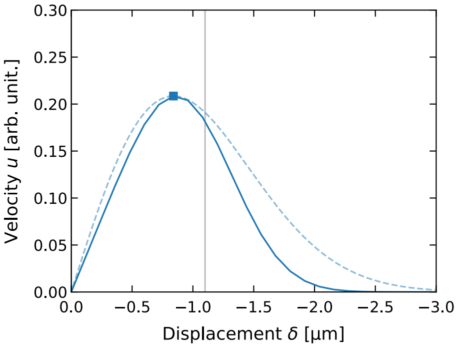

Fig. 4.43: The propulsion velocity u as function of the displacement δ for $R = 1.1$ µm, $w_0 = 0.81$ µm and $\lambda = 0.532$ nm. The solid blue curve follows from Eq. (4.23) and the dashed blue curve represents the approximation with Eq. (4.30). The vertical solid gray line depicts the particle radius R.

4.2.5.4 Beam Waist Dependence

Fig. 4.44 depicts the velocity as function of the displacement δ for different beam waists w_0.

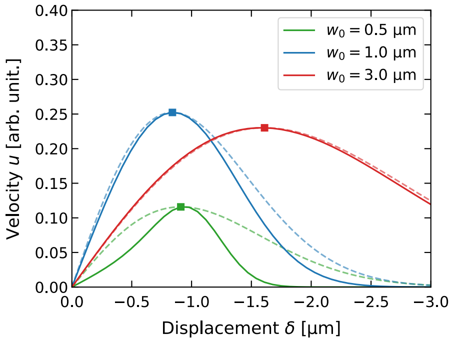

Fig. 4.44: The propulsion velocity u as function of the displacement δ for three different beam waists w_0 ($R = 1.1$ µm and $\lambda = 0.532$ nm). The solid lines depict the numerical solution of Eq. (4.23) and the dashed lines approximations with Eq. (4.30). The squares show $u_{\max}$ for the given beam waist w_0.

The maximum velocity $u_{\max}$ as function of the beam waist w_0 is depicted in Fig. 4.45a. For a particle radius of $R = 1.1$ µm the optimal beam waist is $w_0 = 1.5$ µm, 0.4 µm larger than the particle radius. Fig. 4.45b depicts the optimal displacement $\delta_{\max}$, that is, the displacement at maximum velocity $u(\delta_{\max}) = u_{\max}$, as function of the beam waist w_0. For small beam waists, the optimal displacement is equal to the negative particle radius $R = 1.1$ µm. With increasing beam waist, the optimal displacement $\delta_{\max}$ reaches a negative minimum for $w_0 = 0.8$ µm and approaches $-w_0/2$ for $w_0 \gg R$.

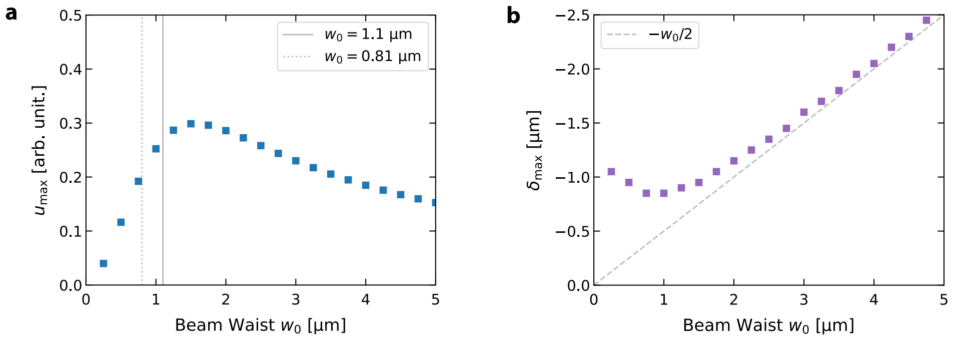

Fig. 4.45: **a**, The maximum velocity $u_{\max}$ and **b**, the displacement $\delta_{\max}$ at maximum velocity as functions of the beam waist w_0 ($R = 1.1$ µm, $\lambda = 0.532$ nm). The solid gray line in (**a**), depicts the particle radius R, whereas the dotted line depicts the beam waist used in our experiments ($w_0 = 0.81$ µm). The dashed gray line in (**b**) represents $\delta_{\max} = -w_0/2$.

4.2.5.5 Size Dependence

Fig. 4.46 depicts the velocity as function of the displacement δ for different particle radii R.

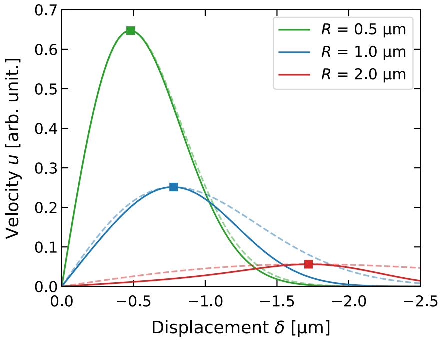

Fig. 4.46: The propulsion velocity u as function of the displacement δ for three different particle radii R ($w_0 = 0.81$ µm, $\lambda = 0.532$ nm). The solid lines depict the numerical solution of Eq. (4.23) and the dashed lines represent Eq. (4.30). The squares show $u_{\max}$ for the given radius R.

The maximum velocity $u_{\max}$ as function of the particle radius R is depicted in Fig. 4.47a. With decreasing particle radius, the maximum velocity is increasing which was previously also shown for Janus particles[12]. However, for nanometer-sized swimmer particles, the surface temperature is not well approximated anymore by Eq. (4.22). When R approaches R_{NP} the self-propulsion velocity will decrease and eventually become zero.

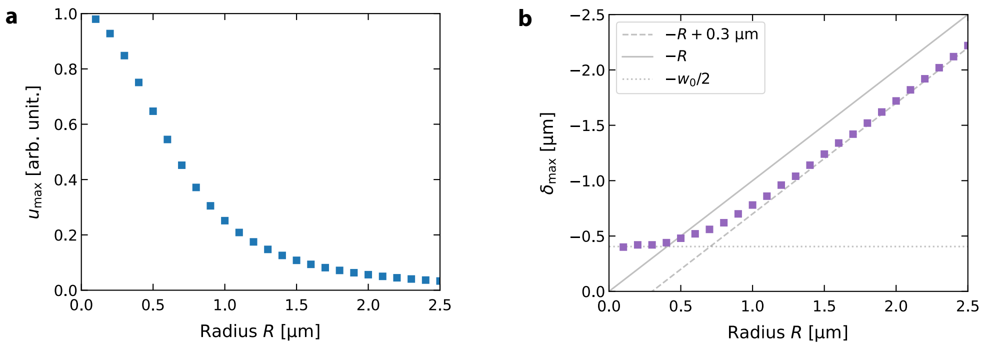

Fig. 4.47: **a**, The maximum velocity $u_{\max}$ and **b**, the displacement $\delta_{\max}$ at maximum velocity as functions of the particle radius R ($w_0 = 0.81$ µm, $\lambda = 0.532$ nm). The solid gray line in (**b**), represents $\delta_{\max} = -R$, the dashed line $\delta_{\max} = -R + 0.3$ [µm] and the dotted line $\delta_{\max} = w_0/2$.

Fig. 4.47b depicts the optimal displacement $\delta_{\max}$ as function of the particle radius R. With decreasing particle size, the optimal displacement approaches $-w_0/2$, where the intensity profile $I(x, y = 0, z = 0)$ of the Gaussian beam has its inflection point. For larger particles, the optimal displacement is linearly decreasing with R as $\delta_{\max} = -R + 0.3$ [µm].

4.2.5.6 5CB Temperature Measurement

To estimate the temperature increment on the swimmer surface, the method introduced in Sec. 3.4 is used. Therefore, symmetric swimmer particles were embedded in a 5CB sample and heated with a focused laser as illustrated in Fig. 4.48a. The radius of the phase transition is expected to increase linearly with the incident laser power since $\Delta T \propto P_0$. The blue squares in Fig. 4.48b depict the obtained phase transition radius R_{pt} as function of the incident laser power P_0 for a $R = 1.1$ µm radius particle heated in the center. If we assume a radially symmetric temperature distribution, the surface temperature increment ΔT is given by

$$\Delta T = \frac{(35\,^{\circ}\mathrm{C} - T_0)(R_{\mathrm{pt}} - R)}{R} \,, \tag{4.31}$$

where R is the radius of the swimmer and $T_0 = 25\,^{\circ}\mathrm{C}$ is the surrounding temperature.

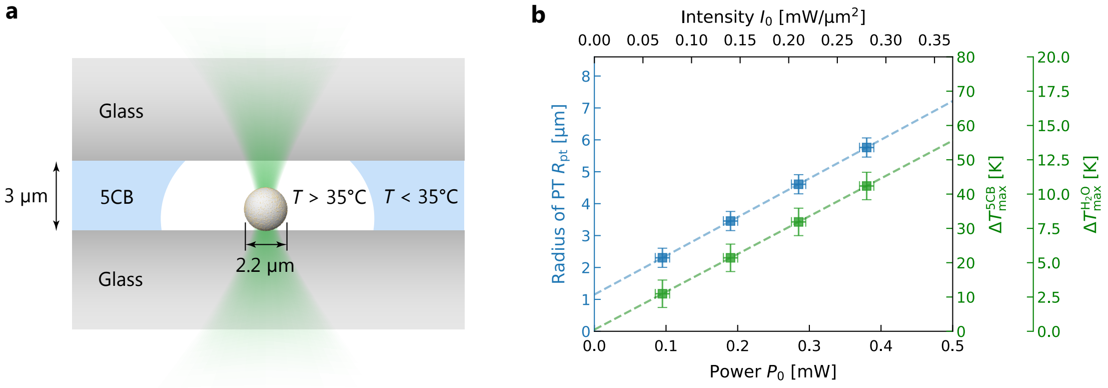

Fig. 4.48: 5CB Temperature Measurement. **a**, Sketch of the measurement principle and the sample geometry. **b**, The measured phase transition radius (R_{pt}, blue squares) and the temperature increment in 5CB ($\Delta T_{\max}^{5\mathrm{CB}}$, green squares) calculated using Eq. (4.31) as functions of the incident laser power P_0. The temperature increment in water ($\Delta T_{\max}^{\mathrm{H_2O}}$) is by a factor of 4 smaller than in 5CB according to the ratio of the thermal conductivities of the water and 5CB in its isotropic phase ($\kappa_{\mathrm{H_2O}}/\kappa_{5\mathrm{CB}} = 4$).

The thermal conductivity of 5CB in its isotropic phase is about $\kappa_{5\mathrm{CB}} = 0.15\ \mathrm{W\,m^{-1}\,K^{-1}}$ (Appendix A2.3). For simplicity the thermal conductivity difference of the nematic phase is neglected since the major part of the temperature distribution is within the isotropic phase. Since the thermal conductivity of water is about $\kappa_{\mathrm{H_2O}} = 0.6\ \mathrm{W\,m^{-1}\,K^{-1}}$, the temperature increment is smaller by the factor of 4 when the microparticle is embedded in water. The obtained temperature increment ($\Delta T_{\max}^{\mathrm{H_2O}}$, Fig. 4.48b) agrees well with the simulation result in Fig. 4.35b.

4.2.5.7 Frame Rate Dependence

The position of the laser focus can only be readjusted with a certain delay due to the finite frame rate τ^{-1} of the image acquisition. During the time τ, the position of the laser is fixed, whereas the particle is moving away from the laser focus due to its self-propelled motion. Since the propulsion velocity depends on the distance to the laser focus (Fig. 4.43), the detected velocity will always be smaller than the instantaneous velocity. To get the total displacement Δx within the time τ, we numerically solve the integral equation

$$\int_0^{\tau} \mathrm{d}t = \tau = \int_{\delta}^{\delta+\Delta x} \frac{1}{u(\delta'; u_{\max}, \delta_{\max})}\, \mathrm{d}\delta' = f(\Delta x; \delta)$$

for Δx as function of the initial displacement δ. Here, we have used $\mathrm{d}\delta = u(\delta)\mathrm{d}t$ and Eq. (4.30) for the distance dependence of the instantaneous velocity. The detected velocity is then obtained from $\langle u \rangle = \Delta x/\tau$. The resulting detected velocity as function of the initial displacement δ is plotted in Fig. 4.49.

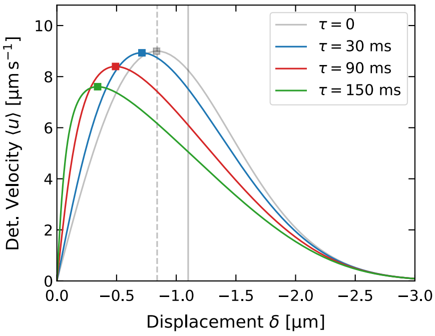

Fig. 4.49: The detected velocity $\langle u \rangle$ as function of the initial displacement δ for different inverse frame rates τ. The solid gray line depicts the particle radius R and the dashed gray line the optimal displacement for $\tau = 0$ corresponding to Fig. 4.43. Squares denote the maximum detected velocity $\langle u \rangle_{\max}$ for the given τ.

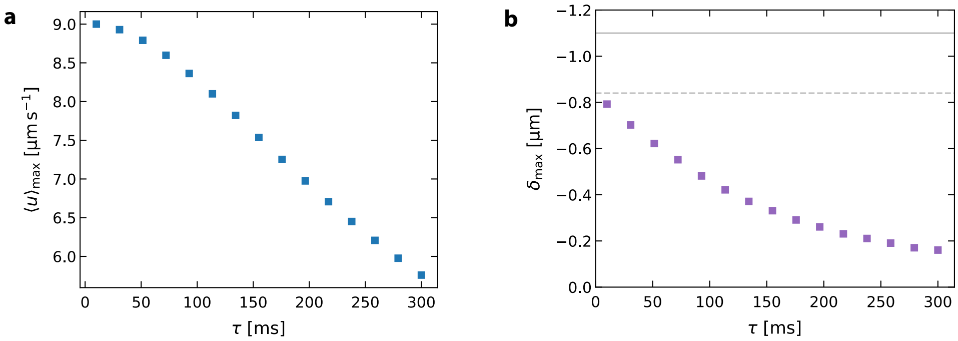

Fig. 4.50: The maximum detected velocity $\langle u \rangle_{\max}$ (**a**) and the optimal initial displacement $\delta_{\max}$ (**b**) as functions of the inverse frame rate τ. **b**, The solid gray line depicts the particle radius R and the dashed gray line the optimal displacement for $\tau = 0$.

Both the maximum detected velocity, $\langle u \rangle_{\max}$, and the optimal initial displacement, $\delta_{\max}$, decrease with decreasing frame rate (Fig. 4.50a, b). When the laser is placed closer to the particle center, the particle will pass through the velocity maximum during the time τ instead of moving away from it, leading to a higher detected velocity.

4.2.5.8 Power Dependence of the Particle Velocity

The non-linear power dependence of the velocity is also a result of the finite frame rate τ^{-1}. Within the time τ, the particle moves and the instantaneous velocity decreases as the laser position is fixed. Similarly as in the previous section, we approximate the distance dependency of the velocity with

$$u(\delta) = u_{\max}(P_0)\frac{\delta}{\delta_{\max}}\,\mathrm{e}^{(-\delta^2+\delta_{\max}^2)/(2\delta_{\max}^2)}\,, \tag{4.32}$$

where we assume that the velocity maximum depends linearly on the incident heating power, $u_{\max} \propto P_0$. To get the total displacement Δx within the time τ, we numerically solve the integral equation

$$\int_0^\tau \mathrm{d}t = \tau = \int_{\delta_{\max}}^{\delta_{\max}+\Delta x} \frac{1}{u(\delta'; u_{\max}, \delta_{\max})}\,\mathrm{d}\delta' = f(\Delta x; v_{\max})$$

for Δx as function of $u_{\max} \propto P_0$ for a fixed initial displacement $\delta_{\max}$. The detected velocity is then obtained from $\langle u \rangle = \Delta x / \tau$. Fig. 4.51 shows that the detected velocity $\langle u \rangle$ increases non-linearly with the incident laser power P_0 and, thus, also the maximum velocity $u_{\max} \propto P_0$. The maximum attainable velocity $\langle u \rangle_{\max} = \lim_{P_0 \to \infty} \langle u \rangle$ turns out to be proportional to the frame rate $\langle u \rangle_{\max} \propto \tau^{-1}$ (Fig. 4.51b).

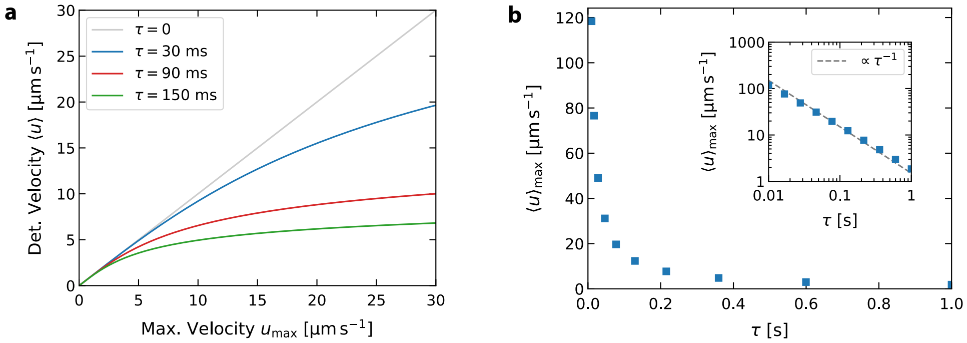

Fig. 4.51: **a**, The detected velocity as function of the incident laser power P_0 ($u_{\max} \propto P_0$) for different inverse frame rates τ. **b**, The maximum attainable velocity $\langle u \rangle_{\max} = \lim_{P_0 \to \infty} \langle u \rangle$ as function of the inverse frame rate τ.

4.2.5.9 Noise Influence Model

Consider the situation depicted in Fig. 4.38 where the microswimmer is propelled to the right in the direction of $\boldsymbol{e}_{\parallel}$. The desired position of the laser is depicted by the black dot at $(-R, 0)$. However, during the time τ between the measurement (determination of the target point for the laser) and switching on the laser, the particle diffuses from the position $(0,0)$ to $(x, -y)$, and, thus, the actual coordinates of the target point for the laser are $(-x - R, y)$ instead of $(R, 0)$. The actual direction of the particle is, thus, declined by the angle $\theta = \arctan(y/(x+R))$ from the intended direction. Due to the stochasticity of the Brownian motion, the angle θ is a random variable. Its probability density can be calculated as

$$p(\theta) = \int_{-\infty}^{\infty} \int_{-\infty}^{\infty} \delta\left(\theta - \arctan\left(\frac{y}{x+R}\right)\right) \frac{1}{4\pi D \tau} \exp\left(-\frac{x^2 + y^2}{4 D \tau}\right) \mathrm{d}x \, \mathrm{d}y \ , \tag{4.33}$$

where we integrate over the Gaussian distribution of the displacements (x, y) during the time τ. The integration can be performed exactly, but the result is not very enlightening. An intuitive formula can be derived if the variances $\langle x^2 \rangle = \langle y^2 \rangle = 2D\tau$ are much smaller than the square particle radius R^2, that is, if the particle diffuses during the time τ by much less than R. Then, the angle θ is small and we can use $\arctan(y/(x+R)) \approx y/R$ yielding the Gaussian probability density

$$p(\theta) \approx \int_{-\infty}^{\infty} \int_{-\infty}^{\infty} \delta\left(\theta - \frac{y}{R}\right) \frac{1}{4\pi D \tau} \exp\left(-\frac{x^2 + y^2}{4 D \tau}\right) \mathrm{d}x \, \mathrm{d}y = \frac{1}{\sqrt{2\pi\sigma_\theta^2}} \exp\left(-\frac{\theta^2}{2\sigma_\theta^2}\right) \tag{4.34}$$

with the variance:

$$\sigma_\theta^2 = \frac{2D\tau}{R^2} \ . \tag{4.35}$$

As a result of the used approximation, the density, Eq. (4.34), is normalized for $\theta \in (-\infty, \infty)$ and not for $\theta \in (-\pi, \pi)$. For the parameters $\tau = 30$ ms, $D = 0.20$ µm^2 s^{-1} and $R = 1.1$ µm used in the experiment, an opening angle of $\theta_{\mathrm{FWHM}} = 2\sqrt{2 \ln 2}\, \sigma_\theta \, 360°/(2\pi) = 13.4°$ is predicted. This value is about four times smaller than the values measured in our experiments (Fig. 4.39a, b). This disagreement follows from the fact that, in experiments, the displacement of the particle during the time τ is caused not only by diffusion but also by the self-propulsion, leading to a significant increase in the variance σ_θ. As expected from Eq. (4.35) the opening angle θ_{FWHM} is approximately constant in our experiments (Fig. 4.40a). For smaller laser powers ($P_0 < 0.1$ mW)

the opening angle θ_{FWHM} is substantially increased and the assumption that θ is small is not valid anymore.
To describe the influence of noise on the directed motion of the swimmer, let us assume that the particle moves due to the average drift velocity $u_{\|} := \langle u \rangle$ along the x- axis a certain distance Δx. The time required for the particle to arrive then is $t = \Delta x / u_{\|}$. On the way, the particle position also spreads in the y-direction. Due to the delay τ, the particle in the y-direction not only diffuses, but also acquires a drift velocity $u_{\perp}$. This drift velocity fluctuates with each step such that the motion of the particle during a single step can be described by the Langevin equation:

$$\begin{aligned} \partial x/\partial t &= u\cos(\theta) + \sqrt{2D}\,\xi_x(t) \ , \\ \partial y/\partial t &= u\sin(\theta) + \sqrt{2D}\,\xi_y(t) \ , \end{aligned}$$

where u denotes the magnitude of the thermophoretic velocity and ξ_x, ξ_y are stochastic variables with a delta-correlated Gaussian distribution and zero mean (Sec. 2.1.2). Assuming that the angle θ between the intended direction (x-direction) and the actual direction is normal distributed according to Eq. (4.34), we find that the first terms on the right-hand side of the Langevin equation obey:

$$\begin{aligned} u_{\|} &= \langle u\cos(\theta)\rangle = u\,\mathrm{e}^{-\sigma_\theta^2/2} \ , \\ u_{\perp} &= \langle u\sin(\theta)\rangle = 0 \ , \\ \langle u^2\cos^2(\theta)\rangle &= u^2\cosh(\sigma_\theta^2)\,\mathrm{e}^{-\sigma_\theta^2} \ , \\ \langle u^2\sin^2(\theta)\rangle &= u^2\sinh(\sigma_\theta^2)\,\mathrm{e}^{-\sigma_\theta^2} \ . \end{aligned}$$

First two moments of the coordinates $x(\tau) = x_0 + \int_0^\tau (u\cos(\theta) + \sqrt{2D}\,\xi(t))\,\mathrm{d}t$ and $y(\tau) = y_0 + \int_0^\tau (u\sin(\theta) + \sqrt{2D}\,\xi(t))\,\mathrm{d}t$ after one time step τ thus read:

$$\langle x\rangle - \langle x_0\rangle = u_{\|}\,\tau \ , \tag{4.36}$$

$$\langle y\rangle - \langle y_0\rangle = 0 \ , \tag{4.37}$$

$$\langle x^2\rangle - \langle x\rangle^2 = \sigma_{\|}^2 = \big(\cosh(\sigma_\theta^2) - 1\big)\,u_{\|}^2\tau^2 + 2D\tau \ , \tag{4.38}$$

$$\langle y^2\rangle - \langle y\rangle^2 = \sigma_{\perp}^2 = \sinh(\sigma_\theta^2)\,u_{\|}^2\tau^2 + 2D\tau \ . \tag{4.39}$$

Fig. 4.40b shows the parallel ($\sigma_{\perp}^2$) and perpendicular ($\sigma_{\perp}^2$) variances as functions of the average velocity in the direction of the propulsion $u_{\|}$ for different opening angles θ_{FWHM}. The experimental results are plotted as squares in Fig. 4.40b and are in good agreement with the predicted variances for an opening angle of $\theta_{\text{FWHM}} = 50°$, in agreement with the experimental value.

4.2.5.10 Video Files

The Supplementary Videos are available at https://www.doi.org/10.5281/zenodo.5831821.

Video 2.1: A symmetric swimmer driven between two target positions.

Video 2.2: A symmetric swimmer confined at a target position.

Video 2.3: Control of nine individual symmetric swimmers that are arranged on a grid and reconfigured to a circle.

4.3 Active Particle Feedback Control with a Single-Shot Detection Neural Network

4.3.1 Abstract

The real-time detection of objects in optical microscopy allows their direct manipulation, which has recently become a new tool for the control, for example, of active particles. For larger heterogeneous ensembles of particles, detection techniques are required that can localize and classify different objects with strongly inhomogeneous optical contrast at video rate, which is often difficult to achieve with conventional algorithmic approaches. We present a convolutional neural network single-shot detector which is suitable for real-time applications in optical microscopy. The network is capable of localizing and classifying multiple microscopic objects at up to 100 frames per second in images as large as 416 × 416 pixels, even at very low signal-to-noise ratios. The detection scheme can be easily adapted and extended to new particle classes and additional parameters as demonstrated for particle orientation. The developed framework is shown to control self-thermophoretic active particles in a heterogeneous ensemble selectively. Our approach will pave the way for new studies of collective behavior in active matter based on artificial interaction rules.

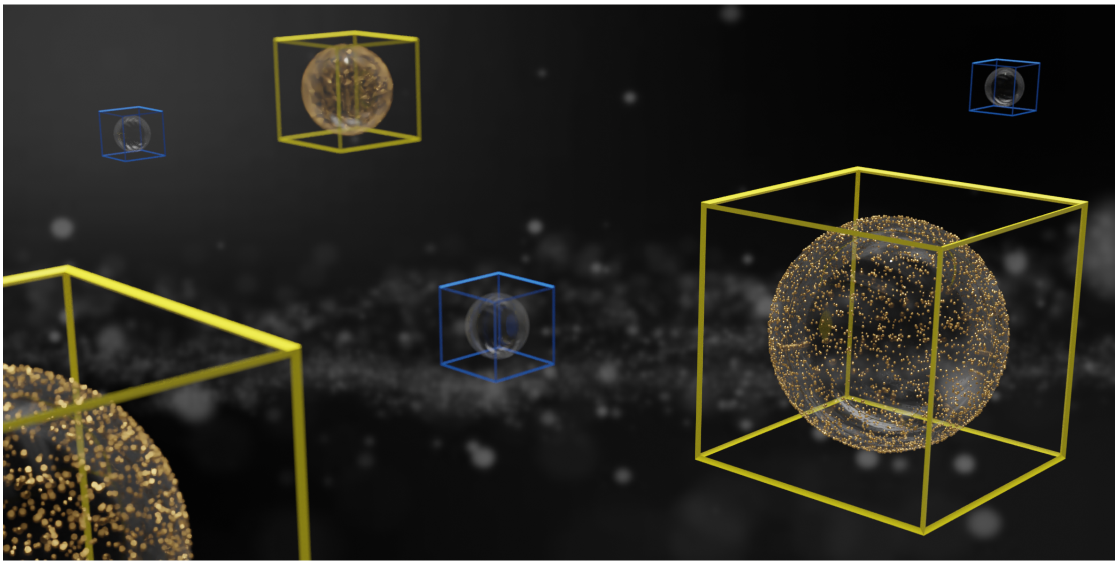

Illustration of the localization and classification of microscopic objects. Rendered using Blender 2.83 and the Cycles Renderer.

The section is based on the following article:

[P3] **M. Fränzl** and F. Cichos, Active Particle Feedback Control with a Single-Shot Detection Convolutional Neural Network, *Sci. Rep.* **10**, 12571 (2020)

The article has been adapted and revised. Details on the author contributions are provided in the “List of Publications” section.

4.3.2 Introduction

Optical microscopy can provide structural information but also allows us to follow dynamical processes from single molecules and nanoparticles to cells and organisms. Images with high spatial, temporal, and also spectral resolution may be obtained. Especially the ability to see dynamic processes opens the possibility to influence these processes in real-time via feedback control. In the field of single-molecule detection, this has been demonstrated with the electrokinetic[89] or the thermophoretic trap[8]. In both cases, the optical images are analyzed in real-time to extract particle or molecule positions to control electric or temperature fields for positioning purposes. Similarly, feedback control can explore new physics in optical tweezers[249] or control active particles by specific rules[10,11,85]. Such synthetic active particles mimic the active propulsion of biological species like bacteria or larger organisms[88]. While the biological species are able to exchange signals to form collective states like swarms or to break the action-reaction principle, their synthetic counterparts are still missing these features. Feedback control of active particles introduces the possibility to respond to external events or neighboring active particles by complex behavioral rules allowing a completely new approach to study the consequences of sensorial interactions in biological species. This field is of quickly growing interest[80,243,250] yet the control is still focused on active particles of the same size and shape due to the lack of more advanced real-time image processing algorithms. New algorithms which can localize and classify a large amount of active species of different size, shape and signal-to-noise ratio will pave the way to new studies. The main requirements for those new approaches are i) to be able to process images at video rate, ii) the ability to differentiate between multiple species, iii) to work at different optical contrasts and signal-to-noise ratios (SNR). These requirements are often met by algorithmic approaches using thresholding and centroid calculation or even more advanced versions. Yet, the more complex the image is, for example, having particles with different contrasts, the bigger is the computational effort that has to be spend at the cost of speed[97–99]. Recently, machine learning methods have been introduced to the field of optical microscopy and single-particle detection. Those methods are used for image segmentation, holographic reconstruction, and also particle tracking[100–105]. Methods for particle and object tracking currently employed in digital microscopy are based on convolutional neural networks designed for post-processing and are not optimized for a small latency. Their approach is limited by the fact that they often slide smaller regions of interest over a larger image to detect multiple objects of the same class. The network therefore has to be called multiple times per frame, which is time consuming. The detection of different object classes then even requires separate networks to be trained, which hampers their use for real-time detection considerably. Using neural networks which detect and classify objects in a single step would therefore be of considerable interest for the above mentioned feedback control applications.

We present a single-shot convolutional neural network enabling the detection and classification of objects in optical microscopy images in real-time. The network is employed in an optical microscopy setup for the manipulation of microparticles propelled by laser-induced self-thermophoresis. The actuation of these active particles is based on a feedback control of a steerable, focused laser beam and hence requires a detection of the positions of the particles as fast as possible. A single-shot neural network architecture[251,252] together with a GPU implementation in LabVIEW allows us to perform the particle localization and classification in real-time at a speed of up to 100 frames per second (fps) for 416 × 416 pixel sized images where the processing speed is not limited by the number of objects available in the image. With the help of this approach we are able to actuate active particles in mixed samples with passive particles and at very low SNRs previously not accessible by algorithmic approaches.

4.3.3 Results and Discussion

Network Structure, Training and Deployment The used single-shot detection (SSD) approach is based on the YOLO framework[251–253] where we adapted the TinyYOLOv2[252] network architecture. It uses 9 convolutional layers with a 3×3 kernel and 6 max-pooling layers with a 2×2 kernel (Fig. 4.52, Tab. 4.1) to simultaneously predict multiple bounding boxes and class probabilities for those boxes. The last convolutional layer has a 1×1 kernel and reduces the data to the output shape $13 \times 13 \times B \cdot (4 + 1 + C)$, where for each 13×13 grid cells B bounding boxes and C class probabilities are predicted.

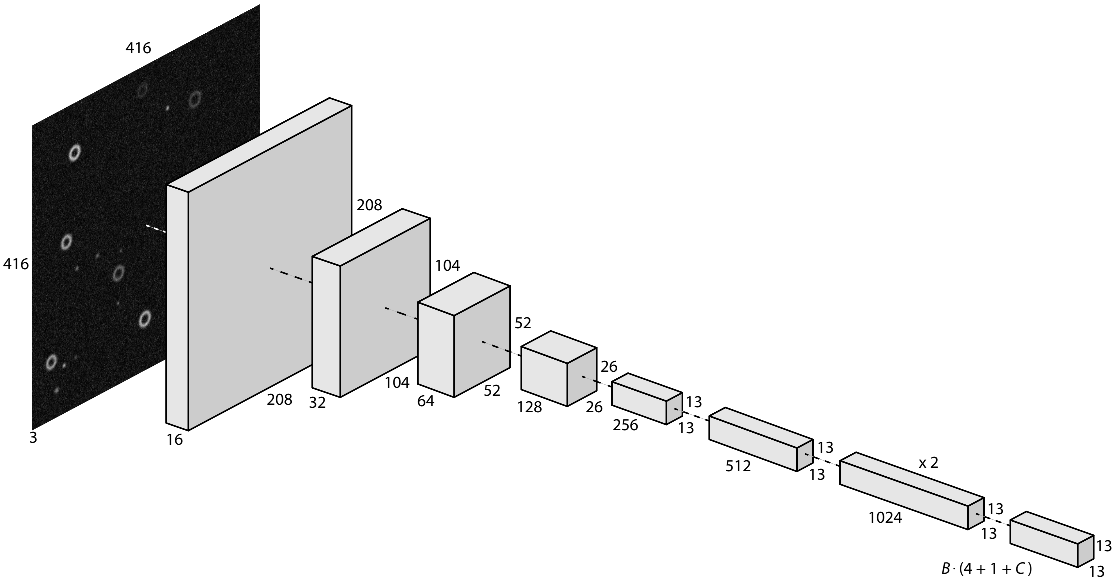

Fig. 4.52: Illustration of the TinyYOLOv2 architecture.

Tab. 4.1: TinyYOLOv2 architecture.

Type	Filters	Size/Stride	Output
Input			416×416
Conv.	16	$3 \times 3/1$	416×416
Maxpool		$2 \times 2/2$	208×208
Conv.	32	$3 \times 3/1$	208×208
Maxpool		$2 \times 2/2$	104×104
Conv.	64	$3 \times 3/1$	104×104
Maxpool		$2 \times 2/2$	52×52
Conv.	128	$3 \times 3/1$	52×52
Maxpool		$2 \times 2/2$	26×26
Conv.	256	$3 \times 3/1$	26×26
Maxpool		$2 \times 2/2$	13×13
Conv.	512	$3 \times 3/1$	13×13
Maxpool		$2 \times 2/1$	13×13
Conv.	1024	$3 \times 3/1$	13×13
Conv.	1024	$3 \times 3/1$	13×13
Conv.	$(4 + 1 + C) \cdot B$	$1 \times 1/1$	13×13
Output			

The input image is divided into 13 × 13 grid cells (Fig. 4.53a). For each grid cell the network predicts 5 bounding boxes. For each bounding box the position and size of an object as well as the confidence of detection and a probability for each class are predicted (Fig. 4.53b). Bounding boxes with confidence values above an object threshold are used for further evaluation (Fig. 4.53c). A non-maximum suppression (NMS) algorithm with a threshold value is used to remove overlapping bounding boxes that belong to the same object. The object class is assigned according to the maximum value of the predicted class probabilities. A more detailed description of the output decoding can be found in Sec. 4.3.5.1.

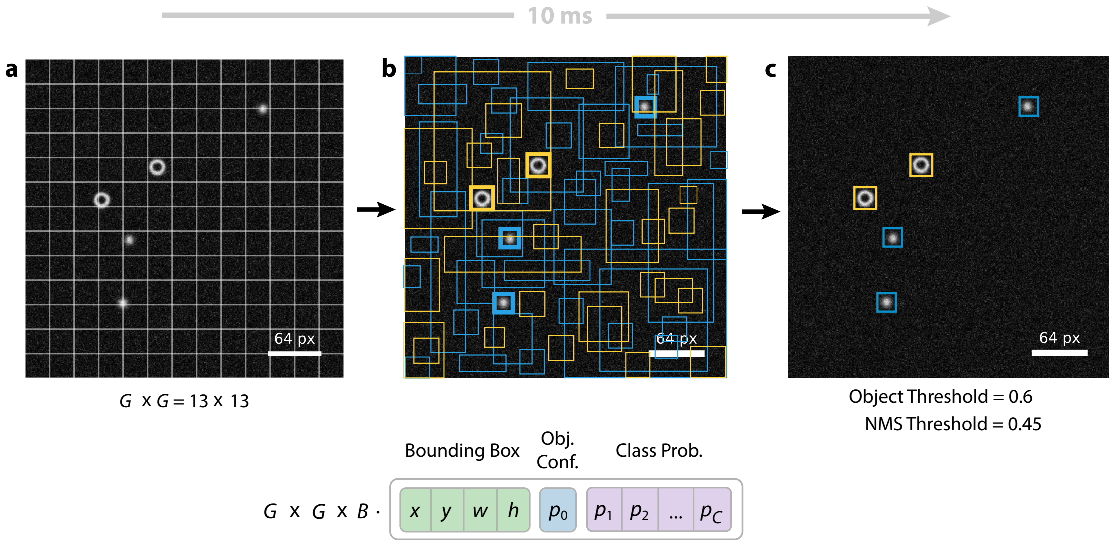

Fig. 4.53: **a**, The network takes an input RGB image of size 416 × 416 pixel and divides it into a $G \times G$ grid. Here, we used $G = 13$. **b**, For each grid cell it predicts B bounding boxes, confidence for those boxes and C class probabilities. Here, we used $B = 5$ and $C = 2$. These predictions are encoded in a $G \times G \times B \cdot (4+1+C)$ output tensor. The line thickness of the bounding boxes in (**b**) depicts the object confidence whereas the color of the bounding box is selected according to the highest class probability. **c**, Only bounding boxes with an object confidence larger than a certain object threshold are retained. A non-maximum suppression (NMS) algorithm and a NMS threshold value is used to remove overlapping bounding boxes that belong to the same object. Typical values are 0.6 and 0.45 for the object and NMS threshold, respectively.

The network is trained in Python/Keras using the TensorFlow backend[254–256] on a GeForce GTX 1660 Ti GPU without any pre-trained weights. The corresponding Python scripts for the training of the network and the generation of synthetic training data are supplied with Supplementary Information and explained in detail in Secs. 4.3.5.2 – 4.3.5.5. While the synthetic datasets used in this work resemble darkfield microscopy images of nano- and microparticles, Janus-type as well as rod-like and elliptical microparticles, any other training set may be used. Note that all images are assumed to be in focus without changing the contrast of diffraction patterns when defocusing. We train the network with a training set of 25000 images and a validation set of 5000 images for 10 epochs and a batch size of 8. The image generation takes about 30 min on an Intel Core i7 9700K 8 × 3.60 GHz CPU and the training process about 1 hour on a GeForce GTX 1660 Ti GPU.

The trained network graph is exported and deployed to a LabVIEW program developed in the lab which is controlling our microscopy setup. The LabVIEW implementation comprises dynamic link libraries (DLLs) written in C that take an RGB image as input and deliver the decoded output. To get the fastest possible image processing the DLLs are using the GPU supported TensorFlow C API. The details concerning the software can be found in Sec. 4.3.5.6. Using a GeForce GTX 1660 Ti GPU an inference time of about 10 ms is achieved for RGB images with a size of 416 × 416 pixels. This inference time might be further improved by employing a faster GPU or smaller input image sizes.

Evaluation of the Network Performance The performance of the network is evaluated for various synthetic datasets. We evaluate the accuracy of the position detection for single objects, close encounters, and the number of false/true positive and negative detections for multiple objects within an image. These parameters are evaluated for single and multiple class training data sets as a function of the SNR. The SNR of an image is defined as the ratio of the particles mean signal to the standard deviation of the signal. The details of the investigated datasets (Dataset 1–3) are provided in Sec. 4.3.5.5.

When trained with a single class dataset a root-mean-square error (RMSE) of the localization of about one pixel is obtained (Fig. 4.54a and Supplementary Fig. 4.76a). We achieve subpixel resolution using a class-dependent offset correction (see Sec. 4.3.5.7 for details). For increasing SNR, the error decreases and saturates at a constant value of about 0.5 pixel after offset correction. This is contrary to algorithmic approaches, where the RMSE scales with the inverse of the SNR[257]. Thus, algorithmic approaches will yield better accuracy for high SNR for single class detection but also a stronger dependence on the SNR. For low SNRs in the range of 1 to 10 our network compares well to the localization accuracy of advanced, algorithmic methods[257]. While recent machine learning approaches have shown even better performance in terms of the localization accuracy[103], their approach for multiple particle, multiple species detection is commonly more time consuming due to sliding window approaches, which require the network to be run multiple times for a single frame. This often precludes the application of these networks in situations where real-time information is required. For a two-class training dataset (Dataset 3), the RMSE slightly increases and saturates for high SNRs at about 1 pixel. For the identification of separate particles in close encounters Fig. 4.54b and Supplementary Fig. 4.76b illustrate that the predicted distance nicely reflects the true distance down to a value of 2σ. Here, 2σ is the size of the particle. Remarkably, for ring-shaped particles, it is even possible to detect overlapping particles (Supplementary Fig. 4.76b). Furthermore, it is shown that even when one particle is by a factor of 10 darker than the other, the network still detects the two particles with the same accuracy as for equal contrast (Fig. 4.54c and Supplementary Fig. 4.76c).

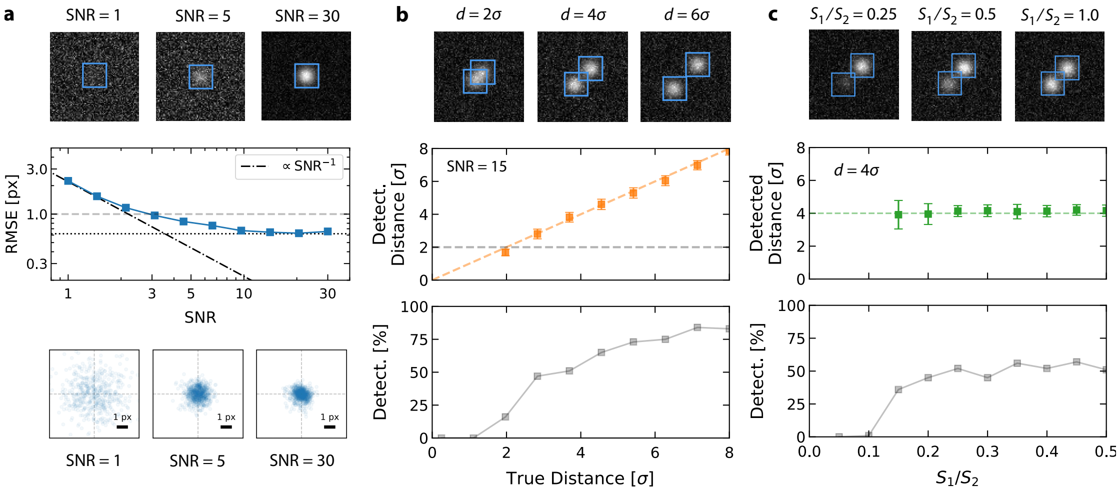

Fig. 4.54: Network performance for a single class training set (Dataset 1). **a**, The root mean-squared error (RMSE), that is, the root mean-squared distance between the true and the detected center position, as function of the SNR. Each SNR value was sampled with 1000 images containing one particle with randomized position. **b**, Detected distance as function of the true distance for SNR = 15. Each distance was sampled with 100 images containing two particles with randomized position and orientation. The error bars indicate the standard deviation of the predicted distances. The lower graph depicts the percentage of images where two particles have been detected. **c**, Predicted distance as function of the signal ratio averaged over 100 sample images containing two particles with randomized position and orientation. The error bars indicate the standard deviation of the predicted distances. The lower graph, again, depicts the percentage of images where two particles have been detected.

For more than two particles within an image, the detection performance is evaluated in terms of the percentage of true positive, false negative, and false positive detections (Fig. 4.55 and Supplementary Fig. 4.77). The number of true positive detections starts to drop at SNR < 3 at the cost of false negatives. At SNR $= 1$, about 50 % of the objects are still detected, while only about 1 % are detected false positive. This is remarkable since at a SNR level of 1 it is even difficult to identify objects by eye (see SNR $= 1$ in Fig. 4.54a). Notably, no classification errors have been observed when tested on synthetic images.

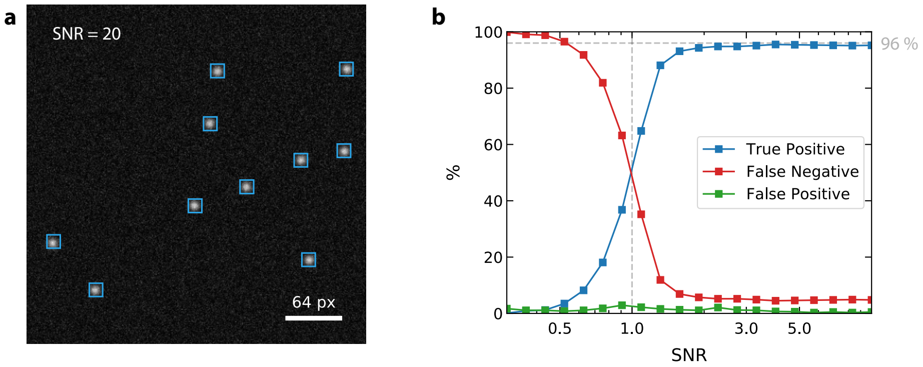

Fig. 4.55: **a**, Detection output for an image with 10 particles and SNR $=$ 20. **b**, Percentage of true positives (blue squares), false negative (red squares) and false positive (green squares) detection as function of the SNR. Each SNR value was a sample with 100 images containing 10 particles at randomized positions as plotted in (**a**). For all images the detection output was decoded with an object threshold of 0.6 and a NMS threshold of 0.45.

The number of classes to be localized and classified in an image can be easily extended to more than two classes (Supplementary Fig. 4.78). In principle, the network can be trained for several thousand object classes[252]. Situations with multiple classes are very challenging for conventional algorithmic localization and classification[91,92,94–99,257,258] even if the individual particles have a high SNR. As a demonstration, we have trained our network with a dataset containing five different particle classes: Spots, ring-shaped and Janus-type particles as well as rod-like and elliptical particles (Dataset 4). Fig. 4.56 illustrates the performance of the model. The different particle classes are accurately identified despite their different sizes, orientations, and intensities. Even rod-like particles are properly distinguished from elliptical particles. The latter two particles are very difficult to separate in algorithmic approaches. The proposed neural network-based detection technique will, therefore, be advantageous, especially in cases with multiple species and heterogeneous optical contrast.

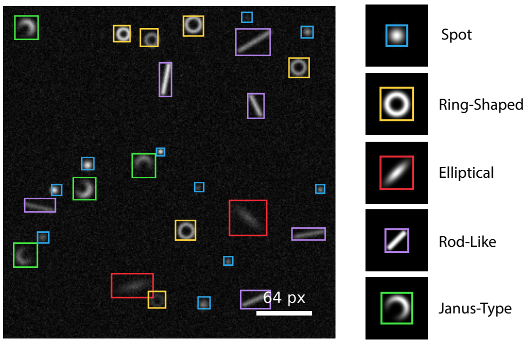

Fig. 4.56: Multiple training classes. Predicted locations, sizes and classes for a test image for a model trained with five different particle classes.

Experimental Feedback Control of Active Particles Considering the inference time of 10 ms and the localization RMSE of about 1 pixel as well as the independence of the processing speed on the number of particles in the image, the above-presented network is well suitable for real-time detection and feedback control of active particles. To demonstrate the capabilities of the network, we studied the feedback-controlled actuation of active particles introduced in Sec. 4.2. The experimental test should also verify the model that has been trained with synthetic data under real experimental conditions, which may differ from the ideal training situation (reality gap). The experimental setup and the sample preparation are similar to Sec. 4.2: We observe 2.2 µm diameter symmetric microswimmer particles and 0.5 µm diameter PS particles in a thin liquid film using a darkfield microscope (see Sec. 3.1 and Sec. 4.2.5.1 for details). In our experimental setup the swimmer particles appear with a ring-shaped intensity profile whereas the smaller PS particles have an approximately Gaussian intensity profile. To effectively control the microswimmers the laser focus needs to be placed with an offset δ from the particle center in real-time requiring the precise detection of the particle center with low latency (Fig. 4.57). Details on the self-propulsion mechanism and its dependence on the offset δ, the laser power and the feedback delay can be found in Sec. 4.2. Here, the detection of the particle center as well as their classification is achieved with the help of our neural network in contrast to the algorithmic approach used in Sec. 4.2.

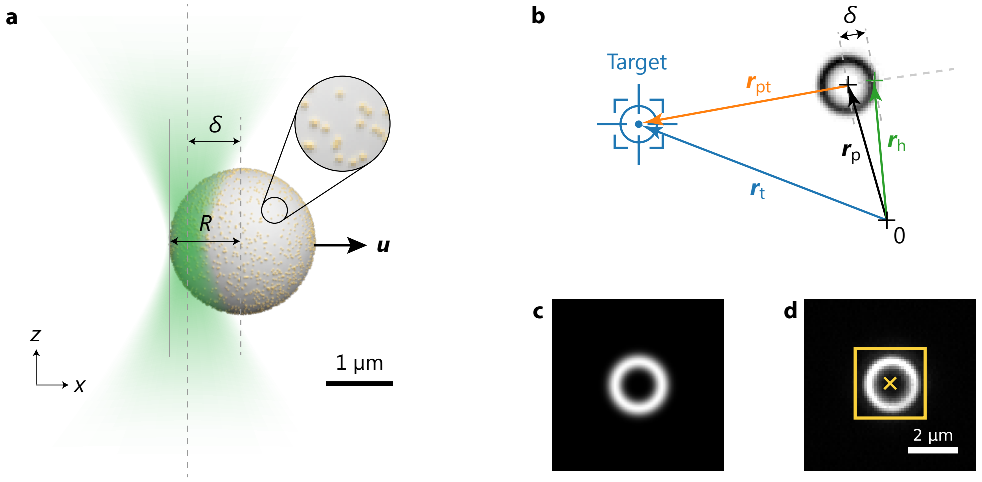

Fig. 4.57: **a**, Sketch of a symmetric microswimmer particle composed of a 2.2 µm diameter melamine formaldehyde (MF) particle (R = 1.1 µm) covered with 8 nm diameter gold nanoparticles with a surface coverage of about 10 %. When asymmetrically heated with a focused laser ($\lambda = 532$ nm) an inhomogeneous surface temperature is generated resulting in a self-thermophoretic motion away from the laser focus. **b**, To control the propulsion direction of the swimmer, the laser focus is placed with an offset δ from the particle center at $\boldsymbol{r}_\mathrm{h}$, opposite to the desired target location $\boldsymbol{r}_\mathrm{t}$. **c**, Synthetic darkfield image of a swimmer particle used to train our neural network. **d**, A swimmer particle as recorded in our experimental setup and detected by the trained neural network (Dataset 3).

For the experimental detection the network was trained with a two-class dataset: Gaussian spots, as observed for the 0.5 µm PS particles and ring-shaped intensity profiles as observed for the 2.2 µm particles. Different magnifications are taken into account by training the network for different scales, that is, different sizes of the two classes (Dataset 3). The camera was set to acquire images with a size of 512 × 512 pixels at an inverse frame rate of 40 ms (25 fps). To match the network input size the monochrome images from the camera are rescaled to 416 × 416 pixels and converted to grayscale RGB images. The inference of particle positions requires only about 10 ms. Additional 30 ms are needed for the processing of the particle positions and writing the uncompressed image data to disk.

We first evaluate the accuracy of the feedback control of a single active particle. Similar to Sec. 4.2 we extract the dependence of the particle velocity on the laser power by driving the particle between two target positions (Fig. 4.58a, Supplementary Video 3.1). We recover the non-linear scaling of the particle velocity with increasing laser power and find a maximum velocity of about $u_\mathrm{max} = 10\ \mu\mathrm{m\,s}^{-1}$ for an inverse framerate of $\tau = 40$ ms. Note, that the maximum velocity decreases exponentially with τ (see Fig. 4.36a, b for ref.) emphasizing the importance of our network's fast execution speed.

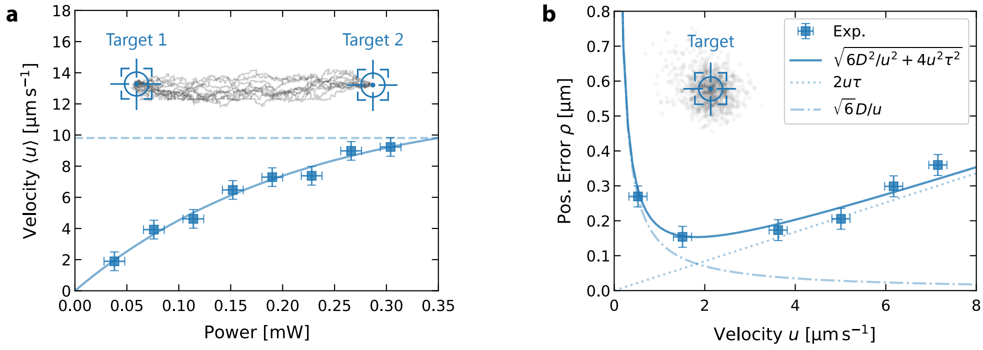

Fig. 4.58: **a**, The particle velocity derived from an experiment driving the particle between two target positions for an inverse frame rate of $\tau = 40$ ms (Supplementary Video 3.1). With increasing laser power the particle velocity saturates at about 10 µm s^{-1} (dashed curve). The solid curve corresponds to the numerical result according to Eq. (4.26). The inset shows the recorded trajectories for a power of 0.2 mW. **b**, The control accuracy as function of the laser power derived from an experiment confining a single particle for a certain time at a target position (Supplementary Video 3.2). The dashed and dotted curves are the contributions from the 2D sedimentation (dashed) and the particle overshooting (dotted). The sum of both contributions is represented by the solid curve. The left inset depicts the 2D position distribution for a power of 0.1 mW.

Similar to Sec. 4.2 we extract the dependence of the control accuracy on the heating power by confining a single particle for a certain time at target position (Fig. 4.58b, Supplementary Video 3.2). We characterize the confinement by the positioning error $\rho = \sqrt{\langle(\boldsymbol{r} - \boldsymbol{r}_\mathrm{t})^2\rangle}$, where $\boldsymbol{r}$ and $\boldsymbol{r}_\mathrm{t}$ are the coordinates of the particle and the target, respectively. As we have already seen in Sec. 4.2, Fig. 4.37a the positioning error has two regimes. (i) If the particle displacement during the inverse frame rate τ due to the self-thermophoretic propulsion is smaller than the displacement due to the diffusion, the positioning error is represented by a simple sedimentation model: The particle is radially driven towards the target with a velocity u against its diffusive motion with the diffusion coefficient D. In the steady state the characteristic length scale is $\rho_1 = \sqrt{6}D/u$ as indicated by the dashed curve in Fig. 4.58b. (ii) With increasing particle velocity the positioning error gets defined by an overshooting of the particle over the target position. This is due to the finite sampling of the particle position with the inverse frame rate τ. The overshooting distance is twice the distance traveled within the inverse frame rate $\rho_2 = 2u\tau$ and increases with increasing power as shown by the dotted curve in Fig. 4.58b. The sum of both contributions, $\rho = \sqrt{\rho_1^2 + \rho_2^2}$, is depicted as solid curve in Fig. 4.58b. The minimum in the positioning error is found as $\rho_\mathrm{min} = 140$ nm for $u_\mathrm{min} = 1.8$ µm s^{-1}. To achieve a control accuracy as high as possible the inverse frame rate τ needs to be as small as possible, again, highlighting the demand for fast image processing in active particle feedback control.

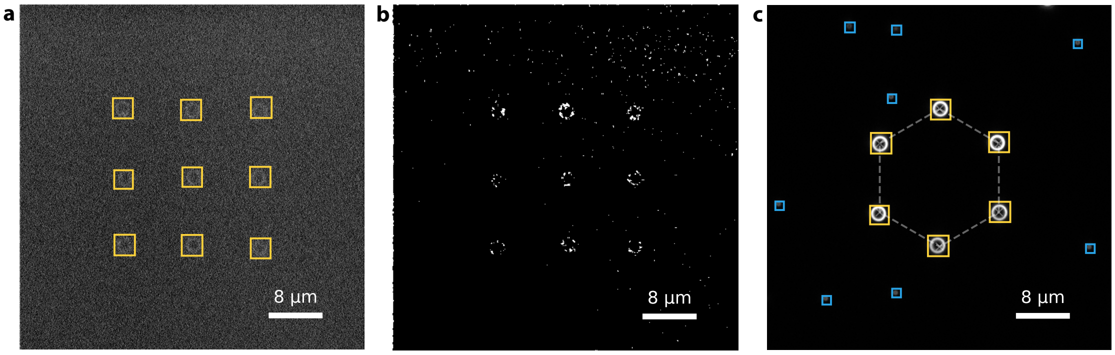

Fig. 4.59: **a**, Experimental feedback control of nine individual active particles in a grid pattern at low SNR (Supplementary Video 3.3). **b**, Threshold representation of the image shown in (**a**) pre-processed with a 3×3 median filter. **c**, Experimental feedback control of six individual active particles in a hexagonal pattern (Supplementary Video 3.4) surrounded by passive 0.5 µm diameter polystyrene particles.

To control multiple particles they are addressed by quickly multiplexing the laser focus with $\Delta t = 100$ µs between the different particle positions within the inverse frame rate time τ. Therefore, the incident laser power is available for a time τ/n to each of the n particles decreasing the average laser power per particle. Fig. 4.59a and Supplementary Video 3.4 demonstrate the control of nine individual active particles in a grid pattern at very low SNR. Initially, the particles were randomly distributed in the field of view. When the feedback control is enabled each particle is driven towards its nearest target and eventually confined there. As the resulting arrangement is constantly actuated the structure is dynamic as can be seen from Supplementary Video 3.4. The structure can be maintained even at very low SNR were a real-time detection of the particles with algorithmic approaches is already quite challenging. Fig. 4.59b shows a threshold representation of Fig. 4.59a, pre-processed with a 3 × 3 media filter for reference. Fig. 4.59c and Supplementary Video 4 demonstrate the control of six active particles (yellow boxes) with a background of passive PS particles (blue boxes). Here, in addition to Fig. 4.59a, a classification of the particles was required. Despite their lower intensity, the PS particles are still detected by the network and all particles are properly classified. Fig. 4.60 and Supplementary Video 3.5 demonstrate the dynamic arrangement of multiple active particles to the letters "OSA", once more, illustrating the networks's detection capabilities. Two additional control patterns are provided with Supplementary Video 3.6. Notably, for all experiments, the same trained network (Dataset 3) was used and no fine-tuning of any parameters was required.

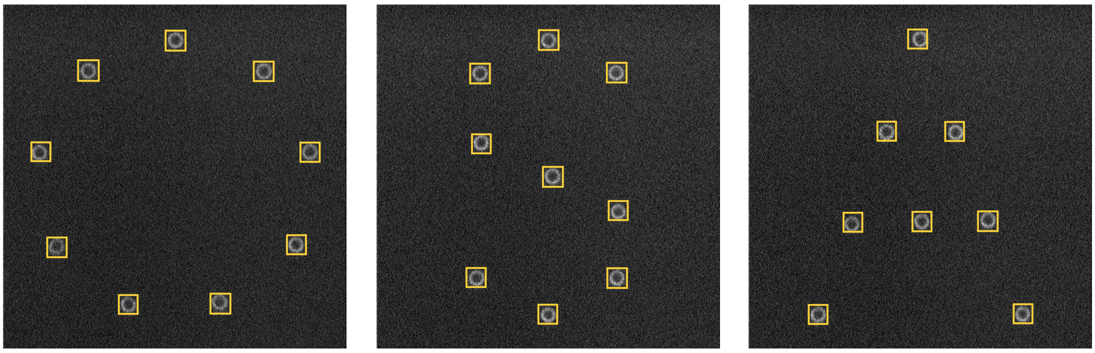

Fig. 4.60: Experimental feedback control of multiple active swimmers particle arranged to the letters "OSA" (Supplementary Video 3.5); a demonstration experiment prepared for a meeting of the Optical Society of America (OSA). The images show a field of view of 57 µm × 57 µm.

Extension to Additional Parameters – Orientation Detection While the discussion so far referred to particle positions and particle classes, one may extend the network also to include other parameters. The orientation of objects becomes particularly interesting when particles lack spherical symmetry or have anisotropic optical properties. As can be seen for the elliptical and rod-like particles in Fig. 4.56 the orientation of objects with a 180° rotational invariance can be partly retrieved from the aspect ratio of the detected bounding boxes. Nevertheless, this yields an ambiguity of 90° since one cannot distinguish between, for example, −45° and 45°. In the case of objects with no rotational invariance and a quadratic bounding box, an orientation detection via the aspect ratio of bounding boxes is not possible at all. This is the case for Janus particles[10,11,95]. Janus particles, when consisting of a hemispherical gold layer on top of a spherical polymer particle (Fig. 4.61a) result in a darkfield image as shown Fig. 4.61b. The image, therefore, allows for detection of the particle orientation but not from the bounding box. To allow also for the prediction of the orientation, the network needs to be modified and a new parameter, that is, an angle φ, needs to be introduced to the loss function and the annotation format (Sec. 4.3.5.10). Fig. 4.61c shows the detection output of the extended network trained for Janus type particles (Dataset 5). An experimental detection example is illustrated in Fig. 4.61b. An extension of the network to detect even more parameters such as the z-position of the particle or the out-of-plane rotation is easily possible emphasizing the flexibility of the network architecture[259,260]. A more detailed description of the extended network can be found in Sec. 4.3.5.10. The detection of multiple classes within the extended network is readily possible and illustrated in Fig. 4.61c for a network trained with Dataset 6.

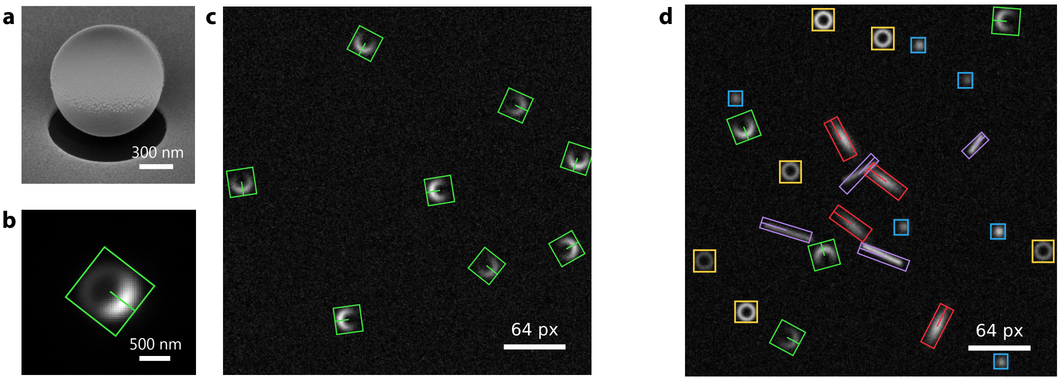

Fig. 4.61: **a**, A scanning electron microscopy (SEM) image of a Janus particle (gold-capped, 1 µm diameter polystyrene particle) taken from the Supplementary Information of Ref. 11. **b**, Darkfield image of a 1 µm diameter Janus particle with in-plane orientation. The green box depicts the detection of the extended network. **c**, A synthetic sample image with multiple Janus-type particles overlayed with the location and orientation detection by the extended network (green boxes). **d**, Detection example for the extended network trained with five particle classes (Dataset 6).

4.3.4 Conclusion

In summary, we have shown that the adaption of a single-shot convolutional neural network allows us to localize and classify objects in optical microscopy images with an inference time of about 10 ms. The speed of the classification and localization is independent of the number of particles and the complexity of the image. While algorithmic approaches will be faster and more accurate for simple images and particle shapes including one species and high signal-to-noise ratio (SNR > 10), our method is suitable for multiple species detection with large signal-to-noise variations in the image. We analyzed the network performance with synthetic images and demonstrated its experimental application to feedback actuated self-thermophoretic active particles while tracking individual gold nanoparticles in the background. Feedback controlled active particle systems deliver a unique possibility to create artificial interactions between synthetic active particles to mimic sensorial interactions in living species which break the action reaction principle in physics. Using this approach we envision further applications in the control of active matter and a combination with other machine learning techniques, for example, reinforcement learning for adaptive control and particle navigation[261]. The real-time localization and classification capability of the network presented here is an important step towards active particle systems that are fully self-regulated by machine learning techniques, where the feedback control and image detection are interconnected. Autonomous systems have the potential to explore new emergent phenomena in heterogeneous active particle ensembles and might be even employed to discover spatial and temporal feedback policies that also drive group formation in living matter. Furthermore, our work has the potential to control processes in even more challenging imaging situations such as in biological species. The source code and scripts of our framework are open source and can be easily adapted and extended for these applications.

4.3.5 Supplementary Information

4.3.5.1 Output Decoding

The network takes an input RGB image of the size 416×416 pixels and divides that input image into 13×13 grid cells (Fig. 4.53a). For each grid cell it predicts B bounding boxes and for each bounding box an object confidence as well as probabilities for each of the C classes. The output is encoded in a $13 \times 13 \times B \cdot (4 + 1 + C)$ tensor. Since there are $13 \times 13 = 169$ grid cells, for $B = 5$, the network predicts $169 \cdot 5 = 845$ bounding boxes at once (Fig. 4.53b). For $C = 2$ classes each bounding box is then described by $4 + 1 + C = 7$ data elements (Fig. 4.62a).

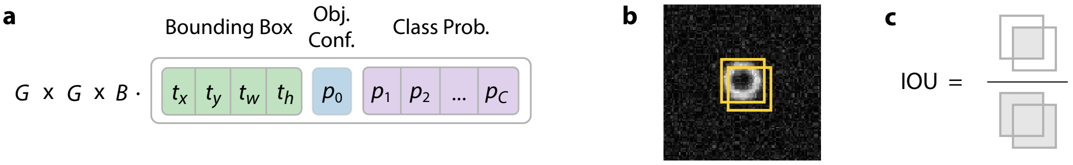

Fig. 4.62: a, The output shape of the YOLOv2 network. **b**, Example of duplicate bounding boxes before the non-maximum suppression (NMS). **c**, The intersection over union (IOU) of the two bounding boxes.

YOLOv2 predicts the coordinates of the bounding boxes relative to the location of the grid cell using anchor boxes. This bounds the ground truth to fall between 0 and 1. If the location of the grid cell is c_x, c_y and the relative width and height of the anchor box are b_w, b_h, the predictions t_x, t_y, t_w, t_h correspond to:

$$\begin{aligned} x &= \sigma(t_x) + c_x \ , \\ y &= \sigma(t_y) + c_y \ , \\ w &= b_w \, \mathrm{e}^{t_w} \ , \\ h &= b_h \, \mathrm{e}^{t_h} \ , \end{aligned}$$

where $\sigma(t) = (1 + \mathrm{e}^{-t})^{-1}$ is the logistic activation function, x, y the center location and w, h the width and height of the bounding box relative to the input image size. The network does not predict the bounding boxes directly. Instead it predicts probabilities and adjustments for a set of anchor boxes. The object confidence p_0 for the bounding box is the probability that the bounding box contains an object whereas $p_1, p_2, \ldots, p_C$ are the probabilities that the object belongs to a certain class. From the 845 predicted bounding boxes most will have a very low object confidence, so we only keep the boxes whose object confidence is larger than a certain object threshold (Fig. 4.53c). There still may be boxes remaining that largely overlap with each other but belong to the same object (Fig. 4.62b). To remove these duplicate bounding boxes a non-maximum suppression (NMS) algorithm is applied. The algorithm selects the bounding box with the highest confidence and removes any bounding boxes with an intersection over union (Fig. 4.62c) larger than a given NMS threshold. Finally, the class of the bounding box is assigned according to the highest class probability.

4.3.5.2 Neural Network Training

The network is trained using a sum-squared error between the predictions and the ground truth to calculate the loss (Sec. 4.3.5.3). We trained the network with synthetic images (Sec. 4.3.5.4) with a size of 416×416 pixels . Whereas we trained the network with grayscale images, it is also possible to train the network with colored images. For each image the ground truth for the bounding boxes and the classes are stored in an associated XML file in the Pascal VOC format. A dataset comprises a set of training images, a set of validation images and a set of test images. Typically, the size of the validation set is 20 % of the size of the training set. We trained the network without pre-trained weights for 10 epochs and batch sizes of 8. For details on the implementation in Python/Keras see Sec. 4.3.5.6.

4.3.5.3 Loss Function

The following section presents a discussion of the loss function mainly reproduced from Ref. 262. YOLOv2 uses the following sum-squared error (SSE) for the loss function:

$$\begin{aligned}\text{Loss} \;=\; & \lambda_{\text{loc}} \sum_{i=0}^{G^2} \sum_{j=0}^{B} 1_{ij}^{\text{obj}} \left(\left(x_i - \hat{x}_i\right)^2 + \left(y_i - \hat{y}_i\right)^2 \right) \\ & + \lambda_{\text{loc}} \sum_{i=0}^{G^2} \sum_{j=0}^{B} 1_{ij}^{\text{obj}} \left(\left((w_i)^{\frac{1}{2}} - (\hat{w}_i)^{\frac{1}{2}}\right)^2 + \left((h_i)^{\frac{1}{2}} - (\hat{h}_i)^{\frac{1}{2}}\right)^2 \right) \\ & + \lambda_{\text{obj}} \sum_{i=0}^{G^2} \sum_{j=0}^{B} 1_{ij}^{\text{obj}} \left(C_i - \hat{C}_i \right)^2 \\ & + \lambda_{\text{no obj}} \sum_{i=0}^{G^2} \sum_{j=0}^{B} 1_{ij}^{\text{no obj}} \left(C_i - \hat{C}_i \right)^2 \\ & + \lambda_{\text{class}} \sum_{i=0}^{G^2} \sum_{j=0}^{B} 1_{i}^{\text{obj}} \sum_{c \,\in\, \text{classes}} \left(p_i(c) - \hat{p}_i(c) \right)^2 . \end{aligned} \tag{4.40}$$

The first two terms represent the localization loss, terms 3 and 4 the confidence loss and the last term the classification loss.

General Remarks

(a) The loss function penalizes classification errors only if an object is present in that grid cell.

(b) Since there are $B = 5$ bounding boxes for each cell we need to choose one of them for the loss. This will be the box with the highest IOU with the ground truth box so the loss will penalize the localization loss if that box is responsible for the ground truth box.

(c) The sum-squared error weights localization errors equally with classification errors.

1st Term

$$\lambda_{\text{loc}} \sum_{i=0}^{G^2} \sum_{j=0}^{B} 1_{ij}^{\text{obj}} \left(\left(x_i - \hat{x}_i\right)^2 + \left(y_i - \hat{y}_i\right)^2 \right)$$

SSE between the predicted box location (x, y) and the ground truth location $(\hat{x}, \hat{y})$. We sum over all 13×13 grid cells ($G = 13$) and for each grid cell we sum over all 5 boxes ($B = 5$). To comply with (a) and (b) a binary variable 1_{ij}^{obj} is used so that $1_{ij}^{\text{obj}} = 1$ if box j in grid i contains an object and box j is responsible for detecting that object, otherwise 0 (The box is responsible for detecting an object if it has the highest IOU with the ground truth box between the B boxes). As mentioned in (c) the SSE weights localization errors equally with classification errors. To give the localization error a higher weight in the loss function the parameter $\lambda_{\text{loc}} = 5$ is used.

2nd Term

$$\lambda_{\text{loc}} \sum_{i=0}^{G^2} \sum_{j=0}^{B} 1_{ij}^{\text{obj}} \left(\left((w_i)^{\frac{1}{2}} - (\hat{w}_i)^{\frac{1}{2}}\right)^2 + \left((h_i)^{\frac{1}{2}} - (\hat{h}_i)^{\frac{1}{2}}\right)^2 \right)$$

The 2nd term is similar to the 1st term, but calculates the SSE in the box dimensions. To reflect that small deviations in large boxes matter less than in small boxes, YOLO uses the square root of w and h. Otherwise the SSE would weight errors in large boxes and small boxes equally.

3rd Term

$$\lambda_{\text{obj}} \sum_{i=0}^{G^2} \sum_{j=0}^{B} 1_{ij}^{\text{obj}} \left(C_i - \hat{C}_i\right)^2$$

This is the confidence error where $0 \leq C \leq 1$ and $\hat{C} = 1$.

4th Term

$$\lambda_{\text{no obj}} \sum_{i=0}^{G^2} \sum_{j=0}^{B} 1_{ij}^{\text{no obj}} \left(C_i - \hat{C}_i\right)^2$$

If there is no object in the grid we only need to take care about the confidence C (The confidence needs to be zero when there is no object). The variable $1_{ij}^{\text{no obj}} = 1$ if box j in grid i contains no object or box j is not responsible for detecting that object, otherwise 0. Since many grid cells do not contain any object, this pushes the confidence scores of those cells quickly towards zero This can lead the training to diverge early. To attenuate the decrease of the loss from confidence predictions of boxes that do not contain objects, the parameter $\lambda_{\text{no obj}} = 0.5$ is used.

5th Term

$$\lambda_{\text{class}} \sum_{i=0}^{G^2} \sum_{j=0}^{B} 1_{i}^{\text{obj}} \sum_{c \in \text{classes}} \left(p_i(c) - \hat{p}_i(c)\right)^2$$

Here, the errors for all class probabilities in the 13×13 grid cells are summed.

4.3.5.4 Synthetic Image Generation

Here we list the generation functions used to simulate the darkfield images of nano- and microparticles, Janus-type as well as rod-like and elliptical microparticles. Note that all images are assumed to be in focus.

Spots

Function used to generate a Gaussian intensity distribution:

$$I(x, y, \{x_0, y_0; \sigma\}) = I_0 \exp\left(-\frac{(x - x_0)^2 + (y - y_0)^2}{2\sigma^2}\right). \tag{4.41}$$

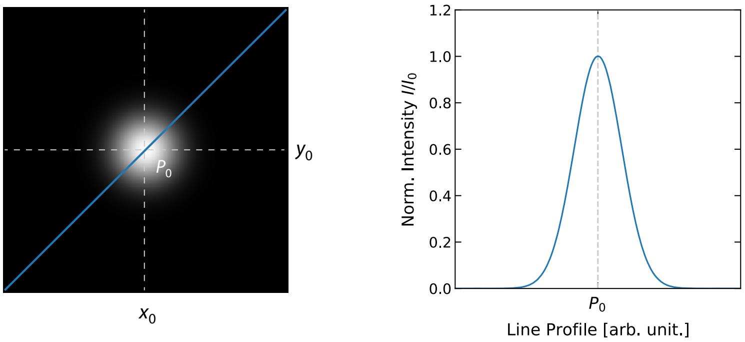

Fig. 4.63: Example of an intensity distribution generated with Eq. (4.41).

Ring-Shaped

Function used to generate a ring-shaped intensity distribution:

$$I(x, y, \{x_0, y_0; \sigma, R\}) = I_0 \exp\left(-\frac{\left(\sqrt{(x-x_0)^2+(y-y_0)^2}-R\right)^2}{2\sigma^2}\right). \tag{4.42}$$

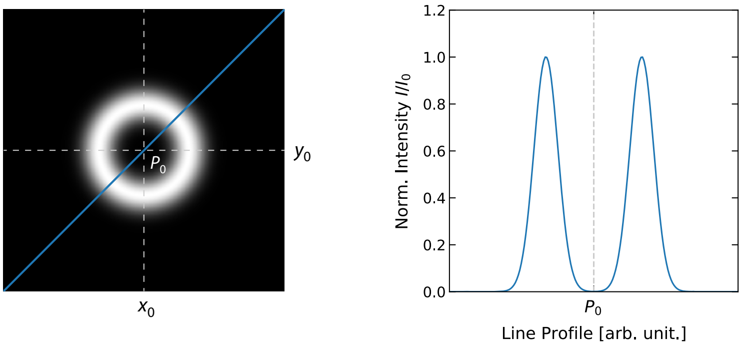

Fig. 4.64: Example of a ring-shaped intensity distribution generated with Eq. (4.42).

Janus-Type

Function used to generate a Janus-type intensity distribution:

$$I(x, y, \{x_0, y_0, \varphi; \sigma, R\}) = I_0 \cos^2(\alpha) \exp\left(-\frac{\left(\sqrt{(x-x_0)^2+(y-y_0)^2}-R\right)^2}{2\sigma^2}\right). \tag{4.43}$$

Here, α is given as:

$$\alpha = \frac{1}{2} \arccos\left(\frac{(x'-x_0)}{\sqrt{(x'-x_0)^2-(y'-y_0)^2}}\right),$$

where x' and y' are coordinates in the reference frame of the particle center:

$$x' = (x-x_0)\,\cos(\varphi) - (y-y_0)\,\sin(\varphi)\;,$$
$$y' = (x-x_0)\,\sin(\varphi) + (y-y_0)\,\cos(\varphi)\;.$$

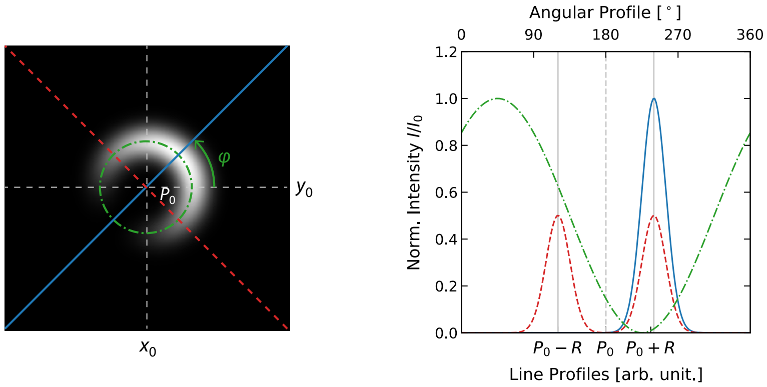

Fig. 4.65: Example of a Janus-type intensity distribution generated with Eq. (4.43).

Ellipse

Function used to generate an elliptical, two-dimensional Gaussian intensity distribution:

$$I(x, y, \{x_0, y_0, \varphi; \sigma_x, \sigma_y\}) = I_0 \exp\left(-(a(x-x_0)^2 + 2b(x-x_0)(y-y_0) + c(y-y_0)^2)\right) \ , \tag{4.44}$$

where a, b and c are given in terms of the orientation angle θ:

$$a = \frac{\cos(\varphi)^2}{2\sigma_x^2} + \frac{\sin(\varphi)^2}{2\sigma_y^2} \ , \quad b = -\frac{\sin(2\varphi)}{4\sigma_x^2} + \frac{\sin(2\varphi)}{4\sigma_y^2} \ , \quad c = \frac{\sin(\varphi)2}{2\sigma_x^2} + \frac{\cos(\varphi)^2}{2\sigma_y^2} \ .$$

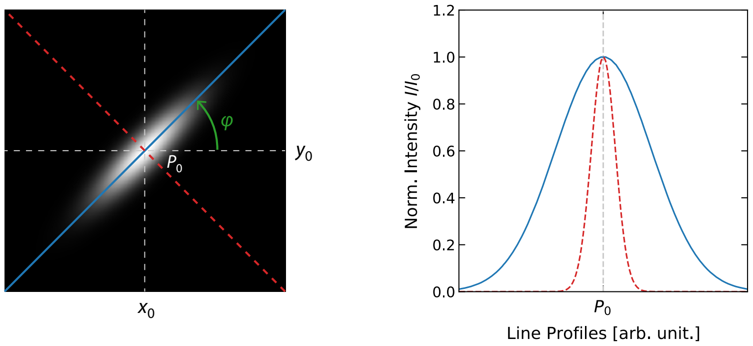

Fig. 4.66: Example of an elliptical intensity distribution generated with Eq. (4.44).

Rod-Like

Function used to generate a rod-like intensity distribution:

$$I(x, y, \{x_0, y_0, \varphi; \ell, w, \sigma\}) = I_0 \left\{\Pi(x_0, y_0, \varphi; \ell, w) * g(\sigma)\right\}(x, y) \ . \tag{4.45}$$

Here, $*$ denotes the convolution of a two-dimensional, rectangular function Π with a Gaussian function g, where ℓ, w are the length and width of the rectangle and σ^2 the variance of the Gaussian function.

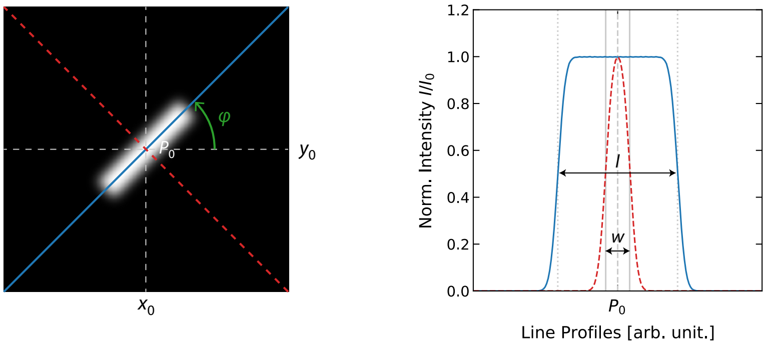

Fig. 4.67: Example of a rod-like intensity distribution generated with Eq. (4.45).

4.3.5.5 Datasets

This section gives an overview of the investigated synthetic datasets and the parameters used for their generation. Here, $[a \dots b]$ denotes a uniform distribution of random samples between a and b. The SNR of an image is defined as the ratio of the average signal value to the standard deviation of the signal.

Dataset 1

Dataset 1 comprises 25000 images for training and 5000 images for validation. The SNR of the images is randomly distributed with SNR $= [1 \dots 30]$.

Tab. 4.2: Parameters for Dataset 1.

Particle Type	Eq.	Parameters	# Particles
Spots	(4.41)	$I_0 = [0.1 \dots 1]$ $\sigma = 3$	$N_1 = [1 \dots 20]$

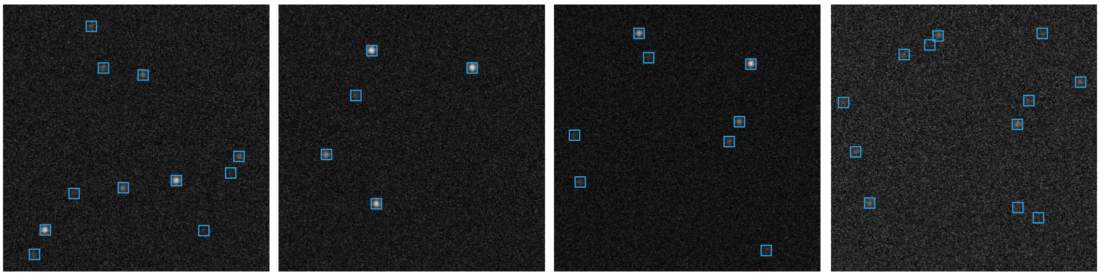

Fig. 4.68: Sample images from Dataset 1.

Dataset 2

Dataset 2 comprises 25000 images for training and 5000 images for validation. The SNR of the images is randomly distributed with SNR $= [1 \dots 30]$.

Tab. 4.3: Parameters for Dataset 2.

Particle Type	Eq.	Parameters	# Particles
Ring-Shaped	(4.42)	$I_0 = [0.1 \dots 1]$ $R = 8$ $\sigma = 4$	$N_2 = [1 \dots 10]$

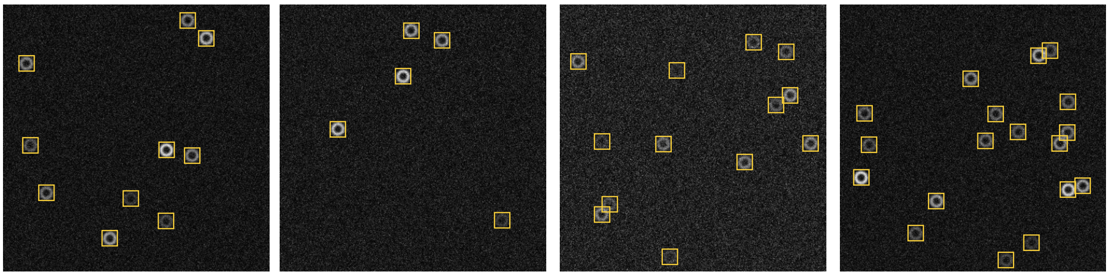

Fig. 4.69: Sample images from Dataset 2.

Dataset 3

Dataset 3 comprises 25000 images for training and 5000 images for validation. The SNR of the images is randomly distributed with SNR $= [1 \dots 30]$.

Tab. 4.4: Parameters for Dataset 3.

Particle Type	**Eq.**	**Parameters**	**# Particles**
Spot	(4.41)	$I_0 = [0.1, \dots 1]$ $\sigma = [2 \dots 4]$	$N_1 = [1 \dots 20]$
Ring-Shaped	(4.42)	$I_0 = [0.1 \dots 1]$ $R = [6 \dots 10]$ $\sigma = 4$	$N_2 = [1 \dots 10]$

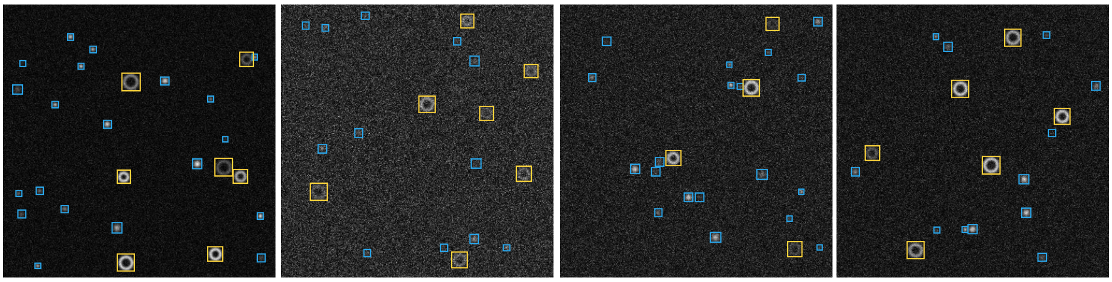

Fig. 4.70: Sample images from Dataset 3.

Dataset 4

Dataset 4 comprises 125000 images for training and 25000 images for validation. The SNR of the images is randomly distributed with SNR $= [1 \dots 30]$.

Tab. 4.5: Parameters for Dataset 4.

Particle Type	**Eq.**	**Parameters**	**# Particles**
Spot	(4.41)	$I_0 = [0.1, \dots 1]$ $\sigma = [2 \dots 4]$	$N_1 = [5 \dots 15]$
Ring-Shaped	(4.42)	$I_0 = [0.1 \dots 1]$ $R = [6 \dots 10]$ $\sigma = 2$	$N_2 = [1 \dots 5]$
Janus-Type	(4.43)	$I_0 = [0.1 \dots 1]$ $R = 8$ $\sigma = 3$	$N_3 = [1 \dots 5]$
Ellipses	(4.44)	$I_0 = [0.1 \dots 1]$ $\sigma_x = 4$ $\sigma_y = 12$	$N_4 = [1 \dots 5]$
Rods	(4.45)	$I_0 = [0.1 \dots 1]$ $w = 3$ $\ell = [15 \dots 30]$ $\sigma = 2$	$N_5 = [1 \dots 5]$

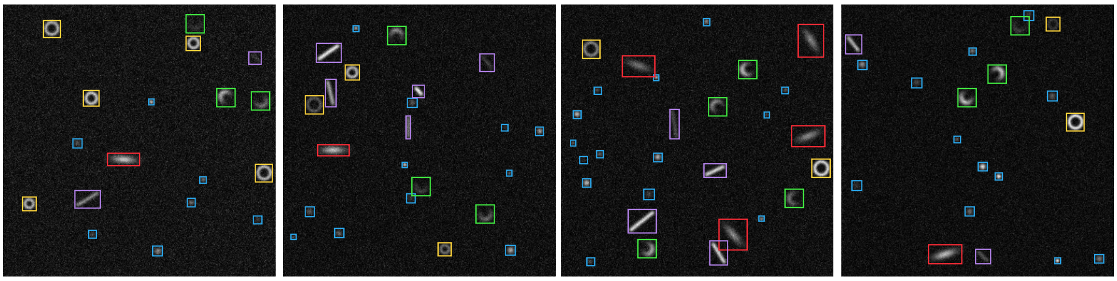

Fig. 4.71: Sample images from Dataset 4.

Dataset 5

Dataset 5 comprises 25000 images for training and 5000 images for validation. The SNR of the images is randomly distributed with SNR = $[1 \dots 30]$.

Tab. 4.6: Parameters for Dataset 5.

Particle Type	Eq.	Parameters	# Particles
Janus-Type	(4.43)	$I_0 = [0.1 \dots 1]$ $R = 8$ $\sigma = 3$	$N_3 = [1 \dots 10]$

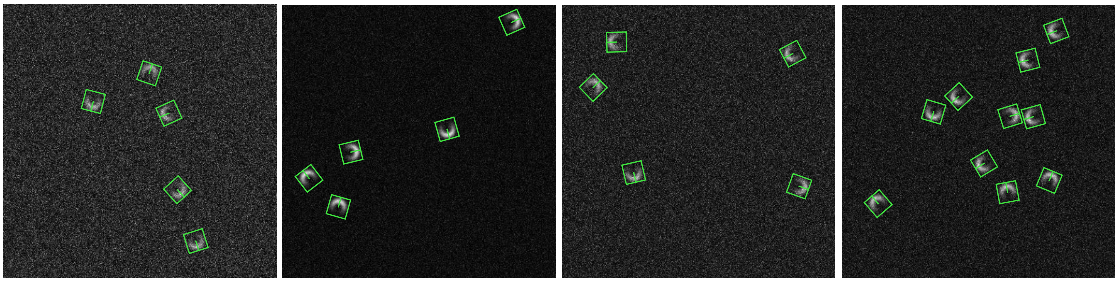

Fig. 4.72: Sample images from Dataset 5.

Dataset 6

Dataset 6 comprises 125000 images for training and 25000 images for validation. The SNR of the images is randomly distributed with SNR = $[1 \dots 30]$. Parameters are the same as in Dataset 4.

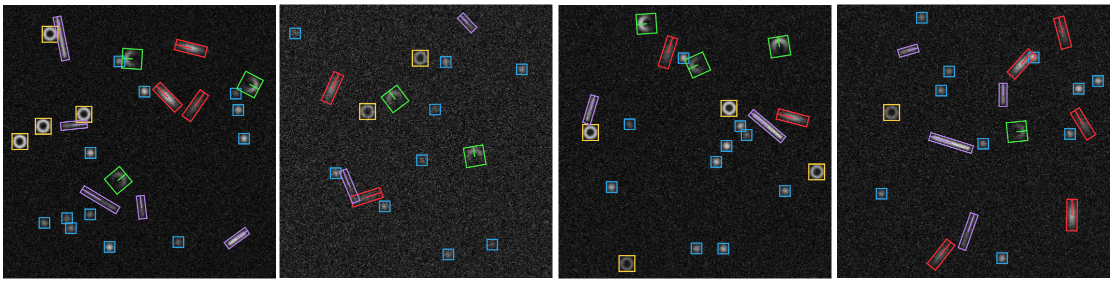

Fig. 4.73: Sample images from Dataset 6.

4.3.5.6 Software Framework (YOLOTrack)

The network is trained and evaluated in Python/Keras using the TensorFlow backend[254–256]. For real-time inference the model graph is exported as protocol buffer file (`*.pb`) and parameters required to decode the YOLOTrack output are exported to a configuration file (`*.ini`). These files are imported by the C based dynamic link libraries `TF.dll`, `YOLOTrack10.dll` that are easily integrable in other programming languages such as LabVIEW and C++. Fig. 4.74 shows the structure of the software framework.

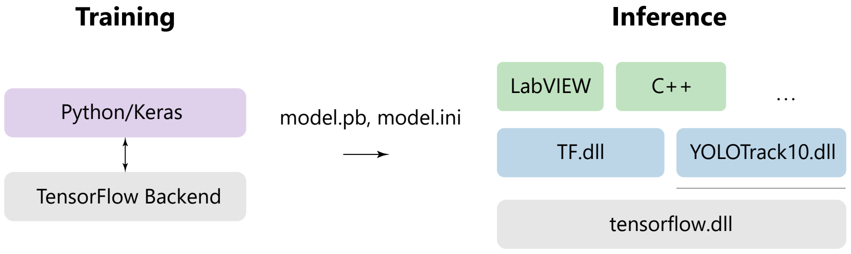

Fig. 4.74: Structure of the developed framework used for training and GPU supported real-time detection.

The `TF.dll` is a general TensorFlow library for model inference build on top of the TensorFlow C API (`tensorflow.dll`). It can be used with any TensorFlow model and is not specific to YOLOTrack. The `YOLOTrack10.dll` adds specific functions required to decode the YOLOTrack output and does not depend on the TensorFlow C API. The source code as well as a detailed documentation is available at https://github.com/molecular-nanophotonics.

4.3.5.7 Offset Correction

The trained network can have a sub-pixel localization offset. However, once trained the offset vector is constant and can be corrected by subtraction (Fig. 4.75). The offset vector is independent of the SNR but depends on the object class. In general, a correction is only required when seeking for sub-pixel resolution.

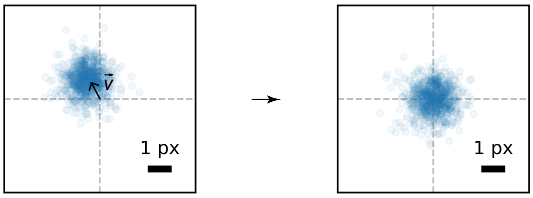

Fig. 4.75: Example for the correction of an offset vector $\boldsymbol{v}$.

To correct the offset for a specific class, the error/offset from the ground truth is sampled with 1000 synthetic images containing only one object of that class at randomized positions. The offset vector is then calculated from the mean of the offset distribution. The offset correction has to be done for every model and individually for all object classes.

4.3.5.8 Detection Performance: Single Class, Ring-Shaped

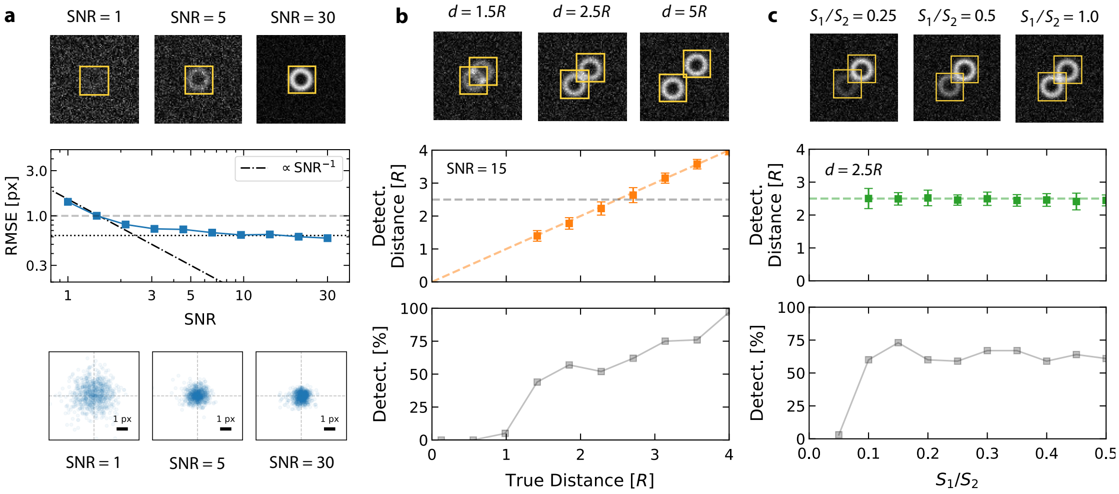

Fig. 4.76: Detection performance for Dataset 2. **a**, The root mean-squared error (RMSE), that is, the root mean-squared distance between the true and the detected center position, as function of the signal-to-noise ratio (SNR). Each SNR value was sampled with 1000 images containing one particle with randomized position. **b**, Detected distance as function of the true distance for SNR = 15. Each distance was sampled with 100 images containing two particles with randomized position and orientation. The error bars indicate the standard deviation of the predicted distances. The lower graph shows the percentage of images where two particles have been detected. **c**, Predicted distance as function of the intensity ratio averaged over 100 sample images containing two particles with randomized position and orientation. The error bars indicate the standard deviation of the predicted distances. The lower graph shows the percentage of images where two particles have been detected.

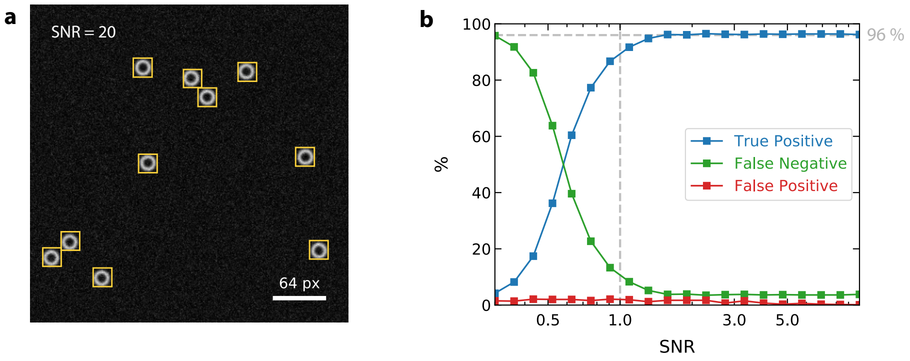

Fig. 4.77: Detection performance for Dataset 2. **a**, Detection output for an image with 10 ring-shaped particles for SNR = 20. **b**, Percentage of true positives (blue squares), false negative (green squares) and false positive (red squares) detection as function of the SNR. Each SNR value was sampled with 100 images containing 10 particles at randomized positions as shown in (**a**). For all images the detection output was decoded with an object threshold of 0.6 and a NMS threshold of 0.45

4.3.5.9 Detection Performance: Two Classes, Spots + Ring-Shaped

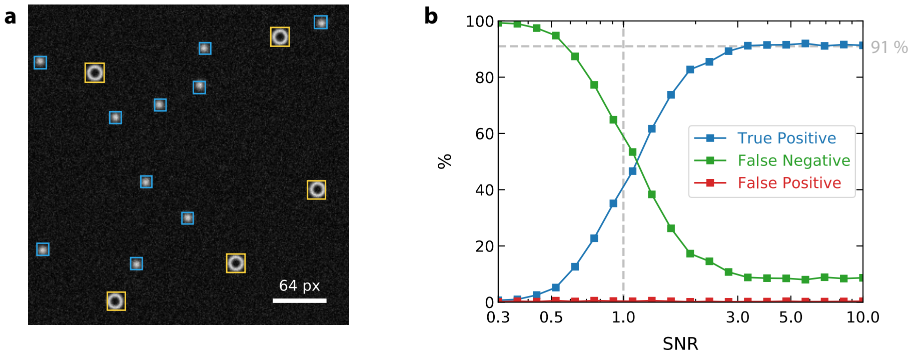

Fig. 4.78: Detection performance for Dataset 3. **a**, Detection output for an image with 10 spot and 5 ring-shaped particles for SNR = 20. **b**, Percentage of true positives (blue squares), false negative (green squares) and false positive (red squares) detection as function of the SNR. Each SNR value was sampled with 100 images containing 10 spot and 5 ring-shaped particles at randomized positions as shown in (**a**). For all images the detection output was decoded with an object threshold of 0.6 and a NMS threshold of 0.45.

4.3.5.10 Extension for Orientation Detection

To allow for an orientation detection the network needs to be modified. We normalized the 360° range of possible orientations to a range from 0 to 1 and adapted YOLOTrack 1.0 to directly predict the orientation of the bounding box via a single regression number φ (Fig. 4.79).

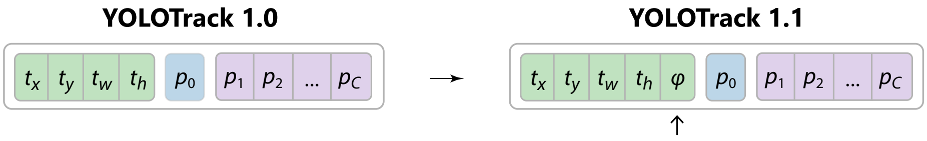

Fig. 4.79: The output shape of YOLOTrack 1.0 vs. YOLOTrack 1.1.

In the loss function the mean squared error between the ground truth $\hat{\varphi}_i$ and the predicted angle φ_i was added:

$$\lambda_\varphi \sum_{i=0}^{G^2} \sum_{j=0}^{B} 1_{ij}^{\text{obj}} \left(\varphi_i - \hat{\varphi}_i\right)^2 \; .$$

The output is bound between 0 and 1 using the logistic activation function $\sigma(t) = (1 + \mathrm{e}^{-t})^{-1}$.

4.3.5.11 Video Files

The Supplementary Videos are available at https://www.doi.org/10.5281/zenodo.5831821.

Video 3.1: Single particle driven between two target positions.

Video 3.2: Single particle confined at a target position.

Video 3.3: Positioning of six active particles at low SNR on a grid pattern.

Video 3.4: Positioning of six active particles in a hexagon with a background of passive particles.

Video 3.5: Arrangement of up to nine active particles to display the letters “OSA”.

Video 3.6: Control of nine active particles that are transformed from a grid to a circular pattern.

4.4 Thermophoretic Trap for Protein Aggregation Studies

4.4.1 Abstract

The aggregation of soluble proteins into highly ordered insoluble amyloid fibrils is fundamental for the understanding of neurodegenerative disorders. One of the challenges in the study of protein aggregation and amyloid formation is the disentanglement of the sample heterogeneity that is inherent to the nucleation and growth process of protein aggregates. So far, most of the information about the growth of fibrillar protein structures is inferred from studies of the ensemble growth kinetics, where all species ranging from monomers via oligomers, protofibrils and fibrils of different length are probed at the same time. Based on these, combined with modelling approaches, a number of processes termed secondary nucleation have been suggested which comprise, for example, the fragmentation of fibrils as important processes for the formation of pathogenic structures. However, none of these secondary processes has ever been observed directly due to the lack of experimental techniques which allows investigating a freely diffusion single fibril for longer time periods. Here, we present a method to isolate and observe single fibrils in heterogeneous ensembles using thermophoretic trapping. With this approach we enable, for the first time, the investigation of single fibrils free in solution for several hours. Combined with rotational diffusion measurements we are able to monitor length changes well below the optical resolution limit allowing to investigate the dynamics of fibril growth, secondary nucleation or fibril breakup which are typically hidden in the ensemble average. We demonstrate our technique for single $A\beta_{40}$, $A\beta_{42}$ and pyroglutamyl-modified amyloid-β variant ($pGlu_3$-$A\beta_{3\text{-}30}$) amyloid fibrils.

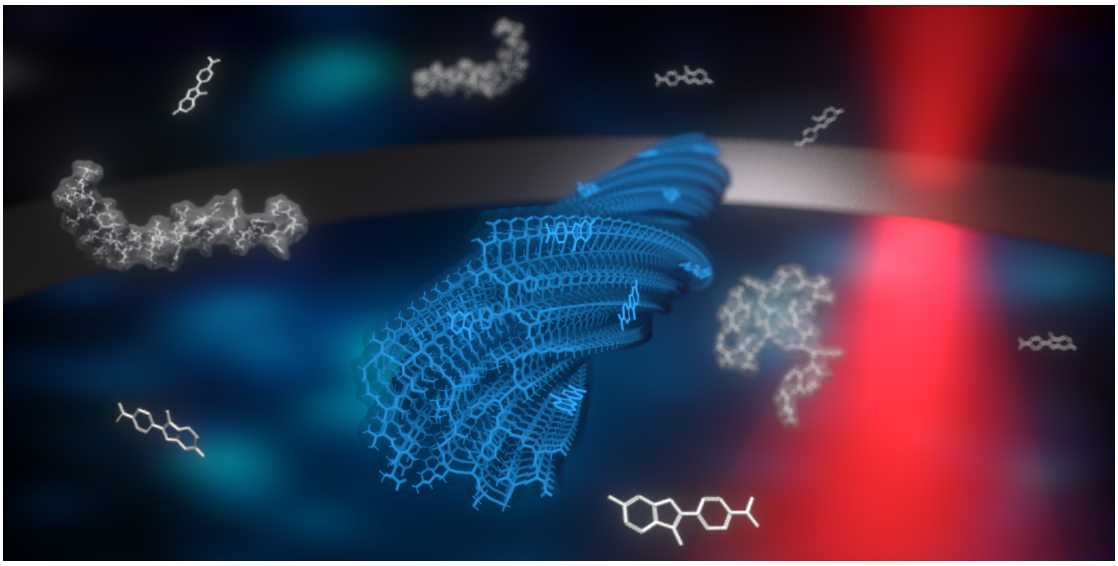

Illustration of an amyloid fibril in a thermophoretic trap. Rendered using Blender 2.83 and the Cycles Renderer.

The section is based on the following article:

[P4] **M. Fränzl**, T. Thalheim, J. Adler, D. Huster, J. Posseckardt, M. Mertig, and F. Cichos, Thermophoretic Trap for Single Amyloid Fibril and Protein Aggregation Studies, *Nat. Methods* **16**, 611 (2019)

The article has been adapted and revised. Details on the author contributions are provided in the "List of Publications" section.

4.4.2 Introduction

The self-organization of individual molecular units into functional or pathological structures is fundamental for life[107–112]. The aggregation of proteins into fibrillar structures may also yield toxic assemblies which are connected to a variety of diseases, ranging from Alzheimer's disease[263] and Parkinson's disease[264] to type II diabetes[265]. In case of amyloid formation proteins undergo a conformational change from their native structure into a β-sheet configuration to form highly-ordered amyloid fibrils[115,266,267]. Fig. 4.80a illustrates the native structure of the Aβ_{40} peptide[268] associated with Alzheimer's disease. Their β-sheet configuration found in Aβ_{40} fibrils[269] is depicted in Fig. 4.80b.

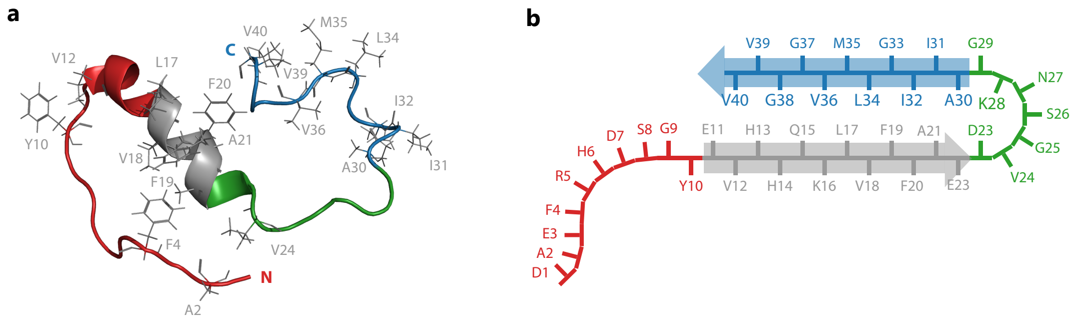
a
V40
M35
L34
C
V12
L17
F20
V39
I32
Y10
A21
V36
V18
A30
I31
F19
F4
V24
N
A2
b
V39 G37 M35 G33 I31 G29
N27
V40 G38 V36 L34 I32 A30 K28
S26
D7 S8 G9
H6
E11 H13 Q15 L17 F19 A21 D23
G25
R5
Y10 V12 H14 K16 V18 F20 E23
V24
F4
E3
A2
D1

Fig. 4.80: **a**, The native structure of Aβ_{40} in aqueous solution. Specific regions on the peptide are colored in red for the N terminus (residues 1 to 16), gray for the central hydrophobic cluster (17 to 21), green for the turn (22 to 29), and blue for the C terminus (30 to 40). The hydrophobic side chains are represented as gray sticks. Adapted from Ref. 270. **b**, Sketch of the β-sheet structure found in Aβ_{40} fibrils. The gray and blue arrow represent the two β-sheets. The unstructured *N* terminus is represented in red and the turn in green. Adapted from Ref. 271.

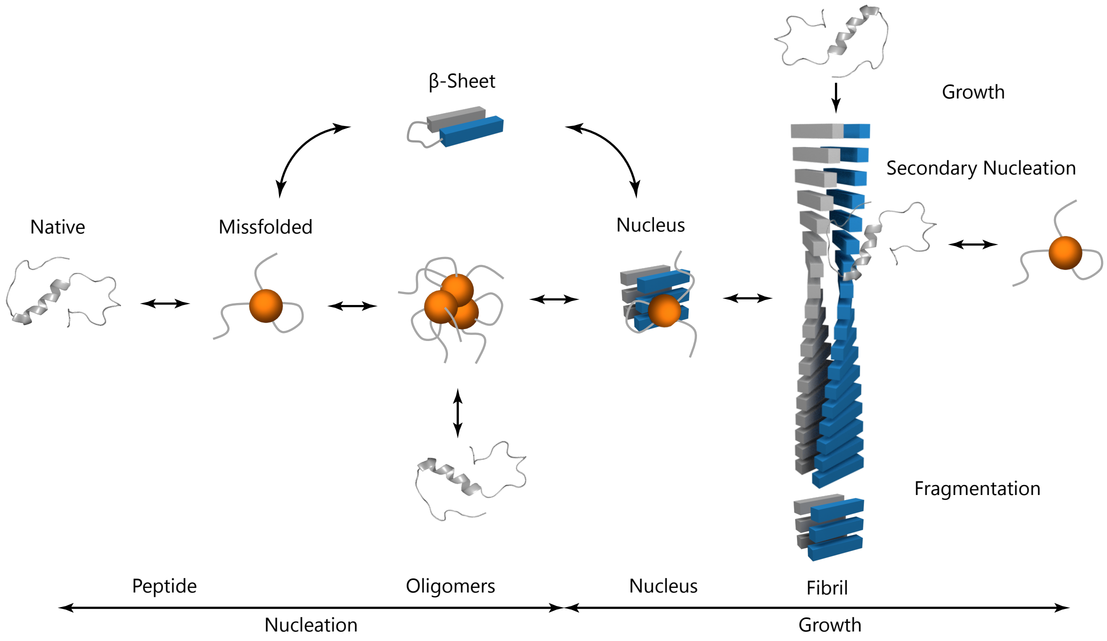
β-Sheet
Growth
Secondary Nucleation
Native
Missfolded
Nucleus
Fragmentation
Peptide
Oligomers
Nucleus
Fibril
Nucleation
Growth

Fig. 4.81: The nucleation of amyloid fibrils starts with a conformational change of the native protein into a misfolded state. These states are transient, heterogeneous and of unknown structure. One of these states initiates formation by assembling into oligomeric species. Some of these oligomers can then associate and transform into a β-sheet-rich nucleus. The nucleus then rapidly assembles into a fibril by recruiting other monomers at its ends. As fibrils grow, they can fragment yielding more fibril ends that are capable of elongation by the addition of monomers and processes, such as secondary nucleation, in which oligomer formation is catalysed on the surface of a fibril have been suggested[112].

It is believed that monomers first assemble into oligomeric species[112,272] initiated by a currently unknown change of their native configuration. These loosely ordered oligomers then transform into a highly ordered β-sheet structured nucleus[273], from which fibrils are growing[113,116] (Fig. 4.81). In case of Aβ the fibrils themselves may be non-toxic[274], but seem to catalyze the formation of pathogenic oligomeric aggregates[272,275] in secondary processes such as fragmentation, branching and surface catalyses[276–280].
A fundamental difficulty in the investigation of protein aggregation and other macromolecular nucleation and growth processes is the heterogeneity of the ensemble studied[281–283]. Ensembles contain aggregates of different sizes which grow in an unsynchronized way. Single fibril optical microscopy studies[284–286] aim to disentangle the heterogeneous ensemble, but none of those experiments has been able to follow the growth of a freely suspended fibril without the perturbing immobilization at a solid interface[287–289]. Secondary processes like fibril fracture have been proposed[116,119,277], but never observed directly. Here, we present a method that allows not only to spatially confine a single fibril over time periods of several hours in solution without any surface immobilization, but also to observe the growth of a single fibril. We show that the rotational diffusion coefficient provides a unique measure for dynamic length changes of fibrils with a precision down to a few nanometers. The long observation periods enable us to identify rare events of fibril fracture visually in the recorded images as well as in the time traces of the rotational diffusion coefficient confirming directly the existence of secondary processes during the growth of amyloid fibrils.

4.4.3 Results and Discussion

We enable the observation of single amyloid fibrils over long time periods by using thermophoretic drifts of single molecules and nano-objects in temperature gradients as a result of the temperature dependent solute–solvent interactions[49,53,56]. A given temperature gradient ∇T causes a thermophoretic drift of a suspended object at a velocity $\boldsymbol{u} = -D_\mathrm{T}\nabla T$ as a result of a variety of physical mechanisms[56] (Sec. 2.3). The strength of this drift is characterized by the thermodiffusion coefficient D_T, which is in most cases found to carry a positive sign. Accordingly, molecules and particles are repelled from the hot regions. In liquids, the thermophoretic drift competes with Brownian motion characterized by the translational diffusion coefficient D_t and the Soret coefficient $S_\mathrm{T} = D_\mathrm{T}/D_\mathrm{t}$ is given by their relative strength. Values of $S_\mathrm{T} = 0.01\ldots10\ \mathrm{K}^{-1}$ are observed depending on the size and the composition of the nano-object[56].

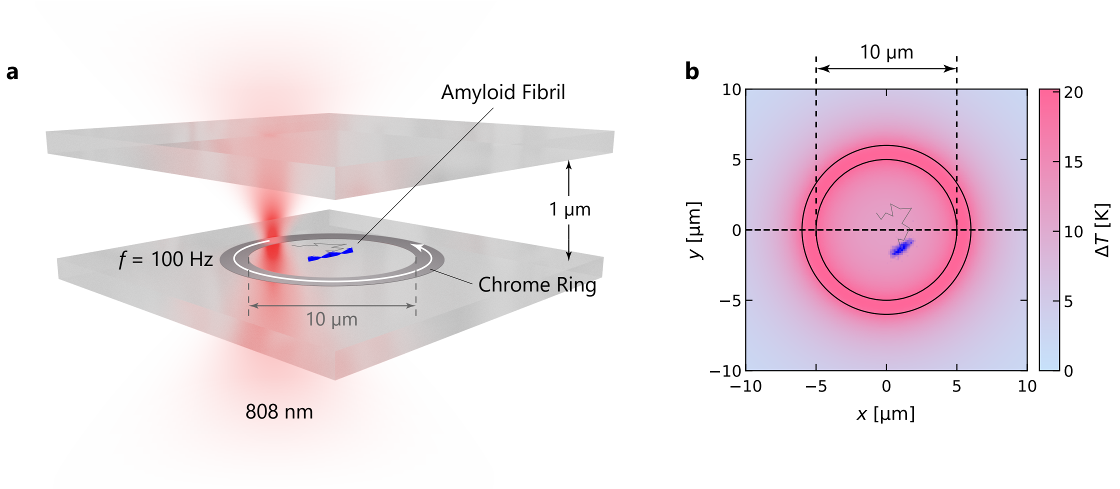

Fig. 4.82: **a**, Illustration of the trapping mechanism and the sample geometry. A chrome ring (10 µm inner diameter, 12 µm outer diameter, 50 nm height) is heated by a focused 808 nm laser rotating along the circumference of the ring at $f = 100$ Hz. The trapped fibril is imaged by the fluorescence of Thioflavin T (ThT). **b**, Simulated time-averaged temperature increment $\Delta T(r) = T(r) - T_0$ in the trap ($T_0 = 20°\mathrm{C}$) for a heating laser power of $P_0 = 1$ mW (Sec. 4.4.5.2). The temperature profile is averaged over the liquid film thickness of 1 µm.

We designed a temperature field with the help of an optically heated, 10 µm diameter chrome ring deposited on a glass coverslip to provide high temperature gradients at low temperature increments (Fig. 4.82a). The chrome structure is heated by a focused laser beam ($w_0 \approx 500$ nm beam waist) of 808 nm wavelength, which is rotated by an acousto-optic deflector (AOD) along the circumference of the ring with a frequency of $f = 100$ Hz. The heat released from the chrome structure creates a time-averaged temperature field in the surrounding liquid film (Fig. 4.82b), which is confined to a thickness of about 1 µm by a second glass coverslip (see Sec. 4.4.5.1 for details on the sample preparation). The temperature field has been obtained from finite element simulations (Sec. 4.4.5.2) and matches the temperature obtained from reference measurements on the Brownian motion of single polystyrene colloids in water (see Sec. 4.4.5.3 for details). At an incident laser power of $P = 1$ mW, the central temperature is elevated by $\Delta T_{\mathrm{center}} = 11.3$ K as compared to the ambient temperature, $T_0 = 20\,^\circ\mathrm{C}$. The temperature contrast from the center to the chrome ring is about $\Delta T_{\max} - \Delta T_{\mathrm{center}} = 8.9$ K.

Fluorescence Detection The fibrils are imaged using Thioflavin T (ThT) as fluorescent marker (Supplementary Fig. 4.94, Supplementary Videos 4.1 and 4.2). In presence of amyloid fibrils, ThT gives a strong fluorescence signal with a peak at approximately 482 nm when excited with 445 nm (Fig. 4.83a). The fluorescence of ThT is enhanced upon binding to the β-sheet structure of amyloid fibrils[290,291]. In absence of fibrils the fluorescence of ThT is quenched by a non-radiative rotational decay about the central C-C bond[290]. The binding of ThT is transient[292], providing the advantage of less photobleaching and no interference with the fibrillation process[293]. We used a ThT concentration of 20 µM which is supposed to be the optimal concentration for Aβ_{40} fibrils[293]. For a continuous excitation of ThT, photobleaching is found to be sufficiently weak to observe single fibrils over at least several 10 minutes at a time resolution of $\tau = 30$ ms (Fig. 4.83b). TEM images of the investigated Aβ_{40} fibrils are provided in Sec. 4.4.5.5.

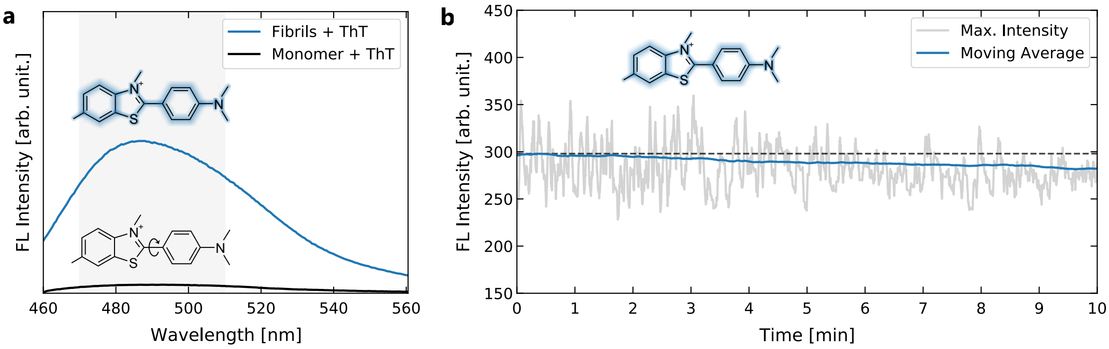

Fig. 4.83: **a**, Fluorescence spectra of Thioflavin T (ThT) in presence of Aβ_{40} monomers (black) and fibrils (blue) excited with 445 nm. The transmission band of the emission filter (Chroma Technology, ET490/40) is depicted in light grey. The insets show the chemical structure of ThT and the non-radiative rotational decay about the central C-C bond. **b**, ThT intensity of a trapped fibril plotted over time. The raw data is shown in gray while the blue line represents a moving average. The dashed black line marks the initial intensity value.

Effective Trapping Potential During the observation periods we have access to the center of mass (COM) position and the in-plane orientation of the fibril in each frame (see Sec. 4.4.5.6 and Supplementary Video 4.3 for details). A recorded COM position distribution for a trapped Aβ_{40} fibril with a length of $L = 1.5$ µm is depicted in Fig. 4.84a (Dataset 1). The probability density to find a particle in a non-uniform temperature is given by (Sec. 2.3.1)

$$p(\boldsymbol{r}) = p_0\,\mathrm{e}^{-S_{\mathrm{T}}\Delta T(\boldsymbol{r})}\ , \tag{4.46}$$

where $S_{\mathrm{T}} = D_{\mathrm{T}}/D_{\mathrm{t}}$ is the Soret coefficient and $\Delta T(\boldsymbol{r})$ is the local temperature increment $\Delta T(\boldsymbol{r}) = T(\boldsymbol{r}) - T_0$ with respect to the ambient temperature T_0. As illustrated in Fig. 4.84b the temperature distribution in the center of the trap has a nearly parabolic shape. Hence, the temperature gradient in the parabolic region is linear and the trap resembles in good approximation a harmonic trap. If the temperature distribution is approximated by a parabolic function

$$\Delta T(x) = \frac{\alpha}{2} x^2 + \Delta T_{\text{center}} \ , \tag{4.47}$$

where α describes the curvature (Fig. 4.84b), the probability distribution is Gaussian:

$$p(x) = p_0 \, \mathrm{e}^{-S_\mathrm{T} \alpha x^2/2} \ . \tag{4.48}$$

A fit of Eq. (4.48) to the experimental data in Fig. 4.84a is depicted as solid black curve in Fig. 4.84b. The probability to find a fibril in the radial interval $[r, r + \mathrm{d}r]$ is then defined by $p_\mathrm{R}(r)\,\mathrm{d}r = p(r)\,2\pi \mathrm{d}r$. With $\int_0^\infty p_\mathrm{R}(r)\,\mathrm{d}r = 1$ and Eq. (4.48) we find

$$p_\mathrm{R}(r) = S_\mathrm{T} \alpha \, r \, \mathrm{e}^{-S_\mathrm{T} \alpha \, r^2/2} \ , \tag{4.49}$$

corresponding to a Rayleigh distribution. A fit of Eq. (4.49) to the experimental data in Fig. 4.84a is depicted as solid black curve Fig. 4.84c. Eq. (4.48) as well as Eq. (4.49) can be used to directly extract the Soret coefficient from the histogram of the particle positions, when the temperature profile $\Delta T(r)$ is known. From the radial distribution we find a Soret coefficient of $S_\mathrm{T} = 1.5\ \mathrm{K}^{-1}$ for a Aβ_{40} fibril with $L = 1.5$ µm length where we have used $\alpha = 0.38$ estimated for the curvature (Sec. 4.4.5.3).

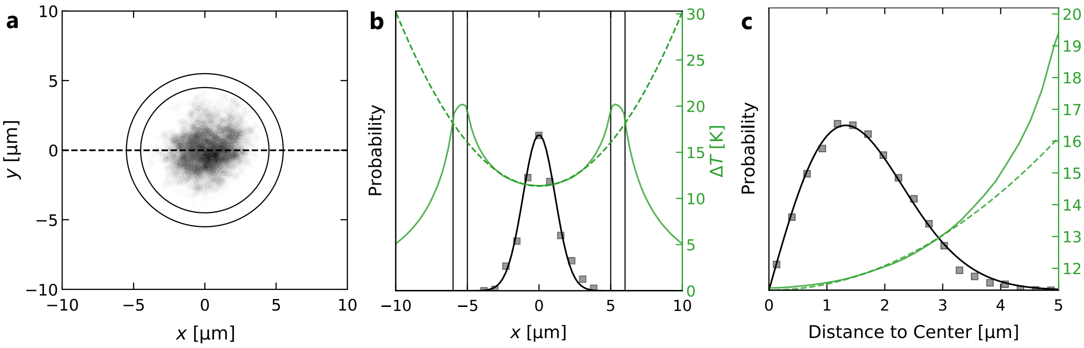

Fig. 4.84: **a**, Detected center of mass (COM) positions of a trapped single Aβ_{40} fibril with $L = 1.5$ µm length recorded over a time period of 5 minutes (Dataset 1). **b**, Line profile through the position distribution in (**a**) fitted with a Gaussian distribution (solid black curve). The solid green line represents a line profile through the time-averaged temperature distribution in Fig. 4.82b. The dashed green curve represents a parabolic approximation of the temperature profile. **c**, Radial position distribution determined from the COM positions and fitted with a Rayleigh distribution (solid black curve). The radial distribution has been used to calculate the Soret coefficient.

Displacement Statistics Displacement statistics is used to obtain the diffusion coefficients of the fibril. Therefore, we calculate the in-plane displacement vector between two subsequent frames:

$$\Delta \boldsymbol{r}(t) = \boldsymbol{r}(t + \tau) - \boldsymbol{r}(t) \ . \tag{4.50}$$

The displacement vector is then used to characterize the motion of the fibril in two different reference frames, the trap structure reference frame and the fibril reference frame (Fig. 4.85). To obtain the diffusion coefficient and the thermophoretic drift velocity, we project the displacement vector $\Delta\boldsymbol{r}$ to the tangential direction $\boldsymbol{e}_\mathrm{t}$ and the radial direction $\boldsymbol{e}_\mathrm{r}$ of the trap reference frame:

$$\Delta r_\mathrm{t}(t) = \Delta \boldsymbol{r}(t) \cdot \boldsymbol{e}_\mathrm{t} \ , \tag{4.51}$$

$$\Delta r_\mathrm{r}(t) = \Delta \boldsymbol{r}(t) \cdot \boldsymbol{e}_\mathrm{r} \ . \tag{4.52}$$

The experimental results for Dataset 1 are depicted in Fig. 4.86a.

The tangential displacements follow a Gaussian statistics (see Eq. (2.16) for ref.):

$$p(\Delta r_{\mathrm{t}}) = \frac{1}{\sqrt{4\pi D_{\mathrm{t}}\tau}}\, \mathrm{e}^{-\Delta r_{\mathrm{t}}^2/(4D_{\mathrm{t}}\tau)}, \tag{4.53}$$

with a variance $\sigma^2 = 2D_{\mathrm{t}}\tau$ and a zero mean as there is no drift acting along the tangential direction of the trap. The radial displacements follow a Gaussian statistics as well, but with a non-zero mean:

$$p(\Delta r_{\mathrm{r}}) = \frac{1}{\sqrt{4\pi D_{\mathrm{t}}\tau}}\, \mathrm{e}^{-(\Delta r_{\mathrm{r}}-u\tau)^2/(4D_{\mathrm{t}}\tau)}\ . \tag{4.54}$$

The non-zero mean is the result of the thermophoretic drift within the time lag τ, which equals $\Delta r_{\mathrm{r}} = u\tau$ assuming that the drift velocity is always radial, $\boldsymbol{u} = u\boldsymbol{e}_{\mathrm{r}}$. The radial drift velocity is varying with the distance R from the center of the trap, $u(R)$. The distance dependence reflects the temperature gradient in the trap ∇T. To measure the radial dependence of the drift velocity, we analyze displacements which start in an interval $[R, R{+}\Delta R]$. Supplementary Fig. 4.97 displays the resulting velocity for 5 different distance intervals from a measurement of a single fibril of length $L = 1.5$ µm. The radial drift velocity is linearly increasing as the temperature profile can be approximated by a parabolic function. For comparison, we also analyzed the mean of the tangential displacement distributions. As there is no thermophoretic drift acting along the tangential direction the drift velocity is close to zero.

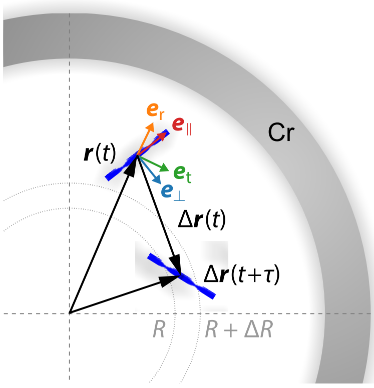
$\boldsymbol{e}_{\mathrm{r}}$
$\boldsymbol{e}_{\parallel}$
Cr
$\boldsymbol{r}(t)$
$\boldsymbol{e}_{\mathrm{t}}$
$\boldsymbol{e}_{\perp}$
$\Delta\boldsymbol{r}(t)$
$\Delta\boldsymbol{r}(t{+}\tau)$
R
$R+\Delta R$

Fig. 4.85: Sketch showing the decomposition of the fibril displacements $\Delta\boldsymbol{r}$ according to the trap structure reference frame (centered at the trap structure, unit vectors $\boldsymbol{e}_{\mathrm{r}}$ and $\boldsymbol{e}_{\mathrm{t}}$) and the fibril reference frame (fixed in the center of mass of the fibril, unit vectors $\boldsymbol{e}_{\parallel}$ and $\boldsymbol{e}_{\perp}$).

The anisotropy of the fibril diffusion is accessed by projecting the displacement $\Delta\boldsymbol{r}$ to the long axis $\boldsymbol{e}_{\parallel}$ and the short axis $\boldsymbol{e}_{\perp}$ of the fibril (Fig. 4.85):

$$\Delta r_{\parallel}(t) = \Delta\boldsymbol{r}(t)\cdot\boldsymbol{e}_{\parallel}\ , \tag{4.55}$$

$$\Delta r_{\perp}(t) = \Delta\boldsymbol{r}(t)\cdot\boldsymbol{e}_{\perp}\ . \tag{4.56}$$

Depending on the orientation of the fibril, the displacements in Eqs. (4.55) and (4.56) contain contributions of the drift velocity u. To obtain the drift-free displacement, we project the displacements along in the fibril frame to the tangential direction in the trap reference frame $\boldsymbol{e}_{\mathrm{t}}$:

$$\Delta r_{\mathrm{t}}^{\parallel}(t) = \Delta r_{\parallel}(t)\,\boldsymbol{e}_{\parallel}\ \cdot\boldsymbol{e}_{\mathrm{t}}\ , \tag{4.57}$$

$$\Delta r_{\mathrm{t}}^{\perp}(t) = \Delta r_{\perp}(t)\,\boldsymbol{e}_{\perp}\cdot\boldsymbol{e}_{\mathrm{t}}\ , \tag{4.58}$$

as depicted in Fig. 4.86b for Dataset 1. The displacements obey Gaussian statistics:

$$p(\Delta r_{\mathrm{t}}^{\parallel}) = \frac{1}{\sqrt{4\pi D_{\mathrm{t}}^{\parallel}\tau}}\, \mathrm{e}^{-(\Delta r_{\mathrm{t}}^{\parallel})^2/(4D_{\mathrm{t}}^{\parallel}\tau)}\ , \tag{4.59}$$

$$p(\Delta r_{\mathrm{t}}^{\perp}) = \frac{1}{\sqrt{4\pi D_{\mathrm{t}}^{\perp}\tau}}\, \mathrm{e}^{-(\Delta r_{\mathrm{t}}^{\perp})^2/(4D_{\mathrm{t}}^{\perp}\tau)}\ , \tag{4.60}$$

and the variances of these projected displacement distributions thus deliver the diffusion coefficients $D_{\mathrm{t}}^{\parallel}$ and $D_{\mathrm{t}}^{\perp}$.

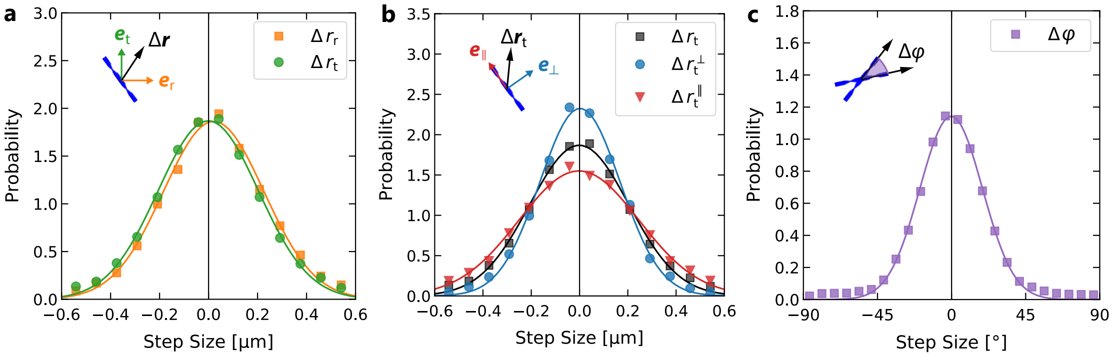

Fig. 4.86: **a**, Probability density distribution of $\Delta \boldsymbol{r}$ projected onto the radial direction $\boldsymbol{e}_\mathrm{r}$ (Δr_r) and tangential direction $\boldsymbol{e}_\mathrm{t}$ (Δr_t) in the trap. The distributions obey Gaussian statistics (solid lines). The width of the distributions deliver the average translation diffusion coefficient D_t. The slight displacement of the radial distribution is due to the thermophoretic drift u. **b**, Decomposition of $\Delta \boldsymbol{r}$ along the long axis $\boldsymbol{e}_\parallel$ ($\Delta r_\parallel$) and short axis $\boldsymbol{e}_\perp$ ($\Delta r_\perp$) of the fibril. The width of the Gaussian statistics (solid lines) deliver the projected principle axes of the diffusion tensor ($D_\mathrm{t}^\parallel$, $D_\mathrm{t}^\perp$). **c**, Probability density distribution of angular displacements $\Delta\varphi$ of the long axis of the fibril. The experimental data follow Gaussian statistics (solid line). The width of the Gaussian is used to determine the rotational diffusion coefficient (D_r).

The rotational diffusion is measured from the in-plane angle of the fibril in the trap structure reference frame. The in-plane angle φ of the long axis with the horizontal axis of the trap structure reference frame is the result of the tracking procedure (Sec. 4.4.5.6). We calculate the angular displacement between two subsequent frames:

$$\Delta\varphi(t) = \varphi(t+\tau) - \varphi(t) \; . \tag{4.61}$$

For small angular displacements, the probability density distribution follows a Gaussian distribution as well:

$$p(\Delta\varphi) = \frac{1}{\sqrt{4\pi D_\mathrm{r}\tau}} \, \mathrm{e}^{-(\Delta\varphi)^2/(4D_\mathrm{r}\tau)} \; . \tag{4.62}$$

The variance of the distribution of the time series can be used to get an estimate of the rotational diffusion coefficient D_r of the fibril.

Length Dependence We demonstrate the method for single Aβ$_{40}$ fibrils of varying length in an aqueous buffer (pH 8.4, 6 mM NaCl) in the absence of Aβ$_{40}$ monomers (Datasets 1–6, see Sec. 4.4.5.9 for details). The fibril length has been estimated from the optical images. Fig. 4.87a, b display the obtained length dependence of the rotational diffusion coefficient D_r, the average translational diffusion coefficient D_t and the Soret coefficient S_T. As predicted for rod-like macromolecules the average translation diffusion coefficient D_t follows an inverse linear dependence on the length (see Sec. 4.4.5.10 for details):

$$D_\mathrm{t} = \frac{1}{2}\left(D_\mathrm{t}^\parallel + D_\mathrm{t}^\perp\right) = \frac{k_\mathrm{B}T\left(3\ln(L/d) + 2\xi_\parallel + \xi_\perp\right)}{8\pi\eta L} \propto L^{-1} \; , \tag{4.63}$$

and the rotational diffusion coefficient D_r is inversely depending on the third power of the length:

$$D_\mathrm{r} = \frac{3k_\mathrm{B}T\left(\ln(L/d) + \xi_\mathrm{r}\right)}{\pi\eta L^3} \propto L^{-3} \; . \tag{4.64}$$

Here, L is the length and d is the diameter of the fibril ($d \approx 10$ nm). The values of the end-correction coefficients are $\xi_\parallel = -0.114$, $\xi_\perp = 0.886$ and $\xi_\mathrm{r} = -0.447$[294]. Furthermore, we find a linear increase of the Soret coefficient S_T with the length of the fibril (Fig. 4.87b). The linear dependence is the result of the inverse dependence of D_t on the length, $S_\mathrm{T} = D_\mathrm{T}/D_\mathrm{t} \propto L$ (see Eq. (2.80) for ref.). In agreement with literature[53], the thermodiffusion coefficient is thus independent of the size of the object and found to be $D_\mathrm{T} = 1.06\ \mu\mathrm{m}^2\,\mathrm{s}^{-1}\,\mathrm{K}^{-1}$. Fig. 4.87a, b also include the corresponding data for Aβ_{40} under varying buffer conditions (pH between 6.1 and 8.8, NaCl concentration between 1 mM and 150 mM in 25 mM phosphate buffer, Datasets 7–11). In all cases, a long time trapping is possible. The found reduced Soret coefficients S_T/L are similar to the ones obtained for a 6 mM NaCl concentration highlighting the applicability of the method to a wide range of buffer conditions. Only the highest salt concentration reveals a decreased electrostatic contribution to the Soret coefficient[128] (see Sec. 2.3.3 for ref.). Other protein fibrils such as a pyroglutamyl-modified Aβ variant[295,296] (pGlu$_3$-Aβ_{3-40}) and Aβ_{42}[118,266,270,297] have been successfully trapped for periods longer than 20 minutes and the extracted results seamlessly integrate with the Aβ_{40} data (Fig. 4.87a, b, Datasets 12–13).

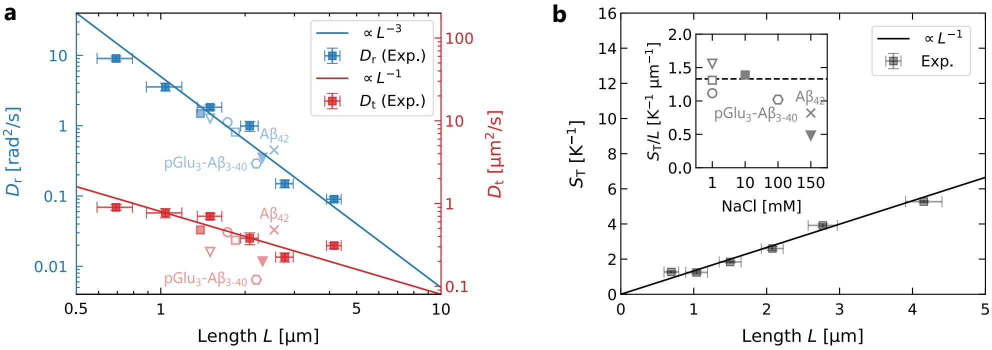

Fig. 4.87: **a**, Length dependence of the average translational D_t and rotational diffusion coefficient D_r for Aβ_{40}. The lines display a fit to the experimental data according to the theoretically predicted dependence of the diffusion of a rod ($D_\mathrm{t} \propto L^{-1}$, $D_\mathrm{r} \propto L^{-3}$, see Eqs. (4.63) and (4.64)). Vertical error bars for translational/rotational diffusion coefficients are calculated according to Sec. 4.4.5.11. The horizontal error bars were estimated from the diffraction limit of the setup and the standard deviation of the major axis length. The measurements on Aβ_{40} for different salt and pH conditions (Datasets 7–11) as well as the two additional amyloid forming peptides, Aβ_{42} and pGlu$_3$-Aβ_{3-40} (Datasets 12–13). The shape of the symbols encodes the pH (circles: pH 6.1, squares: pH 7.4, triangles: pH 8.8). The two additional data points show the results for two different peptides variants: Aβ_{42} (cross, pH 9.2) and pGlu$_3$-A$\beta_{3\text{-}40}$ (hexagon, pH 8.0). For the sample sizes and buffer conditions see Sec. 4.4.5.9. **b**, Dependence of the Soret coefficient S_T on the fibril length L for Aβ_{40}. The line represents the result of a linear regression, which yields a thermodiffusion coefficient of $D_\mathrm{T} = 1.06\ \mu\mathrm{m}^2\,\mathrm{s}^{-1}\,\mathrm{K}^{-1}$. Vertical error bars are calculated according to Sec. 4.4.5.11. The horizontal error bars were estimated as described in (**a**). For the sample sizes and buffer conditions see Sec. 4.4.5.9. The gray symbols in the inset show the reduced Soret coefficient S_T/L for Aβ_{40} for varying salt and pH conditions represented by the same symbols as in (**a**).

The strong length dependence of the rotational diffusion coefficient D_r delivers an extremely sensitive tool to investigate fibril growth. We monitor the rotational diffusion coefficient of three seed fibrils over time in the presence of Aβ_{40} monomers (Datasets 14–16) which enter and leave the trap due to their lower Soret coefficient[298] ($S_\mathrm{T} \approx 10^{-2}\ \mathrm{K}^{-1}$). Fig. 4.88a shows the time evolution of the rotational diffusion coefficient of two different fibrils (A, B) in the same sample (pH 8.4, 6 mM NaCl) and a third fibril (C) under high pH and salt (pH 8.8, 150 mM NaCl). Fibril A appears to be not growing, possibly due to defects at the fibril ends[285]. Fibril B exhibits a decreasing rotational diffusion coefficient. With an initial length of $L = 1.2$ µm, the overall length increase is determined to be 70 nm, which corresponds to a growth rate of $0.06\ \mathrm{nm\,s^{-1}}$. Fibril C shows that growth can be also observed under higher pH and salt conditions as encountered in the biological context and results in a higher growth rate of $0.17\ \mathrm{nm\,s^{-1}}$. Fig. 4.88b depicts the measured data points for fibrils B and C in the expected length dependence of the rotational diffusion coefficients together with the data from Fig. 4.87a. Monitoring the rotational diffusion is therefore an excellent tool for observing fibrillar growth processes in single fibril studies.

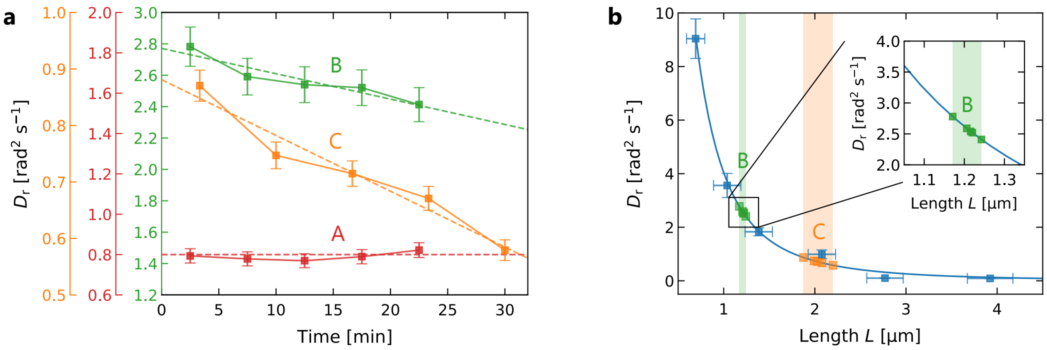

Fig. 4.88: **a**, Time dependence of the rotational diffusion coefficient for three different fibrils (Aβ_{40}) in the presence of Aβ_{40} peptide monomers (Datasets 14–16). The error bars represent the confidence intervals for the statistical sample size and 90 % accuracy. Fibril A has a length of 2.1 µm and an initial rotational diffusion coefficient of $D_r = 0.8$ rad^2 s^{-1}. The rotational diffusion coefficient is unchanged over a time period of 20 minutes. Fibril B has a length of 1.2 µm and an initial rotational diffusion coefficient $D_r = 2.8$ rad^2 s^{-1} which shows a continuous decrease attributed to a growth of 70 nm within a time period of 20 minutes. Fibril C has an initial length of 1.9 µm and a $D_r = 0.88$ rad^2 s^{-1} showing a continuous growth by about 300 nm. For the sample sizes and buffer conditions see Sec. 4.4.5.9. **b**, Data points of fibril B and C converted to a length according to the measured dependence in Fig. 4.87a.

The experimentally accessible time for single fibril studies can be extended to several hours since the trapping mechanism does not require an observation of the fibrils as in feedback traps[8,89]. Fig. 4.89a displays the intensity time trace of a fibril (D) over time periods of 5 minutes interrupted by periods with no fluorescence excitation (Dataset 17). During the first 100 minutes, no change in the rotational diffusion is detected. At about 118 minutes, a fibril fracture event is captured on video. A small part breaks off from the fibril and leaves the trap (Fig. 4.89b, Supplementary Video 4.4). As a result, the rotational diffusion coefficient shows a sudden increase. The length change has been determined to be about 300 nm and delivers a direct hint for a fracture mechanism as one of the suggested mechanisms of secondary nucleation[112].

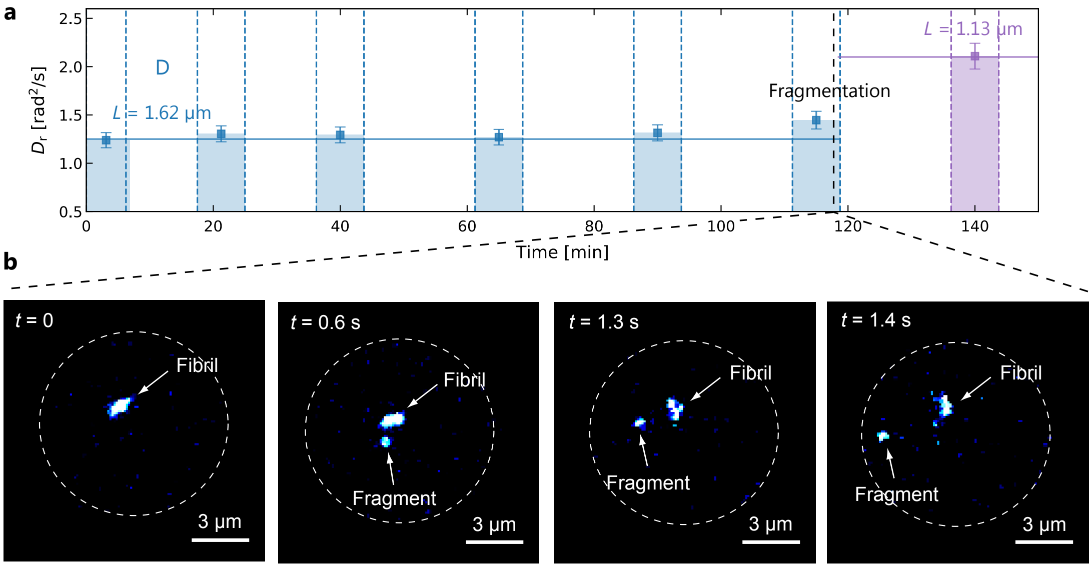

Fig. 4.89: **a**, Single fibril (D) of 1.62 µm length in an intermittent observation scheme (Dataset 17). The fluorescence excitation is switched on for time periods of 5 minutes. The bars indicate the average rotational diffusion coefficient within the observation period. At the end of the 6th observation period, a fibril breakup is observed, which leads in the subsequent period to an increased rotational diffusion coefficient. The change of the rotational diffusion coefficient corresponds to a length change of about 300 nm. **b**, The image series from the fragmentation event indicated in (**a**). The large segment of fibril D stays in the trap, while the short fragment leaves the trap structure (Supplementary Video 4.4).

4.4.4 Conclusion

The thermophoretic trapping method put forward here provides a starting point for more complex studies of molecular interactions and in particular of protein and macromolecular aggregation processes at the single fibril level. The rotational diffusion coefficient has been revealed to be a sensitive indicator of growth and can be combined with advanced statistical analysis methods such as a change point analysis[299] or wavelet transforms[300] to identify changes. The detection of rotational diffusion is not restricted to rod-like objects and can be extended to polarization resolved fluorescence detection[291,301] with photodiodes for fast rotational diffusion measurements, though the trapping of very small aggregates or oligomers will be challenging due to the small Soret coefficients. The trap may be employed to access the size distribution of fibrils also by using multiple traps in parallel. Furthermore, multicolor detection schemes can be introduced to explore surface catalyzed secondary nucleation, and a combination with advanced microfluidics could allow for cross seeding with different peptides variants. Since only relative temperature increments are important for the trapping, the sample temperature can be lowered or increased to provide temperature dependent measurements of fibrillation processes. Thus, thermophoretic trapping of single amyloid fibrils enables a plethora of applications for the investigation of molecular events that provide the basis for the understanding of folding diseases.

4.4.5 Supplementary Information

4.4.5.1 Sample Preparation

The sample is comprised of two glass coverslips (22 mm × 22 mm) confining a thin liquid film. One of the coverslips carries the trap structures fabricated by UV lithography (Fig. 4.90, see paragraph below for details). The trap structures can be located either on the top or on the bottom coverslip, but need to be facing towards the liquid. For the measurements presented in this work the top configuration was used. First, the coverslips were thoroughly cleaned in an ultrasonic bath with Hellmanex III (1%), acetone, isopropyle and Milli-Q water and dried with a nitrogen gun. To prevent sticking of the fibrils, the glass surfaces are passivated with Pluronic F-127. To attain the adsorption of Pluronic F-127 in a brush-like configuration, the cleaned coverslips are rendered hydrophobic with a thin layer of polystyrene (PSS-Polymer, M_w = 88 kDa, PDI = 1.66). 30 µl of 1 % polystyrene in toluene were spin coated at 8000 rpm onto the coverslips, resulting in a polystyrene layer thickness of about 100 nm. Subsequently the coverslips are immersed in 1 % Pluronic F-127 solution for 10 min. Thereafter, the coverslips were briefly dipped in Milli-Q water and dried with a nitrogen gun. Subsequently the edges of the lower coverslip were covered with a thin layer of PDMS for sealing. The fibril solution used for the length dependent experiments was prepared by diluting 5 µl of the fibril stock solution (pH 8.8, 150 mM NaCl, see paragraph below for details) with 100 µl Milli-Q water containing 0.1 % Pluronic F-127[157] resulting in pH 8.4 (1 mM phosphate buffer) and 6 mM NaCl. 0.1 % Pluronic F-127 was added to the solution to prevent the sticking of the peptides and fibrils. Control experiments have been carried out showing that Pluronic F-127 does not alter the fibrillation kinetics. For the buffer-dependent experiments 5 µl of the dialyzed fibril stock solution were diluted with 100 µl of the corresponding buffer containing 0.1 % Pluronic F-127. For growth experiments 0.1 mg of the peptide monomers were added to the solution. Finally, 2 µl of a 1 mM ThT stock solution were added to attain a ThT concentration of about 20 µM[293]. Directly after preparation 0.35 µl of the solution were pipetted in the middle of the lower coverslip. The upper coverslip was placed on top with the chrome structures facing down and the liquid spreads between the glass coverslips. Depending on the wetted area, typically about 18 mm × 18 mm, the resulting thin liquid film is about 1 µm in height. Chemicals, if not otherwise specified, have been obtained from Sigma-Aldrich.

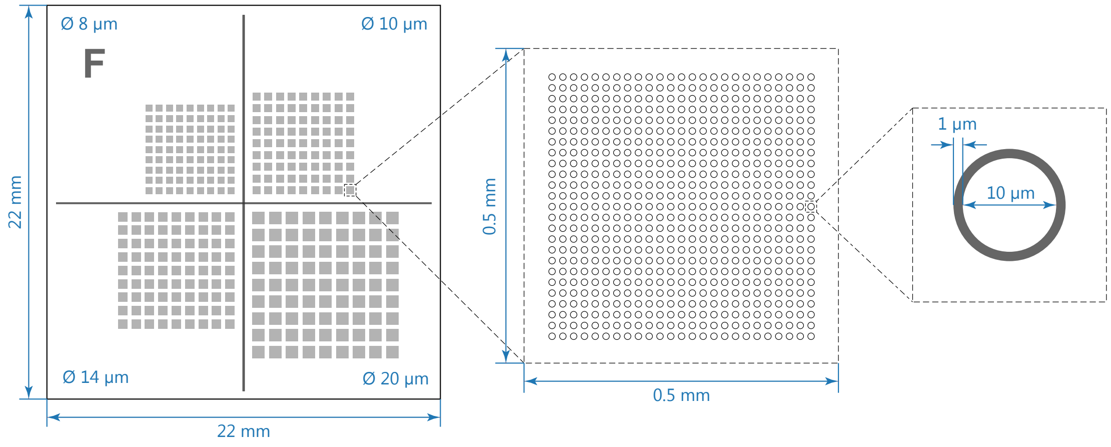

Fig. 4.90: a, CAD images of the trap structures on a 22 mm × 22 mm glass coverslip. The design comprises arrays of rings with inner diameters of 8 µm, 10 µm, 14 µm and 20 µm each ring with a width of 1 µm. In this work the 10 µm traps were used.

UV Lithography The trap structures have been designed using AutoCAD and consist of nested arrays of chrome rings with inner diameters of 8 µm, 10 µm, 14 µm and 20 µm located in four quadrants according to their inner diameter (Fig. 4.90). The ring width is 1 µm. Chrome is used due to its high absorption at the heating laser wavelength of 808 nm (Sec. 2.4.3). The array design allows to transfer nano-objects to a specific trap by heating the adjacent traps and multiple traps may be used to trap multiple objects simultaneously. Here, we have used traps with an inner diameter of 10 µm. The trap structures were fabricated on 22 mm × 22 mm glass coverslips using UV lithography. First, glass coverslips were thoroughly cleaned in an ultrasonic bath with Hellmanex III (1%), acetone and isopropyl and dried on a hotplate at 120 °C for 10 min. Subsequently, 100 µl of an adhesion promoter (MicroChemicals, TI PRIME, 3000 rpm, 30 s, followed by baking at 120 °C for 2 min on a hotplate) as well as 200 µl of a negative photoresist (MicroChemicals, AZ nLOF 2020, 3000 rpm, 30 s, followed by a soft-bake at 110 °C for 60 s on a hotplate) are spin coated successively onto the coverslips. Using a UV lithography system (Süss MicroTech, MJB4 Mask-Aligner) and a 3” photomask the photoresist was exposed (66 $\mathrm{mJ\,cm^{-2}}$, i-line) at regions of the desired chrome structures. The exposure is followed by a post-exposure bake at 110 °C for 60 s. The photoresist is then developed in a developer solution (MicroChemicals, AZ 326 MIF) for 60 s. Finally, a 30 nm chrome layer was thermally evaporated onto the cover slides and the non-depolymerized photoresist is stripped with a remover (MicroChemicals, TechniStrip NI555) in an ultrasonic bath for 30 min. Fig. 4.91 shows brightfield images of the resulting structures. The width of the chrome ring appears wider due to the limited optical resolution of the microscope.

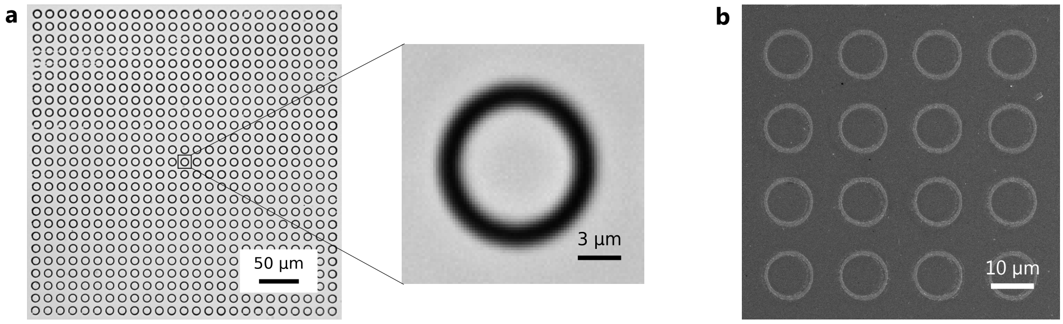

Fig. 4.91: **a**, Images of the structures fabricated using UV lithography recorded with an Olympus Plan N 20x/0.4 objective under bright-field illumination. **b**, SEM images of the trap structures obtained using a Zeiss SEM at 15 kV.

Fibril Preparation Aβ_{40} fibrils were prepared by dissolving lyophilized Aβ_{40} peptide in 25 mM phosphate buffer (pH 8.8) containing 150 mM NaCl at a concentration of 1 $\mathrm{mg\,ml^{-1}}$ followed by incubation for 4 days. For salt dependent measurements 1 ml samples of the fibril stock solution were dialyzed against four different 25 mM phosphate buffer solutions: 10 mM NaCl (pH 7.4) and 1 mM NaCl (pH 6.1, pH 7.4 and pH 8.8). The molecular weight cut-off (MWCO) of the dialysis tube was 1000. The dialysis was performed for 4 h and the dialysis solution was changed after 2 h. Aβ_{42} fibrils were prepared by dissolving lyophilized Aβ_{42} peptide in 25 mM phosphate buffer (150 mM NaCl, pH 9.2) at a concentration of 0.25 $\mathrm{mg\,ml^{-1}}$ followed by incubation for 4 days. pGlu$_3$-Aβ_{3-40} fibrils were prepared similar as described in Ref. 296. The lyophilized peptide was dissolved in 50 mM TRIS buffer (100 mM NaCl, pH 8.0) at a concentration of 0.1 $\mathrm{mg\,ml^{-1}}$ followed by incubation for 4 days. All peptides have been synthesised by the Core Unit Peptid (Medical Department, Leipzig University). For fibrillation, the peptide solutions were incubated at 37 °C and shaken at 450 rpm (Eppendorf, ThermoMixer). The fibril stock solutions were stored at room temperature until usage.

4.4.5.2 Temperature Simulation

The time-dependent temperature distribution in the sample was simulated using the Heat Transfer Module of COMSOL 5.1. The sample geometry was modeled according to the above described dimensions. The glass coverslips have been replaced by two cylindrical objects of a radius of 25 µm and a height of 10 µm. The employed simulation geometry is depicted in Fig. 4.92.

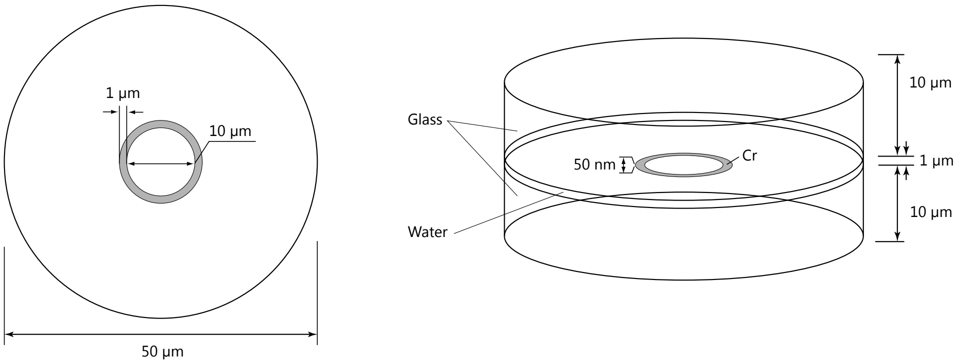

Fig. 4.92: Sketch of the simulation geometry in COMSOL. The gray region represents the chrome ring.

To account for the moving focused heating laser, a time-dependent heat source within the chrome ring was defined as follows (Sec. 2.5.3):

$$Q(x,y,t) = P_0(1-R)\frac{2\alpha}{\pi w_0^2}\exp\left(-\frac{((x-r\sin(2\pi f t))^2+(y-r\cos(2\pi f t))^2}{w_0^2}\right)\mathrm{e}^{-\alpha z}\ , \tag{4.65}$$

where $r = (r_1 + r_2)/2$ is the center between the inner and outer radius, f the frequency for one round trip and w_0 the beam waist of the laser. The outer boundary layers were set to room temperature, that is, $T_0 = 293.15$ K. Because of the small height (1 µm), convection in the liquid film was neglected[32] (Sec. 2.3.6). The material parameters used in the calculations can be found in Appendix A1.16. Fig. 4.93 displays the simulated relative temperature distributions. As the inverse rotation frequency ($f = 100$ Hz) of the laser spot velocity is sufficiently higher than typical thermal equilibration times (Sec. 2.5) the temperature geometry in radial direction is not deformed by the dynamic heating (Fig. 4.93a, b). During an exposure time of 30 ms the laser spot will circle the chrome ring three times and the trapped object experiences a time-averaged temperature distribution as shown in Fig. 4.93c, d. The temperature profiles along the dashed lines are shown in Fig. 4.93e. Moreover, the trapped object is expected to diffuse over the height of the liquid film. Therefore, the temperature is best represented by the height- and time-average (Fig. 4.93f). The temperature distribution is uniquely defined by the maximum temperature increment as compared to the ambient temperature above the chrome structure ΔT_max, or the temperature increment in the trap center ΔT_center. In the center of the trap the temperature profile can be well approximated by a parabolic function (Fig. 4.93f)

$$\Delta T(r) \approx \frac{\alpha}{2}r^2 + \Delta T_\mathrm{center}\ , \tag{4.66}$$

where α represents the curvature and ΔT_center the temperature rise at the center of the trap. Note that the curvature is linearly related to the relative curvature and temperature rise $\alpha = \alpha^\mathrm{rel}\Delta T_\mathrm{max}$. A fit to the numerical simulation (Fig. 4.93f) yields a relative curvature of $\alpha^\mathrm{rel} = 0.019\ \mu\mathrm{m}^{-1}$ and a ratio of $\Delta T_\mathrm{center}/\Delta T_\mathrm{max} = 0.56$ between the center and the maximum temperature increment for the 10 µm trap. The temperature contrast that can be used for trapping is therefore about 44 % of the total temperature rise.

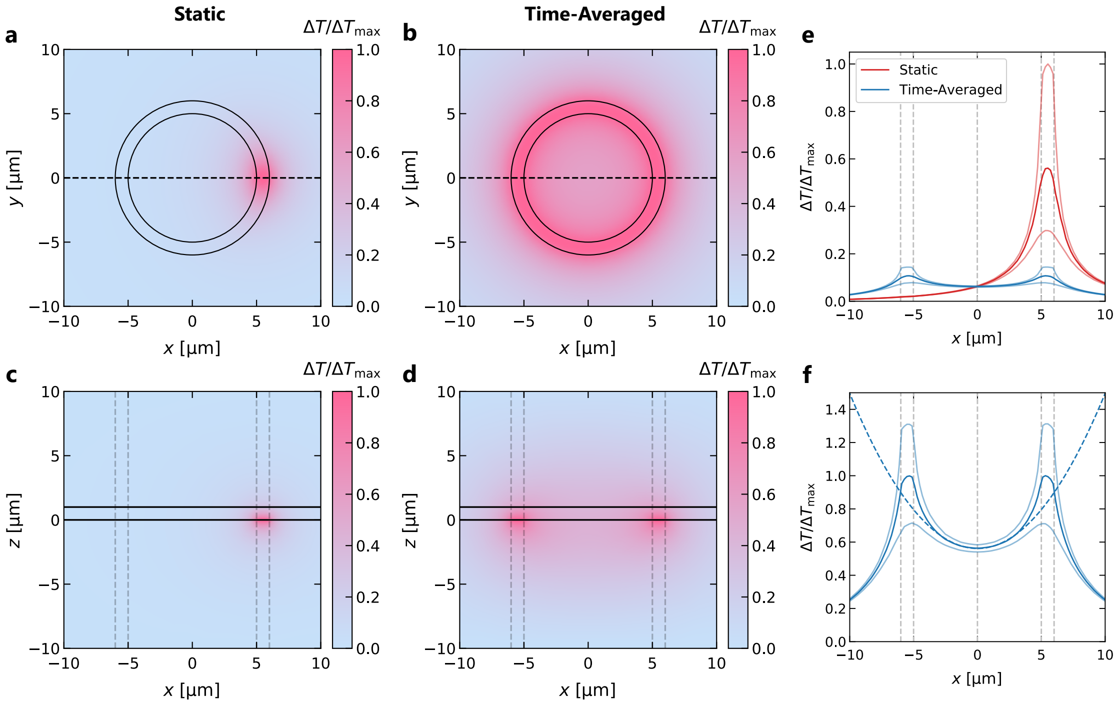

Fig. 4.93: Simulated relative temperature fields. **a**, **b** depict the static and the time-averaged temperature distributions in the xy-plane at the middle of the liquid film, $z = 0.5$ µm. **c**, **d** show the corresponding cross-sections in the xz-plane at $y = 0$ µm. Here, the time-averaged temperature was calculated for one roundtrip (cycle duration $T = 10$ ms). **e**, The temperature profile along the dashed, black line in (**a**) and (**b**) at different heights ($z = 0$ µm, 0.5 µm and 1 µm) in the liquid film. **f**, Fit of a parabolic temperature profile (dashed, blue) in the interval $x \in [-3.5, 3.5]$ µm to the height- and time-averaged temperature profile (blue).

4.4.5.3 Temperature Measurement

To extract the temperature increment from experiments, we studied the diffusion of a spherical, 200 nm diameter polystyrene particle and determined the increase in the diffusion coefficient. The increase is resulting from the elevated average temperature the particle is exposed to while it is trapped. First, the free diffusion of the particle was investigated. The same solvent and sample height as for the fibrils were used. From the mean squared displacement of the particle a diffusion coefficient $D_{\mathrm{t,free}} = 0.80\ \mu\mathrm{m}^2\mathrm{s}^{-1}$ for the free diffusion was obtained. The particle was then trapped with the same parameters used for the trapping of the fibrils (1 mW heating power, 10 µm trap diameter) and the diffusion coefficient was extracted from the tangential step size distribution as $D_{\mathrm{t,trap}} = 1.06\ \mu\mathrm{m}^2\mathrm{s}^{-1}$. With the temperature dependent Stokes–Einstein relation for the diffusion coefficient $D_\mathrm{t}(T) = k_\mathrm{B}T/(6\pi\eta(T)R)$ the ratio of the diffusion coefficients can be written as:

$$\frac{D_{\mathrm{t,free}}}{D_{\mathrm{t,trap}}} = \frac{\eta(T_0 + \Delta T)}{\eta(T_0)} \frac{T_0}{T_0 + \Delta T} \ . \tag{4.67}$$

The temperature dependence of the viscosity can be well approximated by the Vogel–Fulcher equation $\eta(T) = \eta_0 \exp(B/(T - T_{\mathrm{VF}}))$ with the parameters $\eta_0 = 29.84$ Pa s, $B = 496.89$ K and $T_{\mathrm{VF}} = 152.0$ K (Appendix A1.14). With the ratio being $D_{\mathrm{t,free}}/D_{\mathrm{t,trap}} = 0.75$ we can solve Eq. (4.67) numerically, leading to an average temperature increment of $\Delta T = 11.3$ K. Since the particle is located mostly in the center of the trap, we can assume that $\Delta T \approx \Delta T_{\mathrm{center}}$. According to the simulations a temperature rise of 11.3 K in the center of the trap leads to a chrome ring temperature of $\Delta T_{\max} = \Delta T_{\mathrm{center}}/0.56 = 20.2$ K and a curvature of $\alpha = 0.38\ \mathrm{K}/\mu\mathrm{m}^2$. The corresponding temperature profile is shown in Fig. 4.82b of Sec. 4.4.3.

4.4.5.4 Fluorescence Imaging

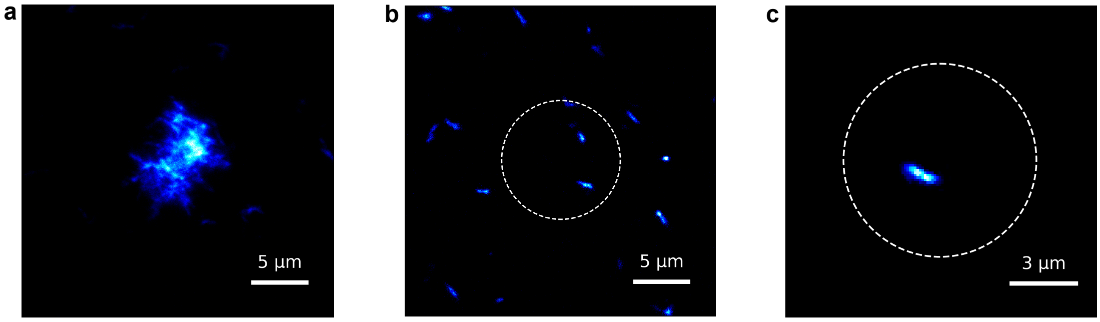

Fig. 4.94: **a**, Fluorescence image of a Aβ$_{40}$ fibril cluster in the employed sample geometry. **b**, Snapshot of freely diffusing Aβ$_{40}$ fibrils in the sample (Supplementary Video 4.1). The dash white circle depicts the inner diameter of a trap structure. **c**, Snapshot of a trapped fibril as recorded for data analysis (Supplementary Video 4.2).

4.4.5.5 TEM Images

The morphology of the fibrils has been verified by transmission electron microscopy (TEM). The TEM images reveal a rich polymorphism of the Aβ$_{40}$ fibrils (Fig. 4.95). Besides single fibrils, also bundles of fibrils and larger aggregates are present in the sample.

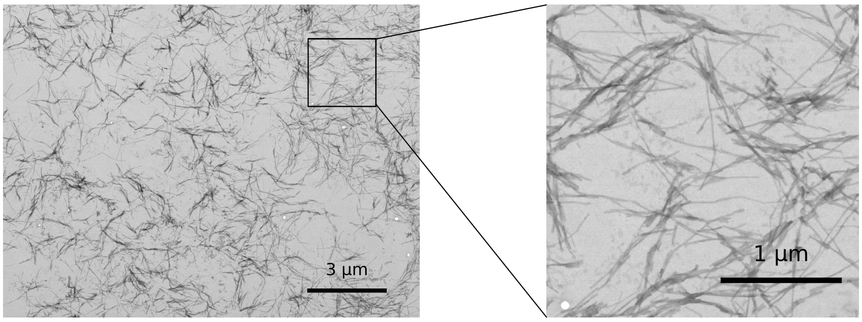

Fig. 4.95: TEM images of the investigated Aβ$_{40}$ fibril sample.

For TEM measurements the fibril solution was diluted 1:20 with Milli-Q water and a 1 ml droplet of this solution was applied to a Formvar coated copper grid, dried for about 2 h and negatively stained with 1 % uranyl acetate in Milli-Q water. TEM images were obtained using a Zeiss EM900 TEM at 80 kV.

4.4.5.6 Tracking Procedure

Fig. 4.96 depicts the main steps in the tracking and orientation determination of the fibril. First, the noise in the raw image was reduced by a three pixel median filter (Fig. 4.96a). To detect only fibrils inside the trap, a mask with a radius equal to the inner radius of the trap was applied. Then, a binary image was computed using a global threshold (Fig. 4.96b). To find the center of mass of the fibril, a connected-component labeling algorithm was used to identify connected regions in the binary image. The regions were then filtered by their area. The center of mass (COM) was then calculated from the unweighted pixel area. The orientation as well as the major and minor axes of the fibril were calculated using a principle component analysis of the binary image (Fig. 4.96c). The trajectories were linked using a memory of three COM positions. Only trajectories with a minimum length of 10 steps were used for analysis.

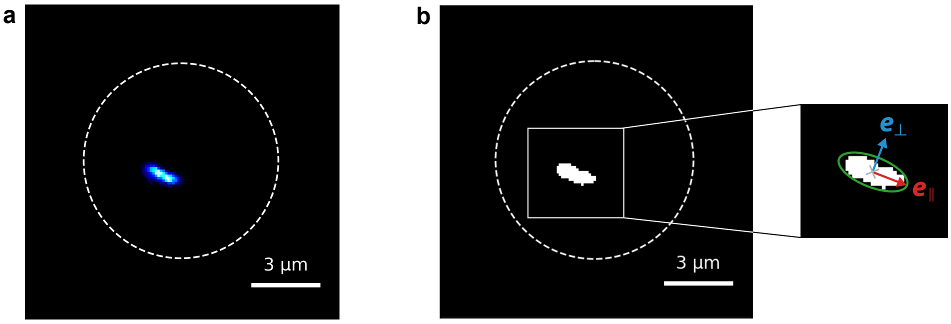

Fig. 4.96: **a**, Typical image recorded with 30 ms exposure time and 2 × 2 binning, processed with a circular mask (white dashed circle) and a three pixel median filter. **b**, Binary image computed using a global threshold. **c**, Center of mass (gray cross) and the minor and major axes (blue and red arrows) found by the connected-component labeling algorithm and the principle component analysis, respectively.

4.4.5.7 Spatially Resolved Drift Velocity

Fig. 4.97 shows the mean values of the displacements of a single fibril of length $L = 1.5$ µm projected onto the radial direction $\boldsymbol{e}_\mathrm{r}$ and the tangential direction $\boldsymbol{e}_\mathrm{t}$ of the trap. The mean values have been analyzed for 5 different distance intervals $[R, R + \Delta R]$ with $\Delta R = 0.9$ µm and $R = 0$ µm, 0.9 µm, 1.8 µm, 2.7 µm and 3.6 µm. The circles indicate the centers of each interval $R + \Delta R/2$. The resulting radial velocity (blue circles) shows a linear dependence on the distance R up to $R = 3$ µm.

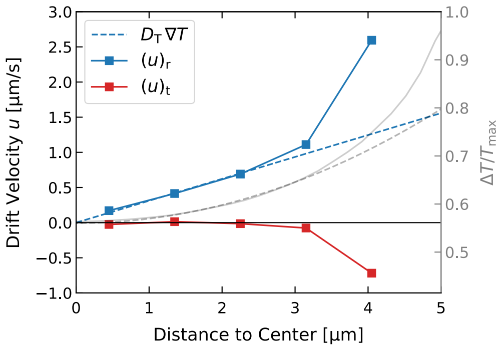

Fig. 4.97: The spatially resolved drift velocity $\boldsymbol{u}$ in the trap.

The linear increase is also indicated for $D_\mathrm{T} = 0.82$ µm^2 s^{-1} K^{-1} with the dashed blue line. The solid grey line depicts the relative temperature profile obtained from the finite element simulation (Sec. 4.4.5.2). The dashed grey line represents the parabolic approximation to the numerical temperature profile. The red line and symbols show the calculation of the mean of the tangential displacements.

4.4.5.8 Alignment

To check whether the temperature gradient causes an alignment, we evaluated the angle between the long axis $\boldsymbol{e}_\parallel$ and the radial direction $\boldsymbol{e}_\mathrm{r}$ of the trap reference frame (Fig. 4.98a):

$$\theta := \arccos\left(\left|\boldsymbol{e}_\parallel \cdot \boldsymbol{e}_\mathrm{r}\right|\right). \tag{4.68}$$

For a typical experiment no alignment is observed (Fig. 4.98b).

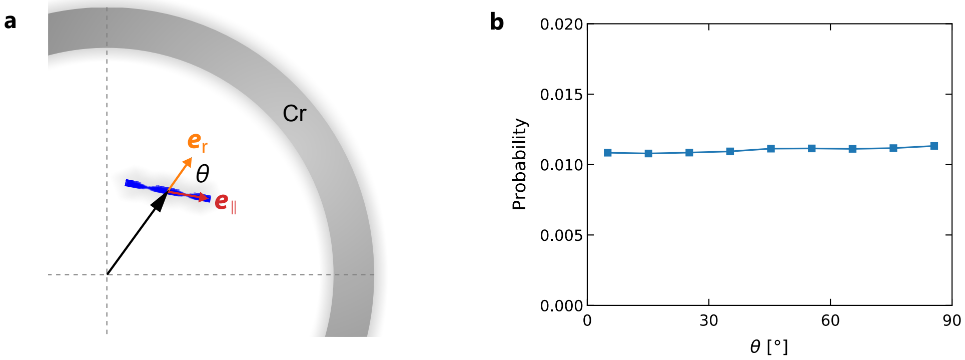

Fig. 4.98: **a**, Definition of the alignment angle θ. **b**, Distribution of θ for a typical experiment.

4.4.5.9 Datasets

Datasets 1–6: Aβ_{40} fibrils with different lengths in 1 mM phosphate buffer, pH 8.4, 6 mM NaCl:

Tab. 4.7: Length dependent datasets for Aβ_{40} (1 mM phosphate buffer, pH 8.4, 6 mM NaCl). L denotes the length of the fibril and N the sample size, that is, the number of recorded frames.

Dataset	L [µm]	NaCl [mM]	pH	N
1	0.7	6	8.4	30000
2	1.0			12500
3	1.5			30000
4	2.1			7500
5	2.5			12500
6	4.1			30000

Datasets 7–11: Aβ_{40} fibrils with varying salt and pH conditions in 25 mM phosphate buffer:

Tab. 4.8: Datasets for Aβ_{40} with varying salt and pH conditions (25 mM phosphate buffer). L denotes the length of the fibril and N the sample size, that is, the number of recorded frames.

Dataset	L [µm]	NaCl [mM]	pH	N
7	1.7	1	6.1	87500
8	1.8	1	7.4	45000
9	1.5	1	8.8	87500
10	1.4	10	7.4	25000
11	2.3	150	8.8	75000

Dataset 12: Aβ_{42} fibril (25 mM phosphate buffer, pH 9.2) with $L = 2.6$ µm ($N = 30000$)

Dataset 13: pGlu$_3$-A$\beta_{3\text{-}40}$ (pyroglutamyl-modified Aβ variant[296]) fibril (50 mM TRIS buffer, pH 8.0) with $L = 2.1$ µm ($N = 60000$)

Dataset 14–16: Aβ_{40} fibrils + 10^{-3} mg µl^{-1} Aβ_{40} monomer:

Tab. 4.9: Datasets for Aβ_{40} + Aβ_{40} monomer (10^{-3} mg µl^{-1}). Here, L denotes the initial length of the fibril and N the sample size, that is, the number of recorded frames.

Dataset	L [µm]	NaCl [mM]	pH	N
14	2.1	6	8.4	75000
15	1.2	6	8.4	
16	1.9	150	8.8	

Dataset 17: Aβ_{40} fibril + 10^{-3} mg µl^{-1} Aβ_{40} monomer (1 mM phosphate buffer, pH 8.4, 6 mM NaCl) with an initial length of $L = 1.6$ µm. The sample size of each interval is $N = 12500$.

4.4.5.10 Diffusion of Rods

The aim of this section is to show that the hydrodynamic theory for the two-dimensional diffusion of rods in a boundary-free fluid can be applied to rods confined in thin films. The hydrodynamic interaction with the glass surface increases the effective friction leading to a higher apparent viscosity, but leaves the length dependence of the diffusion coefficients unchanged. The theory presented here is mainly reproduced from Ref. 302.

Diffusion in a Boundary-Free Fluid For a rod-like macromolecule in a boundary-free fluid the translational diffusion coefficients are[302]

$$D_\mathrm{t}^{\parallel} = \frac{k_\mathrm{B}T\left(\ln(L/d) + \xi_{\parallel}\right)}{2\pi\eta L} \,, \tag{4.69}$$

$$D_\mathrm{t}^{\perp} = \frac{k_\mathrm{B}T\left(\ln(L/d) + \xi_{\perp}\right)}{4\pi\eta L} \,, \tag{4.70}$$

the two-dimensional translational diffusion coefficient is:

$$D_\mathrm{t} = \frac{1}{2}\left(D_\mathrm{t}^{\parallel} + D_\mathrm{t}^{\perp}\right) = \frac{k_\mathrm{B}T\left(3\ln(L/d) + 2\xi_{\parallel} + \xi_{\perp}\right)}{8\pi\eta L} \,, \tag{4.71}$$

and the rotational diffusion coefficient is:

$$D_\mathrm{r} = \frac{3k_\mathrm{B}T\left(\ln(L/d) + \xi_\mathrm{r}\right)}{\pi\eta L^3} \,. \tag{4.72}$$

Here, L is the length and d is the diameter of the macromolecule. For $L/d \to \infty$ the values of the end-correction coefficients are $\xi_{\parallel} = -0.114$, $\xi_{\perp} = 0.886$ and $\xi_\mathrm{r} = -0.447$[294]. The length dependence of the rod diffusion in a boundary-free liquid is shown in Fig. 4.99.

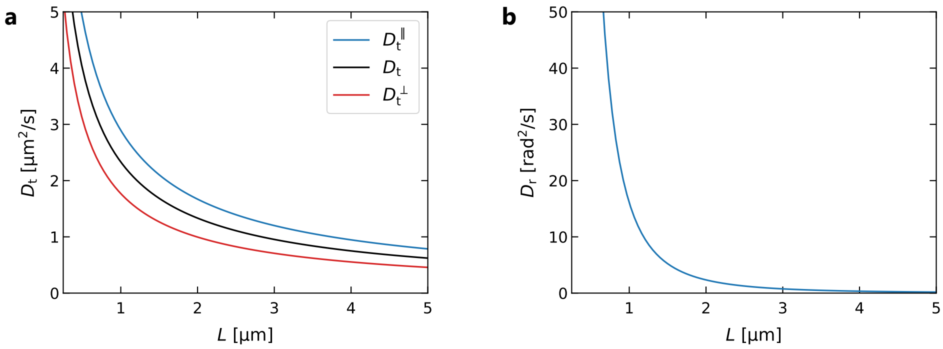

Fig. 4.99: Dependence of the diffusion coefficients on the rod length L in a boundary-free fluid according to Eqs. (4.69), (4.70), (4.71) and (4.72) with $d = 10$ nm assuming a viscosity of water of $\eta = 10^{-3}$ Pa s.

Diffusion within a Thin Layer between Two Walls The diffusion coefficient $D = k_\mathrm{B}T/\gamma$ is inversely proportional to the drag coefficient γ (Sec. 2.1.2). A cylinder feels a larger drag when it is closer to a wall. The drag coefficient per unit length for a cylinder parallel to a wall moving parallel to the cylinder axis is[303]

$$c_\| = \frac{2\pi\eta}{\cosh^{-1}(h/r)} \ , \tag{4.73}$$

where h is the distance from the cylinder axis to the wall and $r = d/2$ is the radius of the cylinder. For a motion parallel to the wall, but perpendicular to the cylinder axis, the drag coefficient per unit length is:

$$c_\perp = 2c_\| \ . \tag{4.74}$$

However, the rod is not always parallel to the walls. Fig. 4.100 shows a side view of a typical state of a rod defined by (z, θ), where z is the center of mass position and θ the tilt angle from the surface.

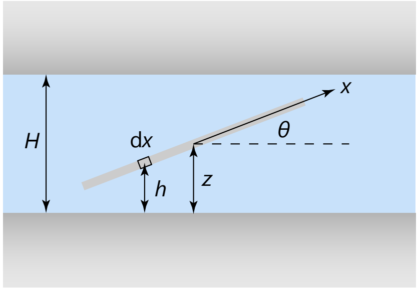

Fig. 4.100: Typical state (z,θ) of a rod between two walls.

To calculate the diffusion coefficient, we need to know the drag coefficient at each state. We assume that:

1. The drag coefficient per unit length $c_\|$ of a section of the cylinder $\mathrm{d}x$ with distance z to the wall is given by Eq. (4.73).
2. The total drag on $\mathrm{d}x$ is the sum of the drags by the two walls.

Therefore, the drag coefficient for each state can be expressed as

$$\gamma_\|(z,\theta) = \int_{-L/2}^{L/2} \left(\frac{2\pi\eta}{\cosh^{-1}((z + x\sin\theta)/R)} + \frac{2\pi\eta}{\cosh^{-1}((H - z - x\sin\theta)/R)} \right) \mathrm{d}x \ . \tag{4.75}$$

The two-dimensional translational diffusion coefficient for this state is[302]

$$D_\mathrm{t}(z,\theta) = \frac{1}{2} \left(\frac{k_\mathrm{B}T}{\gamma_\|(z,\theta)} \cos^2\theta + \frac{k_\mathrm{B}T}{\gamma_\perp(z,\theta)} (1 + \sin^2\theta) \right) . \tag{4.76}$$

The overall translational diffusion coefficient is the average over all states:

$$D_\mathrm{t} = \frac{\displaystyle\int_0^{H/2} \int_{-\theta_\mathrm{max}}^{\theta_\mathrm{max}} D_\mathrm{t}(z,\theta)\ \mathrm{d}\theta\ \mathrm{d}z}{\displaystyle\int_0^{H/2} \int_{-\theta_\mathrm{max}}^{\theta_\mathrm{max}} \mathrm{d}\theta\ \mathrm{d}z} \tag{4.77}$$

with $\theta_\mathrm{max} = \sin^{-1}(2z/L)$. When the rod rotates with angular frequency ω perpendicular to the walls in the state (z,θ) the torque on the rod is:

$$\tau(z,\theta) = \int_{-L/2}^{L/2} c_\perp\, \omega\, x^2 \cos^2\theta\ \mathrm{d}x \ . \tag{4.78}$$

Therefore, the rotational drag coefficient is:

$$\gamma_\mathrm{r}(z,\theta) = \frac{\tau(z,\theta)}{\omega} = \int_{-L/2}^{L/2} \left(\frac{4\pi\eta\, x^2 \cos^2\theta}{\cosh^{-1}((z + x\sin\theta)/R)} + \frac{4\pi\eta\, x^2 \cos^2\theta}{\cosh^{-1}((H - z - x\sin\theta)/R)} \right) \mathrm{d}x$$

and the rotational diffusion coefficient is:

$$D_\mathrm{r}(z,\theta) = \frac{k_\mathrm{B}T}{\gamma_\mathrm{r}(z,\theta)} \ . \tag{4.79}$$

The overall rotational diffusion coefficient is:

$$D_\mathrm{r} = \frac{\displaystyle\int_0^{H/2} \int_{-\theta_\mathrm{max}}^{\theta_\mathrm{max}} D_\mathrm{r}(z,\theta)\ \mathrm{d}\theta\ \mathrm{d}z}{\displaystyle\int_0^{H/2} \int_{-\theta_\mathrm{max}}^{\theta_\mathrm{max}} \mathrm{d}\theta\ \mathrm{d}z} \ . \tag{4.80}$$

Fig. 4.101 shows the length dependence of the diffusion coefficients calculated using Eqs. (4.77) and (4.80) for a sample height of $H = 1$ µm in comparison to diffusion coefficients expected in a boundary-free fluid.

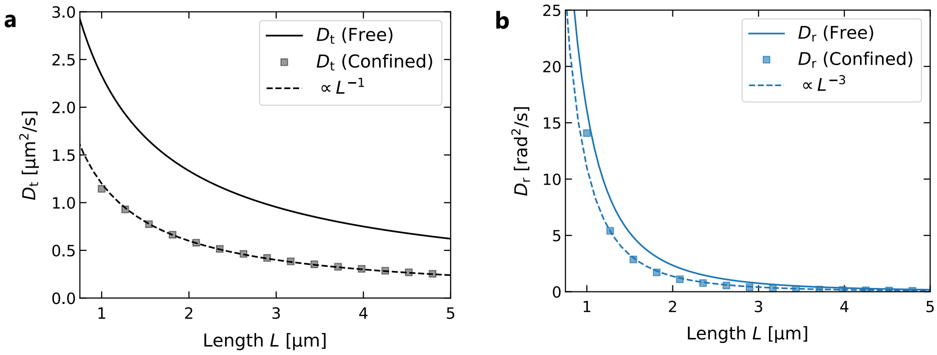

Fig. 4.101: Comparison of the length-dependent diffusion coefficients for a rod confined between two walls of distance $H = 1$ µm according to Eqs. (4.77) and (4.80) (blue, black circles) to the diffusion coefficients in a boundary-free fluid (solid lines), Eqs. (4.71) and (4.72). The dashed lines are power law fits to the confined diffusion coefficient.

The interaction with the walls increases the effective friction leading to higher apparent viscosity, but leaves the general length dependence of the diffusion coefficients unchanged.

4.4.5.11 Measurement Accuracy

Rotational Diffusion Coefficient The rotational diffusion coefficient D_r of the fibril can be inferred from the variance σ^2 of the angular displacement steps $\Delta\varphi$, which follow a normal distribution $\sim \mathcal{N}(\langle\Delta\varphi\rangle, \sigma^2)$, via

$$\sigma^2 = 2D_\mathrm{r}\tau \ . \tag{4.81}$$

For a finite set of angular displacement steps $\Delta\varphi_1, \Delta\varphi_2, \ldots, \Delta\varphi_N$ the true variance, and thus also the true rotational diffusion coefficient, can only be approximated with the help of an estimator. The unbiased estimator for σ^2 is:

$$\hat{\sigma}^2 = \frac{1}{N-1} \sum_{i=1}^{N} \Delta\varphi_i^2 \ . \tag{4.82}$$

A mean squared error defined by $\mathrm{Var}(\hat{\sigma}^2) = \langle(\hat{\sigma}^2 - \sigma^2)^2\rangle$ assesses the quality of the estimator. The mean squared error in our case is[304]:

$$\mathrm{Var}(\hat{\sigma}^2) = \frac{2\sigma^4}{N-1} \ . \tag{4.83}$$

As $\hat{\sigma}^2$ is a random variable with finite mean value $\langle\hat{\sigma}^2\rangle = \sigma^2$ and finite and non-zero variance according to Eq. (4.83), we can use Chebyshev's Inequality (4.84) to explore the dependency of the relative error $\delta_{\sigma^2} = \left|\hat{\sigma}^2 - \sigma^2\right| / \sigma^2$ in dependence on the recorded number of frames N:

$$P\big(\,|X - \langle X\rangle| \geq \hat{k}\big) \leq \frac{\mathrm{Var}(X)}{\hat{k}^2} \ , \tag{4.84}$$

where $\hat{k}$ is a positive, real number. Inserting $X = \hat{\sigma}^2$ we can rewrite the term in the brackets of Ineq. (4.84) as

$$\left|\hat{\sigma}^2 - \langle\hat{\sigma}^2\rangle\right| \geq \hat{k} \quad \Leftrightarrow \quad \delta_{\sigma^2} \geq k \ ,$$

with $k := \hat{k}/\sigma^2$ as an upper bound of the relative error of the rotational diffusion coefficient. Ineq. (4.84) then yields:

$$P(\delta_{\sigma^2} \geq k) \leq \frac{2}{(N-1)\,k^2} \ . \tag{4.85}$$

Considering that $\hat{\sigma}^2 = 2\hat{D}_\mathrm{r}\tau$ with $\hat{D}_\mathrm{r}$ being the estimate for the rotational diffusion coefficient D_r, we can furthermore replace δ_{σ^2} by δ_{D_r} in Ineq. (4.85) since

$$\delta_{\sigma^2} = \frac{|\,\hat{\sigma}^2 - \sigma^2\,|}{\sigma^2} = \frac{|\,\hat{D}_\mathrm{r} - D_\mathrm{r}\,|}{D_\mathrm{r}} =: \delta_{D_\mathrm{r}} \ . \tag{4.86}$$

Ineq. (4.85) then reads:

$$P(\delta_{D_\mathrm{r}} \geq k) \leq \frac{2}{(N-1)\,k^2} \ . \tag{4.87}$$

For finding an estimate of the rotational diffusion coefficient we are interested in the complementary event of what Chebyshev's inequality states, that is:

$$P(\delta_{D_\mathrm{r}} < k) \geq 1 - \frac{2}{(N-1)\,k^2} \geq p \ , \tag{4.88}$$

where p is some fixed value stating the probability that the upper bound of the relative error of the rotational diffusion coefficient is at least fulfilled. A rearrangement of the terms gives us the upper bound of the rotational diffusion coefficient k in dependence on the number of recorded frames N:

$$k \geq \left(\frac{2}{(1-p)(N-1)}\right)^{-1/2} . \tag{4.89}$$

Additionally, one can convert Ineq. (4.89) into an equation for the relative error of the rotational diffusion coefficient:

$$\delta_{D_\mathrm{r}} < k = \left(\frac{2}{(1-p)(N-1)}\right)^{-1/2} . \tag{4.90}$$

The derivation of the measurement accuracy for the translational diffusion coefficient D_t is exactly the same since the spatial step sizes of the COM of the fibril also follow a normal distribution.

Soret Coefficient The Soret coefficient S_T of the fibril can be obtained from the variance σ^2 of the radial particle positions R, which follow a Rayleigh distribution with probability density function:

$$P(R) = \begin{cases} 0 & R < 0 \ , \\ \frac{R}{\sigma^2}\,\mathrm{e}^{-R^2/(2\sigma^2)} & R \geq 0 \ . \end{cases} \tag{4.91}$$

For a finite set of radial particle positions $R_1, R_2, ..., R_N$ the true variance can be approximated with the maximum likelihood estimator:

$$\hat{\sigma}^2 = \frac{1}{2N}\sum_{i=1}^{N} R_i^2 \ , \tag{4.92}$$

which is unbiased as $\langle\hat{\sigma}^2\rangle = \langle R^2\rangle/2 = \sigma^2$. The mean squared error of this estimator, defined as $\mathrm{Var}(\hat{\sigma}^2) = \langle(\hat{\sigma}^2 - \sigma^2)^2\rangle$, is in this case

$$\mathrm{Var}(\hat{\sigma}^2) = \frac{1}{4N}\left(\langle R^4\rangle - \langle R^2\rangle^2\right) = \frac{\sigma^4}{N} \ , \tag{4.93}$$

where we used that $\langle R^4\rangle = 8\sigma^4$. Following the same procedure as for the rotational diffusion coefficient we find for the relative error of the variance σ^2:

$$\delta_{\sigma^2} < k = \left(\frac{1}{(1-p)N}\right)^{-1/2} . \tag{4.94}$$

The uncertainty of the Soret coefficient $\hat{S}_\mathrm{T}$ can be then calculated by using the relation $\hat{\sigma}^2 = 1/(\alpha\hat{S}_\mathrm{T})$ and error propagation via:

$$\delta_{S_\mathrm{T}} = \frac{\delta_{\sigma^2}}{\alpha\hat{\sigma}^4} < \frac{1}{\alpha\hat{\sigma}^4}\left(\frac{1}{(1-p)N}\right)^{-1/2} . \tag{4.95}$$

4.4.5.12 Video Files

The Supplementary Videos are available at https://www.doi.org/10.5281/zenodo.5831821.

Video 4.1: Freely diffusing Aβ$_{40}$ fibrils imaged using Thioflavin T as fluorescence marker inside a typical sample. The dashed circle indicates the inner diameter (10 µm) of a thermophoretic trap. The exposure time and inverse framerate correspond to 30 ms.

Video 4.2: Aβ$_{40}$ fibril of length $L = 1.5$ µm confined inside a thermophoretic trap with an incident laser heating power of $P_0 = 1$ mW. The dashed circle indicates the inner diameter (10 µm) of the trap. The exposure time and inverse framerate correspond to 30 ms.

Video 4.3: Tracked position and orientation of the Aβ$_{40}$ fibril shown in Supplementary Video 4.2. The dashed circle indicates the inner diameter (10 µm) of the trap. The exposure time and inverse framerate correspond to 30 ms.

Video 4.4: Fragmentation of a trapped Aβ$_{40}$ fibril of length $L = 1.1$ µm corresponding to the image sequence Fig. 4.89b. The dashed circle indicates the inner diameter (10 µm) of the trap. The exposure time and inverse framerate correspond to 30 ms.

Summary and Outlook

5

This thesis explored the principles and applications of laser-induced heating of plasmonic structures at the boundary of small liquid volumes. In such systems a variety of micro- and nanoscale phenomena such as thermal convection, thermophoresis, depletion, thermoelectricity as well as thermo-osmosis have been suggested in various experiments. Yet, the relevance of the underlying physical interactions as well as the quantitative interplay of the mentioned effects is not well explored, hampering the development of new applications. To progress this field we have carried out dedicated experiments using, for example, single particle tracking of metal and dielectric nanoparticles under well-defined conditions (Sec. 4.1). One of our key findings is that the local temperature perturbation of van der Waals interactions is responsible for strong thermo-osmotic flows at gold–water interfaces that are often misinterpreted as convective flows. Understanding this interaction gives rise to new applications for the manipulation of nanoparticles by hydrodynamic boundary flows. Sec. 4.2 presented a symmetric self-thermophoretic microswimmmer driven by thermo-osmotic flows on its surface. In comparison to Janus-type particles, where the propulsion direction is fixed, the motion direction of a symmetric microswimmmer can be set by the heating laser itself. This way, the propulsion direction becomes independent of the rotational diffusion, providing a substantially higher level of control than previously possible. We analysed their feedback-controlled actuation within a quantitative framework and revealed a directional uncertainty with general implications for the targeted self-propulsion of microscopic objects. To achieve the actuation of the symmetric microswimmers also in heterogeneous particle ensembles, Sec. 4.3 evaluated a neural network approach for the real-time detection of nano-objects in digital microscopy images. The employed network allows for the feedback control of complex active particle systems in imaging situations that have been impossible to study before. Based on the thermophoretic drift of macromolecules, Sec. 4.4 presented a thermophoretic trap for protein aggregation studies. The aggregation of proteins into amyloid fibrils is fundamental for life, as it is linked to a large range of devastating disorders but also functional structures. A substantial difficulty in the investigation of macromolecular nucleation and growth processes is the heterogeneity of the ensemble studied. Samples contain aggregates of different sizes which grow in an unsynchronized way. Several studies aimed to disentangle heterogeneous ensembles, but none of those experiments has been able to follow the growth of a freely suspended fibril without the perturbing immobilization at a solid surface. With the thermophoretic trap, we enabled for the first time the observation of single amyloid fibrils free in solution and introduced the rotational diffusion coefficient as a very sensitive measure for the growth and fragmentation of single amyloid fibrils. To date, this method is the only one available to measure growth rates and secondary nucleation events at the single fibril level without surface perturbation.

The following paragraphs provide detailed summaries and outlooks for the results presented in Secs. 4.1–4.4 (Publications P1–P4).

Sec. 4.1: Hydrodynamic Manipulation of Nano-Objects by Thermo-Osmotic Flows

In Sec. 4.1 a thin gold film on a glass substrate, locally heated by a focused laser beam, has been used to study temperature-driven effects in a thin liquid film over the gold surface. Based on a detailed analysis of the particle transport in the liquid, we demonstrated that the local temperature gradients on the water–gold interface induce thermo-osmotic flows in the order of several 10 $\mu m\,s^{-1}$ in close proximity to the gold surface. We find that these flows on the water–gold interface are by one order of magnitude larger than previously reported for the water–glass interface[49] and revealed that they are mainly determined by the temperature-dependent perturbation of the van der Waals interaction between water and gold. In the literature these flows are often overlooked or attributed to thermal convection. We showed experimentally as well as numerically that in small liquid volumes the contributions from thermo-osmotic flows are orders of magnitude larger than flows from thermal convection. The resulting long-range hydrodynamic forces acting on suspended nano-objects together with additional van der Waals or depletion induced forces have then been employed to trap micro- and nanoparticles above the heated spot. The vertical confinement of gold nanoparticles has been realized utilizing the secondary minimum of the DLVO potential between nanoparticle and the gold surface which can be well-controlled with the amount of added salt. The NaCl concentration can be adjusted to confine the motion of gold nanoparticles very close to the heated interface. Remarkably, distances down to 10 nm could be achieved which is well below the commonly explored region of hydrodynamic coupling of colloids to walls. Unlike gold nanoparticles, polystyrene particles are repelled from the heated region due to their additional thermophoretic motion. To confine also these type of particles, we added the surfactant SDS to the liquid. The SDS molecules migrate towards colder regions caused by thermophoresis and generate a concentration gradient that drives larger particles to the heated spot due to depletion forces. The trapping of PS nanoparticles as well as micrometer-size PS ellipsoids has been demonstrated with the surfactant SDS. While many experiments have qualitatively described temperature-induced particle transport over heated gold surfaces, we provide a quantitative analysis of the individual effects. In particular, we were able to disentangle thermo-osmotic flows from thermophoretic drifts using nanoparticles with different thermal conductivity. In contrast to other reports, we find that contributions from thermal convection and thermoelectricity can be neglected in the employed sample geometry and our observations can be solely explained in terms of thermo-osmotic flows, DLVO forces and thermally driven depletion. Furthermore, we demonstrated the parallel manipulation of multiple nano-objects with multiplexed flow fields and outlined a general scheme of nanoscopic manipulation with boundary flows. These concepts are the key for future thermo-optofluidic implementations with an extensive range of applications in the fields of nanoparticle assembly and separation[202,305,306], microfluidic lab-on-chips for biotechnology[221] and plasmonic quantum sensors[201,206]. The unique ability to dynamically trap and actuate gold nanoparticles in close proximity to a gold film may be exploited as a reconfigurable plasmonic particle-on-film[206]. The nanocavity formed by a metal nanoparticle separated a few nanometers from a metal film has recently gained considerable interest due to its adjustable optical properties and the confinement of incident light in the gap region. Within the gap the electric field intensity is significantly increased, enhancing optical effects such as fluorescence and Raman scattering[217]. Further investigations may focus on the spectral properties of these systems and explore applications in the field of plasmon-enhanced spectroscopy. The fact that thermo-osmotic flows are particularly strong on water–metal interfaces has direct consequences for nearly all thermoplasmonic trapping schemes and especially the field of plasmonic nano-tweezers. Moreover, our findings are of importance for studying the thermotaxis of metal-capped Janus-particles, where latest experiments suggest a significant difference between the thermo-osmotic coefficients of the gold cap and the polystyrene surface[307]. As several recent reports have drawn the attention to thermo-optofluidic experiments involving surfactants[3,6,52,308], further experiments may focus on the impact of other commonly used surfactants such as CTAC or Triton X-100. While our thermo-optofluidic platform is currently implemented in a simple geometry and controlled with algorithmic approaches, recent developments in the field of machine learning including real-time microscopic feedback (Sec. 4.3) together with an integration in pressure-driven microfluidics, provide the great potential to control even biological and chemical processes on the microscale[309,310].

Sec. 4.2: Symmetric Self-Thermophoretic Microswimmer

Within Sec. 4.2 we studied the actuation of symmetric self-thermophoretic microswimmers. These comprise a micrometer-size polymer particle with 10% of their surface covered with gold nanoparticles. Compared to self-thermophoretic Janus particles, where the propulsion direction is tied to the orientation of their metal cap, the propulsion direction of a symmetric microswimmer is imprinted by the asymmetric illumination of the particle with a highly focused laser beam. This way, the propulsion direction becomes independent of the rotational diffusion providing a substantially higher level of control than previously possible for Janus particles. To control the motion of the symmetric microswimmers, the position of the heating laser needs to be constantly adapted in a feedback loop with the detection of the particle position to adjust for its self-propelled motion as well as for its diffusive motion. We measured the propulsion velocity as function of the asymmetric illumination and found optimal parameter to maximize the propulsion velocity. In agreement with a quantitative model we revealed that the optimal displacement of the heating laser from the particle center is dependent on the size of the particle, the beam waist of the heating laser as well as the frame rate of the image acquisition. Furthermore, it was shown that the propulsion velocity can be well predicted considering the thermo-osmotic flows on the Pluronic F-127 coated particle surface . A maximum velocity in the order of $10\ \mu\mathrm{m\,s}^{-1}$ could be achieved before damaging the particle. It was found that the propulsion velocity scales non-linear with the heating power caused by the finite frame rate of the image acquisition. The position of the laser focus can only be adapted with a certain delay due to the limited speed of image acquisition with the inverse frame rate τ. It could be shown that the propulsion velocity scales with τ^{-1} while the positioning error scales linearly with τ. Hence, a small feedback delay is beneficial for both, a large propulsion velocity as well as for a high positioning accuracy. Further analysis of the directional noise revealed that, if a microscopic object tries to reach a target, large propulsion velocities are actually not beneficial if the object responds with a delay[244]. This suggests, ultimately, also a speed limit for biological species such as bacteria reaching for a target. The design of the microswimmer enables a precise control of large ensembles of these particles to explore, for example, the collective behavior in active particle systems and allows for the preparation of dense ensembles with a well defined number of particles to study hydrodynamic interactions[311] and the self-assembly of non-equilibrium structures[86,87,246]. Thereby the feedback-driven actuation principle provides the unique possibility to introduced non-reciprocal or delayed interactions. Combined with machine learning techniques such as convolutional neural network detectors (Sec. 4.3) and reinforcement learning[261] we envision autonomous active particle systems to explore emergent phenomena on the microscale[243,312].

Sec. 4.3: Active Particle Feedback Control with Neural Networks

To achieve the actuation of active particles also in heterogeneous particle ensembles, Sec. 4.3 introduced a single-shot detection neural network. We adapted the YOLOv2 neural network architecture and trained the network with computer generated optical microscopy images for various particle shapes and sizes. Demonstrated with synthetic test images, the trained network is capable to localize particles with sub-pixel resolution down to very low signal-to-noise ratios and is able to separately detect nearby objects even if one of the objects is by a order of magnitude less intense. Using a GPU the neural network can be executed within less than 10 ms allowing for frame rates of up to 100 fps. The detection speed is thereby independent of the number of particles and the complexity of the image. While neural network detectors have already been introduced to the field of optical microscopy, these methods have been designed for the post-processing of recorded images. With our framework we contribute a neural network detector that is optimized for small latency paving the way for advanced the feedback-controlled applications. We presented a first experimental application with the multiplex-actuation of the symmetric self-thermophoretic microswimmers introduced in Sec. 4.3 while tracking passive particles in the background. As a perspective for future applications, we evaluated the network performance for the detection of five different particle classes, including the detection of their orientation. We found that the network is able to properly localize and classify the particles despite their different sizes, orientation and intensities, a task that is impossible to solve with algorithmic approaches within a time frame of 10 ms. The real-time capability of the presented network is an important step towards active particle system where the feedback control is fully self-regulated by machine learning techniques. These systems have the enormous potential of autonomously learning how to achieve specified goals. Furthermore, our work possesses the ability to control processes in even the most challenging imaging situation such as biological species[313]. In future applications the detection performance may be increased using refined versions of the YOLO architecture[314,315] and the detection output may be connected to sorting networks such as DeepSORT[316] to enable also a real-time tracking capability.

Sec. 4.4: Thermophoretic Trap for Protein Aggregation Studies

Sec. 4.4 presented a thermophoretic trap to isolate and study protein aggregates in heterogeneous ensembles. With this method we enabled, for the first time, the investigation of single fibrils free in solution. We thermophoretically trapped single Aβ fibrils with an optically heated chrome structure and imaged their center of mass position as well as their in-plane orientation using ThT as fluorescent dye. Thereby the distribution of the center of mass position was used to estimate the Soret coefficient of the fibril and displacement statistics has been used to obtain their diffusion coefficients. In agreement with theoretical predictions we find a linear dependence of the Soret coefficient with the fibril length L and a scaling of the translational diffusion coefficient with L^{-1}. The rotational diffusion coefficient has been confirmed to scale with L^{-3}, hence, delivering a very sensitive measure for length changes. By monitoring the time-dependence of the rotational diffusion coefficient, we have been able to resolve length changes well below the optical resolution limit and evaluated growth rates of single $A\beta_{40}$ fibrils in presence of $A\beta_{40}$ monomers. Depending on the buffer conditions we found growth rates in the order of $0.1\ \mathrm{nm\,s^{-1}}$ (~ 1 monomer every 10 s). Nevertheless, under the same buffer conditions we also observed non-growing fibrils, suggesting a heterogeneity even of the fibrillar aggregates. These experiments highlight the unparalleled ability of the thermophoretic trap to estimate growth rates of single amyloid fibrils in heterogeneous ensembles of monomers, oligomers and fibrils of different length and quaternary structure. So far, growth rates of single fibrils could only be estimated for fibrils attached to surfaces, while it has been reported that surfaces significantly alter the nucleation and aggregation[317]. With our technique we give access to the growth rate of single fibrils diffusing in solution. While the trap was exemplified for Aβ fibrils associated to Alzheimers's disease, it can be applied to the entire range of amyloid forming proteins[112]. To further highlight the board applicability of the thermophoretic trap we demonstrated the trapping for a range of NaCl concentrations and pH values as well as under biological buffer condition. Besides the estimation of growth rates for single fibrils the thermophoretic trap holds the unique potential for the observation of secondary nucleation events such as fibril fragmentation and surface nucleation typically hidden in the ensemble average. We recorded, for the first time, a fragmentation of a $A\beta_{40}$ fibril. The detection of this event, once more, highlights the benefit of the thermophoretic trap. Since the orientation detection is based on the analysis of a fluorescence image, it is restricted to fibrils with a length larger than the diffraction limit and the time resolution is limited to the maximum frame rate of the image acquisition. In an extended experimental setup polarization resolved fluorescence detection[291,301,318] with photodiodes might be used for fast rotational diffusion measurements that allows also for the orientation detection of very small aggregates. To achieve the trapping of even the smallest aggregates such as oligomers, advanced trapping schemes may combine a feedback-controlled temperature field with thermo-osmotic flows and depletion forces as discussed in Sec. 4.1. The real-time object detection required for the feedback control would directly benefit from the developments in Sec. 4.3. Furthermore, multicolor detection schemes can be introduced to explore secondary surface nucleation and a combination with advanced micro- and nanofluidic approaches[319] (Sec. 4.1) could allow for a cross-seeding with different peptide variants. The thermophoretic trapping of single amyloid fibrils presented in this work provides only the starting point for more complex studies in the fields of misfolding diseases[111] and functional protein aggregation[320].

Appendix

A

A1 Theoretical Background

A1.1 Stokes Flow Past a Sphere

The velocity field around a sphere that dragged though a liquid by an external force is given by

$$v_r = u\cos\theta\left(1 - \frac{3R}{2r} + \frac{R^3}{2r^3}\right) \ , \tag{A1.1}$$

$$v_\theta = -u\sin\theta\left(1 - \frac{3R}{4r} - \frac{R^3}{4r^3}\right) \ , \tag{A1.2}$$

in the reference frame of the sphere[125]. Fig. 2.1a, b depict the velocity field in the laboratory frame, $v_x - u$.

A1.2 Mean Squared Displacement

We consider Eq. (2.10):

$$\frac{\mathrm{d}x}{\mathrm{d}t} = \sqrt{2D}\,\xi(t) \ ,$$

with

$$x(t) = x(0) + \sqrt{2D}\int_0^t \xi(t')\,\mathrm{d}t' \ .$$

The mean squared displacement then is:

$$\langle \Delta x^2(t)\rangle = \langle (x(t) - x(0))^2\rangle = \underbrace{\langle x^2(t)\rangle}_{2Dt+x^2(0)} - 2\underbrace{\langle x(t)\rangle}_{=x(0)} x(0) + x^2(0) = 2Dt \ .$$

We have used:

$$\langle x(t)\rangle = x(0) + \sqrt{2D}\int_0^t \underbrace{\langle \xi(t')\rangle}_{=0}\,\mathrm{d}t' = x(0) \ ,$$

$$\langle x^2(t)\rangle = x^2(0) + 2\sqrt{2D}\int_0^t \underbrace{\langle \xi(t')\rangle}_{=0}\,\mathrm{d}t'\,x(0) + 2D\int_0^t \underbrace{\left(\int_0^t \underbrace{\langle \xi(t')\xi(t'')\rangle}_{\delta(t'-t'')}\,\mathrm{d}t''\right)}_{=1}\mathrm{d}t' = 2Dt + x^2(0) \ ,$$

with $\langle \xi(t)\rangle = 0$ and $\langle \xi(t)\xi(t')\rangle = \delta(t - t')$.

A1.3 Free Diffusion Equation

We consider Eq. (2.10):

$$\frac{\mathrm{d}x}{\mathrm{d}t} = \sqrt{2D}\,\xi(t) \ ,$$

and Eq. (2.12):

$$p(x,t) = \langle \delta(x - x(t)) \rangle \ .$$

We have:

$$x(t+\Delta t) = x(t) + \Delta x \quad \text{with} \quad \Delta x = \sqrt{2D} \int_t^{t+\Delta t} \xi(t')\,\mathrm{d}t' \ .$$

With Eq. (2.12) the probability density distribution $p(x, t+\Delta t)$ then reads:

$$p(x, t+\Delta t) = \langle \delta(x - x(t+\Delta t)) \rangle = \langle \delta(x - x(t) + \Delta x) \rangle \ .$$

As Δt and Δx are small we can expand both sides of the equation in a Taylor series:

$$p(x,t) + \Delta t \frac{\partial}{\partial t} p(x,t) = \underbrace{\langle \delta(x - x(t) \rangle}_{= p(x,t)} + \underbrace{\langle \Delta x \rangle}_{=0} \frac{\partial}{\partial x} \langle \delta(x - x(t) \rangle + \underbrace{\langle \Delta x^2 \rangle}_{= 2D\Delta t} \frac{1}{2} \frac{\partial^2}{\partial x^2} \underbrace{\langle \delta(x - x(t) \rangle}_{= p(x,t)} \ ,$$

leading to the free diffusion equation:

$$\frac{\partial p(x,t)}{\partial t} = D \frac{\partial^2 p(x,t)}{\partial x^2} \ .$$

We have used:

$$\langle \Delta x \rangle = \sqrt{2D} \int_t^{t+\Delta t} \mathrm{d}t' \underbrace{\langle \xi(t') \rangle}_{=0} = 0 \ ,$$

$$\langle \Delta x^2 \rangle = 2D \int_t^{t+\Delta t} \underbrace{\left(\int_t^{t+\Delta t} \underbrace{\langle \xi(t') \xi(t'') \rangle}_{\delta(t'-t'')} \mathrm{d}t'' \right)}_{=1} \mathrm{d}t' = 2D\Delta t \ ,$$

with $\langle \xi(t) \rangle = 0$ and $\langle \xi(t) \xi(t') \rangle = \delta(t - t')$.

A1.4 Mean First Passage Time

The mean first passage time is defined as

$$\langle \tau(x) \rangle = \int_0^\infty \tau\, f(\tau|x)\, \mathrm{d}\tau \ , \tag{A1.3}$$

where $f(\tau|x)$ is probability that a target x has been reached by the time τ. With the probability distribution $p(x,t)$ defined by the Fokker-Planck equation, Eq.(2.25):

$$\frac{\partial p(x,t)}{\partial t} = \frac{\partial}{\partial x} \left(\frac{1}{k_\mathrm{B} T} D(x) \frac{\partial U(x)}{\partial x} p(x,t) + D(x) \frac{\partial p(x,t)}{\partial x} \right), \tag{A1.4}$$

the mean first passage time satisfies[131]

$$-\frac{1}{k_\mathrm{B} T} D(x) \left(\frac{\mathrm{d}}{\mathrm{d}x} U(x) \right) \frac{\mathrm{d}}{\mathrm{d}x} \langle \tau(x) \rangle + \frac{\mathrm{d}}{\mathrm{d}x} \left(D(x) \frac{\mathrm{d}}{\mathrm{d}x} \langle \tau(x) \rangle \right) = -1 \ . \tag{A1.5}$$

We find

$$\frac{\mathrm{d}}{\mathrm{d}x}\left(D(x)\mathrm{e}^{-\beta U(x)}\frac{\mathrm{d}}{\mathrm{d}x}\langle\tau(x)\rangle\right) = -\mathrm{e}^{-\beta U(x)}\ , \tag{A1.6}$$

with $\beta = 1/(k_\mathrm{B}T)$. Integration from $-\infty$ to x yields:

$$\frac{\mathrm{d}}{\mathrm{d}x}\langle\tau(x)\rangle = -\frac{1}{D(x)}\mathrm{e}^{\beta U(x)}\int_{-\infty}^{x}\mathrm{e}^{-\beta U(x'')}\,\mathrm{d}x''\ . \tag{A1.7}$$

Finally, a second integration from x_min to x with $\langle\tau(x_\mathrm{min})\rangle = 0$ gives:

$$\langle\tau(x)\rangle = \int_{x_\mathrm{min}}^{x}\left(\frac{\mathrm{e}^{\beta U(x')}}{D(x')}\int_{-\infty}^{x'}\mathrm{e}^{-\beta U(x'')}\mathrm{d}x''\right)\mathrm{d}x'\ . \tag{A1.8}$$

A1.5 Solution of the 1D Poisson-Boltzmann Equation

We want to solve:

$$\frac{\mathrm{d}^2\psi}{\mathrm{d}z^2} = \frac{2n_0e}{\varepsilon}\sinh\left(\frac{e\psi}{k_\mathrm{B}T}\right). \tag{A1.9}$$

First, we substitute $y = e\psi/(k_\mathrm{B}T)$ and find:

$$\frac{\mathrm{d}^2y}{\mathrm{d}z^2} = \frac{2n_0e^2}{\varepsilon k_\mathrm{B}T}\sinh y = \frac{1}{\lambda_\mathrm{D}^2}\sinh y \tag{A1.10}$$

with the Debye length λ_D defined in Eq. (2.37). We then multiply $2\,\mathrm{d}y/\mathrm{d}z$ on both sides:

$$2\frac{\mathrm{d}y}{\mathrm{d}z}\frac{\mathrm{d}^2y}{\mathrm{d}z^2} = \frac{2}{\lambda_\mathrm{D}^2}\frac{\mathrm{d}y}{\mathrm{d}z}\sinh y\ , \tag{A1.11}$$

and find:

$$\frac{\mathrm{d}}{\mathrm{d}z}\left(\frac{\mathrm{d}y}{\mathrm{d}z}\right)^2 = \frac{2}{\lambda_\mathrm{D}^2}\frac{\mathrm{d}y}{\mathrm{d}z}\sinh y \tag{A1.12}$$

for the left-hand side. Then, integration of both sides yields:

$$\int\frac{\mathrm{d}}{\mathrm{d}z}\left(\frac{\mathrm{d}y}{\mathrm{d}z}\right)^2\mathrm{d}z = \frac{2}{\lambda_\mathrm{D}^2}\int\frac{\mathrm{d}y}{\mathrm{d}z}\sinh y\ \mathrm{d}z\ , \tag{A1.13}$$

$$\left(\frac{\mathrm{d}y}{\mathrm{d}z}\right)^2 = \frac{2}{\lambda_\mathrm{D}^2}\int\sinh y\ \mathrm{d}y = \frac{2}{\lambda_\mathrm{D}^2}\cosh y + C_1\ . \tag{A1.14}$$

At large distances, $z \to \infty$, the potential ψ must be zero. Hence, y and $\mathrm{d}y/\mathrm{d}z$ at large distances must be zero as well. Since $\cosh(0) = 1$, we find $C_1 = -2\lambda_\mathrm{D}^2$:

$$\left(\frac{\mathrm{d}y}{\mathrm{d}z}\right)^2 = \frac{2}{\lambda_\mathrm{D}^2}\int\sinh y\ \mathrm{d}y = \frac{2}{\lambda_\mathrm{D}^2}(\cosh y - 1)\ , \tag{A1.15}$$

$$\frac{\mathrm{d}y}{\mathrm{d}z} = -\frac{1}{\lambda_\mathrm{D}}\sqrt{2\cosh y - 1}\ . \tag{A1.16}$$

The negative sign of the square-root is used, so that with increasing distance y decreases. With the relation $\sinh y/2 = \sqrt{1/2\cosh y - 1}$ we can write:

$$\frac{\mathrm{d}y}{\mathrm{d}z} = -\frac{2}{\lambda_\mathrm{D}}\sinh(y/2)\ . \tag{A1.17}$$

By separation of variables we find:

$$\frac{\mathrm{d}y}{\sinh(y/2)} = -\frac{2}{\lambda_\mathrm{D}}\mathrm{d}z \; , \tag{A1.18}$$

$$\int \frac{\mathrm{d}y}{\sinh(y/2)} = -\frac{2}{\lambda_\mathrm{D}}\int \mathrm{d}z \; , \tag{A1.19}$$

$$2\ln(\tanh(y/4)) = -\frac{2}{\lambda_\mathrm{D}}z + 2C_2 \; . \tag{A1.20}$$

We define $y_0 = y(z=0) = e\zeta/k_\mathrm{B}T$ and get $C_2 = \ln(\tanh(y_0/4))$. We get:

$$\ln(\tanh(y/4)) - \ln(\tanh(y_0/4)) = \ln\left(\frac{\tanh(y/4)}{\tanh(y_0/4)}\right) = -\frac{z}{\lambda_\mathrm{D}} \; , \tag{A1.21}$$

which eventually gives:

$$\tanh\left(\frac{e\psi}{4k_\mathrm{B}T}\right) = \tanh\left(\frac{e\zeta}{4k_\mathrm{B}T}\right)\mathrm{e}^{-z/\lambda_\mathrm{D}} \; . \tag{A1.22}$$

The surface charge plus the charge of the ions in the double layer must be zero. Thus, we get for the surface charge:

$$\sigma = -\int_0^\infty \varrho \,\mathrm{d}z \; . \tag{A1.23}$$

Using the one-dimensional Poisson equation and the fact that the gradient of the potential is zero at infinity, we find the general relation:

$$\sigma = \varepsilon \int_0^\infty \mathrm{d}^2\psi/\mathrm{d}z^2 \,\mathrm{d}z = -\varepsilon\,\mathrm{d}\psi/\mathrm{d}z|_{z=0} \; . \tag{A1.24}$$

With $\mathrm{d}y/\mathrm{d}z = -2\sinh(y/2)/\lambda_\mathrm{D}$ and:

$$\frac{\mathrm{d}y}{\mathrm{d}z} = \frac{e}{k_\mathrm{B}T}\frac{\mathrm{d}\psi}{\mathrm{d}z} \tag{A1.25}$$

we get the Grahame equation:

$$\sigma = \frac{2\varepsilon k_\mathrm{B}T}{e\lambda_\mathrm{D}}\sinh\left(\frac{e\zeta}{2k_\mathrm{B}T}\right) = \frac{e}{2\pi\lambda_\mathrm{B}\lambda_\mathrm{D}}\sinh\left(\frac{e\zeta}{2k_\mathrm{B}T}\right) \; . \tag{A1.26}$$

Here, we introduced the Bjerrum length:

$$\lambda_\mathrm{B} = \frac{e^2}{4\pi\varepsilon k_\mathrm{B}T} \; . \tag{A1.27}$$

The equation can be rearranged to:

$$\zeta = \frac{2k_\mathrm{B}T}{e}\operatorname{arsinh}\left(\frac{2\pi\sigma\lambda_\mathrm{B}\lambda_\mathrm{D}}{e}\right) \; . \tag{A1.28}$$

A1.6 Hamaker Constant

Within the Lifschitz theory the Hamaker constant of two dielectric media 1 and 2 interacting across a dielectric medium 3 is approximated by[142]

$$A_\mathrm{H} = \frac{3}{4}k_\mathrm{B}T\left(\frac{\varepsilon_1-\varepsilon_3}{\varepsilon_1+\varepsilon_3}\right)\left(\frac{\varepsilon_2-\varepsilon_3}{\varepsilon_2+\varepsilon_3}\right) + \frac{3h\nu_\mathrm{e}}{8\sqrt{2}}\frac{(n_1^2-n_3^2)(n_2^2-n_3^2)}{\sqrt{(n_1^2+n_3^2)(n_2^2+n_3^2)}\left(\sqrt{n_1^2+n_3^2}+\sqrt{n_2^2+n_3^2}\right)} \; ,$$

where ε_1, ε_2, ε_3 and n_1, n_2, n_3 are the permittivities and refractive indices of the media, respectively, and we have assumed that the absorption frequency ν_e is approximately the same for all three media.

Tab. A1.1: The permittivity ε, refractive index n and the absorption frequency ν_e for dielectric materials relevant in this study[142].

Medium	ε	n	ν_e [10^{15} s^{-1}]
Water	80	1.33	3.0
Quartz (SiO$_2$)	3.8	1.45	3.2
Polystyrene (PS)	2.6	1.56	2.3

A1.7 Boundary Layer Approximation

Since $v_x|_{z=0} = 0$, we can write:

$$\eta v_x(z) = \eta \int_0^z \mathrm{d}z' \frac{\mathrm{d}v_x(z')}{\mathrm{d}z'} = \eta\, v_x(z')|_{z'=z} - \eta\, v_x(z')|_{z'=0} \ . \tag{A1.29}$$

Then, the boundary velocity gets:

$$v_\mathrm{B} = v_x(\infty) = \int_0^\infty \mathrm{d}z'\, 1 \cdot \frac{\mathrm{d}v_x(z')}{\mathrm{d}z'} = z' \frac{\mathrm{d}v_x(z')}{\mathrm{d}z'}\bigg|_0^\infty - \int_0^\infty \mathrm{d}z'\, z' \frac{\mathrm{d}^2 v_x(z')}{\mathrm{d}z'^2} \ , \tag{A1.30}$$

where we have used integration in parts. Since $\mathrm{d}v_x/\mathrm{d}z|_{z=\infty} = 0$ the first term vanishes and we find:

$$v_\mathrm{B} = -\int_0^\infty \mathrm{d}z'\, z' \frac{\mathrm{d}^2 v_x(z')}{\mathrm{d}z'^2} = -\frac{1}{\eta}\int_0^\infty \mathrm{d}z'\, z' \left(\frac{\mathrm{d}P}{\mathrm{d}x} - f_x\right) \ . \tag{A1.31}$$

A1.8 Osmotic Pressure

The charge density ϱ and excess ion density n are given by Eqs. (2.33) and (2.34):

$$\varrho = -2en_0 \sinh(e\psi/(k_\mathrm{B}T)) \ , \tag{A1.32}$$

$$n = 2n_0(\cosh(e\psi/(k_\mathrm{B}T)) - 1) \ . \tag{A1.33}$$

The osmotic pressure, $p = nk_\mathrm{B}T$, then reads:

$$\begin{aligned}\nabla p = k_\mathrm{B}T\nabla n + nk_\mathrm{B}\nabla T &= k_\mathrm{B}T\left(\frac{n}{n_0}\nabla n_0 + 2n_0\nabla\cosh(e\psi/(k_\mathrm{B}T))\right) + nk_\mathrm{B}\nabla T \\ &= nk_\mathrm{B}T\frac{\nabla n_0}{n_0} + 2en_0\sinh(e\psi/(k_\mathrm{B}T))\left(\nabla\psi - \psi\frac{\nabla T}{T}\right) + nk_\mathrm{B}\nabla T \\ &= nk_\mathrm{B}T\frac{\nabla n_0}{n_0} - \varrho\nabla\psi + \varrho\psi\frac{\nabla T}{T} + nk_\mathrm{B}\nabla T = -\varrho\nabla\psi + (\varrho\psi + nk_\mathrm{B}T)\frac{\nabla T}{T} + nk_\mathrm{B}T\frac{\nabla n_0}{n_0} \ .\end{aligned}$$

A1.9 Salinity Gradient and Thermoelectricity

The flux of positive and negative ions in a binary electrolyte can be written as[48]

$$\boldsymbol{j}_\pm = -D_\pm\left(\nabla n_\pm + 2n_\pm\alpha_\pm\frac{\nabla T}{T} \mp n_\pm\frac{e\boldsymbol{E}_0}{k_\mathrm{B}T}\right) , \tag{A1.34}$$

where $D_\pm$ are the ionic diffusion coefficients, $n_\pm$ the ion densities, $\alpha_\pm$ the ionic Soret coefficients and $\boldsymbol{E}_0$ denotes the thermoelectric field. We note that the single-ion heat of transport[162] $Q^*_\pm$

and $\alpha_\pm$ are related via $Q^*_\pm = 2\alpha_\pm k_\mathrm{B}T$. In the stationary state, $\boldsymbol{j}_\pm = 0$, we first evaluate:

$$\frac{\boldsymbol{j}_+}{D_+} + \frac{\boldsymbol{j}_-}{D_-} = 2\nabla n_0 + 2(n_+\alpha_+ + n_-\alpha_-)\frac{\nabla T}{T} = 0 \ , \tag{A1.35}$$

where we introduced the salinity n_0 as the mean value of the ion densities, $n_0 = \frac{1}{2}(n_+ + n_-)$. With $n_+\alpha_+ + n_-\alpha_- \approx n_0(\alpha_+ + \alpha_-)$ we get:

$$\nabla n_0 + n_0(\alpha_+ + \alpha_-)\frac{\nabla T}{T} = 0 \ , \tag{A1.36}$$

and with $\alpha = \alpha_+ + \alpha_-$ we find:

$$\frac{\nabla n_0}{n_0} = -\alpha\frac{\nabla T}{T} \ . \tag{A1.37}$$

Next, in the stationary state $\boldsymbol{j}_\pm = 0$, we evaluate:

$$\frac{e\boldsymbol{j}_+}{D_+} - \frac{e\boldsymbol{j}_-}{D_-} = \nabla\varrho + 2e(n_+\alpha_+ - n_-\alpha_-)\frac{\nabla T}{T} - 2n_0\frac{e^2\boldsymbol{E}_0}{k_\mathrm{B}T} = 0 \ , \tag{A1.38}$$

where we used the charge density $\varrho = e(n_+ - n_-)$ already introduced in Sec. 2.2.1. If the ion densities $n_\pm$ deviate only weak from their mean value n_0 we can approximate $n_+\alpha_+ - n_-\alpha_- \approx n_0(\alpha_+ - \alpha_-)$ and get:

$$\nabla\varrho + 2en_0(\alpha_+ - \alpha_-)\frac{\nabla T}{T} - 2n_0\frac{e^2\boldsymbol{E}_0}{k_\mathrm{B}T} = 0 \ . \tag{A1.39}$$

If we further impose $\varrho = 0$ for the charge density we find

$$\boldsymbol{E}_0 = -\psi_0\frac{\nabla T}{T} \tag{A1.40}$$

with $\psi_0 = -\delta\alpha\, k_\mathrm{B}T/e$ and $\delta\alpha = \alpha_+ - \alpha_-$.

A1.10 Thermophoretic Flow Field

The velocity field around a sphere driven by surface flows is given by

$$v_r = u\cos\theta\left(1 - \frac{R^3}{r^3}\right) \ , \tag{A1.41}$$

$$v_\theta = -u\sin\theta\left(1 + \frac{R^3}{2r^3}\right) \ , \tag{A1.42}$$

in the reference frame of the sphere[55]. Fig. 2.14a depicts the velocity field in the laboratory frame, $v_x - u$.

A1.11 Total Power of a Gaussian Beam

Using Eq. (2.92) the power through an circular aperture with radius a can be estimated with:

$$P(a) = \int_0^a \int_0^{2\pi} I(r,0)\, r\,\mathrm{d}r\,\mathrm{d}\varphi = I_0\int_0^a 2\pi r\exp\left(-\frac{2r^2}{w_0^2}\right)\mathrm{d}r = \frac{I_0 w_0^2\pi}{2}\left(1 - \exp\left(-\frac{2a^2}{w_0^2}\right)\right) \ .$$

For the total power $P(\infty) := P_0$ we find:

$$P_0 = \frac{I_0 w_0^2 \pi}{2} \ . \tag{A1.43}$$

A1.12 Mie Theory

Mie Coefficients The Mie coefficients a_n and b_n are defined as[180]:

$$a_n = \frac{\psi_n(x)\,\psi_n'(mx) - m\,\psi_n'(x)\,\psi_n(mx)}{\xi_n(x)\,\psi_n'(mx) - m\,\xi_n'(x)\,\psi_n(mx)}\ , \tag{A1.44}$$

$$b_n = \frac{m\,\psi_n(x)\,\psi_n'(mx) - \psi_n'(x)\,\psi_n(mx)}{m\,\xi_n(x)\,\psi_n'(mx) - \xi_n'(x)\,\psi_n(mx)}\ , \tag{A1.45}$$

where the size parameter x and the relative refractive index m are:

$$x = \frac{2\pi r\, n_1}{\lambda}\ , \qquad m = \frac{n_2}{n_1}\ . \tag{A1.46}$$

n_1 and n_2 are the refractive indices of the medium and sphere, respectively. The functions $\psi_n(x)$ and $\xi_n(x)$ are defined as

$$\psi_n(x) = x\,j_n(x)\ , \qquad \xi_n(x) = x\,h_n^{(1)}(x)\ , \tag{A1.47}$$

where $h_n^{(1)}(x) = j_n(x) + \mathrm{i}y_n(x)$ is the spherical Hankel function defined in terms of the spherical Bessel functions $j_n(x)$ and $y_n(x)$.

Plane Waves For a spherical particle illuminated by a plane wave the scattering and extinction cross-sections are defined by:

$$\sigma_{\mathrm{sca}} = \frac{2\pi R^2}{x^2}\sum_{n=1}^{\infty}(2n+1)(|a_n|^2 + |b_n|^2)\ , \tag{A1.48}$$

$$\sigma_{\mathrm{ext}} = \frac{2\pi R^2}{x^2}\sum_{n=1}^{\infty}(2n+1)\,\mathrm{Re}\,(a_n + b_n)\ \ . \tag{A1.49}$$

For a plane wave propagating in positive z-direction the optical force is given by $F_z = \sigma_{\mathrm{pr}}/c$ in terms of the radiation pressure cross-section:

$$\sigma_{\mathrm{pr}} = \frac{4\pi r^2}{x^2}\sum_{n=1}^{\infty}\left(\frac{2n+1}{2}\mathrm{Re}\,(a_n+b_n) - \frac{2n+1}{n(n+1)}\mathrm{Re}\,(a_n b_n^*) - \frac{n(n+2)}{n+1}\mathrm{Re}\left(a_n a_{n+1}^* + b_n b_{n+1}^*\right)\right).$$

Gaussian Beams For a spherical particle illuminated by a Gaussian beam the scattering and extinction cross-sections are defined by:

$$\sigma_{\mathrm{sca}} = \frac{2\pi R^2}{x^2}\sum_{n=1}^{\infty}\sum_{m=-n}^{n}\frac{2n+1}{n(n+1)}\frac{(n+|m|)!}{(n-|m|)!}\left(|a_n|^2|g_{n,\mathrm{TM}}^m|^2 + |b_n|^2|g_{n,\mathrm{TE}}^m|^2\right)\ , \tag{A1.50}$$

$$\sigma_{\mathrm{ext}} = \frac{2\pi R^2}{x^2}\sum_{n=1}^{\infty}\sum_{m=-n}^{n}\frac{2n+1}{n(n+1)}\frac{(n+|m|)!}{(n-|m|)!}\mathrm{Re}\left(a_n|g_{n,\mathrm{TM}}^m|^2 + b_n|g_{n,\mathrm{TE}}^m|^2\right)\ , \tag{A1.51}$$

where $g_{n,\mathrm{TM}}^m$ and $g_{n,\mathrm{TE}}^m$ are beam shape coefficients given by:

$$\begin{pmatrix} g_{n,\mathrm{TM}}^m \\ g_{n,\mathrm{TE}}^m \end{pmatrix} = \frac{1}{2(1+2\mathrm{i}\hat{z}_0)}\exp\left(\frac{\mathrm{i}\hat{z}_0}{s^2} - \frac{\hat{x}_0^2 + \hat{y}_0^2}{1+2\mathrm{i}\hat{z}_0}\right)\exp\left(-\frac{n+1/2)^2 s^2}{1+2\mathrm{i}\hat{z}_0}\right) R_n^m (-\mathrm{i})^{|m|}\begin{pmatrix} \mathrm{i}F_{n,\mathrm{TM}}^m \\ F_{n,\mathrm{TE}}^m \end{pmatrix}$$

for a Gaussian beam with offset x_0, y_0, z_0 from the particle center. Here, $\hat{x}_0 = x_0/w_0$, $\hat{y}_0 = y_0/w_0$, $\hat{z}_0 = z_0/(2z_\mathrm{R})$, $s = w_0/(2z_\mathrm{R})$,

$$R_n^m = \begin{cases} \dfrac{2n(n+1)}{2n+1} & \text{if} \quad m = 0 \ , \\ \left(\dfrac{2}{2n+1}\right)^{|m|-1} & \text{if} \quad m \neq 0 \ , \end{cases}$$

and

$$\begin{pmatrix} F_{n,\mathrm{TM}}^m \\ F_{n,\mathrm{TE}}^m \end{pmatrix} = \begin{cases} \begin{pmatrix} 2\hat{x}_0 \\ 2\mathrm{i}\hat{y}_0 \end{pmatrix} \displaystyle\sum_{j=0}^{\infty} a^{2j+1} \frac{\hat{x}_-^j \hat{x}_+^j}{j!(j+1)!} & \text{if} \quad m = 0 \ , \\ a^{m-1} \dfrac{\hat{x}_-^{m-1}}{(m-1)!} + \displaystyle\sum_{j=m}^{\infty} a^{2j-m+1} \frac{\hat{x}_-^j \hat{x}_+^{j-m}}{j!(j-m)!} \begin{pmatrix} \frac{\hat{x}_+}{j-m+1} + \frac{\hat{x}_-}{j+1} \\ \frac{\hat{x}_+}{j-m+1} - \frac{\hat{x}_-}{j+1} \end{pmatrix} & \text{if} \quad m > 0 \ , \\ a^{|m|-1} \dfrac{\hat{x}_-^{|m|-1}}{(|m|-1)!} + \displaystyle\sum_{j=|m|}^{\infty} a^{2j-|m|+1} \frac{\hat{x}_-^{j-|m|} \hat{x}_+^j}{j!(j-|m|)!} \begin{pmatrix} \frac{\hat{x}_-}{j-|m|+1} + \frac{\hat{x}_+}{j+1} \\ \frac{\hat{x}_-}{j-|m|+1} - \frac{\hat{x}_+}{j+1} \end{pmatrix} & \text{if} \quad m < 0 \ , \end{cases}$$

with $a = (n + 1/2)s/(1 + 2\mathrm{i}\hat{z}_0)$, $\hat{x}_- = \hat{x}_0 - \mathrm{i}\hat{y}_0$ and $\hat{x}_+ = \hat{x}_0 + \mathrm{i}\hat{y}_0$. The expressions for the radiation pressure cross-sections can be found in Ref. 180.

On-Axis Gaussian Beam For $x_0, y_0 = 0$ the beam shape coefficients can be simplified to[321]:

$$g_n = Q \exp\big(-Qs^2(n-1)(n+2)\big) \exp\big((\mathrm{i}\gamma s^{-1}/2\big) \ . \tag{A1.52}$$

with $Q = (1 + \mathrm{i}s\gamma)^{-1}$ and $\gamma = 2z_0/w_0$. The expression for the scattering and extinction cross-section then read:

$$\sigma_\mathrm{sca} = \frac{2\pi R^2}{x^2} \sum_{n=1}^{\infty} (2n+1) \left|g_n\right|^2 \left(\left|a_n\right|^2 + \left|b_n\right|^2\right) \ , \tag{A1.53}$$

$$\sigma_\mathrm{ext} = \frac{2\pi R^2}{x^2} \sum_{n=1}^{\infty} (2n+1) \left|g_n\right|^2 \mathrm{Re}\left(a_n + b_n\right) \ . \tag{A1.54}$$

A1.13 Optical Forces in the Small Particle Limit

In literature the optical force is often given by[181,322]:

$$\langle \boldsymbol{F} \rangle = \frac{\varepsilon}{2} \mathrm{Re}\left(\sum_j \alpha_\mathrm{r} E_j \nabla E_j^* \right) = \frac{\varepsilon}{4} \mathrm{Re}(\alpha_\mathrm{r}) \nabla (E \cdot E^*) - \frac{\varepsilon}{2} \mathrm{Im}(\alpha_\mathrm{r}) \mathrm{Im}\left(\sum_j E_j \nabla E_j^* \right) \ , \tag{A1.55}$$

where the right-hand side is obtained using $\mathrm{Re}(z_1 z_2) = \mathrm{Re}(z_1)\mathrm{Re}(z_2) - \mathrm{Im}(z_1)\mathrm{Im}(z_2)$, $\sum_j E_j \nabla E_j^* = (\boldsymbol{E} \cdot \nabla)\boldsymbol{E}^* + \boldsymbol{E} \times (\nabla \times E^*)$ and $\mathrm{Re}((\boldsymbol{E} \cdot \nabla)\boldsymbol{E}^*) = \frac{1}{2}\nabla(\boldsymbol{E} \cdot E^*) - \mathrm{Re}(\nabla \times (\nabla \times E^*))$. Expansion of the term $\mathrm{Im}(\sum_j E_j \nabla E_j^*)$ yields

$$\langle F \rangle = \frac{n_1^2 \varepsilon_0}{4} \mathrm{Re}(\alpha_\mathrm{r}) \nabla |\boldsymbol{E}|^2 + n_1 k \, \mathrm{Im}(\alpha_\mathrm{r}) \left(\frac{\mathrm{Re}(\boldsymbol{E} \times \boldsymbol{H}^*)}{2c_0} + \frac{\varepsilon_0}{4k_0 \mathrm{i}} \nabla \times (\boldsymbol{E} \times \boldsymbol{E}^*) \right) \ , \tag{A1.56}$$

in agreement with Eq. (2.100). We have used $\mathrm{Im}((\boldsymbol{E} \cdot \nabla)\boldsymbol{E}^*) = -(\nabla \times (\boldsymbol{E} \times \boldsymbol{E}^*))/(2\mathrm{i})$ with $\nabla \cdot \boldsymbol{E} = 0$ and $\nabla \times E^* = -\mathrm{i}\omega \boldsymbol{H}^*/(\varepsilon_0 c_0^2)$, $\mathrm{Im}(\mathrm{i}z) = \mathrm{Re}(z)$ with $\omega = c_0 k_0$ and $\varepsilon = n_1^2 \varepsilon_0$.

Gaussian Beams Using Eq. (2.91) the optical force components for a Gaussian beam in the small particle limit are obtained as follows[323,324]:

$$\langle F_r^{\mathrm{grad}}\rangle = -\frac{2\varepsilon}{\pi}\mathrm{Re}(\alpha_\mathrm{r})\,|E_0|^2 r\frac{w_0^2}{w^4(z)}\,\mathrm{e}^{-2r^2/w^2(z)}\ , \tag{A1.57a}$$

$$\langle F_z^{\mathrm{grad}}\rangle = -\frac{\varepsilon}{\pi}\mathrm{Re}(\alpha_\mathrm{r})\,|E_0|^2 z\frac{w_0^4}{z_\mathrm{R}^2}\left(\frac{1}{w^4(z)}-\frac{2r^2}{w^6(z)}\right)\mathrm{e}^{-2r^2/w^2(z)}\ , \tag{A1.57b}$$

$$\langle F_r^{\mathrm{ext}}\rangle = \frac{\varepsilon}{\pi}\mathrm{Im}(\alpha_\mathrm{r})\,|E_0|^2 r\frac{w_0^2}{w^2(z)}\frac{k}{R(z)}\,\mathrm{e}^{-2r^2/w^2(z)}\ , \tag{A1.57c}$$

$$\langle F_z^{\mathrm{ext}}\rangle = \frac{\varepsilon}{\pi}\mathrm{Im}(\alpha_\mathrm{r})\,|E_0|^2 \frac{w_0^2}{w^2(z)}\left(k\left(1-\frac{r^2}{2}\frac{z^2-z_\mathrm{R}^2}{(z^2+z_\mathrm{R}^2)^2}\right)-\frac{w_0^2}{z_\mathrm{R}w^2(z)}\right)\mathrm{e}^{-2r^2/w^2(z)}\ . \tag{A1.57d}$$

The electric field amplitude is given by $|E_0|^2 = 2I_0/(\varepsilon_0 c_0)$ with $I_0 = 2P_0/(w_0^2\pi)$.

A1.14 Density and Viscosity of Water as Function of the Temperature

The density of water as function the temperature is depicted in Fig. A1.1a. The blue data points depict the experimental values[325] and the dash lines two linear approximations

$$\varrho(T) = \varrho_0(1-\beta(T-T_0)) \tag{A1.58}$$

with $\beta = 0.2{\cdot}10^{-3}\mathrm{K}^{-1}$ and $\beta = 0.4{\cdot}10^{-3}\mathrm{K}^{-1}$, respectively. The temperature-dependent viscosity of water is depicted in Fig. A1.1b. The blue data points depict experimental values[326] and the blue dashed line a fit to the Vogel–Fulcher equation

$$\eta(T) = \eta_0\,\mathrm{e}^{B/(T-T_\mathrm{VF})} \tag{A1.59}$$

with $\eta_0 = 29.84$ Pa s, $B = 496.89$ K and $T_\mathrm{VF} = 152.0$ K[327].

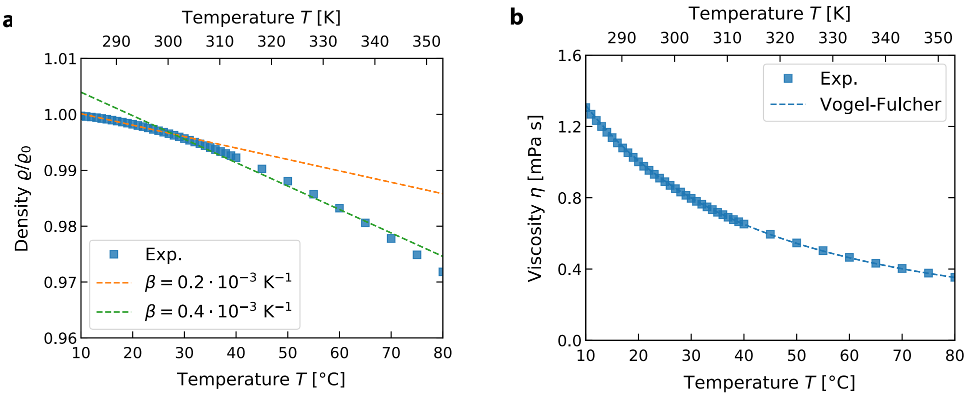

Fig. A1.1: The temperature-dependence of the relative density ϱ/ϱ_0 (**a**) and viscosity η (**b**) of water. The dashed lines in (**a**) represent linear approximations using Eq. (A1.58). The blue dashed line in (**b**) depicts a fit to the Vogel-Fulcher equation, Eq. (A1.59). The experimental values have been taken from Ref. 326.

A1.15 Optical Properties

Fig. A1.2 depicts the wavelength-dependence of the refractive index $n = n' + \mathrm{i}n''$ and the permittivity $\varepsilon = \varepsilon' + \mathrm{i}\varepsilon''$ in the visible range for Au and Cr. The curves have been obtained from a interpolation of the experimental values in Ref. 173. The reflective index and the permittivity are linked by the relation $\varepsilon = n^2$ with the real- and imaginary part of the permittivity given by:

$$\varepsilon' = n'^2 - n''^2\ , \tag{A1.60}$$

$$\varepsilon'' = 2n'n''\ . \tag{A1.61}$$

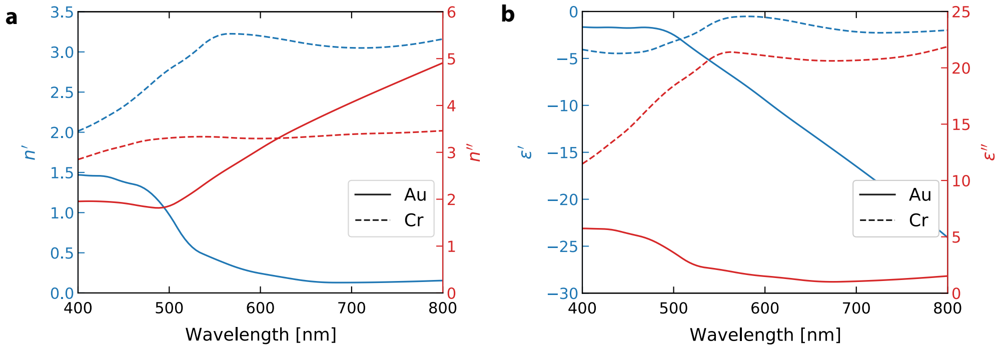

Fig. A1.2: The real- and imaginary parts of the refractive index $n = n' + \mathrm{i}n''$ (**a**) and the permittivity $\varepsilon = \varepsilon' + \mathrm{i}\varepsilon''$ (**b**) for Au and Cr in the visible range. The curves have been obtained from the an interpolation of the experimental values in Ref. 173.

Within the visible range the refractive index of dielectric materials is approximately constant and the imaginary part is very small. Tab. A1.2 lists the refractive index values used for the dielectric materials in this work.

Tab. A1.2: The refractive index values used for the dielectric materials in this work taken from Refs. 328–330.

Material	n
Water	1.33
Glass (BK7)	1.51
Quartz (SiO_2)	1.46
Polystyrene (PS)	1.56

A1.16 Thermal Properties

Tab. A1.3: The thermal properties of materials used in numerical simulation and analytical calculations. Here, κ is the thermal conductivity, ρ the density and c_p the heat capacity at constant pressure. The values have been taken from Refs. 325, 331, 332.

Material	κ [$\mathrm{W\,m^{-1}\,K^{-1}}$]	ϱ [$\mathrm{g\,cm^{-3}}$]	c_p [$\mathrm{J\,kg^{-1}\,K^{-1}}$]
Water	0.6	1.0	4182
Glass (BK7)	1.1	2.5	858
Quartz (SiO_2)	1.3	2.2	730
Au	318	19.3	129
Cr	94	7.1	449
Polystyrene (PS)	0.1	1.1	1100
Melamine (MF)	0.5	1.5	1200

A2 Experimental Prerequisites

A2.1 Experimental Setup 1

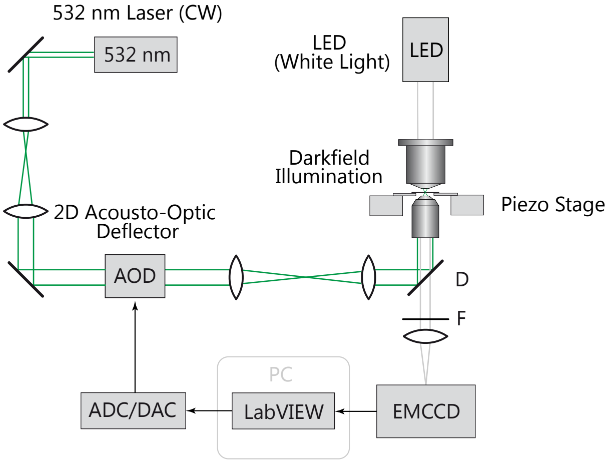
532 nm Laser (CW)
532 nm
LED
(White Light)
LED
Darkfield
Illumination
Piezo Stage
2D Acousto-Optic
Deflector
AOD
D
F
PC
ADC/DAC
LabVIEW
EMCCD

Fig. A2.1: Sketch of experimental setup used in Secs. 4.1, 4.2 and 4.3.

A2.2 Experimental Setup 2

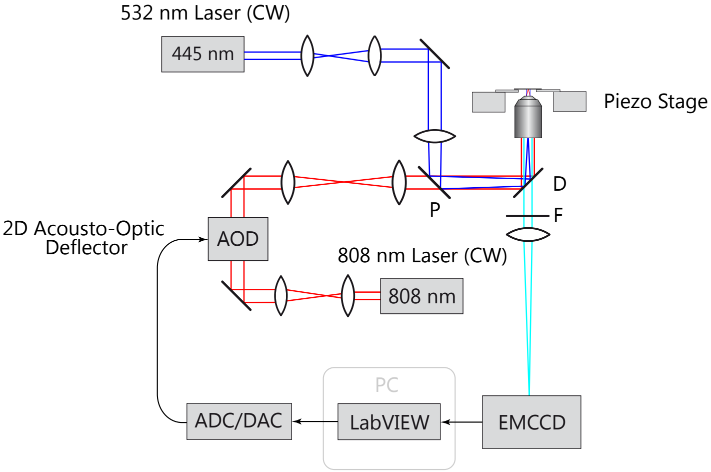
532 nm Laser (CW)
445 nm
Piezo Stage
D
P
F
2D Acousto-Optic
Deflector
AOD
808 nm Laser (CW)
808 nm
PC
ADC/DAC
LabVIEW
EMCCD

Fig. A2.2: Sketch of experimental setup used in Sec. 4.4.

A2.3 Properties of 5CB

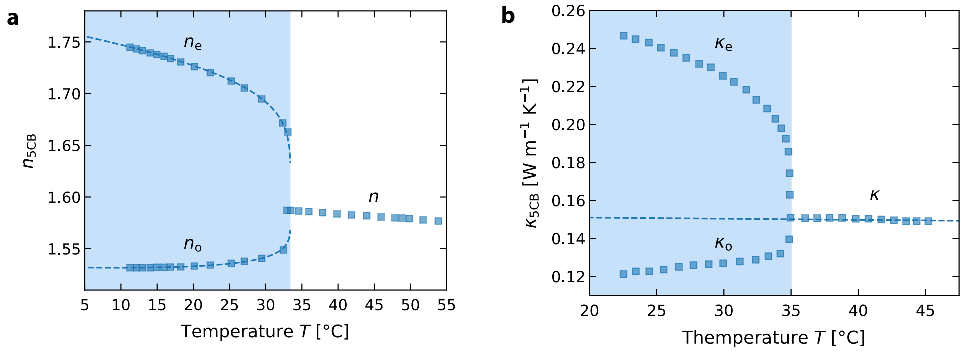

Fig. A2.3: The refractive index (**a**) and the thermal conductivity (**b**) of 5CB as function of the temperature. The experimental values have been digitized from Refs. 196 and 227. The blue dashed curves in (**a**) depict fit functions given in Ref. 196. The blue dashed line in (**b**) represents linear fit to the isotropic part.

List of Publications

Peer-Reviewed Articles

The following articles have been published in peer-reviewed journals:

[P1] **M. Fränzl** and F. Cichos, Hydrodynamic Manipulation of Nano-Objects by Thermo-Osmotic Flows, *Nat. Commun.* **13**, 656 (2022).

M.F. and F.C. designed the experiments. M.F. performed the experiments. M.F. and F.C. analyzed the experimental data. M.F. and F.C. implemented and evaluated the numerical calculations. M.F. and F.C. wrote the manuscript.

[P2] **M. Fränzl**, S. Muiños-Landin, V. Holubec and F. Cichos, Fully Steerable Symmetric Thermoplasmonic Microswimmers, *ACS Nano* **15**, 3434 (2021).

M.F., S.M.-L., and F.C. designed the experiments. M.F. performed the experiments. M.F., S.M.-L., and F.C. analyzed the experimental data. M.F. and F.C. implemented and evaluated the numerical calculations. V. H. contributed the noise influence model. M.F. and F.C. wrote the manuscript. All authors discussed the results and commented on the manuscript.

[P3] **M. Fränzl** and F. Cichos, Active Particle Feedback Control with a Single-Shot Detection Convolutional Neural Network, *Sci. Rep.* **10**, 12571 (2020).

M.F. and F.C. designed the experiments, M.F. implemented the software framework and conducted the experiments, M.F. and F.C. analyzed the results and wrote the manuscript.

[P4] **M. Fränzl**, T. Thalheim, J. Adler D. Huster, J. Posseckardt, M. Mertig and F. Cichos, Thermophoretic Trap for Single Amyloid Fibril and Protein Aggregation Studies, *Nat. Methods* **18**, 611 (2019).

M.F., T.T. and F.C. designed the experiments. M.F. and T.T. performed the experiments. M.F., T.T. and F.C. analyzed the data. J.A. prepared the amyloid samples and carried out fibrillation kinetics measurements. J.P., M.F., T.T., F.C. and M.M. developed the trap preparation procedure. D.H. and F.C. provided the experimental equipment. M.F., T.T., J.A., D.H. and F.C. wrote the manuscript. All authors discussed the results and commented on the manuscript.

The following articles have been published in peer-reviewed journal in the context of external projects not related to this thesis:

[E1] **M. Fränzl**, S. Moras, O. D. Gordan, D.R.T. Zahn, Interaction of One-Dimensional Photonic Crystals and Metal Nanoparticle Arrays, *J. Phys. Chem. C* **122**, 10153 (2018).

[E2] C.-W. Tu, **M. Fränzl**, Q. Gao, H.-H. Tan *et al.* and H. P. Wagner, Lasing from InP Nanowire Photonic Crystals on InP Substrate, *Adv. Opt. Mater.* **9**, 2001745 (2020).

[E3] G. Aman, F. Mohammadi, **M. Fränzl**, M. Lysevych, H.-H Tan. *et al.* and H. P. Wagner and H. P. Wagner, Effect of Au Substrate and Coating on the Lasing Characteristics of GaAs Nanowires, *Sci. Rep.* **11**, 21378 (2021).

[E4] C.-W. Tu, M. Kaveh, **M. Fränzl**, Q. Gao, H.-H. Tan *et al.* and H. P. Wagner, Unique Reflectance from Birefringent Uncoated and Gold-Coated InP Nanowire Crystal Arrays, accepted at *Opt. Express* on 2021-12-30.

Online Protocols

[O1] **M. Fränzl**, T. Thalheim, J. Adler D. Huster, J. Posseckhardt, M. Mertig and F. Cichos, Thermophoretic Trap for Single Amyloid Fibril and Protein Aggregation Studies, *Protoc. Exch.* (2019).

Conference Proceedings

[C1] **M. Fränzl** and F. Cichos, Single Amyloid Fibrils Studied in a Thermophoretic Trap, OSA Biophotonics Congress 2019: Optics in the Life Sciences, Optical Manipulation and Its Applications, AM2E.3 (2019).

[C2] **M. Fränzl** and F. Cichos, Reconfigurable Plasmonic Particles-on-Film using Thermo-Osmotic Flows, OSA Biophotonics Congress 2021: Optics in the Life Sciences, Optical Manipulation and Its Applications, AM2D.4 (2021).

Talks

The following talks were given at international conferences:

1. Soft Matter Day, Transport of Colloids Driven by Thermo-Viscous Flows, Leipzig, Germany (2017)
2. 5th SFB TRR 102 Minisymposium, Single Amyloid Fibrils Studied in a Thermophoretic Trap, Leipzig, Germany (2018)
3. OSA Biophotonics Congress, Single Amyloid Fibrils Studied in a Thermophoretic Trap, Tucson, USA (2019)
4. Soft Matter Day, Thermo-Osmotic Flow in Electrolyte Solution, Leipzig, Germany (2019)
5. DPG Spring Meeting, Single Amyloid Fibrils Studied in a Thermophoretic Trap, Regensburg, Germany (2019)
6. BuildMoNa Conference, Single Amyloid Fibrils Studied in a Thermophoretic Trap, Leipzig, Germany (2019)
7. SPIE Optics + Photonics, Emerging Topics in Artificial Intelligence, Real-Time Localization and Classification for Digital Microscopy using Single-Shot Convolutional Neural Networks, Online (2020)
8. OSA Biophotonics Congress, Reconfigurable Plasmonic Particles-on-Film using Thermo-Osmotic Flows, Online (2021)

Poster Presentations

The following posters have been presented at international conferences:

1. DPG Spring Meeting, Thermoelectric Charging of a Hot Spot in Electrolyte Solution, Dresden, Germany (2017)
2. GRC Plasmonically-Powered Processes, Thermoelectric Charging of a Hot Spot in Electrolyte Solution, Hongkong (2017)

3. DPG Spring Meeting, Thermophoresis of Charged Colloids in Electrolyte Solutions, Berlin, Germany (2018)
4. BuildMoNa Conference, Thermophoresis of Charged Colloids in Electrolyte Solutions, Leipzig, Germany (2018)
5. Photothermal Effects in Plasmonics (Summer School), Optically Driven Thermoviscous Flows, Porquerolles Island, France (2018)
6. BuildMoNa Conference, Nanoparticle Manipulation by Thermo-Osmotic Flows in Electrolyte Solutions, Leipzig, Germany (2021)
7. LMC Liquid Matter Conference Gold Nanoparticle Manipulations by Thermo-Osmotic Flows in Electrolyte Solutions, Online (2021)
8. Photothermal Effects in Plasmonics (Summer School), Van der Waals Assisted Thermo-Osmotic Manipulation Near Surfaces, Porquerolles Island, France (2021)

Bachelor and Master Thesis

The following Bachelor and Master thesis have been supervised:

1. H. Falk, Thermophoretic and Thermoelectric Effects of Polystyrene Nanoparticles in Dielectric Liquids (2018)
2. A. Hentrich, Quantitative Phase Contrast Microscopy with an LED Array (2018)
3. F. Welzel, Temperature Measurement of Gold Nanoparticle using Anit-Stokes Luminescence (2019)
4. F. H. Patzschke, Finite Element Simulations of Optical Torques on Metal-Dielectric Janus Particles (2020)
5. N. Devaraju, Orientation Detection of Janus Particles using Single-Shot Convolutional Neural Networks (2020)

Declaration

I hereby certify that this thesis was written by the author himself and that no means of help were used other than those mentioned in the text. All work and thoughts from other authors and sources have been duly acknowledged and clearly marked as such in the thesis.

I hereby name Ralf Süß, Dr. Tobias Thalheim and Prof. Dr. Frank Cichos as the only persons who assisted the author during the compilation of this thesis by careful reading and helpful comments. The author contributions to the individual publications are given in detail in the "List of Publications" section.

Apart from the above mentioned individuals, no other person has been involved in the process of the compilation and work on the present thesis. Especially, no attempt has been made to make use of doctoral consulting. No other individuals have received payment of any kind by the author, neither direct nor indirect, for work which is connected with the contents of this thesis.

I further certify that this neither this thesis nor any derivative thereof has been submitted or presented to any other examination department for the purpose of achieving a PhD. Neither has it been presented to any other examination office and has not yet been published in its full form.

No earlier attempts to achieve a PhD degree have been made.

I acknowledge the Doctoral Regulations of the Faculty of Physics and Earth Science (Promotionsordnung der Fakultät für Physik und Geowissenschaften) dated 24th August 2016 in their full sense.

Martin Fränzl

Acknowledgement

At this point, I would like to thank the people who made this work possible.

First of all I want to thank my supervisor Prof. Dr. Frank Cichos for giving me the opportunity to work on the topic and his time for numerous stimulating discussions. I am grateful for his dedicated support and guidance as well as his patience during my PhD study. His scientific curiosity and constant strive for innovation have been very inspiring for me and encouraged many aspects of this thesis. It was a pleasure to work in the Molecular Nanophotonics Group at the Leipzig University. Thanks to all the staff at the Faculty of Physics and Earth Science and the Peter Debye Institute for Soft Matter Physics.

I am especially grateful to Dr. Tobias Thalheim for our collaboration on the topic of thermophoretic trapping. Furthermore, I want to thank Dr. Juliane Adler and Prof. Dr. Daniel Huster from the Institute for Medical Physics and Biophysics for the preparation of amyloid fibrils and their scientific advice. I also thank Dr. Juliane Posseckardt and Prof. Dr. Michael Mertig from the Kurt Schwabe Institute for Measuring and Sensor Technology Meinsberg e.V. for their support with the design and fabrication of the thermophoretic trapping structures. Moreover, I want to thank Santiago Muiños-Landin and Dr. Viktor Holubec (Institute of Theoretical Physics) for their contributions to the topic of symmetric microswimmers. My special thanks goes out to Prof. Dr. Alois Würger from the University of Bordeaux for valuable discussions on thermo-hydrodynamic effects throughout the years.

My gratitude extends to the whole Molecular Nanophotonics Group for providing a nice working atmosphere and numerous memorable moments in the lab and in social settings. I especially thank André Heber and Nicola Söker for sharing the office with me and Andrea Kramer for guiding me through the labyrinth of administration and carefully reading many of my manuscripts.

I thank Ralf Süß, Dr. Tobias Thalheim and Prof. Dr. Frank Cichos for carefully reading the manuscript of this thesis.

Furthermore, I thank the Free State of Saxony, the European Union and DFG for funding as well as the Research Academy Leipzig and Graduate School BuildMoNa for financial support.

In particular I want to thank my family and especially my parents for their continuous support and for giving me all these opportunities.

Finally, I would like to express my gratitude to my dearest wife Dr. Marlene Kautzner. Without her support and encouragement in the past few years this work would have been impossible to finish. Thank you for making my life complete and filling me with joy every day.

Bibliography

[1] M. Braun and F. Cichos, Optically Controlled Thermophoretic Trapping of Single Nano-Objects, *ACS Nano* **7**, 11200 (2013).

[2] M. Braun, A. Würger, and F. Cichos, Trapping of Single Nano-Objects in Dynamic Temperature Fields, *Phys. Chem. Chem. Phys.* **16**, 15207 (2014).

[3] L. Lin, J. Zhang, X. Peng, Z. Wu, A. C. H. Coughlan, Z. Mao, M. A. Bevan, and Y. Zheng, Opto-Thermophoretic Assembly of Colloidal Matter, *Sci. Adv.* **3**, 1700458 (2017).

[4] L. Lin, X. Peng, Z. Mao, X. Wei, C. Xie, and Y. Zheng, Interfacial-Entropy-Driven Thermophoretic Tweezers, *Lab Chip* **17**, 3061 (2017).

[5] L. Lin, X. Peng, and Y. Zheng, Reconfigurable Opto-Thermoelectric Printing of Colloidal Particles, *Chem. Commun.* **53**, 7357 (2017).

[6] L. Lin, M. Wang, X. Peng, E. N. Lissek, Z. Mao *et al.*, Opto-Thermoelectric Nanotweezers, *Nat. Photonics* **12**, 195 (2018).

[7] J. N. Pedersen, C. J. Lüscher, R. Marie, L. H. Thamdrup, A. Kristensen, and H. Flyvbjerg, Thermophoretic Forces on DNA Measured with a Single-Molecule Spring Balance, *Phys. Rev. Lett.* **113**, 268301 (2014).

[8] M. Braun, A. P. Bregulla, K. Günther, M. Mertig, and F. Cichos, Single Molecules Trapped by Dynamic Inhomogeneous Temperature Fields, *Nano Lett.* **15**, 5499 (2015).

[9] H.-R. Jiang, N. Yoshinaga, and M. Sano, Active Motion of a Janus Particle by Self-Thermo-phoresis in a Defocused Laser Beam, *Phys. Rev. Lett.* **105**, 268302 (2010).

[10] B. Qian, D. Montiel, A. Bregulla, F. Cichos, and H. Yang, Harnessing Thermal Fluctuations for Purposeful Activities: The Manipulation of Single Micro-Swimmers by Adaptive Photon Nudging, *Chem. Sci.* **4**, 1420 (2013).

[11] A. P. Bregulla, H. Yang, and F. Cichos, Stochastic Localization of Microswimmers by Photon Nudging, *ACS Nano* **8**, 6542 (2014).

[12] A. P. Bregulla and F. Cichos, Size Dependent Efficiency of Photophoretic Swimmers, *Faraday Discuss.* **184**, 381 (2015).

[13] G. Baffou and R. Quidant, Nanoplasmonics for Chemistry, *Chem. Soc. Rev.* **43**, 3898 (2014).

[14] H.-H. Shin, J.-J. Koo, K. S. Lee, and Z. H. Kim, Chemical Reactions Driven by Plasmon-Induced Hot Carriers, *Appl. Mater. Today* **16**, 112 (2019).

[15] D. Mateo, J. L. Cerrillo, S. Durini, and J. Gascon, Fundamentals and Applications of Photo-Thermal Catalysis, *Chem. Soc. Rev.* **50**, 2173 (2021).

[16] M. Li, T. Lohmüller, and J. Feldmann, Optical Injection of Gold Nanoparticles into Living Cells, *Nano Lett.* **15**, 770 (2015).

[17] A. Bahadori, L. B. Oddershede, and P. M. Bendix, Hot-Nanoparticle-Mediated Fusion of Selected Cells, *Nano Res.* **10**, 2034 (2017).

[18] G. Qiu, Z. Gai, L. Saleh, J. Tang, T. Gui, G. A. Kullak-Ublick, and J. Wang, Thermo-Plasmonic-Assisted Cyclic Cleavage Amplification for Self-Validating Plasmonic Detection of SARS-CoV-2, *ACS Nano* **15**, 7536 (2021).

[19] Z. Zhou, E. Sakr, Y. Sun, and P. Bermel, Solar Thermophotovoltaics: Reshaping the Solar Spectrum, *Nanophotonics* **5**, 1 (2016).

[20] T. Burger, C. Sempere, B. Roy-Layinde, and A. Lenert, Present Efficiencies and Future Opportunities in Thermophotovoltaics, *Joule* **4**, 1660 (2020).

[21] C. Chang, C. Yang, Y. Liu, P. Tao, C. Song, W. Shang, J. Wu, and T. Deng, Efficient Solar-Thermal Energy Harvest Driven by Interfacial Plasmonic Heating-Assisted Evaporation, *ACS Appl. Mater. Interfaces* **8**, 23412 (2016).

[22] S. V. Makarov, A. S. Zalogina, M. Tajik, D. A. Zuev, M. V. Rybin, A. A. Kuchmizhak, S. Juodkazis, and Y. Kivshar, Light-Induced Tuning and Reconfiguration of Nanophotonic Structures, *Laser Photonics Rev.* **11**, 1700108 (2017).

[23] J. Cunha, T.-L. Guo, G. Della Valle, A. N. Koya, R. Proietti Zaccaria, and A. Alabastri, Controlling Light, Heat, and Vibrations in Plasmonics and Phononics, *Adv. Optical Mater.* **8**, 2001225 (2020).

[24] I. de Miguel, I. Prieto, A. Albornoz, V. Sanz, C. Weis, P. Turon, and R. Quidant, Plasmon-Based Biofilm Inhibition on Surgical Implants, *Nano Lett.* **19**, 2524 (2019).

[25] T. Shang, X. Yu, S. Han, and B. Yang, Nanomedicine-Based Tumor Photothermal Therapy Synergized Immunotherapy, *Biomater. Sci.* **8**, 5241 (2020).

[26] H. S. Han and K. Y. Choi, Advances in Nanomaterial-Mediated Photothermal Cancer Therapies: Toward Clinical Applications, *Biomedicines* **9**, 305 (2021).

[27] L. Jauffred, A. Samadi, H. Klingberg, P. M. Bendix, and L. B. Oddershede, Plasmonic Heating of Nanostructures, *Chem. Rev.* **119**, 8087 (2019).

[28] G. Baffou, F. Cichos, and R. Quidant, Applications and Challenges of Thermoplasmonics, *Nat. Mater.* **19**, 946 (2020).

[29] J. Chen, J. F.-C. Loo, D. Wang, Y. Zhang, S.-K. Kong, and H.-P. Ho, Thermal Optofluidics: Principles and Applications, *Adv. Opt. Mater.* **8**, 1900829 (2020).

[30] S. Liu, L. Lin, and H.-B. Sun, Opto-Thermophoretic Manipulation, *ACS Nano* **15**, 5925 (2021).

[31] G. Baffou, *Thermoplasmonics: Heating Metal Nanoparticles Using Light*, 1st ed. (Cambridge University Press, 2017).

[32] J. S. Donner, G. Baffou, D. McCloskey, and R. Quidant, Plasmon-Assisted Optofluidics, *ACS Nano* **5**, 5457 (2011).

[33] B. J. Roxworthy, A. M. Bhuiya, S. P. Vanka, and K. C. Toussaint, Understanding and Controlling Plasmon-Induced Convection, *Nat. Commun.* **5**, 3173 (2014).

[34] C. M. Jin, W. Lee, D. Kim, T. Kang, and I. Choi, Photothermal Convection Lithography for Rapid and Direct Assembly of Colloidal Plasmonic Nanoparticles on Generic Substrates, *Small* **14**, 1803055 (2018).

[35] S. A. Putnam and D. G. Cahill, Transport of Nanoscale Latex Spheres in a Temperature Gradient, *Langmuir* **21**, 5317 (2005).

[36] S. Duhr and D. Braun, Thermophoretic Depletion Follows Boltzmann Distribution, *Phys. Rev. Lett.* **96**, 168301 (2006).

[37] S. Duhr and D. Braun, Optothermal Molecule Trapping by Opposing Fluid Flow with Thermophoretic Drift, *Phys. Rev. Lett.* **97**, 038103 (2006).

[38] S. Duhr and D. Braun, Why Molecules Move along a Temperature Gradient, *Proc. Natl. Acad. Sci. USA* **103**, 19678 (2006).

[39] H. Ning, J. K. G. Dhont, and S. Wiegand, Thermal-Diffusive Behavior of a Dilute Solution of Charged Colloids, *Langmuir* **24**, 2426 (2008).

[40] M. Braibanti, D. Vigolo, and R. Piazza, Does Thermophoretic Mobility Depend on Particle Size?, *Phys. Rev. Lett.* **100**, 108303 (2008).

[41] F. M. Weinert and D. Braun, Observation of Slip Flow in Thermophoresis, *Phys. Rev. Lett.* **101**, 168301 (2008).

[42] F. M. Weinert and D. Braun, An Optical Conveyor for Molecules, *Nano Lett.* **9**, 4264 (2009).

[43] K. A. Eslahian, A. Majee, M. Maskos, and A. Würger, Specific Salt Effects on Thermophoresis of Charged Colloids, *Soft Matter* **10**, 1931 (2014).

[44] R.-Y. Dong, Y. Zhou, C. Yang, and B.-Y. Cao, Experimental Study on Thermophoresis of Colloids in Aqueous Surfactant Solutions, *J. Phys. Condens. Matter* **27**, 495102 (2015).

[45] O. Syshchyk, D. Afanasenkau, Z. Wang, H. Kriegs, J. Buitenhuis, and S. Wiegand, Influence of Temperature and Charge Effects on Thermophoresis of Polystyrene Beads, *Eur. Phys. J. E* **39**, 129 (2016).

[46] H.-R. Jiang, H. Wada, N. Yoshinaga, and M. Sano, Manipulation of Colloids by a Nonequilibrium Depletion Force in a Temperature Gradient, *Phys. Rev. Lett.* **102**, 208301 (2009).

[47] Y. T. Maeda, T. Tlusty, and A. Libchaber, Effects of Long DNA Folding and Small RNA Stem-Loop in Thermophoresis, *Proc. Natl. Acad. Sci. USA* **109**, 17972 (2012).

[48] D. Vigolo, S. Buzzaccaro, and R. Piazza, Thermophoresis and Thermoelectricity in Surfactant Solutions, *Langmuir* **26**, 7792 (2010).

[49] A. P. Bregulla, A. Würger, K. Günther, M. Mertig, and F. Cichos, Thermo-Osmotic Flow in Thin Films, *Phys. Rev. Lett.* **116**, 188303 (2016).

[50] J. Gargiulo, T. Brick, I. L. Violi, F. C. Herrera, T. Shibanuma *et al.*, Understanding and Reducing Photothermal Forces for the Fabrication of Au Nanoparticle Dimers by Optical Printing, *Nano Lett.* **17**, 5747 (2017).

[51] F. Winterer, C. M. Maier, C. Pernpeintner, and T. Lohmüller, Optofluidic Transport and Manipulation of Plasmonic Nanoparticles by Thermocapillary Convection, *Soft Matter* **14**, 628 (2018).

[52] Q. Jiang, B. Rogez, J.-B. Claude, G. Baffou, and J. Wenger, Quantifying the Role of the Surfactant and the Thermophoretic Force in Plasmonic Nano-optical Trapping, *Nano Lett.* **20**, 8811 (2020).

[53] R Piazza and A Parola, Thermophoresis in Colloidal Suspensions, *J. Phys. Condens. Matter* **20**, 153102 (2008).

[54] S. Fayolle, T. Bickel, and A. Würger, Thermophoresis of Charged Colloidal Particles, *Phys. Rev. E* **77**, 041404 (2008).

[55] A. Würger, Transport in Charged Colloids Driven by Thermoelectricity, *Phys. Rev. Lett.* **101**, 108302 (2008).

[56] A. Würger, Thermal Non-Equilibrium Transport in Colloids, *Rep. Prog. Phys.* **73**, 126601 (2010).

[57] A. Würger, Is Soret Equilibrium a Non-Equilibrium Effect?, *Comptes Rendus Mécanique* **341**, 438 (2013).

[58] J. Burelbach, D. Frenkel, I. Pagonabarraga, and E. Eiser, A Unified Description of Colloidal Thermophoresis, *Eur. Phys. J. E* **41**, 7 (2018).

[59] J. Burelbach and H. Stark, Determining Phoretic Mobilities with Onsager's Reciprocal Relations: Electro- and Thermophoresis Revisited, *Eur. Phys. J. E* **42**, 4 (2019).

[60] Z. Kang, J. Chen, S.-Y. Wu, and H.-P. Ho, Plasmonic Absorption Activated Trapping and Assembling of Colloidal Crystals with Non-Resonant Continuous Gold Films, *RSC Adv.* **5**, 105409 (2015).

[61] L. Lin, X. Peng, X. Wei, Z. Mao, C. Xie, and Y. Zheng, Thermophoretic Tweezers for Low-Power and Versatile Manipulation of Biological Cells, *ACS Nano* **11**, 3147 (2017).

[62] L. Lin, X. Peng, M. Wang, L. Scarabelli, Z. Mao, L. M. Liz-Marzán, M. F. Becker, and Y. Zheng, Light-Directed Reversible Assembly of Plasmonic Nanoparticles Using Plasmon-Enhanced Thermophoresis, *ACS Nano* **10**, 9659 (2016).

[63] J. L. Anderson, Colloid Transport by Interfacial Forces, *Annu. Rev. Fluid Mech.* **21**, 61 (1989).

[64] B. Derjaguin and G. Sidorenkow, Thermo-Osmosis at Ordinary Temperatures and Its Analogy with the Thermomechanical Effect in Helium II, *Doklady Akademii Nauk SSSR* **32**, 622 (1941).

[65] B. Derjaguin and N. Churaev, "Structure of the Boundary Layers of Liquids and Its Influence on the Mass Transfer in Fine Pores", in *Progress in Surface and Membrane Science*, Vol. 14, 1st ed. (Elsevier, 1981), pp. 69–130.

[66] F. M. Weinert, J. A. Kraus, T. Franosch, and D. Braun, Microscale Fluid Flow Induced by Thermoviscous Expansion Along a Traveling Wave, *Phys. Rev. Lett.* **100**, 164501 (2008).

[67] F. M. Weinert and D. Braun, Optically Driven Fluid Flow along Arbitrary Microscale Patterns Using Thermoviscous Expansion, *J. Appl. Phys.* **104**, 104701 (2008).

[68] W. F. Paxton, K. C. Kistler, C. C. Olmeda, A. Sen, S. K. St. Angelo *et al.*, Catalytic Nanomotors: Autonomous Movement of Striped Nanorods, *J. Am. Chem. Soc.* **126**, 13424 (2004).

[69] R. Dreyfus, J. Baudry, M. L. Roper, M. Fermigier, H. A. Stone, and J. Bibette, Microscopic Artificial Swimmers, *Nature* **437**, 862 (2005).

[70] J. R. Howse, R. A. L. Jones, A. J. Ryan, T. Gough, R. Vafabakhsh, and R. Golestanian, Self-Motile Colloidal Particles: From Directed Propulsion to Random Walk, *Phys. Rev. Lett.* **99**, 048102 (2007).

[71] S. J. Ebbens and J. R. Howse, In Pursuit of Propulsion at the Nanoscale, *Soft Matter* **6**, 726 (2010).

[72] I. Buttinoni, G. Volpe, F. Kümmel, G. Volpe, and C. Bechinger, Active Brownian Motion Tunable by Light, *J. Phys.: Condens. Matter* **24**, 284129 (2012).

[73] C. W. Shields and O. D. Velev, The Evolution of Active Particles: Toward Externally Powered Self-Propelling and Self-Reconfiguring Particle Systems, *Chem.* **3**, 539 (2017).

[74] A. C. H. Tsang, E. Demir, Y. Ding, and O. S. Pak, Roads to Smart Artificial Microswimmers, *Adv. Intell. Syst.* **2**, 1900137 (2020).

[75] X. Peng, Z. Chen, P. S. Kollipara, Y. Liu, J. Fang, L. Lin, and Y. Zheng, Opto-Thermoelectric Microswimmers, *Light Sci Appl* **9**, 141 (2020).

[76] C. Maggi, J. Simmchen, F. Saglimbeni, J. Katuri, M. Dipalo, F. De Angelis, S. Sanchez, and R. Di Leonardo, Self-Assembly of Micromachining Systems Powered by Janus Micromotors, *Small* **12**, 446 (2016).

[77] A. Aubret, M. Youssef, S. Sacanna, and J. Palacci, Targeted Assembly and Synchronization of Self-Spinning Microgears, *Nat. Phys.* **14**, 1114 (2018).

[78] Y. Alapan, B. Yigit, O. Beker, A. F. Demirörs, and M. Sitti, Shape-Encoded Dynamic Assembly of Mobile Micromachines, *Nat. Mater.* **18**, 1244 (2019).

[79] A.-I. Bunea, D. Martella, S. Nocentini, C. Parmeggiani, R. Taboryski, and D. S. Wiersma, Light-Powered Microrobots: Challenges and Opportunities for Hard and Soft Responsive Microswimmers, *Adv. Intell. Syst.* **3**, 2000256 (2021).

[80] T. Bäuerle, R. C. Löffler, and C. Bechinger, Formation of Stable and Responsive Collective States in Suspensions of Active Colloids, *Nat. Commun.* **11**, 2547 (2020).

[81] E. M. Purcell, Life at Low Reynolds Number, *Am. J. Phys.* **45**, 3 (1977).

[82] R Golestanian, T. B. Liverpool, and A Ajdari, Designing Phoretic Micro- and Nano-Swimmers, *New J. Phys.* **9**, 126 (2007).

[83] J. L. Moran and J. D. Posner, Phoretic Self-Propulsion, *Annu. Rev. Fluid Mech.* **49**, 511 (2017).

[84] M. Guix, S. M. Weiz, O. G. Schmidt, and M. Medina-Sánchez, Self-Propelled Micro/-Nanoparticle Motors, *Part. Part. Syst. Charact.* **35**, 1700382 (2018).

[85] U. Khadka, V. Holubec, H. Yang, and F. Cichos, Active Particles Bound by Information Flows, *Nat. Commun.* **9**, 3864 (2018).

[86] Z. Wang, Z. Wang, J. Li, C. Tian, and Y. Wang, Active Colloidal Molecules Assembled via Selective and Directional Bonds, *Nat. Commun.* **11**, 2670 (2020).

[87] A. Aubret, Q. Martinet, and J. Palacci, Metamachines of Pluripotent Colloids, *Nat. Commun.* **12**, 6398 (2021).

[88] C. Bechinger, R. Di Leonardo, H. Löwen, C. Reichhardt, G. Volpe, and G. Volpe, Active Particles in Complex and Crowded Environments, *Rev. Mod. Phys.* **88**, 045006 (2016).

[89] A. E. Cohen and W. E. Moerner, Suppressing Brownian Motion of Individual Biomolecules in Solution, *Proc. Natl. Acad. Sci. USA* **103**, 4362 (2006).

[90] Q. Wang and W. E. Moerner, An Adaptive Anti-Brownian Electrokinetic Trap with Real-Time Information on Single-Molecule Diffusivity and Mobility, *ACS Nano* **5**, 5792 (2011).

[91] J. C. Crocker and D. G. Grier, Methods of Digital Video Microscopy for Colloidal Studies, *J. Colloid Interface Sci.* **179**, 298 (1996).

[92] L. Shen, X. Song, M. Iguchi, and F. Yamamoto, A Method for Recognizing Particles in Overlapped Particle Images, *Pattern Recognit. Lett.* **21**, 21 (2000).

[93] M. Honkanen, P. Saarenrinne, T. Stoor, and J. Niinimäki, Recognition of Highly Overlapping Ellipse-like Bubble Images, *Meas. Sci. Technol.* **16**, 1760 (2005).

[94] S. S. Rogers, T. A. Waigh, X. Zhao, and J. R. Lu, Precise Particle Tracking against a Complicated Background: Polynomial Fitting with Gaussian Weight, *Phys. Biol.* **4**, 220 (2007).

[95] S. M. Anthony, M. Kim, and S. Granick, Single-Particle Tracking of Janus Colloids in Close Proximity, *Langmuir* **24**, 6557 (2008).

[96] R. Parthasarathy, Rapid, Accurate Particle Tracking by Calculation of Radial Symmetry Centers, *Nat Methods* **9**, 724 (2012).

[97] X. Wang, B. Gao, S. Masnou, L. Chen, I. Theurkauff, C. Cottin-Bizonne, Y. Zhao, and F. Shih, Active Colloids Segmentation and Tracking, *Pattern Recognit.* **60**, 177 (2016).

[98] H. Yücel and N. T. Okumuşoğlu, A New Tracking Algorithm for Multiple Colloidal Particles Close to Contact, *J. Phys.: Condens. Matter* **29**, 465101 (2017).

[99] V. Kapoor, W. G. Hirst, C. Hentschel, S. Preibisch, and S. Reber, MTrack: Automated Detection, Tracking, and Analysis of Dynamic Microtubules, *Sci. Rep.* **9**, 3794 (2019).

[100] Y. Rivenson, Z. Göröcs, H. Günaydin, Y. Zhang, H. Wang, and A. Ozcan, Deep Learning Microscopy, *Optica* **4**, 1437 (2017).

[101] J. M. Newby, A. M. Schaefer, P. T. Lee, M. G. Forest, and S. K. Lai, Convolutional Neural Networks Automate Detection for Tracking of Submicron-Scale Particles in 2D and 3D, *Proc. Natl. Acad. Sci. USA* **115**, 9026 (2018).

[102] M. D. Hannel, A. Abdulali, M. O'Brien, and D. G. Grier, Machine-Learning Techniques for Fast and Accurate Feature Localization in Holograms of Colloidal Particles, *Opt. Express* **26**, 15221 (2018).

[103] S. Helgadottir, A. Argun, and G. Volpe, Digital Video Microscopy Enhanced by Deep Learning, *Optica* **6**, 506 (2019).

[104] Y. Rivenson, Y. Wu, and A. Ozcan, Deep Learning in Holography and Coherent Imaging, *Light Sci Appl* **8**, 85 (2019).

[105] H. Pinkard, Z. Phillips, A. Babakhani, D. A. Fletcher, and L. Waller, Deep Learning for Single-Shot Autofocus Microscopy, *Optica* **6**, 794 (2019).

[106] B. Midtvedt, S. Helgadottir, A. Argun, J. Pineda, D. Midtvedt, and G. Volpe, Quantitative Digital Microscopy with Deep Learning, *Appl. Phys. Rev.* **8**, 011310 (2021).

[107] C. M. Dobson, Protein Folding and Misfolding, *Nature* **426**, 884 (2003).

[108] F. Chiti and C. M. Dobson, Protein Misfolding, Functional Amyloid, and Human Disease, *Annu. Rev. Biochem.* **75**, 333 (2006).

[109] F. Chiti and C. M. Dobson, Amyloid Formation by Globular Proteins under Native Conditions, *Nat. Chem. Biol.* **5**, 15 (2009).

[110] T. P. J. Knowles, M. Vendruscolo, and C. M. Dobson, The Amyloid State and Its Association with Protein Misfolding Diseases, *Nat. Rev. Mol. Cell Bio.* **15**, 384 (2014).

[111] F. Chiti and C. M. Dobson, Protein Misfolding, Amyloid Formation, and Human Disease: A Summary of Progress Over the Last Decade, *Ann. Rev. Biochem.* **86**, 27 (2017).

[112] M. G. Iadanza, M. P. Jackson, E. W. Hewitt, N. A. Ranson, and S. E. Radford, A New Era for Understanding Amyloid Structures and Disease, *Nat. Rev. Mol. Cell Biol.* **19**, 755 (2018).

[113] A. K. Buell, The Growth of Amyloid Fibrils: Rates and Mechanisms, *Biochem. J.* **476**, 2677 (2019).

[114] T. P. J. Knowles, C. A. Waudby, G. L. Devlin, S. I. A. Cohen, A. Aguzzi *et al.*, An Analytical Solution to the Kinetics of Breakable Filament Assembly, *Science* **326**, 1533 (2009).

[115] R. Tycko, Solid-State NMR Studies of Amyloid Fibril Structure, *Annu. Rev. Phys. Chem* **62**, 279 (2011).

[116] J. S. Schreck and J.-M. Yuan, A Kinetic Study of Amyloid Formation: Fibril Growth and Length Distributions, *J. Phys. Chem. B* **117**, 6574 (2013).

[117] S. Linse, Monomer-Dependent Secondary Nucleation in Amyloid Formation, *Biophys. Rev.* **9**, 329 (2017).

[118] P. Flagmeier, S. De, T. C. T. Michaels, X. Yang, A. J. Dear *et al.*, Direct Measurement of Lipid Membrane Disruption Connects Kinetics and Toxicity of Aβ42 Aggregation, *Nat. Struct. Mol. Biol.* **27**, 886 (2020).

[119] T. C. T. Michaels, L. X. Liu, G. Meisl, and T. P. J. Knowles, Physical Principles of Filamentous Protein Self-Assembly Kinetics, *J. Phys. Condens. Matter* **29**, 153002 (2017).

[120] A. Ashkin, J. M. Dziedzic, J. E. Bjorkholm, and S. Chu, Observation of a Single-Beam Gradient Force Optical Trap for Dielectric Particles, *Opt. Lett.* **11**, 288 (1986).

[121] J. R. Moffitt, Y. R. Chemla, S. B. Smith, and C. Bustamante, Recent Advances in Optical Tweezers, *Annu. Rev. Biochem.* **77**, 205 (2008).

[122] G. Pesce, P. H. Jones, O. M. Maragò, and G. Volpe, Optical Tweezers: Theory and Practice, *Eur. Phys. J. Plus* **135**, 949 (2020).

[123] M. I. Bespalova, S. Mahanta, and M. Krishnan, Single-Molecule Trapping and Measurement in Solution, *Curr. Opin. Chem. Biol.* **51**, 113 (2019).

[124] D Niether and S Wiegand, Thermophoresis of Biological and Biocompatible Compounds in Aqueous Solution, *J. Phys.: Condens. Matter* **31**, 503003 (2019).

[125] L. D. Landau and E. M. Lifshitz, *Fluid Mechanics*, 2nd ed., Vol. 6, Course of Theoretical Physics (Pergamon Press, 1987).

[126] H. Bruus, *Theoretical Microfluidics*, 1st ed., Oxford Master Series in Physics 18 (Oxford University Press, 2008).

[127] P. Langevin, Sur La Théorie Du Mouvement Brownien, *C. R. Acad. Sci.* **146**, 530 (1908).

[128] M. Reichl, M. Herzog, A. Götz, and D. Braun, Why Charged Molecules Move Across a Temperature Gradient: The Role of Electric Fields, *Phys. Rev. Lett.* **112**, 198101 (2014).

[129] P. H. Jones, O. M. Maragò, and G. Volpe, *Optical Tweezers: Principles and Applications*, 1st ed. (Cambridge University Press, 2015).

[130] J. Honerkamp, *Stochastic Dynamical Systems: Concepts, Numerical Methods, Data Analysis*, 1st ed. (Wiley, 2009).

[131] H. Risken, *The Fokker-Planck Equation*, edited by H. Haken, 2nd ed., Vol. 18, Springer Series in Synergetics (Springer, 1989).

[132] F. Schwabl, *Statistical Mechanics*, 2nd ed. (Springer, 2010).

[133] A. Einstein, Über die von der molekularkinetischen Theorie der Wärme geforderte Bewegung von in ruhenden Flüssigkeiten suspendierten Teilchen, *Ann. Phys.* **322**, 549 (1905).

[134] M. von Smoluchowski, Zur kinetischen Theorie der Brownschen Molekularbewegung und der Suspensionen, *Ann. Phys.* **326**, 756 (1906).

[135] R Kubo, The Fluctuation-Dissipation Theorem, *Rep. Prog. Phys.* **29**, 255 (1966).

[136] J. Happel and H. Brenner, *Low Reynolds Number Hydrodynamics*, edited by R. J. Moreau, 1st ed., Vol. 1, Mechanics of Fluids and Transport Processes (Springer, 1981).

[137] H. Brenner, The Slow Motion of a Sphere through a Viscous Fluid towards a Plane Surface, *Chem. Eng. Sci.* **16**, 242 (1961).

[138] B. Lin, J. Yu, and S. A. Rice, Direct Measurements of Constrained Brownian Motion of an Isolated Sphere between Two Walls, *Phys. Rev. E* **62**, 3909 (2000).

[139] M. Mason and W. Weaver, The Settling of Small Particles in a Fluid, *Phys. Rev.* **23**, 412 (1924).

[140] B. U. Felderhof, Sedimentation of Brownian Particles in a Gravitational Potential, *J. Stat. Phys.* **109**, 483 (2002).

[141] H.-J. Butt, K. Graf, and M. Kappl, *Physics and Chemistry of Interfaces*, 1st ed. (Wiley, 2003).

[142] J. N. Israelachvili, *Intermolecular and Surface Forces*, 3rd ed. (Elsevier Academic Press, 2011).

[143] C. Pfeiffer, C. Rehbock, D. Huhn, C. Carrillo-Carrion, D. J. de Aberasturi, V. Merk, S. Barcikowski, and W. J. Parak, Interaction of Colloidal Nanoparticles with Their Local Environment: The (Ionic) Nanoenvironment around Nanoparticles Is Different from Bulk and Determines the Physico-Chemical Properties of the Nanoparticles, *J. R. Soc. Interface* **11**, 20130931 (2014).

[144] P. K. Das, Effect of Thermodiffusion on pH-regulated Surface Charge Properties of Nanoparticle, *Electrophoresis* **37**, 347 (2016).

[145] W. B. Russel, D. A. Saville, and W. R. Schowalter, *Colloidal Dispersions*, 1st ed., Cambridge Monographs on Mechanics and Applied Mathematics (Cambridge University Press, 1989).

[146] H. Hamaker, The London-van Der Waals Attraction between Spherical Particles, *Physica* **4**, 1058 (1937).

[147] I. Dzyaloshinskii, E. Lifshitz, and L. Pitaevskii, The General Theory of van Der Waals Forces, *Adv. Phys.* **10**, 165 (1961).

[148] V. Parsegian and G. H. Weiss, Spectroscopic Parameters for Computation of van Der Waals Forces, *J. Colloid Interface Sci.* **81**, 285 (1981).

[149] M. Giesbers, J. Kleijn, and M. A. Cohen Stuart, The Electrical Double Layer on Gold Probed by Electrokinetic and Surface Force Measurements, *J. Colloid Interface Sci.* **248**, 88 (2002).

[150] B. V. Derjaguin and L. D. Landau, Theory of the Stability of Strongly Charged Lyophobic Sols and of the Adhesion of Strongly Charged Particles in Solutions of Electrolytes, *Acta Physicochimica URSS* **14**, 633 (1941).

[151] E. J. W. Verwey and J. T. G. Overbeek, *Theory of the Stability of Lyophobic Colloids: The Interaction of Sol Particles Having an Electric Double Layer*, 1st ed. (Elsevier, 1948).

[152] S. Alexander, Polymer Adsorption on Small Spheres. A Scaling Approach, *J. Phys. France* **38**, 977 (1977).

[153] P. de Gennes, Polymers at an Interface; a Simplified View, *Adv. Colloid Interface Sci.* **27**, 189 (1987).

[154] D. Kleshchanok, R. Tuinier, and P. R. Lang, Direct Measurements of Polymer-Induced Forces, *J. Phys.: Condens. Matter* **20**, 073101 (2008).

[155] M. R. Nejadnik, A. L. J. Olsson, P. K. Sharma, H. C. van der Mei, W. Norde, and H. J. Busscher, Adsorption of Pluronic F-127 on Surfaces with Different Hydrophobicities Probed by Quartz Crystal Microbalance with Dissipation, *Langmuir* **25**, 6245 (2009).

[156] T. Hueckel, G. M. Hocky, J. Palacci, and S. Sacanna, Ionic Solids from Common Colloids, *Nature* **580**, 487 (2020).

[157] V. N. Luk, G. C. Mo, and A. R. Wheeler, Pluronic Additives: A Solution to Sticky Problems in Digital Microfluidics, *Langmuir* **24**, 6382 (2008).

[158] C. Ludwig, Diffusion Zwischen Ungleich Erwärmten Orten Gleich Zusammengesetzter Lösungen, *Sitzber. K. Akad. Wiss.* **20**, 539 (1856).

[159] C. Soret, Sur l'état d'équilibre Que Prend, Du Point de Vue de Sa Concentration, Une Dissolution Saline Primitivement Homogène, Dont Deux Parties Sont Portées à Des Températures Différentes, *Arch. Sci. Phys. Nat.* **2**, 48 (1879).

[160] B. V. Derjaguin, N. V Churaev, and V. M Muller, *Surface Forces*, 1st ed. (Springer, 2013).

[161] A. Velikonja, E. Gongadze, V. Kralj-Iglič, and A. Iglič, Charge Dependent Capacitance of Stern Layer and Capacitance of Electrode/Electrolyte Interface, *Int. J. Electrochem. Sci.* **9**, 10 (2014).

[162] J. N. Agar, C. Y. Mou, and J. L. Lin, Single-Ion Heat of Transport in Electrolyte Solutions: A Hydrodynamic Theory, *J. Phys. Chem.* **93**, 2079 (1989).

[163] J. Morthomas and A. Würger, Thermoelectric Effect on Charged Colloids in the Hückel Limit, *The European Physical Journal E* **27**, 425 (2008).

[164] A. Würger, Temperature Dependence of the Soret Motion in Colloids, *Langmuir* **25**, 6696 (2009).

[165] M. Selmke, U. Khadka, A. P. Bregulla, F. Cichos, and H. Yang, Theory for Controlling Individual Self-Propelled Micro-Swimmers by Photon Nudging I: Directed Transport, *Phys. Chem. Chem. Phys.* **20**, 10502 (2018).

[166] A. Würger, Thermophoresis in Colloidal Suspensions Driven by Marangoni Forces, *Phys. Rev. Lett.* **98**, 138301 (2007).

[167] J. Chan, J. J. Popov, S. Kolisnek-Kehl, and D. G. Leaist, Soret Coefficients for Aqueous Polyethylene Glycol Solutions and Some Tests of the Segmental Model of Polymer Thermal Diffusion, *J. Solut. Chem.* **32**, 197 (2003).

[168] K. Devanand and J. C. Selser, Asymptotic Behavior and Long-Range Interactions in Aqueous Solutions of Poly(Ethylene Oxide), *Macromolecules* **24**, 5943 (1991).

[169] T. Bickel, A. Majee, and A. Würger, Flow Pattern in the Vicinity of Self-Propelling Hot Janus Particles, *Phys. Rev. E* **88**, 012301 (2013).

[170] T. M. Squires and S. R. Quake, Microfluidics: Fluid Physics at the Nanoliter Scale, *Rev. Mod. Phys.* **77**, 977 (2005).

[171] B. E. A. Saleh and M. C. Teich, *Fundamentals of Photonics*, edited by B. E. A. Saleh, 2nd ed., Wiley Series in Pure and Applied Optics (Wiley, 2007).

[172] C. F. Bohren and D. R. Huffman, *Absorption and Scattering of Light by Small Particles*, 1st ed. (Wiley, 2004).

[173] P. B. Johnson and R. W. Christy, Optical Constants of the Noble Metals, *Phys. Rev. B* **6**, 4370 (1972).

[174] S. A. Maier, *Plasmonics: Fundamentals and Applications*, 1st ed. (Springer, 2007).

[175] M. Quinten, *Optical Properties of Nanoparticle Systems: Mie and Beyond*, 1st ed. (Wiley, Weinheim, 2011).

[176] P. Yeh, *Optical Waves in Layered Media*, 1st ed. (Wiley, 2005).

[177] S. Byrnes, Python Package Tmm v0.1.8, https://pypi.org/project/tmm/ (visited on 12/08/2021).

[178] B. Rogez, Z. Marmri, F. Thibaudau, and G. Baffou, Thermoplasmonics of Metal Layers and Nanoholes, *APL Photonics* **6**, 101101 (2021).

[179] A. Salandrino, S. Fardad, and D. N. Christodoulides, Generalized Mie Theory of Optical Forces, *J. Opt. Soc. Am. B* **29**, 855 (2012).

[180] G. Gouesbet and G. Gréhan, *Generalized Lorenz-Mie Theories*, 2nd ed. (Springer, 2017).

[181] O. M. Maragò, P. H. Jones, P. G. Gucciardi, G. Volpe, and A. C. Ferrari, Optical Trapping and Manipulation of Nanostructures, *Nat. Nanotechnol.* **8**, 807 (2013).

[182] E. Fällman and O. Axner, Design for Fully Steerable Dual-Trap Optical Tweezers, *Applied Optics* **36**, 2107 (1997).

[183] D. Ross, M. Gaitan, and L. E. Locascio, Temperature Measurement in Microfluidic Systems Using a Temperature-Dependent Fluorescent Dye, *Anal. Chem.* **73**, 4117 (2001).

[184] F. Vetrone, R. Naccache, A. Zamarrón, A. Juarranz de la Fuente, F. Sanz-Rodríguez *et al.*, Temperature Sensing Using Fluorescent Nanothermometers, *ACS Nano* **4**, 3254 (2010).

[185] D. Jaque and F. Vetrone, Luminescence Nanothermometry, *Nanoscale* **4**, 4301 (2012).

[186] S. Li, K. Zhang, J.-M. Yang, L. Lin, and H. Yang, Single Quantum Dots as Local Temperature Markers, *Nano Lett.* **7**, 3102 (2007).

[187] P. Neumann, I. Jakobi, F. Dolde, C. Burk, R. Reuter *et al.*, High-Precision Nanoscale Temperature Sensing Using Single Defects in Diamond, *Nano Lett.* **13**, 2738 (2013).

[188] S. Sotoma, C. P. Epperla, and H.-C. Chang, Diamond Nanothermometry, *ChemNanoMat* **4**, 15 (2018).

[189] S. D. McGrane, D. S. Moore, P. M. Goodwin, and D. M. Dattelbaum, Quantitative Tradeoffs between Spatial, Temporal, and Thermometric Resolution of Nonresonant Raman Thermometry for Dynamic Experiments, *Appl. Spectrosc.* **68**, 1279 (2014).

[190] G. Baffou, P. Bon, J. Savatier, J. Polleux, M. Zhu, M. Merlin, H. Rigneault, and S. Monneret, Thermal Imaging of Nanostructures by Quantitative Optical Phase Analysis, *ACS Nano* **6**, 2452 (2012).

[191] X. Xie and D. G. Cahill, Thermometry of Plasmonic Nanostructures by Anti-Stokes Electronic Raman Scattering, *Appl. Phys. Lett.* **109**, 183104 (2016).

[192] A. Carattino, M. Caldarola, and M. Orrit, Gold Nanoparticles as Absolute Nanothermometers, *Nano Lett.* **18**, 874 (2018).

[193] G. Baffou, Anti-Stokes Thermometry in Nanoplasmonics, *ACS Nano* **15**, 5785 (2021).

[194] P. M. Bendix, S. N. S. Reihani, and L. B. Oddershede, Direct Measurements of Heating by Electromagnetically Trapped Gold Nanoparticles on Supported Lipid Bilayers, *ACS Nano* **4**, 2256 (2010).

[195] R. Horn, Refractive Indices and Order Parameters of Two Liquid Crystals, *J. Phys. France* **39**, 105 (1978).

[196] J. Li, S. Gauza, and S.-T. Wu, Temperature Effect on Liquid Crystal Refractive Indices, *J. Appl. Phys.* **96**, 19 (2004).

[197] R. J. Hunter, *Zeta Potential in Colloid Science: Principles and Applications* (Academic Press, 1988).

[198] K. Makino and H. Ohshima, Electrophoretic Mobility of a Colloidal Particle with Constant Surface Charge Density, *Langmuir* **26**, 18016 (2010).

[199] D. Gao, W. Ding, M. Nieto-Vesperinas, X. Ding, M. Rahman, T. Zhang, C. Lim, and C.-W. Qiu, Optical Manipulation from the Microscale to the Nanoscale: Fundamentals, Advances and Prospects, *Light Sci. Appl.* **6**, 17039 (2017).

[200] C. Bradac, Nanoscale Optical Trapping: A Review, *Adv. Opt. Mat.* **6**, 1800005 (2018).

[201] J. Xavier, S. Vincent, F. Meder, and F. Vollmer, Advances in Optoplasmonic Sensors – Combining Optical Nano/Microcavities and Photonic Crystals with Plasmonic Nanostructures and Nanoparticles, *Nanophotonics* **7**, 1 (2018).

[202] Y. Xie, J. Rufo, R. Zhong, J. Rich, P. Li, K. W. Leong, and T. J. Huang, Microfluidic Isolation and Enrichment of Nanoparticles, *ACS Nano* **14**, 16220 (2020).

[203] I. A. Favre-Bulle, A. B. Stilgoe, E. K. Scott, and H. Rubinsztein-Dunlop, Optical Trapping in Vivo: Theory, Practice, and Applications, *Nanophotonics* **8**, 1023 (2019).

[204] D. Choudhary, A. Mossa, M. Jadhav, and C. Cecconi, Bio-Molecular Applications of Recent Developments in Optical Tweezers, *Biomolecules* **9**, 23 (2019).

[205] M. Kayci, H.-C. Chang, and A. Radenovic, Electron Spin Resonance of Nitrogen-Vacancy Defects Embedded in Single Nanodiamonds in an ABEL Trap, *Nano Lett.* **14**, 5335 (2014).

[206] G.-C. Li, Q. Zhang, S. A. Maier, and D. Lei, Plasmonic Particle-on-Film Nanocavities: A Versatile Platform for Plasmon-Enhanced Spectroscopy and Photochemistry, *Nanophotonics* **7**, 1865 (2018).

[207] M. L. Juan, M. Righini, and R. Quidant, Plasmon Nano-Optical Tweezers, *Nat. Photonics* **5**, 349 (2011).

[208] Y. Zhang, C. Min, X. Dou, X. Wang, H. P. Urbach, M. G. Somekh, and X. Yuan, Plasmonic Tweezers: For Nanoscale Optical Trapping and Beyond, *Light Sci. Appl.* **10**, 59 (2021).

[209] I. De Vlaminck and C. Dekker, Recent Advances in Magnetic Tweezers, *Annu. Rev. Biophys.* **41**, 453 (2012).

[210] M. C. Wu, Optoelectronic Tweezers, *Nat. Photonics* **5**, 322 (2011).

[211] A. Kotnala and R. Gordon, Quantification of High-Efficiency Trapping of Nanoparticles in a Double Nanohole Optical Tweezer, *Nano Lett.* **14**, 853 (2014).

[212] J. C. Ndukaife, A. V. Kildishev, A. G. A. Nnanna, V. M. Shalaev, S. T. Wereley, and A. Boltasseva, Long-Range and Rapid Transport of Individual Nano-Objects by a Hybrid Electrothermoplasmonic Nanotweezer, *Nat. Nanotechnol.* **11**, 53 (2016).

[213] C. Hong, S. Yang, and J. C. Ndukaife, Stand-off Trapping and Manipulation of Sub-10 Nm Objects and Biomolecules Using Opto-Thermo-Electrohydrodynamic Tweezers, *Nat. Nanotechnol.* **15**, 908 (2020).

[214] B. Ciraulo, J. Garcia-Guirado, I. de Miguel, J. Ortega Arroyo, and R. Quidant, Long-Range Optofluidic Control with Plasmon Heating, *Nat. Commun.* **12**, 2001 (2021).

[215] E. Lauga and T. R. Powers, The Hydrodynamics of Swimming Microorganisms, *Rep. Prog. Phys.* **72**, 096601 (2009).

[216] F. M. Weinert, C. B. Mast, and D. Braun, Optical Fluid and Biomolecule Transport with Thermal Fields, *Phys. Chem. Chem. Phys.* **13**, 9918 (2011).

[217] R. Chikkaraddy, B. de Nijs, F. Benz, S. J. Barrow, O. A. Scherman *et al.*, Single-Molecule Strong Coupling at Room Temperature in Plasmonic Nanocavities, *Nature* **535**, 127 (2016).

[218] Y. T. Maeda, A. Buguin, and A. Libchaber, Thermal Separation: Interplay between the Soret Effect and Entropic Force Gradient, *Phys. Rev. Lett.* **107**, 038301 (2011).

[219] S. J. Rehfeld, Adsorption of Sodium Dodecyl Sulfate at Various Hydrocarbon-Water Interfaces, *J. Phys. Chem.* **71**, 738 (1967).

[220] Q. Zhang, H. Yu, M. Barbiero, B. Wang, and M. Gu, Artificial Neural Networks Enabled by Nanophotonics, *Light Sci Appl* **8**, 42 (2019).

[221] J. Xavier, D. Yu, C. Jones, E. Zossimova, and F. Vollmer, Quantum Nanophotonic and Nanoplasmonic Sensing: Towards Quantum Optical Bioscience Laboratories on Chip, *Nanophotonics* **10**, 1387 (2021).

[222] J. Peng, H.-H. Jeong, Q. Lin, S. Cormier, H.-L. Liang, M. F. L. De Volder, S. Vignolini, and J. J. Baumberg, Scalable Electrochromic Nanopixels Using Plasmonics, *Sci. Adv.* **5**, eaaw2205 (2019).

[223] E. Mohammadi, A. Tittl, K. L. Tsakmakidis, T. V. Raziman, and A. G. Curto, Dual Nanoresonators for Ultrasensitive Chiral Detection, *ACS Photonics* **8**, 1754 (2021).

[224] D. B. Allan, T. Caswell, N. C. Keim, and C. M. van der Wel, *Trackpy v0.4.2*, version v0.4.2, Zenodo, Oct. 16, 2019.

[225] M. Speidel, A. Jonáš, and E.-L. Florin, Three-Dimensional Tracking of Fluorescent Nanoparticles with Subnanometer Precision by Use of off-Focus Imaging, *Opt. Lett.* **28**, 69 (2003).

[226] G. Langer, J. Hartmann, and M. Reichling, Thermal Conductivity of Thin Metallic Films Measured by Photothermal Profile Analysis, *Rev. Sci. Instrum.* **68**, 1510 (1997).

[227] M. Marinelli, F. Mercuri, U. Zammit, and F. Scudieri, Thermal Conductivity and Thermal Diffusivity of the Cyanobiphenyl (nCB) Homologous Series, *Phys. Rev. E* **58**, 5860 (1998).

[228] H. Kuwata, H. Tamaru, K. Esumi, and K. Miyano, Resonant Light Scattering from Metal Nanoparticles: Practical Analysis beyond Rayleigh Approximation, *Appl. Phys. Lett.* **83**, 4625 (2003).

[229] M. Zarei and M. Zarei, Self-Propelled Micro/Nanomotors for Sensing and Environmental Remediation, *Small* **14**, 1800912 (2018).

[230] L. Wang, A. Kaeppler, D. Fischer, and J. Simmchen, Photocatalytic TiO_2 Micromotors for Removal of Microplastics and Suspended Matter, *ACS Appl. Mater. Interfaces* **11**, 32937 (2019).

[231] L. Sonntag, J. Simmchen, and V. Magdanz, Nano-and Micromotors Designed for Cancer Therapy, *Molecules* **24**, 3410 (2019).

[232] L. Baraban, D. Makarov, R. Streubel, I. Mönch, D. Grimm, S. Sanchez, and O. G. Schmidt, Catalytic Janus Motors on Microfluidic Chip: Deterministic Motion for Targeted Cargo Delivery, *ACS Nano* **6**, 3383 (2012).

[233] Y. Yoshizumi, T. Honegger, K. Berton, H. Suzuki, and D. Peyrade, Trajectory Control of Self-Propelled Micromotors Using AC Electrokinetics, *Small* **11**, 5630 (2015).

[234] J. Guo, J. J. Gallegos, A. R. Tom, and D. Fan, Electric-Field-Guided Precision Manipulation of Catalytic Nanomotors for Cargo Delivery and Powering Nanoelectromechanical Devices, *ACS Nano* **12**, 1179 (2018).

[235] O. Ilic, I. Kaminer, Y. Lahini, H. Buljan, and M. Soljačić, Exploiting Optical Asymmetry for Controlled Guiding of Particles with Light, *ACS Photonics* **3**, 197 (2016).

[236] H. Brenner, Self-Thermophoresis and Thermal Self-Diffusion in Liquids and Gases, *Phys. Rev. E* **82**, 036325 (2010).

[237] K. Kroy, D. Chakraborty, and F. Cichos, Hot Microswimmers, *Eur. Phys. J.: Spec. Top.* **225**, 2207 (2016).

[238] J. R. Gomez-Solano, A. Blokhuis, and C. Bechinger, Dynamics of Self-Propelled Janus Particles in Viscoelastic Fluids, *Phys. Rev. Lett.* **116**, 138301 (2016).

[239] J. Palacci, S. Sacanna, A. P. Steinberg, D. J. Pine, and P. M. Chaikin, Living Crystals of Light-Activated Colloidal Surfers, *Science* **339**, 936 (2013).

[240] A. P. Bregulla and F. Cichos, Flow Fields around Pinned Self-Thermophoretic Microswimmers under Confinement, *J. Chem. Phys.* **151**, 044706 (2019).

[241] M. Selmke, U. Khadka, A. P. Bregulla, F. Cichos, and H. Yang, Theory for Controlling Individual Self-Propelled Micro-Swimmers by Photon Nudging II: Confinement, *Phys. Chem. Chem. Phys.* **20**, 10521 (2018).

[242] S. Muiños Landin, K. Ghazi-Zahedi, and F. Cichos, “Reinforcement Learning of Artificial Microswimmers”, 2018.

[243] F. Cichos, K. Gustavsson, B. Mehlig, and G. Volpe, Machine Learning for Active Matter, *Nat. Mach. Intell.* **2**, 94 (2020).

[244] P. Romanczuk and G. Salbreux, Optimal Chemotaxis in Intermittent Migration of Animal Cells, *Phys. Rev. E* **91**, 042720 (2015).

[245] R. Niu, A. Fischer, T. Palberg, and T. Speck, Dynamics of Binary Active Clusters Driven by Ion-Exchange Particles, *ACS Nano* **12**, 10932 (2018).

[246] F. Schmidt, B. Liebchen, H. Löwen, and G. Volpe, Light-Controlled Assembly of Active Colloidal Molecules, *J. Chem. Phys.* **150**, 094905 (2019).

[247] U. Choudhury, D. P. Singh, T. Qiu, and P. Fischer, Chemical Nanomotors at the Gram Scale Form a Dense Active Optorheological Medium, *Adv. Mater.* **31**, 1807382 (2019).

[248] S. Heckel, J. Grauer, M. Semmler, T. Gemming, H. Löwen, B. Liebchen, and J. Simmchen, Active Assembly of Spheroidal Photocatalytic $BiVO_4$ Microswimmers, *Langmuir* **36**, 12473 (2020).

[249] J. Gieseler, L. Novotny, and R. Quidant, Thermal Nonlinearities in a Nanomechanical Oscillator, *Nat. Phys.* **9**, 806 (2013).

[250] T. Bäuerle, A. Fischer, T. Speck, and C. Bechinger, Self-Organization of Active Particles by Quorum Sensing Rules, *Nat. Commun.* **9**, 3232 (2018).

[251] J. Redmon, S. Divvala, R. Girshick, and A. Farhadi, "You Only Look Once: Unified, Real-Time Object Detection", 2016.

[252] J. Redmon and A. Farhadi, "YOLO9000: Better, Faster, Stronger", 2016.

[253] J. Redmon and A. Farhadi, "YOLOv3: An Incremental Improvement", 2018.

[254] M. Abadi, A. Agarwal, P. Barham, E. Brevdo, Z. Chen *et al.*, "TensorFlow: Large-Scale Machine Learning on Heterogeneous Distributed Systems", 2016.

[255] F. Chollet, Keras, keras.io (visited on 10/12/2019).

[256] F. Chollet, *Deep Learning with Python*, 1st ed. (Manning Publications, 2018).

[257] N. Chenouard, I. Smal, F. de Chaumont, M. Maška, I. F. Sbalzarini *et al.*, Objective Comparison of Particle Tracking Methods, *Nat. Methods* **11**, 281 (2014).

[258] M. K. Cheezum, W. F. Walker, and W. H. Guilford, Quantitative Comparison of Algorithms for Tracking Single Fluorescent Particles, *Biophys. J.* **81**, 2378 (2001).

[259] L. Xiao, Y. Qiao, Y. He, and E. S. Yeung, Three Dimensional Orientational Imaging of Nanoparticles with Darkfield Microscopy, *Anal. Chem.* **82**, 5268 (2010).

[260] S. M. Anthony, L. Hong, M. Kim, and S. Granick, Single-Particle Colloid Tracking in Four Dimensions, *Langmuir* **22**, 9812 (2006).

[261] S. Muiños Landin, A. Fischer, V. Holubec, and F. Cichos, Reinforcement Learning with Artificial Microswimmers, *Sci. Robot.* **6**, eabd9285 (2021).

[262] J. Hui, Real-Time Object Detection with YOLO, YOLOv2 and Now YOLOv3, medium.com (visited on 10/18/2019).

[263] S.-Y. Ow and D. E. Dunstan, A Brief Overview of Amyloids and Alzheimer's Disease, *Protein Sci.* **23**, 1315 (2014).

[264] K. Araki, N. Yagi, K. Aoyama, C.-J. Choong, H. Hayakawa *et al.*, Parkinson's Disease Is a Type of Amyloidosis Featuring Accumulation of Amyloid Fibrils of α-Synuclein, *Proc. Natl. Acad. Sci. USA* **116**, 17963 (2019).

[265] A. Mukherjee, D. Morales-Scheihing, P. C. Butler, and C. Soto, Type 2 Diabetes as a Protein Misfolding Disease, *Trends Mol. Med.* **21**, 439 (2015).

[266] M. Schmidt, C. Sachse, W. Richter, C. Xu, M. Fandrich, and N. Grigorieff, Comparison of Alzheimer A (1-40) and A (1-42) Amyloid Fibrils Reveals Similar Protofilament Structures, *Proc. Natl. Acad. Sci. USA* **106**, 19813 (2009).

[267] A. W. P. Fitzpatrick, G. T. Debelouchina, M. J. Bayro, D. K. Clare, M. A. Caporini *et al.*, Atomic Structure and Hierarchical Assembly of a Cross-Beta Amyloid Fibril, *Proc. Natl. Acad. Sci. USA* **110**, 5468 (2013).

[268] S. Vivekanandan, J. R. Brender, S. Y. Lee, and A. Ramamoorthy, A Partially Folded Structure of Amyloid-Beta(1–40) in an Aqueous Environment, *Biochem. Biophys. Res. Commun.* **411**, 312 (2011).

[269] C. Sachse, M. Fandrich, and N. Grigorieff, Paired -Sheet Structure of an A (1-40) Amyloid Fibril Revealed by Electron Microscopy, *Proc. Natl. Acad. Sci. USA* **105**, 7462 (2008).

[270] P. N. Nirmalraj, J. List, S. Battacharya, G. Howe, L. Xu, D. Thompson, and M. Mayer, Complete Aggregation Pathway of Amyloid β (1-40) and (1-42) Resolved on an Atomically Clean Interface, *Sci. Adv.* **6**, eaaz6014 (2020).

[271] H. A. Scheidt, I. Morgado, S. Rothemund, and D. Huster, Dynamics of Amyloid β Fibrils Revealed by Solid-state NMR, *J. Biol. Chem.* **287**, 2017 (2012).

[272] F. Bemporad and F. Chiti, Protein Misfolded Oligomers: Experimental Approaches, Mechanism of Formation, and Structure-Toxicity Relationships, *Chem. Biol.* **19**, 315 (2012).

[273] J. C. Stroud, C. Liu, P. K. Teng, and D. Eisenberg, Toxic Fibrillar Oligomers of Amyloid-Have Cross- Structure, *Proc. Natl. Acad. Sci. USA* **109**, 7717 (2012).

[274] J. Bieschke, M. Herbst, T. Wiglenda, R. P. Friedrich, A. Boeddrich *et al.*, Small-Molecule Conversion of Toxic Oligomers to Nontoxic β-Sheet–Rich Amyloid Fibrils, *Nat. Chem. Biol.,* **8**, 93 (2012).

[275] E. N. Cline, M. A. a. Bicca, K. L. Viola, and W. L. Klein, The Amyloid-β Oligomer Hypothesis: Beginning of the Third Decade, *J. Alzheimer's Dis.* **64**, S567 (2018).

[276] C. B. Andersen, H. Yagi, M. Manno, V. Martorana, T. Ban *et al.*, Branching in Amyloid Fibril Growth, *Biophys. J.* **96**, 1529 (2009).

[277] T. P. J. Knowles, D. A. White, A. R. Abate, J. J. Agresti, S. I. A. Cohen *et al.*, Observation of Spatial Propagation of Amyloid Assembly from Single Nuclei, *Proc. Natl. Acad. Sci. USA* **108**, 14746 (2011).

[278] H. Yagi, Y. Abe, N. Takayanagi, and Y. Goto, Elongation of Amyloid Fibrils through Lateral Binding of Monomers Revealed by Total Internal Reflection Fluorescence Microscopy, *Biochim. Biophys. Acta Proteins Proteom.* **1844**, 1881 (2014).

[279] T. Scheidt, U. Ł apińska, J. R. Kumita, D. R. Whiten, D. Klenerman *et al.*, Secondary Nucleation and Elongation Occur at Different Sites on Alzheimer's Amyloid-β Aggregates, *Sci. Adv.* **5**, eaau3112 (2019).

[280] S. Hadi Alijanvand, A. Peduzzo, and A. K. Buell, Secondary Nucleation and the Conservation of Structural Characteristics of Amyloid Fibril Strains, *Front. Mol. Biosci.* **8**, 669994 (2021).

[281] C. Goldsbury, P. Frey, V. Olivieri, U. Aebi, and S. A. Müller, Multiple Assembly Pathways Underlie Amyloid-β Fibril Polymorphisms, *J. Mol. Biol.* **352**, 282 (2005).

[282] T. Eichner and S. E. Radford, A Diversity of Assembly Mechanisms of a Generic Amyloid Fold, *Molecular Cell* **43**, 8 (2011).

[283] J. Adamcik and R. Mezzenga, Amyloid Polymorphism in the Protein Folding and Aggregation Energy Landscape, *Angew. Chem. Int. Ed.* **57**, 8370 (2018).

[284] H. Blackley, G. Sanders, M. Davies, C. Roberts, S. Tendler, and M. Wilkinson, In-Situ Atomic Force Microscopy Study of β-Amyloid Fibrillization, *J. Mol. Biol.* **298**, 833 (2000).

[285] D. Pinotsi, A. K. Buell, C. Galvagnion, C. M. Dobson, G. S. Kaminski Schierle, and C. F. Kaminski, Direct Observation of Heterogeneous Amyloid Fibril Growth Kinetics via Two-Color Super-Resolution Microscopy, *Nano Lett.* **14**, 339 (2014).

[286] M. H. Horrocks, S. F. Lee, S. Gandhi, N. K. Magdalinou, S. W. Chen *et al.*, Single-Molecule Imaging of Individual Amyloid Protein Aggregates in Human Biofluids, *ACS Chem. Neurosci.* **7**, 399 (2016).

[287] T. Ban, D. Hamada, K. Hasegawa, H. Naiki, and Y. Goto, Direct Observation of Amyloid Fibril Growth Monitored by Thioflavin T Fluorescence, *J. Biol. Chem.* **278**, 16462 (2003).

[288] T. Ban, K. Yamaguchi, and Y. Goto, Direct Observation of Amyloid Fibril Growth, Propagation, and Adaptation, *Acc. Chem. Res.* **39**, 663 (2006).

[289] F. Grigolato and P. Arosio, The Role of Surfaces on Amyloid Formation, *Biophys. Chem.* **270**, 106533 (2021).

[290] M. Biancalana and S. Koide, Molecular Mechanism of Thioflavin-T Binding to Amyloid Fibrils, *Biochim. Biophys. Acta Proteins Proteom.* **1804**, 1405 (2010).

[291] H. A. Shaban, C. A. Valades-Cruz, J. Savatier, and S. Brasselet, Polarized Super-Resolution Structural Imaging inside Amyloid Fibrils Using Thioflavine T, *Sci. Rep.* **7**, 12482 (2017).

[292] K. Spehar, T. Ding, Y. Sun, N. Kedia, J. Lu, G. R. Nahass, M. D. Lew, and J. Bieschke, Super-Resolution Imaging of Amyloid Structures over Extended Times by Using Transient Binding of Single Thioflavin T Molecules, *ChemBioChem* **19**, 1944 (2018).

[293] C. Xue, T. Y. Lin, D. Chang, and Z. Guo, Thioflavin T as an Amyloid Dye: Fibril Quantification, Optimal Concentration and Effect on Aggregation, *Royal Soc. Open Sci.* **4**, 160696 (2017).

[294] S. Broersma, Viscous Force and Torque Constants for a Cylinder, *J. Chem. Phys.* **74**, 6989 (1981).

[295] S. Jawhar, O. Wirths, and T. A. Bayer, Pyroglutamate Amyloid-β (Aβ): A Hatchet Man in Alzheimer Disease, *J. Biol. Chem.* **286**, 38825 (2011).

[296] H. A. Scheidt, J. Adler, M. Krueger, and D. Huster, Fibrils of Truncated Pyroglutamyl-Modified Aβ Peptide Exhibit a Similar Structure as Wildtype Mature Aβ Fibrils, *Sci. Rep.* **6**, 33531 (2016).

[297] M. Schmidt, A. Rohou, K. Lasker, J. K. Yadav, C. Schiene-Fischer, M. Fändrich, and N. Grigorieff, Peptide Dimer Structure in an Aβ(1–42) Fibril Visualized with Cryo-EM, *Proc. Natl. Acad. Sci. USA* **112**, 11858 (2015).

[298] M. Wolff, J. J. Mittag, T. W. Herling, E. D. Genst, C. M. Dobson, T. P. J. Knowles, D. Braun, and A. K. Buell, Quantitative Thermophoretic Study of Disease-Related Protein Aggregates, *Sci. Rep.* **6**, 22829 (2016).

[299] L. P. Watkins and H. Yang, Detection of Intensity Change Points in Time-Resolved Single-Molecule Measurements, *J. Phys. Chem. B* **109**, 617 (2005).

[300] H. Yang, Detection and Characterization of Dynamical Heterogeneity in an Event Series Using Wavelet Correlation, *J. Chem. Phys.* **129**, 074701 (2008).

[301] P. Obstarczyk, M. Lipok, M. Grelich-Mucha, M. Samoć, and J. Olesiak-Bańska, Two-Photon Excited Polarization-Dependent Autofluorescence of Amyloids as a Label-Free Method of Fibril Organization Imaging, *J. Phys. Chem. Lett.* 1432 (2021).

[302] G. Li and J. X. Tang, Diffusion of Actin Filaments within a Thin Layer between Two Walls, *Phys. Rev. E* **69**, 061921 (2004).

[303] A. Hunt, F. Gittes, and J. Howard, The Force Exerted by a Single Kinesin Molecule against a Viscous Load, *Biophys. J.* **67**, 766 (1994).

[304] G. Casella and R. L. Berger, *Statistical Inference*, 2nd ed. (Duxbury/Thomson Learning, 2002).

[305] P. Zemánek, G. Volpe, A. Jonáš, and O. Brzobohatý, Perspective on Light-Induced Transport of Particles: From Optical Forces to Phoretic Motion, *Adv. Opt. Photon.* **11**, 577 (2019).

[306] J. Li, E. H. Hill, L. Lin, and Y. Zheng, Optical Nanoprinting of Colloidal Particles and Functional Structures, *ACS Nano* **13**, 3783 (2019).

[307] S. Auschra, V. Holubec, N. A. Söker, F. Cichos, and K. Kroy, Polarization-Density Patterns of Active Particles in Motility Gradients, *Phys. Rev. E* **103**, 062601 (2021).

[308] J. Kim and O. J. F. Martin, Surfactants Control Optical Trapping near a Glass Wall, *J. Phys. Chem. C* **126**, 378 (2021).

[309] N. Lee and S. Wiegand, Thermophoretic Micron-Scale Devices: Practical Approach and Review, *Entropy* **22**, 950 (2020).

[310] Z. Chen, J. Li, and Y. Zheng, Heat-Mediated Optical Manipulation, *Chem. Rev.* **122**, 3122 (2021).

[311] J. Katuri, W. E. Uspal, M. N. Popescu, and S. Sánchez, Inferring Non-Equilibrium Interactions from Tracer Response near Confined Active Janus Particles, *Sci. Adv.* **7**, eabd0719 (2021).

[312] G. Gompper, R. G. Winkler, T. Speck, A. Solon, C. Nardini *et al.*, The 2020 Motile Active Matter Roadmap, *J. Phys.: Condens. Matter* **32**, 193001 (2020).

[313] E. Moen, D. Bannon, T. Kudo, W. Graf, M. Covert, and D. Van Valen, Deep Learning for Cellular Image Analysis, *Nat. Methods* **16**, 1233 (2019).

[314] Z. Du, J. Yin, and J. Yang, Expanding Receptive Field YOLO for Small Object Detection, *J. Phys.: Conf. Ser.* **1314**, 012202 (2019).

[315] A. Bochkovskiy, C.-Y. Wang, and H.-Y. M. Liao, "YOLOv4: Optimal Speed and Accuracy of Object Detection", 2020.

[316] N. Wojke, A. Bewley, and D. Paulus, "Simple Online and Realtime Tracking with a Deep Association Metric", 2017.

[317] T. Ban, K. Morigaki, H. Yagi, T. Kawasaki, A. Kobayashi, S. Yuba, H. Naiki, and Y. Goto, Real-Time and Single Fibril Observation of the Formation of Amyloid β Spherulitic Structures, *J. Bio. Chem.* **281**, 33677 (2006).

[318] J. Mahato, K. K. Ray, S. Das, P. Kadu, S. K. Maji, and A. Chowdhury, Investigation of Structural Heterogeneity in Individual Amyloid Fibrils Using Polarization-Resolved Microscopy, *J. Phys. Chem. B* **125**, 13406 (2021).

[319] J. Charmet, P. Arosio, and T. P. Knowles, Microfluidics for Protein Biophysics, *J. Mol. Biol.* **430**, 565 (2018).

[320] T. P. J. Knowles and R. Mezzenga, Amyloid Fibrils as Building Blocks for Natural and Artificial Functional Materials, *Adv. Mater.* **28**, 6546 (2016).

[321] G. Gouesbet, J. A. Lock, and G. Gréhan, Partial-Wave Representations of Laser Beams for Use in Light-Scattering Calculations, *Appl. Opt.* **34**, 2133 (1995).

[322] A. Ashkin and J. P. Gordon, Stability of Radiation-Pressure Particle Traps: An Optical Earnshaw Theorem, *Opt. Lett.* **8**, 511 (1983).

[323] R. R. Agayan, F. Gittes, R. Kopelman, and C. F. Schmidt, Optical Trapping near Resonance Absorption, *Appl. Opt.* **41**, 2318 (2002).

[324] A. S. Urban, S. Carretero-Palacios, A. A. Lutich, T. Lohmüller, J. Feldmann, and F. Jäckel, Optical Trapping and Manipulation of Plasmonic Nanoparticles: Fundamentals, Applications, and Perspectives, *Nanoscale* **6**, 4458 (2014).

[325] D. R. Lide, ed., *CRC Handbook of Chemistry and Physics*, 84th ed. (CRC Press, 2003).

[326] M. L. Huber, R. A. Perkins, A. Laesecke, D. G. Friend, J. V. Sengers *et al.*, New International Formulation for the Viscosity of H_2O, *J. Phys. Chem. Ref. Data* **38**, 101 (2009).

[327] D. Rings, R. Schachoff, M. Selmke, F. Cichos, and K. Kroy, Hot Brownian Motion, *Phys. Rev. Lett.* **105**, 090604 (2010).

[328] M. Daimon and A. Masumura, Measurement of the Refractive Index of Distilled Water from the Near-Infrared Region to the Ultraviolet Region, *Appl. Opt.* **46**, 3811 (2007).

[329] I. H. Malitson, Interspecimen Comparison of the Refractive Index of Fused Silica, *J. Opt. Soc. Am.* **55**, 1205 (1965).

[330] N. Sultanova, S. Kasarova, and I. Nikolov, Dispersion Properties of Optical Polymers, *Acta Phys. Pol. A* **116**, 585 (2009).

[331] N. A. Lange, *Lange's Handbook of Chemistry*, edited by J. A. Dean, 15th ed., McGraw-Hill Handbooks (McGraw-Hill, 1999).

[332] J. F. Shackelford and W. Alexander, eds., *CRC Materials Science and Engineering Handbook*, 3rd ed. (CRC Press, 2001).

In memory of F. K.
We miss you.